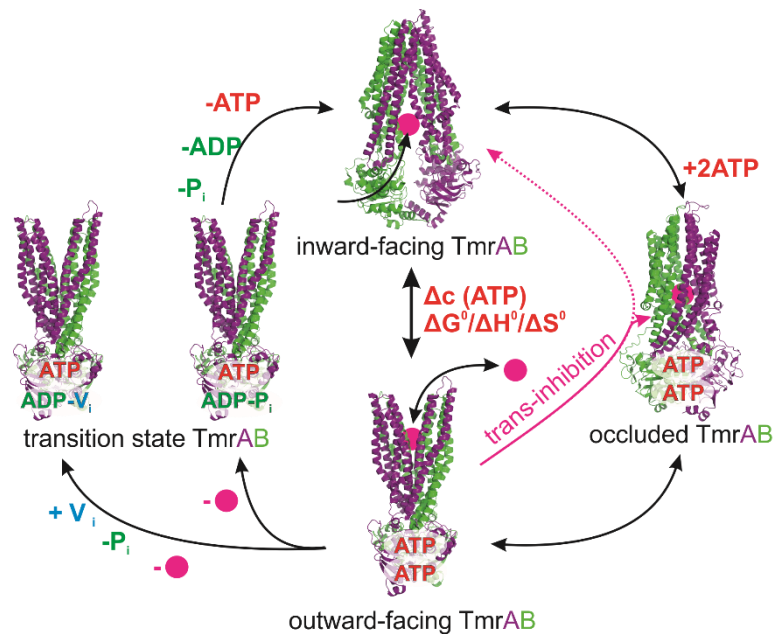


Transport mechanism of a multidrug resistance protein investigated by pulsed EPR spectroscopy



Dissertation

for attaining the PhD degree of Natural Sciences

Submitted to the Department 14

of the Johann Wolfgang Goethe University

in Frankfurt am Main

by

Katja Barth

from Wiesbaden, Germany

Frankfurt am Main 2019

(D30)

Accepted by Department 14: biochemistry, chemistry and pharmacy
of the Johann Wolfgang Goethe University as a dissertation

Dean: Prof Clemens Glaubitz

First expert assessor: Prof Thomas F. Prisner

Second expert assessor: Dr Benesh Joseph

Date of the disputation: 14.11.19

"The past can hurt. But the way I see it, you can either run from it, or learn from it."

— *Rafiki, The Lion King*

In memory of

Volker Barth (1959-2016)

Balou (2002-2015)

Abstract

In human several diseases result from malfunctions of ATP-binding cassette (ABC) systems, which form one of the largest transport system superfamily. Many ABC exporters contain asymmetric nucleotide-binding sites (NBSs) and some of them are inhibited by the transported substrate.¹ For the active transport of diverse chemically substrates across biological membranes, ABC transport complexes use the energy of ATP binding and subsequent hydrolysis. In this thesis, the heterodimeric ABC exporter TmrAB^{2,3} from *Thermus thermophilus*, a functional homolog of the human antigen translocation complex TAP, was investigated by using pulsed electron-electron double resonance (PELDOR/DEER) spectroscopy. In the presence of ATP, TmrAB exists in an equilibrium between inward- and outward-facing conformations. This equilibrium can be modulated by changing the ATP concentration, showing asymmetric behaviour in the open-to-close equilibrium between the consensus and the degenerate NBSs. At the degenerate NBS the closed conformation is more preferred and closure of one of the NBSs is sufficient to open the periplasmic gate at the transmembrane domain (TMD).³ By determining the temperature dependence of this conformational equilibrium, the thermodynamics of the energy coupling during ATP-induced conformational changes in TmrAB were investigated. The results demonstrate that ATP-binding alone drives the global conformational switching to the outward-facing state and allows the determination of the entropy and enthalpy changes for this step. With this knowledge, the Gibbs free energy of this ATP induced transition was calculated. Furthermore, an excess of substrate, meaning trans-inhibition of the transporter is resulting mechanistically in a reverse transition from the outward-facing state to an occluded conformation predominantly.³ This work unravels the central role of the reversible conformational equilibrium in the function and regulation of an ABC exporter. For the first time it is shown that the conformational thermodynamics of a large membrane protein complex can be investigated. The presented experiments give new possibilities to investigate other related medically important transporters with asymmetric NBSs or other similar protein complexes.

Table of Contents

Abstract	7
Abbreviations	13
1 Introduction	17
1.1 Overview of methodological approaches to investigate membrane proteins	17
1.2 ABC transporter	19
1.2.1 Architecture of ABC transporters	19
1.2.1.1 Structural and functional aspects of the NBDs	20
1.2.1.2 Structural and functional aspects of the TMDs	23
1.2.1.2.1 ABC importers (type I-III)	24
1.2.1.2.2 ABC exporters (type IV-V)	27
1.2.1.2.3 Extractors and Efflux pumps (type VI-VII)	32
1.2.2 The heterodimeric ABC exporter TmrAB	34
1.3 Electron paramagnetic resonance	35
1.3.1 Spin Hamiltonian	35
1.3.1.1 Electron Zeeman interaction	36
1.3.1.2 Hyperfine interaction	37
1.3.1.3 Electron spin-electron spin interaction	38
1.3.2 Site-directed spin labelling	39
1.3.2.1 Strategy for labelling positions	41
1.3.3 Nitroxide-spectrum in continuous wave EPR	42
1.3.4 Pulsed electron-electron double resonance (PELDOR)	44
1.3.4.1 4-Pulse PELDOR	45
1.3.4.2 7-Pulse CP-PELDOR	47
1.3.4.3 PELDOR data analysis	50
1.3.4.3.1 Data analysis with DeerAnalysis	50
1.3.4.3.2 Data analysis with DD	53
2 Motivation and aim	55
3 Materials, methods and sample preparation	57
3.1 Materials	57
3.1.1 Plasmid	57
3.1.2 Crystal structures and homology models	57
3.1.3 Peptides used as substrates for TmrAB	58
3.1.4 Chemicals	58

3.1.5 Nucleotides and trapping reagents	60
3.1.6 Kits and columns	60
3.1.7 Equipment	60
3.1.8 Enzymes and cells	62
3.1.9 Buffers, media and solutions	62
3.1.10 Molecular rulers and loading dyes	63
3.1.11 Software	64
3.2 Methods	64
3.2.1 Cloning of TmrAB cysteine single or double mutants	64
3.2.2 Agarose gel electrophoresis	67
3.2.3 <i>DpnI</i> fast digest	67
3.2.4 Generation of competent <i>E. coli</i> cells	67
3.2.5 Transformation and retransformation	68
3.2.6 Sequencing	68
3.2.7 Expression	69
3.2.8 Purification	69
3.2.9 MTSSL labelling of TmrAB or K5F	71
3.2.10 Preparation of liposomes	72
3.2.11 Reconstitution of protein into liposomes	72
3.2.12 Transport assay	73
3.2.13 MMM software	74
3.2.14 Continuous wave measurements	74
3.2.15 PELDOR measurements	75
3.3 Sample preparation	76
3.3.1 Samples for the investigation of the alternating access mechanism of TmrAB	76
3.3.2 Samples for the investigation of the conformational equilibrium by ATP binding	77
3.3.3 Samples for the investigation of the trans-inhibition by K5F peptide	77
4 Results	79
4.1 Alternating access mechanism of TmrAB	80
4.1.1 Mutant planning and simulations of labelling positions	80
4.1.2 Experimental distance measurements on TmrAB	86
4.1.2.1 Periplasmic gate	87
4.1.2.2 Cytosolic gate	93
4.1.2.3 Nucleotide binding domains	95

<u>4.1.3 Discussion of the alternating access mechanism of TmrAB</u>	<u>107</u>
<u>4.2 The conformational equilibrium induced by ATP binding</u>	<u>112</u>
<u>4.2.1 Influence of different ATP concentrations to the conformational equilibrium</u>	<u>113</u>
<u>4.2.2 Influence of different temperatures to the conformational equilibrium</u>	<u>121</u>
<u>4.2.3 Discussion of the conformational equilibrium induced by ATP binding</u>	<u>142</u>
<u>4.3 The role of substrate in the transport mechanism of TmrAB</u>	<u>145</u>
<u>4.3.1 Trans-inhibition of TmrAB</u>	<u>145</u>
<u>4.3.2 Discussion of the trans-inhibition of TmrAB</u>	<u>151</u>
<u>4.4 Summary</u>	<u>152</u>
<u>4.5 Outlook</u>	<u>154</u>
<u>Deutsche Zusammenfassung</u>	<u>159</u>
<u>List of amino acids</u>	<u>165</u>
<u>List of figures</u>	<u>167</u>
<u>List of tables</u>	<u>171</u>
<u>Supporting information</u>	<u>173</u>
<u>Cooperation partner</u>	<u>181</u>
<u>References</u>	<u>183</u>
<u>Acknowledgement</u>	<u>197</u>

Abbreviations

ABC	ATP-binding cassette
ADP	adenosine diphosphate
AMP-PNP	adenylyl imidodiphosphate
ATP	adenosine triphosphate
ATPase	adenosine triphosphatase
bp	base pair
CP	Carr-Purcell
Cryo-EM	cryo-electron microscopy
cw	continuous wave
DD	dipole-dipole coupling
DD (software)	DEER data
ddH ₂ O	double distilled water
DDM	<i>n</i> -dodecyl- β -D-maltopyranoside
DEER	double electron-electron resonance
DMSO	dimethyl sulfoxide
DNA	deoxyribonucleic acid
DNase	deoxyribonuclease
DNP	dynamic nuclear polarization
dNTP	deoxyribonucleotide triphosphate
DOPC	dioleoyl- <i>sn</i> -glycero-3-phosphocholine
DTPA	diethylenetriaminepentaacetic acid
<i>E. coli</i>	<i>Escherichia coli</i>
ECF	energy coupling factor
EDNMR	ELDOR-detected nuclear magnetic resonance
EDTA	ethylenediamine tetraacetic acid

e.g.	<i>exempli gratia</i> , for example
ELDOR	electron-electron double resonance
ELISA	enzyme-linked immunosorbent assay
ENDOR	pulse electron-nuclear double resonance
EPR	electron paramagnetic resonance
ER	endoplasmic reticulum
ESR	electron spin resonance
FC	Fermi contact
FRET	Förster resonance energy transfer
HEPES	4-(2-hydroxyethyl)-1-piperazineethanesulfonic acid
HPLC	high-pressure liquid chromatography
IASL	iodacetamido
IMAC	immobilized metal ion chromatography
IPTG	isopropyl- β -D-thiogalactopyranoside
<i>L. brevis</i>	<i>Lactobacillus brevis</i>
LB	Lysogeny Broth
LLO	lipid-linked oligosaccharides
LPS	lipopolysaccharide
MAS	magic angle spinning
MBP	maltose-binding protein
MD	molecular dynamics
MMM	Multiscale Modelling of Macromolecular systems
mRNA	messenger RNA
MSL	maleimido

MTSSL/MTSL	(1-oxyl-2,2,5,5-tetramethylpyrroline-3-methyl)-methanethiosulfonate
NBD	nucleotide binding domain
NBS	nucleotide binding site
NMR	nuclear magnetic resonance
NO	nitroxide
NOE	nuclear overhauser effect
NOESY	nuclear overhauser effect spectroscopy
NTA	nitriolotriacetic acid
NTPase	nucleotide triphosphatase
OD	optical density
P-gp	P-glycoprotein
P _i	orthophosphate
PBS	phosphate-buffered saline
PCR	polymerase chain reaction
PDB	protein data bank
PEI	polyethylenimine
PELDOR	pulsed electron-electron double resonance
PIPES	piperazine-N,N'-bis(2-ethane sulfonic acid)
PLS	proteoliposomes
PRE	paramagnetic relaxation enhancement
R1	unnatural side-chain after MTSSL labelling
RDCs	residual dipolar couplings
RNA	ribonucleic acid
SAXS	small-angle X-ray scattering

SDS	sodium dodecyl sulfate
SDSL	site-directed spin labelling
ssNMR	solid-state nuclear magnetic resonance
TEMPOL	4-hydroxy-2,2,6,6-tetramethylpiperidin-1-oxyl
TM	transmembrane
TMD	transmembrane domain
TRIS	tris(hydroxymethyl)aminomethane
UV-Vis	ultraviolet-visible spectroscopy
w/v	weight per volume
v/v	volume per volume
V _i	ortho-vanadate

1 Introduction

1.1 Overview of methodological approaches to investigate membrane proteins

The class of membrane proteins plays a major role in cell communication, transport across membrane barriers, the use of energy and also in triggering the initiation of signalling pathways.⁴ As membrane proteins are important drug targets, structure determination and the transition from structure to mechanism become highly important.^{4,5} In primary active transporters, like ATP-binding cassette (ABC)-transporters, the energy is delivered by ATP hydrolysis and in secondary active transporters by ion translocation.⁵

Due to their specific functional role proteins can have different conformational dynamics or underlying mechanisms, although they adopt similar folds.⁶ There are various methods that can address different questions in the investigation of the structure and function of an ABC transporter. Although the structure of a membrane protein or also a homology model, if a structure determination is not possible, gives a lot of information about the protein, it remains a static picture.⁷ Yet, by knowing the structure it becomes possible to plan experiments on a reasonable basis.⁷

For the determination of the fundamental structure, methods that can be used include X-ray crystallography, Small Angle X-ray Scattering (SAXS) or Cryo-Electron Microscopy (Cryo-EM). With X-ray crystallography it is possible to resolve the atomistic structure with a high resolution (standard medium resolution starts at 2.7 Å, a 1.2 Å resolution can resolve the full atomic constitution⁸), but due to crystal packing it is not possible to gain information about the structure and dynamics of molecules in their natural environment for membrane proteins. Moreover, it is challenging in crystallography to find the ideal conditions to crystallize the protein and to resolve its different conformational states. Another possibility for structure determination is SAXS, which gives a snapshot of the thermodynamic state in a buffer solution, without broadening or attenuation of the signal, if applied to dynamic or flexible systems.⁹ While in X-ray crystallography a crystalline order is necessary for diffraction reflections, scattering of a macromolecule with SAXS is always possible. Nevertheless, SAXS is a low-resolution method, which can gain resolutions of 10-20 Å.¹⁰ In addition to that, Cryo-EM is a widely used method to solve structures since this method can also investigate biologic macromolecules in different conformations in their native environment.¹¹ In comparison to X-ray spectroscopy, a smaller amount of sample is required and furthermore very large protein complexes can be investigated.¹¹ In Cryo-EM a lower molecular weight limit is the main challenge, which is expected around 38 kDa and is characterized by a low signal to noise ratio.¹¹

If a structure is resolved, other methods are required to get further insights into the function, dynamics and mechanisms of membrane proteins since the structure only gives a static picture as already mentioned. At this point spectroscopic methods like nuclear magnetic resonance (NMR), electron paramagnetic resonance (EPR) or Förster resonance energy transfer (FRET) can be used, which gain insight in different time scales and amplitude of structural changes.⁶ In the case of liquid-state NMR, it is possible to resolve the structure and heterogeneity of proteins at high resolution and to monitor conformational changes of the backbone to the domain levels with high sensitivity. Nevertheless, most membrane proteins are not suitable for liquid-state NMR,⁶ because of size restrictions (up to 50 kDa).¹² These restrictions can be partially overcome with solid-state NMR (ssNMR) together with magic angle spinning (MAS).¹³ With ssNMR it is moreover possible to investigate membrane proteins in phospholipid bilayers, which give a similar environment compared to biological membranes in contrast to detergent solutions.¹³ To overcome the small energy difference of the nuclear spin states and the small Boltzmann polarization, which leads to the intrinsically low sensitivity of liquid NMR and ssNMR, it is possible to use dynamic nuclear polarization (DNP).¹⁴ With DNP the high polarization of an electron spin can be transferred to a nuclear spin like ^1H or ^{13}C , which results in an increase of the NMR signal.¹⁴ Based on the nuclear overhauser effect (NOE) it is possible to determine qualitatively distances in proteins with NMR spectroscopy. With the development of two-dimensional NMR spectroscopy nuclear overhauser effect spectroscopy (NOESY) experiments can be used to obtain distance restraints in the range of 0.5-0.7 nm.¹⁵ To determine longer distances with NMR spectroscopy, Residual Dipolar Couplings (RDCs) or Paramagnetic Relaxation Enhancement (PREs) (3 – 3.5 nm) are detected, which are both labelling-based techniques.¹⁵

FRET¹⁶ and EPR^{17,18} are important techniques to investigate membrane proteins since they are not dependent on the size of the biomolecule which is of interest.

With single-molecule FRET, it is possible to monitor the kinetics of a conformational change of individual molecules, in a distance range of 1-10 nm.¹⁹ Yet, relatively large labelling-probes are necessary, which is a limiting factor for placement of the probes in the sequence and might affect conformational changes of the membrane protein. In addition, the extraction of distances from FRET efficiencies is not straight-forward.^{6,16,19}

The analysis of a spin-labelled protein with EPR makes it possible to directly observe structural rearrangements in domains and secondary structural elements in detergent micelles, proteoliposomes and nanodiscs. Furthermore, small amounts of proteins are

sufficient for EPR measurements because of a larger Boltzmann polarization compared to NMR. Finally, the typically smaller probe size of EPR spin labels gives negligible structural and functional perturbations of the conformations and the shorter linker leads to higher accuracy of the observed distance distribution compared to FRET.⁶ With continuous wave (cw) EPR it is possible to measure distances up to 1.8 nm and to investigate dynamics.¹⁸ To measure larger distances with EPR spectroscopy, pulsed techniques like pulsed electron-electron double resonance (PELDOR) are necessary, which is also called double electron-electron resonance (DEER). With PELDOR it is possible to measure distances in the range of 2-8 nm.^{18,20} For longer distances Carr-Purcell pulsed electron-electron double resonance can be used, where the time window can be prolonged.²¹

Besides the afore mentioned experimental approaches, molecular dynamics (MD) simulations can be used to study membrane proteins.²² Various improvements in the field of MD simulations made it possible to already investigate conformational ensembles²² or especially for ABC transporters the cycle for conformational changes during ATP hydrolysis.²³ Nevertheless, for ABC transporters, it was not yet possible to observe any transport events due to the fact that MD simulations are mainly limited by computational power and the lack of initial structures.²³

In this thesis, EPR spectroscopy was used to investigate the heterodimeric ABC exporter TmrAB from *Thermus thermophilus*.

1.2 ABC transporter

In the class of ATP-binding cassette (ABC) transport complexes the use of ATP binding and subsequent hydrolysis of the bond between the γ - and the β -phosphate is necessary to translocate substrates across membranes.^{1,24,25} By conversion of ATP to ADP and the orthophosphate (P_i) in the transport process approximately $-30.5 \text{ kJ mol}^{-1}$ energy is released, which is necessary for the translocational movement of substrates across membranes.²⁵ This transporter class has been widely investigated and several reviews^{1,23-28} and books^{29,30} show the current scientific knowledge of ABC transporter systems. The following section lays the basis for the understanding of the complexity of the ABC transporter classes. In the result part, more details are explained where it is relevant.

1.2.1 Architecture of ABC transporters

Primarily ABC transporters can be classified into importers, exporters and extruders, according to the direction of substrate translocation. Various different substrates can be

transported across membranes, like antibiotics, toxins, vitamins, steroids, lipids, ions, polysaccharides, peptides and proteins.¹ While ABC exporters are found in all three phyla of life, ABC importers are only found in bacteria, chloroplasts and mitochondria of plants.³¹

In general, all ABC transporters contain two solvent-exposed, conserved nucleotide binding domains (NBDs), which can bind and hydrolyse ATP and two transmembrane domains (TMDs) which are variable and form the pathway necessary for the substrate translocation. NBDs and TMDs are shown schematically in Figure 1.

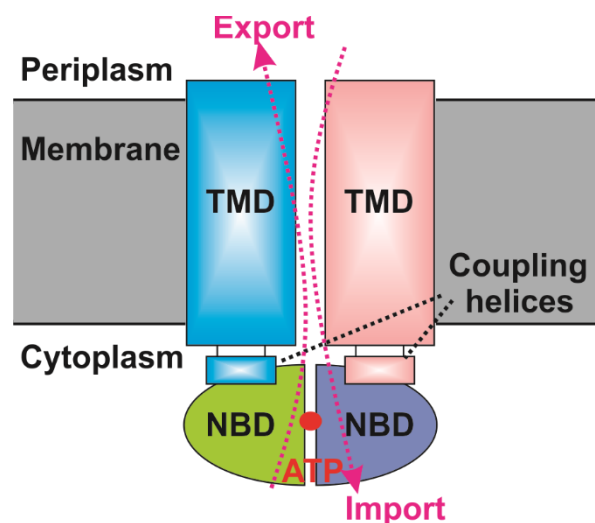


Figure 1: Schematic architecture of an ABC transporter: Two TMDs are located in the membrane and coupled to two NBDs via two coupling helices. The NBDs are located in the cytoplasm and bind and hydrolyse ATP, while the TMDs build a pathway through the membrane from the cytoplasm to the periplasm for substrate export and in the other direction for substrate import. (Based on the model of [24])

In eubacteria and archaea, NBDs and TMDs often exist as distinct subunits, while in higher organisms they are usually combined into half-transporters, containing one NBD and one TMD each. If an ABC transporter is assembled from two half-transporters, it can either be homodimeric or heterodimeric. The NBDs contain several conserved motifs that are necessary for ATP-binding and hydrolysis, as for the communication between both NBDs and the TMD and NBD interaction. Another possibility is a full-transporter containing all four domains in a single polypeptide chain.³²

1.2.1.1 Structural and functional aspects of the NBDs

The NBDs are characterised by a highly conserved structure and sequence, therefore they are the hallmark of the ABC family. In every ABC transporter, two NBDs are present which

are responsible for ATP binding and hydrolysis in the presence of catalytic magnesium ions. They belong to the superfamily of P-loop nucleotide triphosphatases (NTPases)³³ and consist of two subdomains, the larger RecA-like domain, which can also be found in other P-loop adenosine triphosphatases (ATPases), and an α -helical subdomain, that can only be found in ABC transporters.^{1,24,25}

Significant for the role of the NBDs in the transport process are seven highly conserved motifs, which are shown in Figure 2, illustrated by the heterodimeric ABC exporter TmrAB (pdb code 5MKK).²

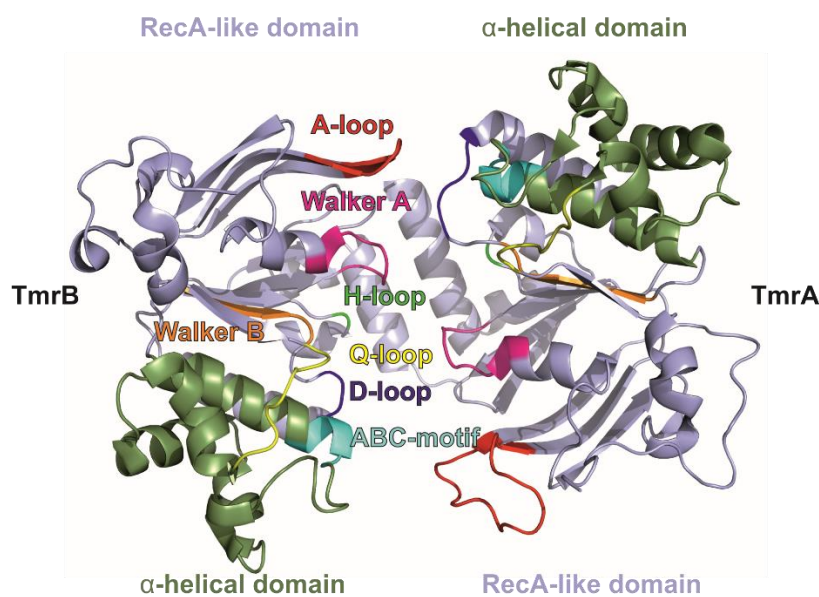


Figure 2: Conserved motifs of the NBDs shown by the heterodimeric ABC exporter TmrAB (pdb code 5MKK). View from the top onto the NBDs with all the highly conserved sequence motifs highlighted in the following colour code: α -helical domain – green, RecA like domain – light blue, A-loop – red, Walker A – magenta, Walker B – orange, D-loop – blue, H-loop – green, ABC motif – cyan, Q-loop – yellow.

The aromatic residue in the A-loop (red), which is usually a tyrosine, helps to position the ATP by stacking with the adenine ring. Also involved in the ATP-binding is the P-loop or Walker A-motif (magenta; GXXGXGK(S/T) – X can be any amino acid), which is a phosphate-binding loop containing a highly conserved lysine residue. Here the amide nitrogens of the backbone and the ϵ -amino group of the lysine form a network of interactions with the β - and γ -phosphate of ATP. The Walker B-motif (orange; $\phi\phi\phi\phi$ DE – ϕ can be any hydrophobic amino acid) supports the coordination of the catalytic magnesium ion via the conserved aspartate residue. In addition, the second acidic residue at the end of the Walker

B-motif, which is often glutamate, is very likely the general base that polarizes the attacking water molecule.

Directly after the Walker B-motif follows the D-loop (blue; SALD), where the two monomers from the dimeric ensemble run parallel. As a consequence changes in their conformation affect the geometry of the catalytic site and support the formation of the ATP hydrolysis site. The H-loop (green) or switch region contains a highly conserved histidine residue which forms a hinge between a β strand and the α helix close by the C-terminus of the NBD. This histidine residue builds interactions with the conserved aspartate of the D-loop and with the γ -phosphate of ATP and thereby helps with the positioning of attacking water, the general base and the magnesium ion.

Located at the interface between the RecA-like and the α -helical subdomains, the Q-loop (yellow) contains approximately eight residues with a conserved glutamine residue at its N-terminus. Changes in the conformation of the Q-loop allow the conserved glutamine residue to move in and out of the active site during the cycle of ATP hydrolysis, thereby forming the active site when Mg-ATP is bound and breaks it when ATP is hydrolysed. In addition, the Q-loop plays also a role in the interaction with the TMDs.

The last important conserved motif is the ABC signature motif or C motif (cyan; LSGGQ) which is located in the α -helical subdomain and is only found in the ABC superfamily and not in other P-loop NTPases. It is found at the N-terminal end of a long helix that guides the positive charge of the helical dipole towards the γ -phosphate of ATP.²⁵

As shown in Figure 3a, the NBDs in ABC transporter can have different orientations towards each other. They either can be in an open conformation (left), where the two nucleotide binding sites (NBSs) are free, or in a closed conformation (right), where ATP is bound to both NBSs. As shown in the top view (Fig. 3b), two ATP-binding sites exist at the interface between the NBDs, which are connected by twofold (pseudo) symmetry. The NBDs are coupled to the TMDs via coupling helices, which lead to open TMDs at the cytoplasmic side and closed TMDs at the periplasmic side when the NBDs are open. When ATP is bound the NBDs are closed which leads to a closing of the TMDs at the cytoplasmic side and an opening on the periplasmic side. This ATP binding process and closing mechanism are supported by all the conserved motifs mentioned previously. After ATP hydrolysis, which is only possible if the NBDs are packed against each other as indicated (Fig. 3b), ADP and P_1 get released and the NBDs can move apart. If one or more of the conserved amino acids are substituted, this leads to a non-canonical ATP-binding site,

where ATP binding is assumed to be still possible, but ATP hydrolysis should not be possible anymore, which is a typical feature of heterodimeric transporters.

During ATP hydrolysis the chemical energy can be transformed into a mechanical force for alternating access of the substrate-translocation pathway in the TMDs to the periplasmic or the cytosolic side of the membrane.²⁵

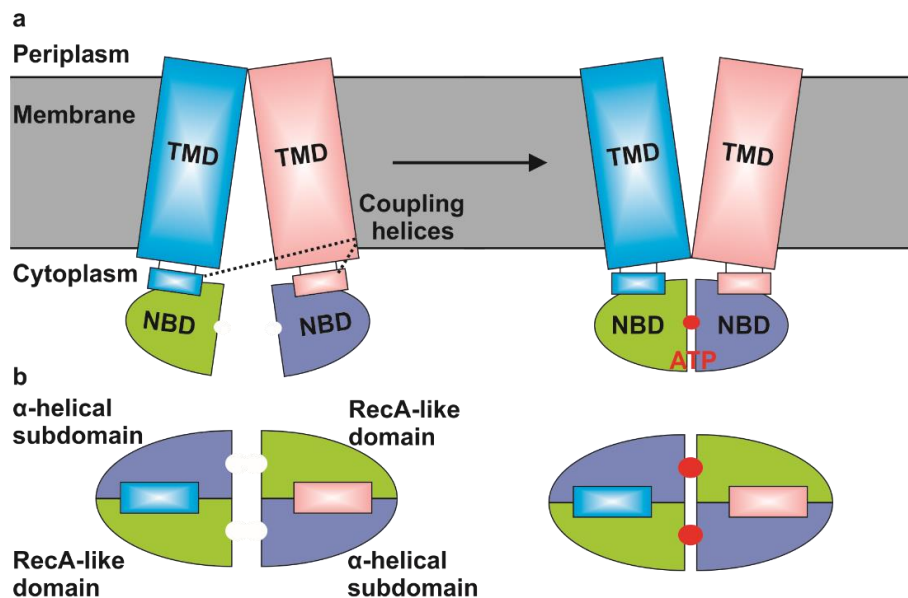


Figure 3: Schematic representation of NBDs and coupling helices. (a) Side view from the membrane plane, in which the NBDs are coupled to TMDs located in the membrane via coupling helices on the cytoplasmic side. On the left NBDs are open and the ATP binding sites are free, while on the right the NBDs are closed upon ATP-binding. (b) Top view on the twofold (pseudo) symmetry of the NBDs. On the left, both ATP binding sites are free, while on the right the NBDs are closed by ATP binding in both ATP-binding sites. (Based on the model of [25])

In prokaryotes, ABC transporters are localized in the plasma membrane, with ATP hydrolysis taking place on the cytoplasmic side. In eukaryotes, ABC transporters are also located in organelle membranes, where ATP hydrolysis is taking place on the cytosolic side of the membrane. In mitochondria and chloroplasts, the ATP binding domains are located on the matrix or stroma side.²⁵

1.2.1.2 Structural and functional aspects of the TMDs

While the NBDs are highly conserved through all ABC transporter classes, the two TMDs, which form the substrate translocation pathway, are highly variable. Based on their sequence and structural homology in the TMDs it is possible to classify ABC transporter into seven distinct types, which can be further grouped by their function. Responsible for

substrate import are types I-III, while types IV and V function as substrate exporter and members of type VI function as extractors. Type VII ABC transporters are representatives which are included in efflux pumps and therefore act as lipoprotein extractors or regulate cell division.¹

1.2.1.2.1 ABC importers (type I-III)

As shown in Figure 4 there are three types of ABC importers, illustrated with the X-ray structures of the *Escherichia coli* (*E. coli*) maltose transporter MalFGK₂³⁴ (type I; Figure 4a), the *E. coli* vitamin B12 transporter BtuCD³⁵ (type II; Figure 4b) and the folate³⁶ energy-coupling factor (ECF) transporter from *Lactobacillus brevis* (*L. brevis*) (type III; Figure 4c).

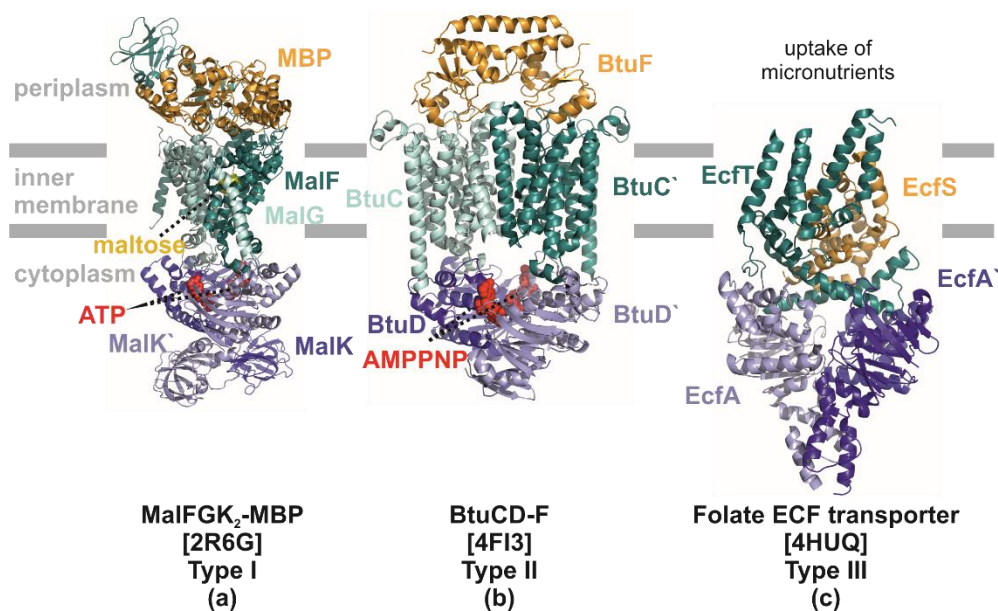


Figure 4: Representative bacterial ABC importers involved in substrate uptake: (a) Crystal structure of the maltose importer MalFGK₂ from *E. coli*, a type I ABC transporter, in complex with the maltose-binding protein (MBP) located in the periplasm (pdb code 2R6G). (b) Crystal structure of the vitamin B₁₂ importer BtuCD from *E. coli*, a type II ABC transporter, in complex with the substrate-binding protein BtuF situated in the periplasm (pdb code 4FI3). (c) Crystal structure of the folate energy-coupling factor (ECF) importer from *L. brevis*, a type III ABC transporter, in complex with the folate-binding protein EcfS located in the inner membrane (pdb code 4HUQ). (Based on the model of [1])

Importers of type I and II, which are primarily found in bacteria, feature TMDs that consist of five to ten transmembrane (TM) helices.¹ Type I importers enable the uptake of diverse nutrients including ions, sugars, amino acids, short peptides and oligosaccharides. Based on the well-studied maltose transporter from *E. coli*, a mechanism for type I importers can be proposed (Figure 5a).²⁴ The transport cycle starts putatively in an inward-facing

conformation, where the TMDs are closed on the extracellular side and open to the cytoplasm, while the NBDs are separated. Hereby a substrate-loaded binding protein located on the extracellular side is approaching (state 1, Figure 5a). From state 1 to state 2 the key conformational transition is the closing of the NBDs, which moves the coupling helices towards each other and thereby converts the TMDs into an outward-facing conformation. This conformational change leads to the formation of a tunnel between the attached binding protein and a low-affinity substrate-binding pocket located halfway across the membrane (state 2, Figure 5a).²⁴

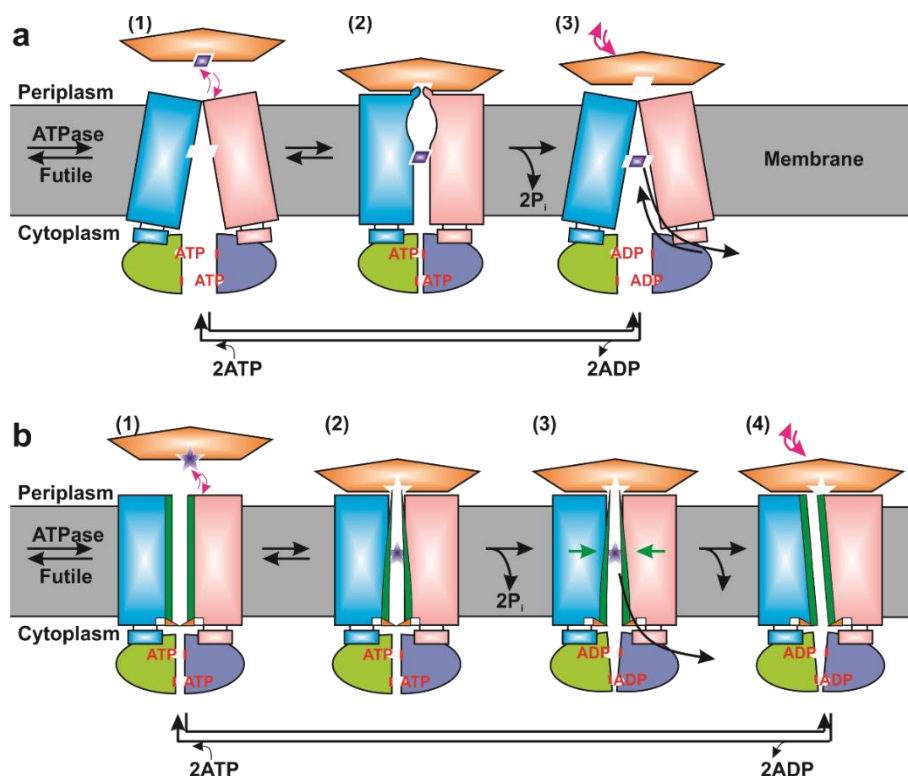


Figure 5: Mechanisms of type I and II ABC importers, with the following colour code: TMDs in blue and rose, NBDs in green and dark blue, binding proteins in orange, substrates in dark violet, ATP and ADP are shown in red, P_i represents the inorganic phosphate and the red lines in the NBDs display the ABC signature motifs. (a) Import mechanism of a type I transporter shown schematically. (b) Schematic view of type II import mechanism containing three distinct gates. Represented by dark green lines is TM5 in the TMDs and shows cyto gate 2, which is formed by the loop between TM2 and TM3. The small green arrows in state 3 indicate forces working on the translocation pathway and trapped substrate. (Based on the model of [24])

Especially in the maltose transporter, two specific effects lead to the release of the substrate from the binding protein: The binding pocket is slightly distorted and the periplasmic TMD loops arrange a steric clash with the bound substrate.³⁴ In the irreversible step from state 2 to state 3 ATP is hydrolysed and inorganic phosphate (P_i) gets released. Therefore, the NBD

dimer is opening and pulling the coupling helices outward, which triggers the conversion to an inward-facing conformation, whereby the substrate can be released into the cytoplasm. By the exchange of ADP to ATP the system gets finally restored (state 3 to 1, Figure 5a).³⁵

In type II ABC importers, which are generally part of high-affinity uptake pathways for metal chelates including heme and other iron-containing complexes and cobalamins, the substrates are larger and more hydrophobic compared to type I ABC importers. In addition, the substrates are only available at low concentrations.²⁴ A mechanism for type II importers can be proposed based on the vitamin B12 transporter BtuCD-BtuF (BtuCD-F) from *E. coli*^{35,37} and is shown in Figure 5b. There is no measurable affinity for vitamin B12 in the TMDs of BtuCD-F, which is different compared to the maltose transporter. Based on the crystal structures^{35,37} three gate regions are found in the transmembrane BtuC subunit, whereby two are located on the cytoplasmic side (cyto gates 1 and 2) and one on the periplasmic side (peri gate).

Different to type I importers, ATP binding and hydrolysis does not itself generate an inward-facing conformation. Instead, the two cytoplasmic gates separate the cytoplasm from the main translocation pathway in both the ATP-bound and the nucleotide-free states, as long as no substrate is available. The import cycle is supposed to start in an ATP-bound state (state 1, Figure 5b) with the NBDs closed and the coupling helices pushed together, therefore closing cyto gate 2. This is an outward-facing conformation since the peri gate is open. For a conformational change to state 2, the docking of the substrate-binding protein and release of the substrate into a hydrophobic cavity is necessary. Like in type I importers the high-affinity pocket in the substrate-binding protein is distorted by docking and the loops of the TMD cause a steric clash. In the following irreversible conformational change from state 2 to state 3, ATP hydrolysis and the release of phosphate is taking place. In this step, the NBD dimer has to at least open partially and thereby is separating the coupling helices and opening cyto gate 2. Because of the size of the transported substrate cyto gate 1 cannot be closed, which probably is leading to a tensed conformation and pressure from the sides to the substrate, which might contribute to the substrate release to the cytoplasm. Upon substrate release, BtuCD changes into a relaxed conformation (state 4, Figure 5b), in which cyto gate 1 and peri gate are closed and therefore does not contain a central cavity anymore. This asymmetric structure is unique to type II importers and is a very stable conformation, especially *in vitro*. On the pathway back to state 1, the transporter might be restored via an

inward-facing conformation which is nucleotide-free. Since this state has not been observed yet, it is not included in the cycle shown in Figure 5b.²⁴

Type III systems are responsible for the uptake of certain micronutrients into eubacteria and are moreover found in archaea and plants. As shown in Figure 4c, ECF systems are not built by two related TMDs, but rather contain a transmembrane component (EcfT) and a membrane-embedded substrate-binding protein (EcfS).¹ The number of helices, which build the transmembrane component, varies for different ECF systems. In the case of ECF type systems, no additional substrate-binding protein is necessary since the membrane-embedded substrate-binding protein, also called S-component, binds and transports the substrate with high affinity. This S-component contains a core of six TM-helices, while a few S-components also contain an additional N-terminal helix³⁸, and it is assumed that the translocation pathway is restricted to this part of the transporter, where an unique alternating access mechanism is ongoing.²⁵ So far it was not possible to elucidate the transport mechanism of this type since only crystal structures without substrate are available. Especially in EcfT, two long X-shaped α -helices interact with the NBDs and the S-component of the complex. Therefore, the coupling of transitions in the NBDs and proposed changes in the S-component have to be mediated by EcfT. A scissor-like movement of the α -helices could change the orientation of the S-component or might dissociate from the complex during the cycle.²⁵

1.2.1.2.2 ABC exporters (type IV-V)

Grouped into seven subfamilies, ABCA to ABCG, the human genome encodes 48 different ABC proteins (*E. coli* encodes 80 and *Saccharomyces cerevisiae* 31 ABC transporters respectively)³⁹. Thereby the ABC proteins are sorted by their gene organization and their auxiliary domains.⁴⁰

All known eukaryotic ABC transport systems are exporters, except the retinal importer ABCA4, the chloride channel CFTR⁴¹⁻⁴³ and the sulfonylurea receptors SUR1⁴⁴⁻⁴⁷ and SUR2. ABC transporters of the subfamilies ABCB and ABCC and very likely ABCD contain six TM helices, which are arranged in a typical way for type IVABC systems. This was first shown for the bacterial resistance protein Sav1866⁴⁸. Due to differences in their domain organization and other structural elements, it is possible for human ABC proteins to fulfil various different physiological functions, like removal of xenobiotics, translocation of lipids and antigenic peptides or chloride ion conduction.¹

The architecture of the TMDs in human ABCA and ABCG proteins (type V) is different compared to other subfamilies, which has been shown for the structures of ABCA1, ABCG2 and ABCG5/ABCG8. In the ribosome recycling factor ABCE1, which is the only ABCE member, and the three ABCF proteins no transport function is present, due to the lack of any TMDs.¹ Instead they are involved in protein translation⁴⁹ and mRNA surveillance⁵⁰. Important examples of eukaryotic ABC exporters are CFTR^{41–43}, TAP1/2⁵¹, SUR1^{44–47} and MRP1³¹. Malfunction of CFTR leads to the most frequent hereditary disease cystic fibrosis. TAP1/2, which is part of the MHC I peptide loading complex⁵², is responsible for the transport of peptides across the ER-membrane and thereby plays an important role in the immune system. SUR1 is serving as a regulatory subunit in Kir6.2⁵³, which is an integral membrane protein and both together, SUR1 and Kir6.2 build a potassium ion channel which has been associated with congenital hyperinsulinism and neonatal diabetes. At last, MRP1 extrudes a wide range of anti-cancer drugs in tumour cells and is associated with chemotherapy failure.³¹

In Figure 6 two types of ABC exporters are shown, illustrated with the X-ray structures of the *Campylobacter jejuni* flippase PglK⁵⁴ (type IV; Figure 6a), the exporter MsbA⁵⁵ from *E. Coli* (type IV; Figure 6b) and the O-antigen transporter Wzm-Wzt from *Aquifex aeolicus* (type V; Figure 6c).

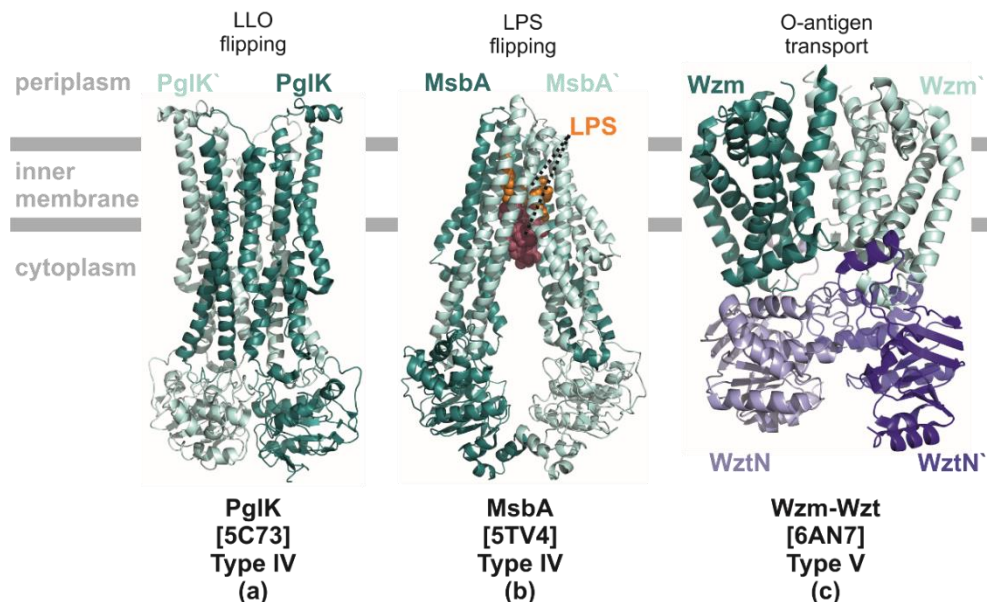


Figure 6: Representative bacterial ABC exporters: (a) Crystal structure of the flippase PglK from *Campylobacter jejuni* (pdb code 5C73), a type IV ABC transporter. (b) Crystal structure of the exporter MsbA from *E. coli* (pdb code 5TV4), also a type IV ABC transporter. (c) Crystal structure of the O-antigen transporter Wzm-Wzt from *Aquifex aeolicus*, a type V ABC transporter (pdb code 6AN7). (Based on the model of [1])

ABC transporters have a broad substrate specificity, they are not only restricted to hydrophilic, water-soluble substances, but approximately half of the transporters are involved in the translocation of lipidic substrates⁵⁶. These ABC transporters, called flippases, move lipid-linked polar substrates through the membrane leaflets. One example in bacteria is PglK (Figure 6a, type IV), that flips lipid-linked oligosaccharides (LLOs) from the cytoplasm to the periplasmic leaflet, where its glycan moieties are provided for protein N-glycosylation. The actual mechanism of this flipping process remains unknown. The occluded conformation, which is shown in Figure 6a, seems to be an important intermediate of the translocation cycle. A unique feature of PglK is a short helix at the periplasmic side of the membrane, which forms a hydrophobic groove. Based on biochemical experiments an ‘outward-only’ mechanism has been proposed for the flipping. In the beginning, the substrate lipid anchor has to interact with the hydrophobic groove PglK with bound ATP, where a positively-charged collection of arginines is exposed in a cavity of the outward-facing flippase. The substrate with its hydrophilic head group moves from the cytoplasmic side to the arginines, where the pyrophosphates build strong interactions, which finally lead to a reorientation of the head group. By ATP hydrolysis and release of the free phosphate that is stimulated by LLO binding, the LLO gets finally flipped through the small TMD opening. This happens via occluding the arginine assembly and pushing the polar head group into the aqueous phase.¹

Another representative of type IV exporters is MsbA, shown in Figure 6b, which is a homodimeric ABC transporter and carries out lipid-A-core flipping.⁵⁷ Elucidation of the structure in the nucleotide-free (apo) state (Figure 6b), the ADP-vanadate-bound state and the ADP-bound state revealed further understanding of the substrate identification by MsbA.⁵⁵ In the nucleotide-free structure, electron density in the cryo-EM structure showed that co-purified lipopolysaccharide (LPS) is binding deeply inside a pocket, which is formed by the TMDs, whereby the acyl chains are already located at the height of the periplasmic leaflet. It has been shown that lipid A-core binding is supported by hydrophobic and hydrophilic interactions. In addition, affinity and substrate specificity are given by interactions with the glucosamines and the acyl chains, whereas the core oligosaccharide remains more flexible. The entry pathway is suggested to be at an opening between TM4 and TM6. In the ADP-vanadate trapped state an occluded conformation is observed, in which the LPS-binding site is inhibited by TM helices, similar to a post flipping state. All

in all the mechanism of MsbA seems to be different compared to PglK, nevertheless, they belong to the same transporter type.¹

A representative of the last exporter class (type V), Wzm-Wzt⁵⁸ is shown in Figure 6c. In this transporter, Wzm forms a central transmembrane pathway, which is open to the intracellular and periplasmic side and the substrate entry and exit are controlled by cytosolic and periplasmic gate helices. The assembly of the TMDs is different compared to PglK, but similar to mammalian ABCA and ABCG subfamilies. Because of the closed structure of the isolated NBDs and functional experiments, a transport mechanism for O-antigen transport was proposed, which is different to other classical alternating access mechanisms, and seems to be typical for transporters with polymeric substrates⁵⁹. In the absence of substrate, the transmembrane pathway has to be closed for Wzm-Wzt to prevent leakage of solutes. By binding of the lipid anchor to the cytosolic gate and recognition of the O-antigen by the carbohydrate domains, the opening of the pathway gets triggered. Afterwards, the lipid head group is suggested to move into the channel and flip to the periplasmic side. It is not known if this mechanism either happens spontaneously or by energy from the proton-motive force through the inner membrane. In the next step, the polysaccharide is transported through the channel in a stepwise manner, driven by various ATP binding and hydrolysis steps. When the substrate is released the transporter moves back into the closed resting state.¹

Although new insight into different transporters could be gained, it is not yet possible to fully understand the whole mechanism e.g. the catalyzed lipid-flipping. It is moreover not possible to define a general mechanism for ABC exporters, because it seems like there is a high variation for different transporters.

This diversity is illustrated in Figure 7, where different mechanisms are shown schematically. In 7a the classical alternating access mechanism is shown for MsbA, where the transporter is in an inward-facing-state without nucleotide (state 1), in which the substrate, here lipid A, can bind (state 2). By ATP binding the transporter gets converted into an outward-facing conformation, where the substrate can be released (state 3) and the NBDs are closed. After ATP hydrolysis the transporter gets restored, back to the inward-facing conformation, whereby ADP gets released.²⁸

For McjD (Figure 7b) an occluded conformation is typical in absence of nucleotides and substrate, in which the TMDs are closed on both the periplasmic side and the cytosolic side (state 1), but the NBDs are separated. When ATP and the antibacterial peptide MccJ25 are

present, the substrate enters the TMDs, where it is bound in an occluded conformation (state 2), in which the NBDs are closed upon ATP binding. For substrate-release, the TMDs are opening on the periplasmic side (state 3), afterwards, the TMDs are closing again on the periplasmic side and the transporter moves back to an occluded conformation, with bound ATP (state 4). After ATP hydrolysis McjD gets restored (back to state 1).²⁸

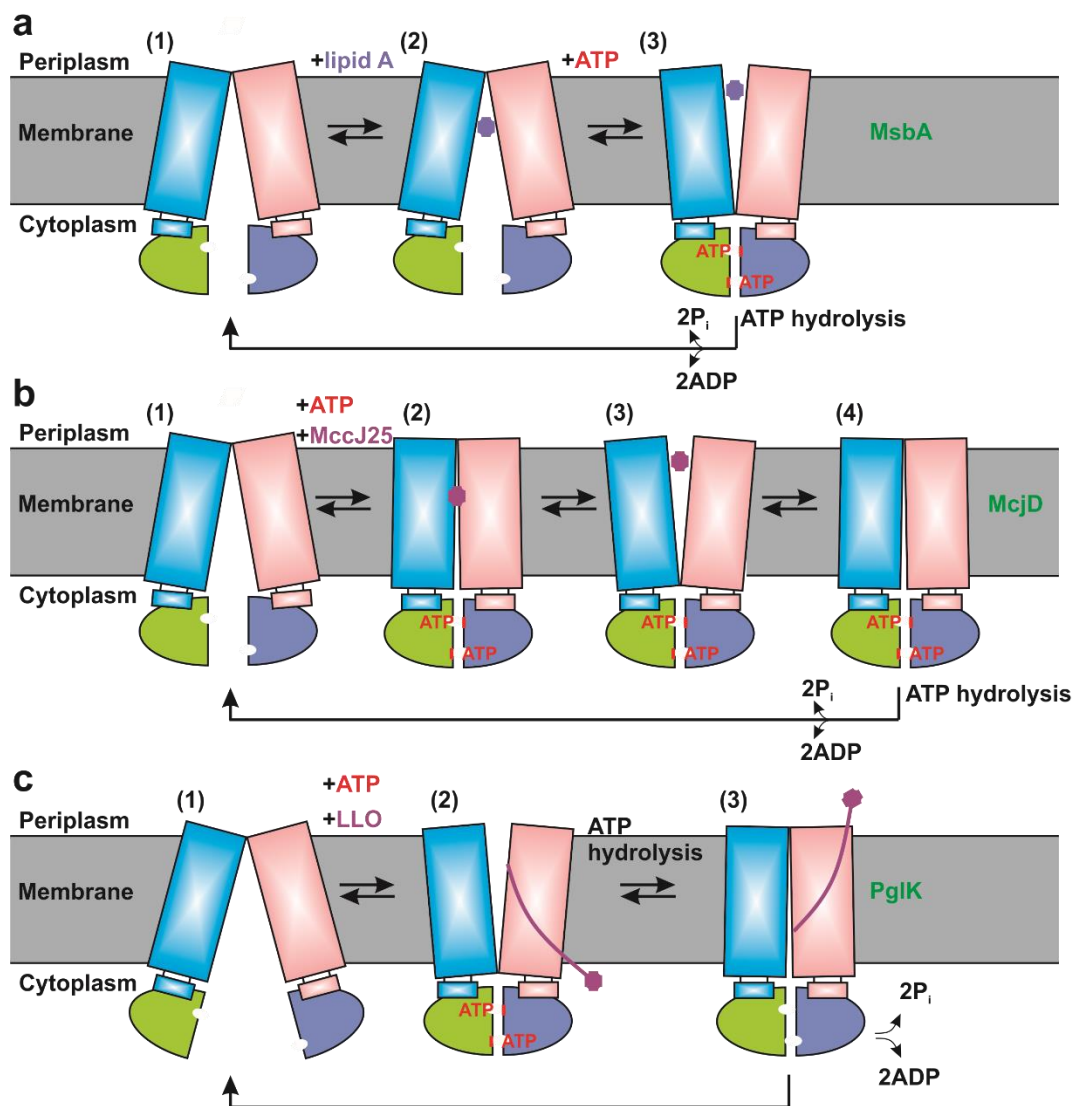


Figure 7: Mechanisms of ABC exporters with the following colour code: TMDs in blue and rose, NBDs in green and dark blue, substrates blue or violet as indicated, ATP is shown in red, P_i represents the inorganic phosphate and the red lines in the NBDs display the ABC signature motifs. (a) Alternating access mechanism of MsbA. (b) Export mechanism of McjD, where the occluded conformation is mainly present. (c) Export mechanism of the flippase PglK, where ATP hydrolysis pushes the substrate out of the transporter. (Based on the model of [28])

In Figure 7c the proposed mechanism for PglK is shown, where the NBDs are widely separated in the substrate- and nucleotide-free apo-state (state 1). By ATP-binding, the

transporter changes to an outward-facing conformation with closed NBDs and the TMDs are open on the periplasmic side (state 2). Here the substrate LLO (shown in violet) can enter the flippase cavity in the TMDs. By ATP hydrolysis LLO gets pushed out of the cavity and the transporter gets into an outward-occluded conformation.²⁸

1.2.1.2.3 Extractors and Efflux pumps (type VI-VII)

Type VI ABC transporters act as extruders, and members of type VII ABC transporters represent parts of efflux pumps, that act as lipoprotein extractors or regulate cell division.¹ In Figure 8a a representative of group VI is shown. The extruder is built of LptB₂FG⁶⁰ from *Pseudomonas aeruginosa*, LptC⁶¹ from *E. coli*, LptA⁶² from *E. coli* and LptD-LptE⁶³ from *Salmonella typhimorium*. In Figure 8b the MacAB-TolC⁶⁴ efflux pump from *E. coli* is shown, which is a representative of type VII.

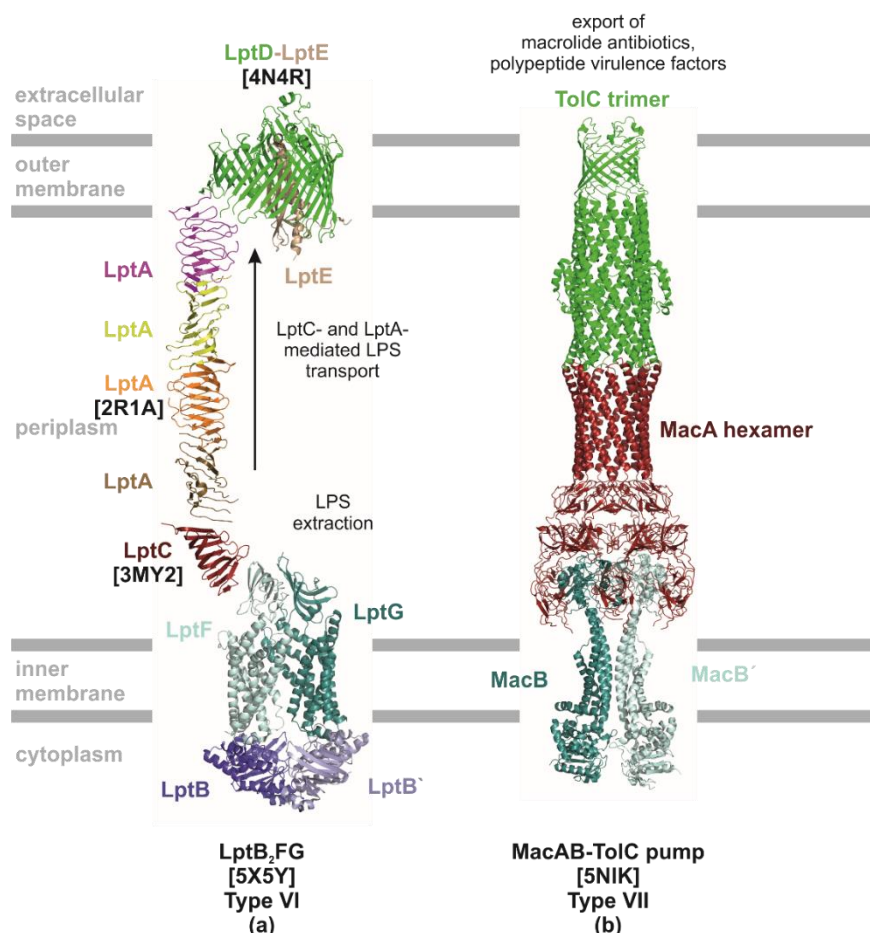


Figure 8: Representative Extractor (type VI) and Efflux pump (type VII): (a) Crystal structure of an Extractor build of LptB₂FG from *Pseudomonas aeruginosa* (pdb code 5X5Y), LptC from *E. coli* (pdb code 3MY2), LptA from *E. coli* (pdb code 2R1A) and LptD-LptE from *Salmonella typhimorium* (pdb code 4N4R), a type VI ABC transporter. (b) Crystal structure of the Efflux pump MacAB-TolC from *E. coli* (pdb code 5NIK). (Based on the model of [1])

In most Gram-negative bacteria the extracellular leaflet of the outer membrane consists mainly of lipid A. This is typically a hexa-acylated and phosphorylated disaccharide of glucosamine, which forms the anchor of the complex glycolipid called lipopolysaccharide (LPS). Concerned with the extraction of LPS from the inner membrane is the ABC transporter LptB₂FG⁶⁰ (type VI). After extraction from LptB₂FG, LPS is hand over to LptC⁶¹, which transports the LPS to LptA⁶², LptA finally delivers the LPS across the periplasm to the extracellular leaflet of LptD-LptE⁶³. This bridging function of the different components could be shown with functional studies⁶⁵, but the actual extrusion mechanism remains unknown. LptF and LptG form the TMDs, which have a unique fold and no helix swapping in contrast to other ABC transporters. In addition, there is only a weak interaction between LptF and LptG and a large cavity between them in the outward-facing state. Both contain β -jellyroll-like domains. The structure proposes that ATP binding by the NBD LptB opens a gate into the cavity, through which LPS can enter. Afterwards, it is driven out into the periplasmic β -jellyroll-like domains by conformational changes driven by ATP hydrolysis. To understand the complete mechanism further investigations are necessary.¹

The tripartite MacAB-TolC⁶⁴ pump (Figure 8b) connects the inner to the outer membrane through the periplasmic space in *E. coli* or other related Gram-negative bacteria. The pump plays an important role in the efflux of e.g. macrolide antibiotics and polypeptide virulence factors. It is built of the homodimeric MacB transporter, which is located in the inner membrane, the hexameric MacA in the periplasm and the TolC trimer located in the outer membrane. With the cryo-EM structure, it was shown that the nucleotide-free MacB protomers own a large periplasmic domain and the TMDs consist of four TM helices, which is typical for type VII ABC transport systems. The MacB dimer interface is too tight for substrate binding, while the NBDs are significantly separated. Since there is no substrate cavity in the TMDs, the MacB dimer shows an opening at the membrane-periplasm border, which was visible in the cryo-EM data as additional density and could work as an entry pathway for substrates from the periplasm. Furthermore, it could be shown that the large periplasmic domain of MacB makes contact with the MacA hexamer. In addition, the MacA hexamer and TolC trimer build a tunnel through the periplasm, which is interrupted by a glutamine gating ring in MacA, which is supposed to act as a one-way barrier to control substrate translocation. But this barrier is not present in all transporters of this type. For further understanding of this transporter type more experiments have to be performed to finally get a transport mechanism.¹

1.2.2 The heterodimeric ABC exporter TmrAB

The heterodimeric ABC exporter TmrAB^{2,66,67} from the Gram-negative eubacterium *Thermus thermophilus* is a type IV ABC transporter and the only exporter in *Thermus thermophilus*. A wide range of substrates can be exported by TmrAB like dyes, peptides and lipids. In Figure 9 the crystal structure of the transporter is shown, which has been solved with a resolution of 2.7 Å in the apo inward-facing conformation.²

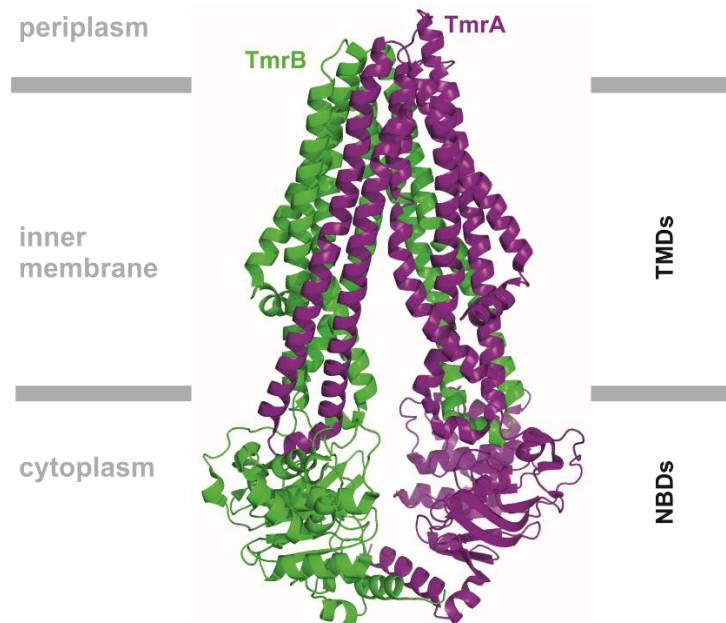


Figure 9: The heterodimeric ABC exporter TmrAB: Crystal structure of TmrAB² from *Thermus Thermophilus*, with TmrA shown in violet and TmrB in green. (pdb code 5MKK)

Due to the homology to various multidrug transporters, the subunits were named *Thermus thermophilus* multidrug resistance protein A (TmrA) and B (TmrB). Both can be expressed in *E. coli* and can be co-purified as a stable complex, with a combined theoretical mass of approximately 135 kDa (TmrA –His₁₀– 70.5 kDa and TmrB – 64.4 kDa), whereby TmrA has a His-tag implemented.⁶⁷

As it is characteristic for exporters, TmrA and TmrB are built of six transmembrane helices. All ABC signature motifs, which are important for ATP binding and hydrolysis are found in TmrA and TmrB. In TmrB the supposedly catalytic glutamate beside the Walker B motif is substituted by aspartate and the A-loop tyrosine is substituted by an arginine, which leads to a non-canonic ATP-binding site.^{2,66,67}

It has been shown that TmrAB is a functional homologue of human TAP and it shows similarities to the lipid flipping behaviour of PglK.²

1.3 Electron paramagnetic resonance

For the investigation of the heterodimeric ABC exporter TmrAB, electron paramagnetic resonance (EPR) was used. The method EPR, also called electron spin resonance (ESR), is useful for structure characterization and to observe dynamics and spatial distributions of paramagnetic spin systems with an unpaired electron. Compared to nuclear magnetic resonance (NMR), the basic principles are similar, but EPR is more sensitive. Besides naturally paramagnetic systems, diamagnetic systems can be investigated through the introduction of nitroxide radicals or transition metal ions.⁶

In this thesis, only the quantum mechanical description and the theoretical background which is necessary to understand the presented nitroxide spectra is described. More information about EPR spectroscopy in general⁶⁸⁻⁷⁰, specifically about pulsed EPR⁷¹ or in particular EPR in applications^{72,73} can be found in several books.

1.3.1 Spin Hamiltonian

The energy of an unpaired electron with spin S and the surrounding nuclei n with spin I_k can be described by the static spin Hamiltonian ($\hat{\mathcal{H}}_0$), which is shown in Equation (1).

$$\hat{\mathcal{H}}_0 = \hat{\mathcal{H}}_{EZ} + \hat{\mathcal{H}}_{NZ} + \hat{\mathcal{H}}_{HF} + \hat{\mathcal{H}}_{ZFS} + \hat{\mathcal{H}}_{ee} \quad (1)$$

This equation consists of the electron Zeeman interaction ($\hat{\mathcal{H}}_{EZ}$), the nuclear Zeeman interaction ($\hat{\mathcal{H}}_{NZ}$), the hyperfine coupling between electron and nuclear spins ($\hat{\mathcal{H}}_{HF}$), the zero-field splitting ($\hat{\mathcal{H}}_{ZFS}$) and the interaction between two electrons ($\hat{\mathcal{H}}_{ee}$). Depending on the external magnetic field, the magnitude of the electron ($\hat{\mathcal{H}}_{EZ}$) and nuclear ($\hat{\mathcal{H}}_{NZ}$) Zeeman interactions are varying. By performing EPR experiments at different magnetic fields, different interactions in the static spin Hamiltonian ($\hat{\mathcal{H}}_0$) can be detected. Since the nuclear Zeeman interaction and the zero-field splitting are not important for the performed experiments with nitroxide spin labels, only the other relevant terms are briefly discussed in the following subchapters.

1.3.1.1 Electron Zeeman interaction

In Equation (2) the electron Zeeman interaction is described, which characterizes the interaction between the electron spin and the external magnetic field.

$$\hat{\mathcal{H}}_{EZ} = \frac{\mu_B}{\hbar} \vec{B}_0^T \mathbf{g} \hat{S} \quad (2)$$

Hereby μ_B is the Bohr magneton, \hbar the reduced Planck constant and \vec{B}_0^T depicts the transpose of the magnetic field vector. \mathbf{g} describes a tensor, containing the orientation dependence of the interaction or can be an effective g value. \hat{S} is the electron spin vector operator. If one is looking on an effective g value of a nitroxide radical with the spin $S = \frac{1}{2}$ the energy of the two spin states is given by the eigenvalues of this Hamiltonian operator, which is shown in Figure 10 and described by Equation (3).

$$E = \pm \frac{1}{2} g \mu_B B_0 \quad (3)$$

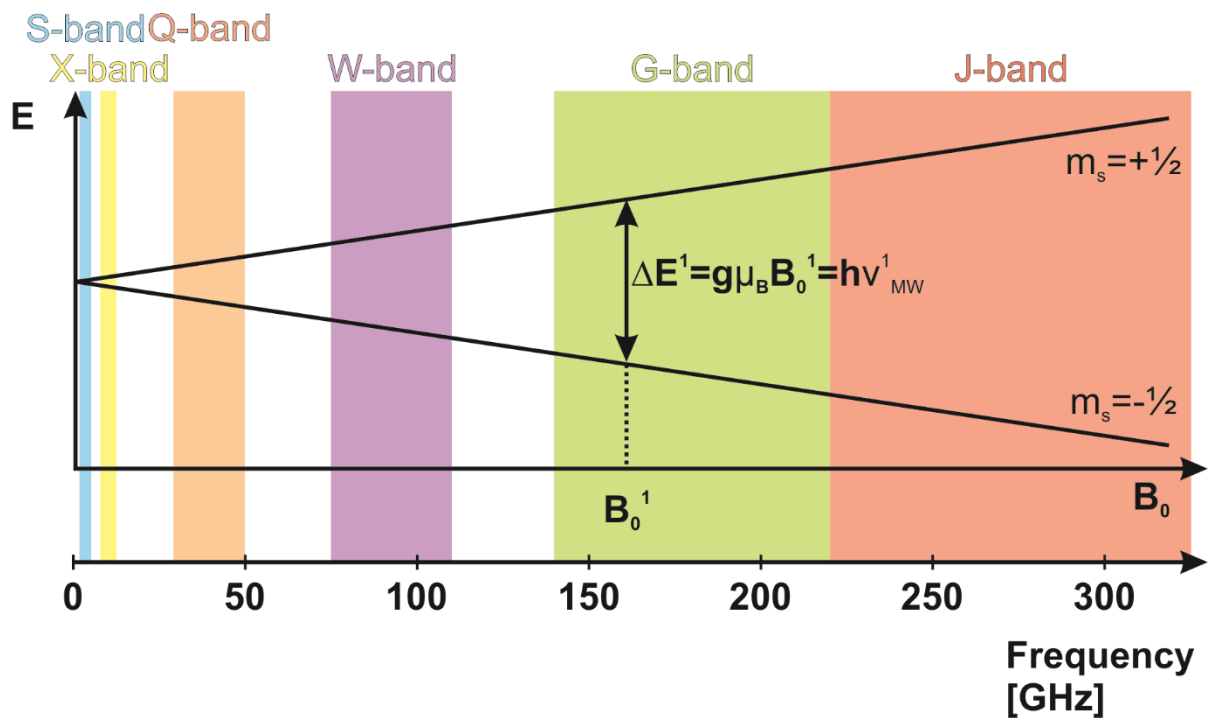


Figure 10: Zeeman splitting of energy levels in a system with spin $S = \frac{1}{2}$. The transition between the two shown split energy states $m_s = \pm \frac{1}{2}$ can be induced by microwave irradiation ($h\nu_{MW}$). At higher frequencies, the Boltzmann population difference is increased. Frequently used microwave frequency ranges for EPR are indicated with colours (S-band, X-band, Q-band, W-band, G-band and J-band).

While the g -value of a free electron is $g_e \cong 2.0023$, it is different for unpaired electrons that are located in atomic or molecular orbitals, due to spin-orbit interaction. For most organic radicals these differences are very small, in the range $\Delta g \sim 0.01$. If the g tensor is described by an ellipsoid with orthorhombic symmetry ($g_x \neq g_y \neq g_z$) and the orientation of the magnetic field \vec{B}_0 is defined by the polar angles θ and ϕ , then the effective g value (g_{eff}) for a special orientation is determined by Equation (4).

$$g_{eff} = \sqrt{g_x^2 \sin^2 \theta \cos^2 \phi + g_y^2 \sin^2 \theta \sin^2 \phi + g_z^2 \cos^2 \theta} \quad (4)$$

In case of the high-field approximation, where the electron Zeeman interaction is much larger than all other interactions, then only components including \hat{S}_z and \hat{I}_z are considered in the hyperfine interaction.

1.3.1.2 Hyperfine interaction

In Equation (5) the Hamiltonian for the hyperfine interaction (HF) is given, for the case that the electron spin S is coupled to nuclear spins \hat{I}_k .

$$\hat{\mathcal{H}}_{HF} = \sum_{k=1}^n \hat{S}^T \mathbf{A}_k \hat{I}_k \quad (5)$$

\mathbf{A}_k depicts the hyperfine tensor, which is a combination of two interactions, the isotropic Fermi contact (FC) interaction and the anisotropic electron-nuclear dipole-dipole coupling (DD). The FC interaction is depending on the electron spin density at the nucleus. There will be no isotropic interaction (a_{iso}) for an unpaired electron in any orbital, except the s-orbitals, because of the node of these orbitals at the nucleus. However, spin polarization induces a slight difference between up and down spins in an s-orbital if an unpaired electron is located close to the s-orbital. The Hamiltonian which describes the FC interaction is shown in Equation (6) and the isotropic hyperfine coupling constant a_{iso} is given by Equation (7).

$$\hat{\mathcal{H}}_{HF-FC} = a_{iso} \hat{S}^T \hat{I}_k \quad (6)$$

$$a_{iso} = \frac{2}{3} \frac{\mu_0}{\hbar} g_e \mu_B g_n \mu_n |\Psi_0(0)|^2 \quad (7)$$

In Equation (7) μ_0 represents the permeability of the vacuum and $|\Psi_0(0)|^2$ describes the electron density at the nucleus. The anisotropic dipolar part of the hyperfine coupling describes the orientation-dependent through-space interaction of the magnetic moments of the electron and the nucleus, which is described by Equation (8).

$$\hat{\mathcal{H}}_{HF-DD} = \frac{\mu_0}{4\pi\hbar} g_e \mu_B g_n \mu_n \left(\frac{(3\hat{S}^T \vec{r})(\vec{r}^T \hat{I}_k)}{r^5} - \frac{\hat{S}^T \hat{I}_k}{r^3} \right) = \hat{S}^T \mathbf{T}_{DD} \hat{I}_k \quad (8)$$

Here r gives the distance between the electron and the nucleus and \mathbf{T}_{DD} is the dipolar hyperfine tensor. If the distance r between the unpaired electron and unpaired nuclear spin equals or is larger than 0.25 nm the unpaired electron density may be considered at the nucleus. In such a case, the interaction is an average of all important spin density centres or its spatial integral over all electron spin density.

1.3.1.3 Electron spin-electron spin interaction

The weak interaction between two electron spins is described by the spin-spin interaction, which can also be expressed by their individual spins S_1 and S_2 . In Equation (9) the spin-spin interaction term is shown, which describes the interaction of two paramagnetic spin centres.

$$\hat{\mathcal{H}}_{ee} = \hat{S}_1 \mathbf{D}_{DD} \hat{S}_2 + J \hat{S}_1 \hat{S}_2 \quad (9)$$

Hereby \mathbf{D}_{DD} is the dipole-dipole tensor and J is the exchange coupling (Heisenberg exchange coupling). If there is significant overlapping of the two spin orbitals, the Heisenberg exchange coupling term gets relevant, which is the case for solids with interspin distances <1 nm or for heavily delocalized unpaired electrons. In case of both radicals freely moving in solution, where the radicals can collide with each other, the overlap can be transient. Since the nitroxide labels are attached via saturated chains to the biomolecule, the J coupling term is at least one order smaller than the dipole-dipole coupling for distances longer than 1.5 nm. A frozen buffer or lipid environment with weak conductivity reduces J coupling and therefore the overall J coupling can be neglected for frozen samples containing nitroxide spins attached to protein molecules. If the electron spins are assumed to be localized in the centre of the N-O bond in nitroxide radicals and parallel orientation of the quantization axis along the external magnetic field, a point-dipole approximation for the

electron-electron dipolar tensor can be made. Therefore, the Hamiltonian can be described as a sum of secular and pseudo-secular terms ($\hat{\mathcal{H}}_{ee,sec}$ and $\hat{\mathcal{H}}_{ee,psec}$), which are shown in Equations (10) and (11).

$$\hat{\mathcal{H}}_{ee,sec} = [J + \omega_{dd}(1 - 3 \cos^2 \theta)] \hat{S}_{1,z} \hat{S}_{2,z} \quad (10)$$

$$\hat{\mathcal{H}}_{ee,psec} = \left[J - \frac{1}{2} \omega_{dd}(1 - 3 \cos^2 \theta) \right] (\hat{S}_{1,x} \hat{S}_{2,x} + \hat{S}_{1,y} \hat{S}_{2,y}) \quad (11)$$

Here θ represents the angle between the spin-to-spin vector and the external magnetic field axis and ω_{dd} is the dipolar frequency depicted in Equation (12).

$$\omega_{dd} = \frac{1}{r_{12}^3} \frac{\mu_0}{4\pi\hbar} g_1 g_2 \mu_B^2 = \frac{D}{r_{12}^3} \quad (12)$$

An isotropic g value of $g_1 = g_2 = 2.006$ is approximated for nitroxide spins and as a consequence D has a value of $52 \text{ MHz} \cdot \text{nm}^3$ for nitroxide spins. In the case of the high field approximation, the pseudo secular term shown in Equation (11), which describes the mixing of $|\alpha_1\beta_2\rangle$ and $|\beta_1\alpha_2\rangle$, can be neglected since the difference of resonance frequencies for the coupled spins is typically much larger than ω_{dd} .

1.3.2 Site-directed spin labelling

Site-directed spin labelling (SDSL) combined with EPR spectroscopy is an approved and widely used method in the field of structural biology, which has been first established on bacteriorhodopsin.^{74,75} Over the years a lot of proteins were investigated with this method for gaining structural and functional information.¹⁸ Similar to proteins, other large biomolecules like DNA or RNA can also be spin labelled for EPR measurements.^{76,77}

A stable unpaired electron is needed for EPR spectroscopy. Such stable radicals are typically attached by cysteine cross-linking at the desired position (Figure 11). If the protein is containing natural cysteines, they first have to be removed to gain a ‘‘Cys-less’’ mutant, to avoid non-specific labelling of those cysteines. It is therefore important that this ‘‘Cys-less’’ variant has still the same or at least similar functionality.

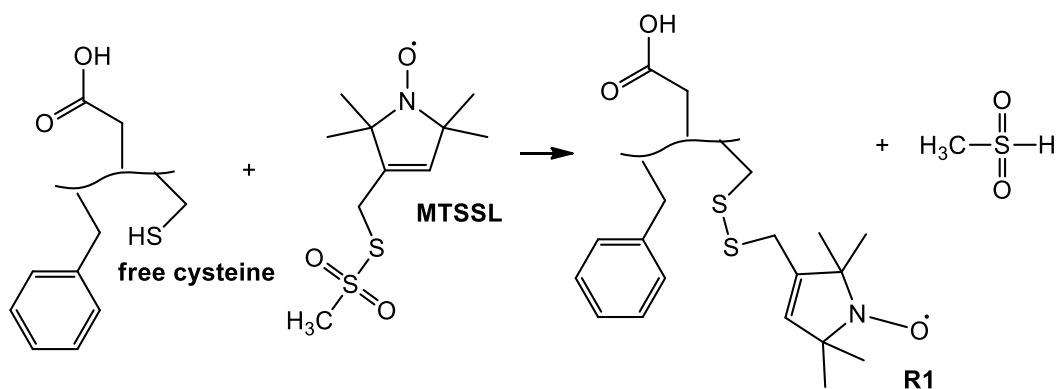


Figure 11: Site-directed spin labelling: Reaction of a free cysteine incorporated in a protein and MTSSL, which reacts with the free sulfhydryl group of the cysteine. The label gets attached via disulphide-linkage, resulting in the unnatural side chain R1 with an unpaired electron. During or after this reaction no reducing agents should be present.

Typically (1-oxyl-2,2,5,5-tetramethylpyrroline-3-methyl)-methanethiol-sulfonate (MTSSL or MTSL) is used for protein spin labelling, which contains a nitroxide moiety (referred to as NO). MTSSL has the advantages that it is smaller than other spin labels and the size is similar to a tryptophan side chain. Further benefits are its high specificity for the free thiol of cysteines and high flexibility. Depending on the position of the C_{α} -NO the flexibility can also be a disadvantage, which is shown in Figure 12, since the distance can vary in a 4-8 Å range. This makes it difficult to compare the NO-NO distance to a coordinate of the native side chain.

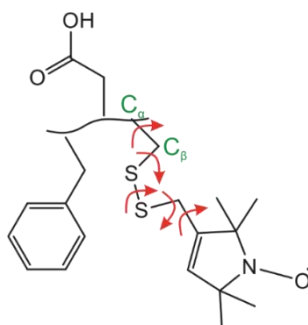


Figure 12: Structure of the unnatural side chain R1. C_{α} and C_{β} are indicated in green and the flexible bonds, where free rotation is possible, are tagged with red arrows. The flexible bonds between NO and C_{α} are critical factors.

Since it is not always possible to prevent reducing conditions, there are other spin labels for slightly reducing surroundings available, like maleimido (MSL) or iodacetamido (IASL). For the case that naturally existing cysteines cannot be removed from the protein of interest, labelling with a hydroxylamine spin label of a genetically encoded unnatural amino acid, *p*-

acetyl-L-phenylalanine, is possible, which has been demonstrated for a T4 lysozyme.⁷⁸ In this method, an acidic pH of 4.0 is needed for labelling, which limits this approach for general application. Another important class of spin labels are gadolinium(III)-based labels⁷⁹ (Figure 13), which can be used in SDSL-EPR in pair or orthogonally to the classical nitroxide-based labels.^{80–82} One big advantage of these labels is their resistance to reduction, which makes it attractive for in-cell EPR approaches.

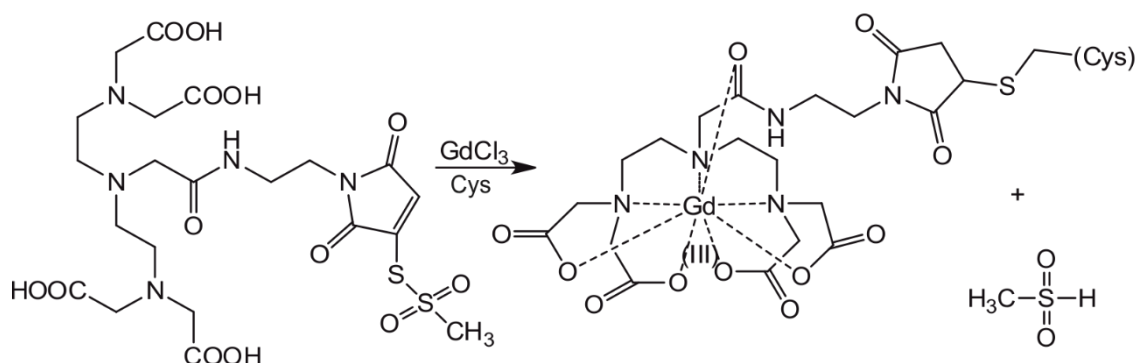


Figure 13: Gadolinium(III)-based labelling of cysteines. Here the maleimido monoamide DTPA acts as a chelating agent for Gd(III), which reacts with the free sulfhydryl group of the cysteine as shown. Reducing agents can be present after spin labelling of the protein.

1.3.2.1 Strategy for labelling positions

It is important to carefully validate the position of cysteines before spin labelling via SDSL and estimate how reliable the extracted EPR data will be. Therefore, the MATLAB-based simulation software MMM⁸³ can be used, which simulates based on an implemented rotamer library⁸⁴ the selected positions after replacing the residue by cysteine. But before the structure gets loaded into the MMM software, suitable positions for the simulations should be identified. Here the amino acids valine, leucine, isoleucine, serine, threonine are the best to exchange by cysteine. Aspartic acid, glutamic acid, glutamine, lysine and arginine can still be taken into account, but because of their charge and the possible important role of this charge for the functionality, they are the second choice only. Other amino acids, like for example alanine because of its small size, are not good for exchange by cysteine.

The MMM software determines the relative energies of the spin rotamers, which are calculated from MD trajectories of the dihedral angles of free MTSSL, attached to a specific position as a sum of pairwise Lennard-Jones potential energies between atoms of the label and atoms of the protein. The important information of the simulation are the number of rotamers and the partition function. Hereby a small number of rotamers (less than 10) means

that the accessibility is small and that it is a tight site where the spin label could disturb the protein. In contrast, a very high number of rotamers, which means the spin label is very flexible, could lead to a broad distribution. Typically a number of rotamers around 50 is considered as a good number. Moreover, the partition function Z also provides a measure of the tightness of the labelling site. Values under 0.05 are considered as tight sites, which can lead to insufficient labelling. Typically values of around 0.6 or 0.7 are considered as good values.

1.3.3 Nitroxide-spectrum in continuous wave EPR

Continuous wave (cw) EPR spectroscopy of nitroxide spin labelled biomacromolecules gives the possibility to gain insights into the solvent accessibility, polarity, side-chain mobility, and distances between spin labels.⁸⁵ By measuring various different positions in the protein of interest it is possible to elucidate a secondary structure element, its orientation and the protein topography.

A typical cw EPR spectrum of a nitroxide radical with spin $S = \frac{1}{2}$ shows three lines, because of the hyperfine interaction with the nuclear spin $I = 1$ (^{14}N), as shown in Figure 14. Since the hyperfine interactions with protons which are close to the nitroxide are typically very small, they are typically unresolved in the spectral line width. Sometimes so-called “satellites” are visible in the cw EPR spectrum, which means small intensity-doublets around each of the three spectral lines. Satellite signals are due to hyperfine interactions with close-by naturally abundant ^{13}C atoms. These interactions are visible when the nitroxide is in the fast isotropic motion limit.

The principal axis system of nitroxides is defined in such a way that the z-axis is parallel to the direction of the $2p_z$ orbital of the nitrogen atom and the x-axis is parallel to the N-O bond. The properties of the nitroxide spectrum, which are dependent on the orientation with respect to the external magnetic field, are determined by the anisotropy of the A and g tensors. For MTSSL the hyperfine values are typically in the range of $A_{xx} \sim A_{yy} = 0.45 - 0.50$ mT and $A_{zz} = 3.3 - 3.7$ mT. The hyperfine principal values are known to be polarity-dependent. Typical g values are $g_{xx} = 2.0081 - 2.0091$, which is polarity and proticity dependent, $g_{yy} = 2.0061$ and $g_{zz} = 2.0021$.

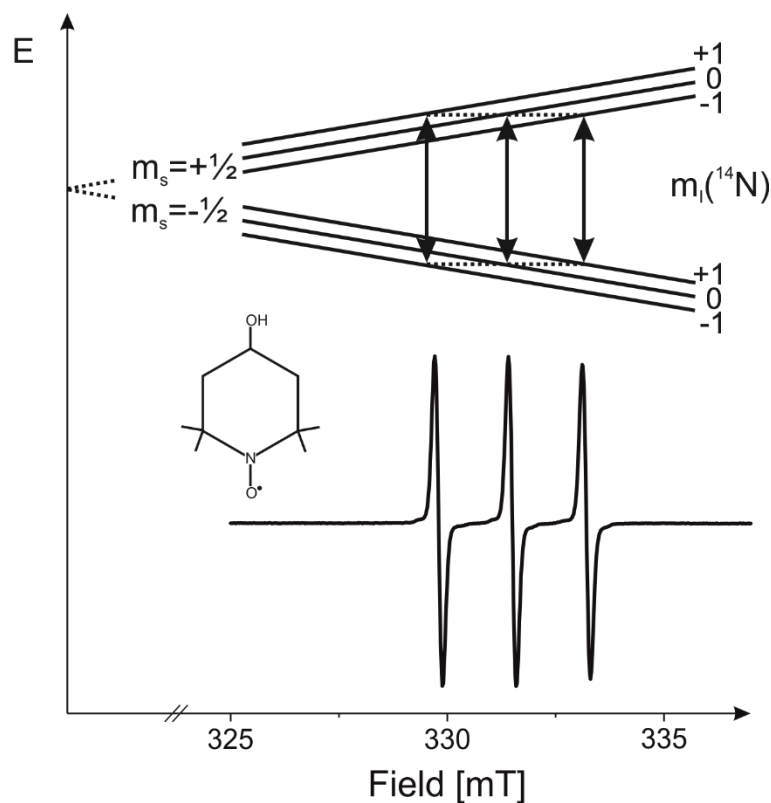


Figure 14: Nitroxide cw spectrum ($S=1/2$, $I=1$): Zeeman and hyperfine splitting scheme for a free and fast tumbling nitroxide radical is shown on top. At the bottom, a typical cw nitroxide spectrum is shown for a free TEMPOL radical (the structure is depicted) in solution and at room temperature, measured at X-band.

The spectrum of MTSSL, if it is freely tumbling in solution, consists of three narrow lines with equal distance, centred at an average g value due to the fast averaging of the anisotropies. In the case of low-temperature measurements, where the rigid limit is reached, the super-positioning of all possible molecular orientations result in the so-called powder spectrum. This spectrum is characterized by a central line for $m_I = 0$ with the frequency scattering completely caused by g anisotropy. The high field line is typically broader than the low field line due to the relative sign of the A and g values.

In addition, the EPR spectra are sensitive to the rotational correlation time of the entire protein. For example at X-band (9.5 GHz), the spectrum of a nitroxide is mainly characterized by the hyperfine splitting, typically with high tumbling and isotropic coupling. At slower tumbling rates the high field line gets smaller and at even slower tumbling rates the high-field lines get broad leading to the solid limit due to the anisotropic hyperfine coupling (powder spectrum). At X-band, this powder spectrum is still characterized by the hyperfine coupling and therefore the orientation information is mainly due to the A_{zz} anisotropy. However, at higher frequencies (like W-Band, 95GHz), the g -Tensor anisotropy is also visible and all orientations can be resolved.

If a spin label is attached to a protein, the spin label side chain can still rotate, but typically not in the same extent as free in solution. These motions are described in the EPR line shape, where the motion depends on the rotational correlation time of the entire protein, motion of the backbone relative to the protein and the rotational isomerization of the bonds linking the spin label to the protein. In Figure 15 this is illustrated by the comparison of a free tumbling MTSSL to a MTSSL bound to the protein TmrAB: The lines are broader due to the binding to the protein and the related motional restrictions.

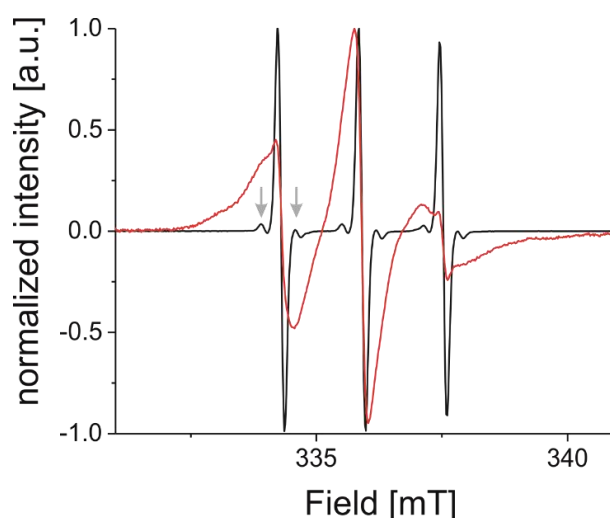


Figure 15: Comparison of free MTSSL- and bound MTSSL-cw EPR spectrum: The free MTSSL in solution is shown in black, which shows three equidistant sharp lines. Also visible are the previously described ^{13}C “satellites”, which are marked with grey arrows for the first line. The cw EPR spectrum for MTSSL bound to the protein TmrAB (labelled at TmrA61 and TmrB56) in the nucleotide-free apo-state is shown in red. It is clear to see that the lines are significantly broader compared to the free label. Both spectra were measured at X-band.

1.3.4 Pulsed electron-electron double resonance (PELDOR)

Basically, cw EPR experiments could be used to estimate interspin distances up to 2 nm, however, for distances longer than 2 nm, pulsed EPR methods are necessary. Pulsed electron-electron double resonance (PELDOR), which is also called double electron-electron resonance (DEER), is a method to measure weak dipolar couplings between two unpaired electrons, in a range of 2-8 nm or in very favourable cases up to 10 nm.¹⁸ This technique with a 3-pulse sequence has been introduced by Milov et al.⁸⁶, a later extended dead-time free, 4-pulse sequence by Pannier et al.²⁰, lead to its wide use for various applications. Dead-time is the time during and directly after a pulse, in which the sensitive detector needs to be protected from the high power present in the resonator. This leads to a time, depending on the bandwidth of the resonator, where no signal can be recorded. As a

consequence, for the 3-pulse sequence, no broad distributions with distances lower than 3 nm could be detected and furthermore, uncertainties in the zero time determination occur. Recently the classical PELDOR technique has been further extended by Spindler et al.²¹ to a 7-pulse Carr-Purcell (CP) sequence, which is a useful tool to extend the time window, for example for membrane proteins, where long-distance measurements can become difficult.

1.3.4.1 4-Pulse PELDOR

Nowadays dead-time free 4-pulse PELDOR is widely used for structure and dynamic studies of biomacromolecules with nitroxide labels. As shown in Figure 16 the PELDOR experiment consists of two spins, the observer spins and the pump spins. At the observer frequency ν_A (Fig. 16a) the refocused echo sequence creates an echo, which is modulated as a function of the timing of the pumped spins (ν_B). The modulation of the echo is induced by the changes of the local magnetic field due to the dipole field change from the flipped pumped spins (Figure 16c).

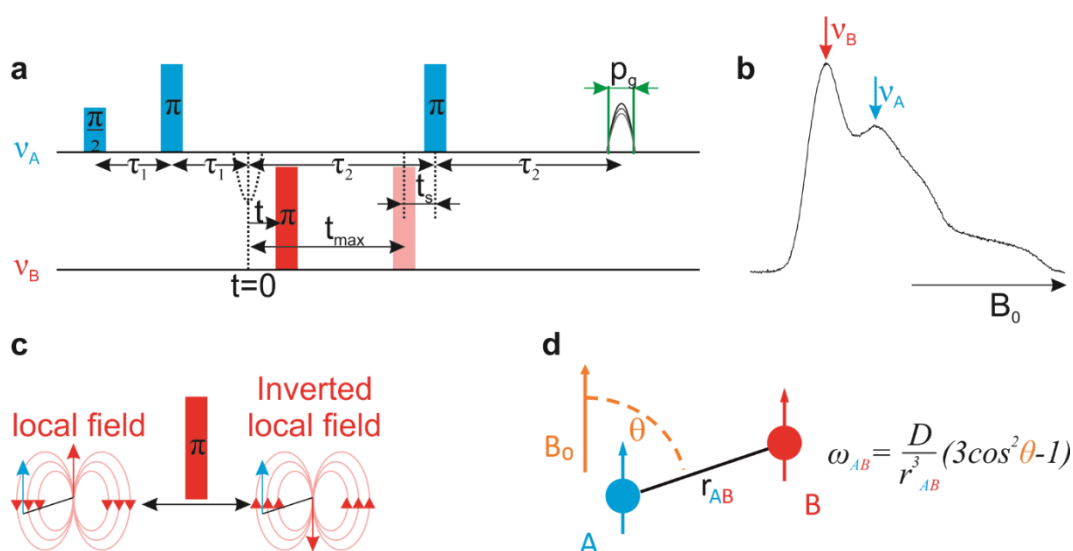


Figure 16: Dead-time free 4-pulse PELDOR: a) Pulse sequence for 4-pulse PELDOR, whereby time t is varied from $t=0$ to t_{max} and the variation of the integral echo intensity p_g is recorded. The refocused echo is generated by a sequence (blue) containing one $\pi/2$ and two π pulses at the observer frequency ν_A . A π pulse (red) is applied at different time intervals at the pump frequency ν_B . b) Typical Q-band field sweep spectrum of nitroxide radicals, with the positions for pump (red) and observer (blue) pulses indicated. c) The π pulse at frequency ν_B inverts the pumped spins (red) and thereby changes the local field at the observer spins (blue). d) Two spins are separated by the distance r_{AB} and the distance vector is tilted to the external magnetic field B_0 by θ . The dipolar coupling (ω_{AB}) of the two spins is proportional to the distance by r^{-3} and dependent on the angle θ . ($D = 52 \text{ MHz nm}^3$ for nitroxide radicals²¹)

At X- or Q-band frequencies the spectra of a nitroxide radical are rather broad and it is possible to choose only a fraction of spins which gets excited (Fig. 16b). Two different frequencies are used for a PELDOR experiment, one at the observer frequency to create a refocused echo and the second frequency to invert the pump spins, both excitation should not overlap and are typically separated by +65 MHz or -100 MHz at X- or Q-band, respectively. During the experiment, the refocused echo sequence is kept constant and only the timing of the pump pulse is varied. The dipolar coupling between the two spins, which is investigated in this experiment is depending on the distance between the spin labels and the angle between the distance vector and the external magnetic field (Figure 16d). In Figure 17 an example of experimental PELDOR data and its analysis is shown.

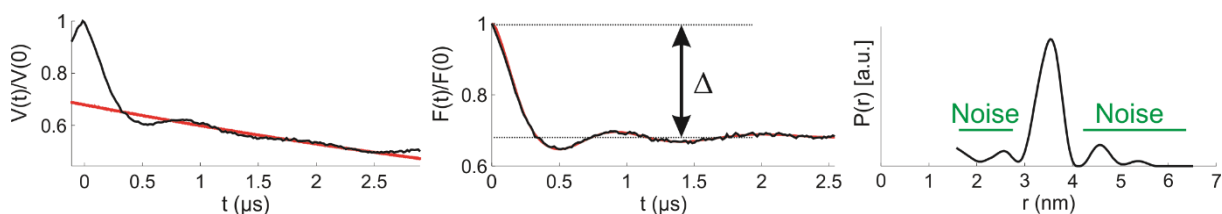


Figure 17: PELDOR Data analysis example (*TmrAB* labelled at *TmrA288* and *TmrB272* with *MTSSL*): On the left side the normalized primary data $V(t)/V(0)$ is shown fitted with an exponentially decaying background function. In the middle, the resulting form factor $F(t)/F(0)$ is shown, which has been obtained by dividing the primary data by the background. The modulation depth Δ is also indicated. Δ depends on the inversion efficiency of the pump pulse and is influenced by the labelling efficiency. The oscillation is defined by a frequency including the interspin distance. After fitting of the form factor with Tikhonov regularization, the interspin distance distribution $P(r)$ is obtained, shown on the right. Green bars indicate noise artefacts.

The obtained experimental signal ($V(t)$) consists of two parts as shown in Equation (13).

$$V(t) = B(t) \times F(t) \quad (13)$$

First, the exponentially or stretched exponentially decaying background function $B(t)$, which describes the intermolecular contributions coming from interactions between spin labels of surrounding protein molecules or protein complexes. The second term is the form factor ($F(t)$), which describes the interaction of the coupled spins in the same biomolecule, the so-called intramolecular interaction. Assuming an exponential background function with $V(0) = 1$, depending on the dimensionality of the spin label distribution, $B(t)$ is given by Equation (14).

$$B(t) = \exp(-kt^{\frac{D}{3}}) \quad (14)$$

Here k quantifies the density of the spins and D is the dimension of the spin distribution. For proteins, which are homogeneously distributed in three dimensions in a frozen solution $D = 3$. For reconstituted membrane proteins in liposomes, the spin distribution can be limited to a two-dimensional bilayer and therefore $D = 2$ can be assumed. By comparison of double-labelled proteins and the corresponding single-labelled proteins, the value of D can also be obtained experimentally. The primary PELDOR data is divided by the background function to obtain the form factor. The form factor is a function of the dipolar frequency ω_{dd} (Equation (12)) and the modulation depth Δ , which is determined by the inversion efficiency of the pump pulse and the labelling efficiency as shown in Equation (15), whereby θ describes the angle between the interspin vector and the external magnetic field.

$$F(t) = 1 - \lambda[1 - \cos((1 - 3 \cos^2 \theta)\omega_{dd}t)] \quad (15)$$

According to Equation (12), long distances imply low dipolar frequencies ω_{dd} , leading to the need for long observation times for precise measurements. If the protein sample is frozen, the PELDOR data describes the interspin distances arising from both rotameric transitions and backbone fluctuations, resulting in a distance distribution with a certain mean distance. By assuming a distribution of the interspin vectors along the external magnetic field, the form factor of each distance can be transformed into a Pake pattern by Fourier transformation. Thus the experimental $F(t)$ is fitted by a linear combination of multiple traces, whereby each is according to a single distance. The distance distribution $P(r)$ is built by the coefficients in this linear combination of multiple traces.

1.3.4.2 7-Pulse CP-PELDOR

The observation time window in which the dipolar frequency can be measured is restricted by the phase memory time T_m of the introduced paramagnetic centre. This results in an upper limit for the length and resolution of the interspin distance of interest. Especially for membrane proteins, which are mostly measured in detergent or liposomes, the transversal relaxation time of nitroxide radicals is very short, which leads to a typical limit for the observation time window of approximately 5 μ s.

For prolongation of the pulsed EPR time window, three approaches can be used. First dilution of the spin concentration removes the strong background slope, whereby the ideal concentration depends on the time window. Especially in membranes clustering of protein can be a problem, which can be overcome by adding unlabelled protein. Deuteration of the protein, lipid or detergent leads to a longer relaxation time and thereby to a higher limit for the observation time window.^{87,88} Finally a Carr-Purcell⁸⁹ sequence can be used, with multiple observer spin refocusing pulses, which prolongs the total time window for observation of the dipolar evolution. This was, for example, already used for 5-pulse-PELDOR.^{21,90}

To use this approach for dipolar spectroscopy, each of the refocusing pulses on the observer frequency (ν_A), must be combined by an inversion pulse on the dipolar coupled pump spin at the pump frequency (ν_B) (Figure 18). Each of the refocusing pulses has to be combined with one pump pulse to get the maximum effect out of the sequence.²¹

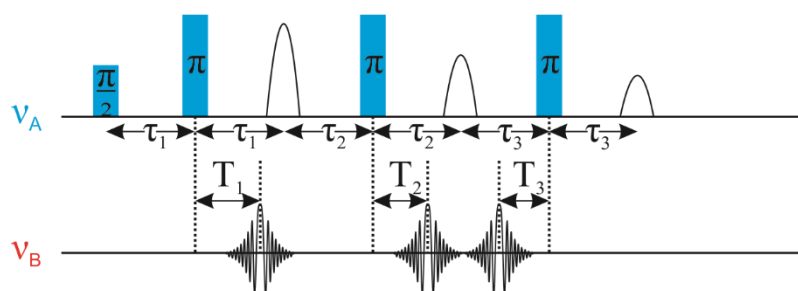


Figure 18: Pulse Sequence for 7P-CP-PELDOR. At the observer frequency, one $\pi/2$ pulse and three π pulses create the refocused echo and after every π -pulse, at the observer frequency, a sech/tanh pulse is applied at the pump frequency for inversion.

Classical rectangular microwave pulses⁹⁰ cannot be used for these multiple pump pulses since large artefacts are created by their frequency offset dependent nonuniform inversion evolution function. For the Carr-Purcell concept adiabatic sech/tanh pump pulses⁹¹ can be used since they possess a high inversion efficiency. To take into account the nonideal behaviour of the pump inversion pulses the additional parameter p has to be defined, which describes the probability of spin inversion in the bandwidth of the sech/tanh pulse. In contrast to the modulation depth parameter, λ , which defines the overall inversion efficiency of B-spins inverted by one pump pulse, p describes the probability for the B-spin being inverted by both pump pulses. The ideal performance of sech/tanh pulses are reduced due to transversal relaxation during the pulse, bandwidth limitations and inhomogeneity of the

magnetic field B_1 of the resonator. If the p value is less than the ideal one, then 2^N dipolar signals with varying intensities, time-zeros and time-increments add to the signal, in which N is the number of pump pulses.²¹

The signal of the 7-pulse CP-PELDOR sequence (Fig. 18) is obtained by observation of the last refocused echo modulated by the pump pulses at times T_1 , T_2 and T_3 , whereby the time axis, T , of the experiment is given by Equation (16).

$$T = \tau_1 + \tau_2 + \tau_3 - (|T_1| + |T_2| + |T_3|) \quad (16)$$

Furthermore, the phase of the 7-pulse CP-PELDOR signal, defined by the time increments before the pump pulses, is described by Equation (17).

$$\varphi_{dip} = (\tau_1 + \tau_2 + \tau_3 - |T_1| - |T_2| - |T_3|) \cdot \omega_{dip} \quad (17)$$

The intramolecular signal of interest, which describes the dipolar interaction between the two spin labels in one biomolecule, is a superposition of all dipolar pathways weighted by their related probabilities as described in Equation (18).

$$\begin{aligned} V_{intra} = & \lambda \bar{p}^2 (\cos \varphi_{1\bar{2}\bar{3}} + \cos \varphi_{\bar{1}2\bar{3}} + \cos \varphi_{\bar{1}\bar{2}3}) \\ & + \lambda p \bar{p} (\cos \varphi_{12\bar{3}} + \cos \varphi_{\bar{1}23} + \cos \varphi_{1\bar{2}3}) \\ & + \lambda p^2 \cos \varphi_{123} + 1 - \lambda \end{aligned} \quad (18)$$

\bar{p} is defined as $\bar{p} = 1 - p$. As an example $\varphi_{1\bar{2}\bar{3}}$ represents the path, in which only the first pump pulse inverts the B-spin. For the calculation of the intermolecular background interaction, similar calculations can be performed. Every experiment separates the complete B-spin ensemble into sub ensembles, corresponding to one certain pathway. Each sub ensemble contributes differently to the intermolecular function, but every A-spin, however, is affected by all of these B-spin sub ensembles. The total intermolecular function is the product of all the different B-spin sub ensembles, as shown in Equation (19).

$$V_{inter} = V_{int_1} \cdot V_{int_2} \cdot V_{int_3} \quad (19)$$

Whereby V_{int_n} describes the intermolecular decay function coming from n pump pulses and are further defined in Equations (20)-(22).

$$V_{int_1} = e^{(-\lambda ac p^2 (|\tau_1 - |T_1|| + |\tau_2 - |T_2|| + |\tau_3 - |T_3||))} \quad (20)$$

$$V_{int_2} = e^{(-\lambda ac p^2 (|\tau_1 + \tau_2 - |T_1| - |T_2|| + |\tau_3 - \tau_1 + |T_1| - |T_3|| + |\tau_2 + \tau_3 - |T_2| - |T_3||))} \quad (21)$$

$$V_{int_3} = e^{(-\lambda ac p^2 (|\tau_1 + \tau_2 + \tau_3 - |T_1| - |T_2| - |T_3||))} \quad (22)$$

The concentration of the radical (c) has to be taken into account and a is further described in Equation (23).

$$a = \frac{2\pi g^2 \mu_B^2 \mu_0}{9\sqrt{3}\hbar} \quad (23)$$

For gaining a good signal-to-noise ratio for mainly the intramolecular interaction, p has to be larger than 0.7, to get an artefact as small as possible, which can be subtracted off the true dipolar evolution function with an approximate correction.²¹

1.3.4.3 PELDOR data analysis

By fitting the form factor the distance distribution $P(r)$ of the PELDOR data can be obtained. A commonly used method is the Tikhonov regularization with a L-curve criterion that is integrated in the MATLAB-based software package DeerAnalysis.⁹² Besides that, also model-based fitting can be used, where the known distance and width can be implemented to fit the data accordingly and the ratios of different fractions can be calculated. With DeerAnalysis One- or Two-Gaussian fits can be performed. If the trace of interest contains more than two different distances the MATLAB-based software package DD can be used.^{93,94} With this software it is possible to take up to eight distances into account for Gaussian fitting.

1.3.4.3.1 Data analysis with DeerAnalysis

The determination of the distance distribution $P(r)$ from the form factor $F(t)$ is an ill-posed problem. The reliability of the distance distribution is therefore strongly dependent on the

signal-to-noise ratio of the original data. Thus the main goal is to improve the resolution in the distance distribution while the influence of the experimental noise gets minimized. A distance distribution is characterized by the mean distance $\langle r \rangle$, the width σ_r and its overall shape. For reliable determination of all three parameters, it is necessary to measure the dipolar evolution at least two periods of the dipolar oscillation, because the mean distance and the background needs to be fitted longer than one period. In Equation (24) the time-domain signal $S(t)$ for a given distance distribution $P(r)$ is described. Thereby $S(t)$ is calculated by the DeerAnalysis software using the kernel function K and fitting to the experimental form factor $F(t)$ with minimal deviation. The kernel function is given in Equation (25) for PELDOR experiments with ideal pulses.

$$S(t) = K(t, r)P(r) \quad (24)$$

$$K(t, r) = \int_0^1 \cos[(3x^2 - 1)\omega_{ad}t] dx \quad (25)$$

Direct fitting of $S(t)$ to $F(t)$ would lead to significant noise artefacts. With the DeerAnalysis software, a Tikhonov regularization can be used to overcome this issue. Therefore, a regularization parameter α is introduced and by minimizing the function given in Equation (26) for every regularization parameter α the optimal distance distribution can be obtained, with $D(t)$ as shown in Equation (27). In the first term of Equation (26), the error of fitting the simulated dipolar evolution function $S(t)$ to the experimental data $D(t)$ gets minimized. The second term describes the square norm of the second derivative of $P(r)$ weighted by the regularization parameter α . Since α is a measure of the roughness of $P(r)$, it is large for broad distance distributions and small for well-defined narrow distances.

$$G_\alpha(P) = \|S(t) - D(t)\|^2 + \alpha \left\| \frac{d^2}{dr^2} P(r) \right\|^2 \quad (26)$$

$$D(t) = \frac{F(t) - (1 - \lambda)}{\lambda} \quad (27)$$

For the determination of the optimal α value the L-curve criterion can be used, which is shown in Figure 19. This is a plot of $\log \eta(\alpha)$ against $\log \rho(\alpha)$, which defines the mean square deviation and the smoothness as shown in Equation (28) and (29).

$$\rho(\alpha) = \|S(t) - D(t)\|^2 \quad (28)$$

$$\eta(\alpha) = \left\| \frac{d^2}{dr^2} P(r) \right\|^2 \quad (29)$$

In case of a good signal-to-noise ratio, the plot is L-shaped (Figure 19) and the red circle in the curve shows the optimal value for the regularization parameter (here: $\alpha = 23.16$). Whereas the blue and green circles show an unrealistic regularization parameter, leading to unrealistic peak splitting or a smoothed over distribution, respectively.

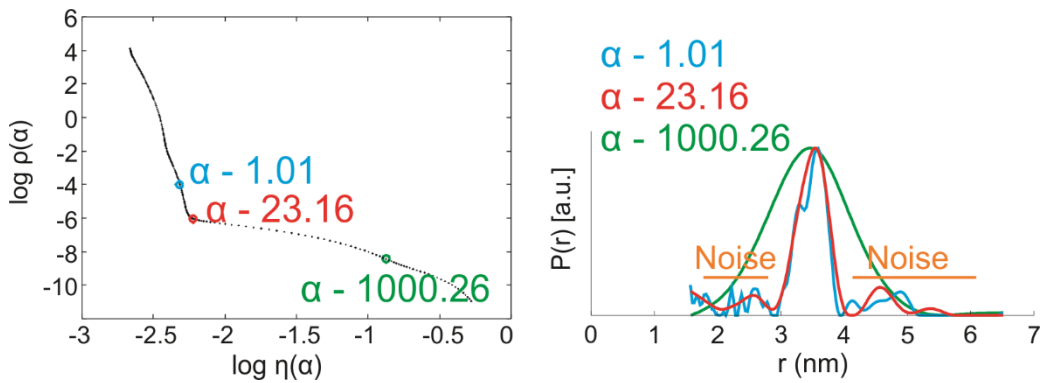


Figure 19: Tikhonov regularization L curve (DeerAnalysis 2016). The left side shows the plot that describes the relation between the mean square deviation ρ and smoothness of the distribution η with different α values, whereby the best is shown with a red circle. On the right side, distance distribution is shown for different α values. The blue line with $\alpha = 1.01$ shows an unrealistic peak splitting, the green line with $\alpha = 1000.26$ shows a smoothed over distribution with artificial broadening and the red line for $\alpha = 23.16$ shows the most realistic distance distribution.

If the measurement was long enough and the distance distribution is reliable the distance $\langle r \rangle$ and the width σ_r can be used for Gaussian Fitting. If an equilibrium between two conformations is present, DeerAnalysis can fit $F(t)$ with a two Gaussian model fit and thereby determine the value pI , which describes the fraction of peak 1 in relation to peak 2. If $pI=1$, then only the conformation with the smallest distance is present and if $pI=0$, then only the conformation with the larger distance is present. The Gauss function is described in Equation (30).

$$f(x) = ae^{-\frac{(x-b)^2}{2\sigma^2}} \quad (30)$$

The factor a is defining the maximum probability of the curve, which is the ratio of $p1$ and $p2$, b defines the position of the centre peak, which is the mean distance $\langle r \rangle$ and σ describes the width, which is σ_r . It should be mentioned, that the knowledge of the distance and width are not necessary for one or two Gaussian fittings. The program DeerAnalysis can also fit these parameters, but with the implementation of these parameters, the results get more reliable.

1.3.4.3.2 Data analysis with DD

Since DeerAnalysis is restricted to two Gaussian fittings with the implemented scripts, data with more than two fractions cannot be analysed with this software in a sufficient manner. Here DD^{93,94} (DEER data) can help, which allows using Gaussian fittings with up to eight different distances and widths. As explained before, this software can also give the relative ratio from the different fractions as output. In DD, one either sets the number of expected distances or one sets the known distances and widths directly into the program.

While it is possible in DeerAnalysis to adjust the range of the background fit, this is not possible with DD. As shown in Figure 20 the primary data set gets fitted as good as possible, while the background gets adjusted accordingly. Since the software is varying the background during fitting, it is not possible to change the set background.

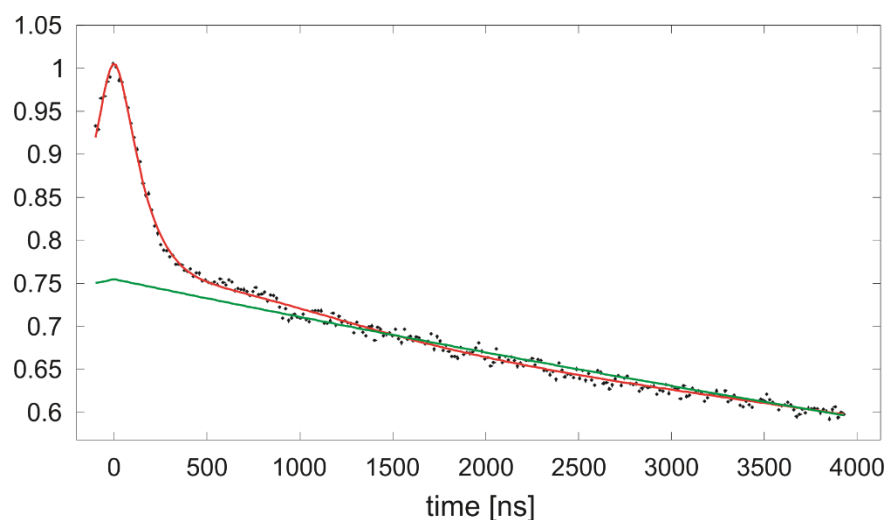


Figure 20: Data analysis with the DD software (TmrAB labelled at TmrA461 and TmrB349 with MTSSL). The original data is presented as black points and the fit is shown in red. In green, the corresponding background is shown, which was set accordingly to the best fit.

2 Motivation and aim

The class of ABC proteins is one of the largest active membrane transporter families, which are essential for import and export of a wide range of substrates. Although these systems are widely investigated a lot of questions remain open for ABC exporters about the transport mechanism and process. Because of their involvement in various diseases, especially in human cells, it is very important to understand this complex system.

In this thesis, the main aim is to improve the current understanding of the transport mechanism for ABC exporters using EPR spectroscopy, whereby the heterodimeric ABC exporter TmrAB is the model system. Several crystal structures of ABC exporter are available, but important details like the substrate binding and release, the molecular mechanism for nucleotide-induced NBD closure and the inward-outward transition of TMDs remain unknown. Especially for heterodimeric exporters, like TmrAB, the functional role of the two asymmetric ATP binding sites is unclear, whereby only one of them is supposed to be ATPase active. Moreover, the interaction of proteins and lipids, and how the native membrane environment is influencing the structure and function of the transporter, remains unknown. During a substrate transport cycle of ABC exporters, structural transitions occur, which are modulated by nucleotides and/or substrate binding. While crystal structures show a static picture of one of these conformational ensembles, it is very difficult to crystallize an ABC exporter in all the different conformational states, due to their very dynamic nature. Therefore, EPR spectroscopy is a useful technique to gain structural information with high precision on an ABC exporter in several of the intermediate states in detergent or membrane environment. During previous studies⁹⁵ the protocol for protein expression, purification and spin labelling of TmrAB has been optimized to address various of these questions using EPR spectroscopy. Thus nitroxide spin labels were introduced to the transporter at key positions, like the periplasmic gate, the cytosolic gate and both NBSs. Taking all labelling positions together, the overall structural rearrangements of the transporter can be observed and can be used to investigate the alternating access mechanism with nucleotides, the response to substrate and the asymmetry of the NBSs. In addition, it is possible with EPR spectroscopy to get insights into the thermodynamics of the transporter, which is not so easy to tackle with other methods. Crystal structures typically do not exhibit the lowest energy-state, but the state in which the system could be crystallized. With MD simulations thermodynamics can be investigated, but typically crystal structures serve as starting point and computational limitations make it difficult to observe the complete transport cycle.

3 Materials, methods and sample preparation

3.1 Materials

3.1.1 Plasmid

In Figure 21 the map of the expression vector used for TmrAB expression is shown.⁶⁶ The plasmid with the TmrA_C416A mutation is the cys-less version which was used as a basis for single or double mutants.

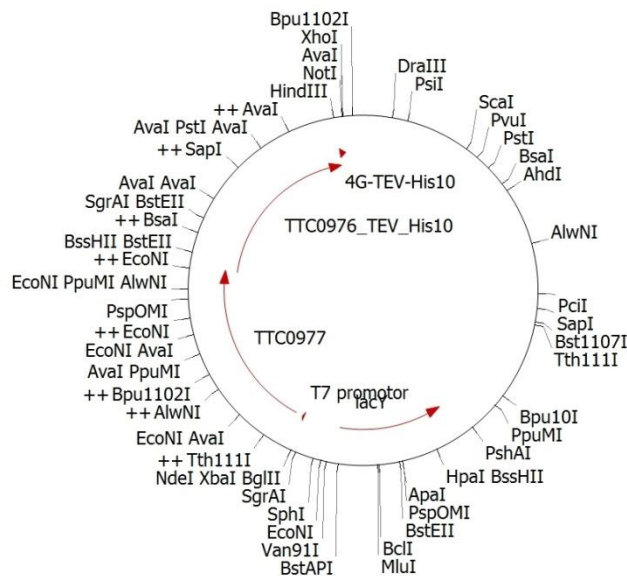


Figure 21: Schematic description of the pET22 vector, which carries the TmrAB gene. In TmrA, a 10x His-tag is implemented, via a TEV cleavage site. All restriction enzymes sites are shown. The expression of TmrAB is driven by the T7 promoter, which can be induced with IPTG.

A T7 promoter is included in the vector, which can be induced by IPTG. A TEV cleavage site coupled to a 10x His-tag is located on TmrA. In addition, the vector contains an ampicillin resistance gene.

3.1.2 Crystal structures and homology models

Simulations for the mutant planning were based on the crystal structure of TmrAB (pdb code 5MKK), which was determined via X-ray crystallography in the inward-facing state.²

Homology models were made with SWISS-MODEL⁹⁶, based on the outward-facing structure of Sav1866 with bound AMP-PNP⁹⁷ (pdb code 2ONJ) and on the occluded structure of McjD⁹⁸ (pdb code 4PL0). For comparison also the crystal structure of TM287/288⁹⁹ (pdb code 4Q4H) was used.

3.1.3 Peptides used as substrates for TmrAB

In this thesis, the peptides C4F and K5F were used. The peptide C4F was provided by the charité Berlin and was produced by solid-phase synthesis and purified by HPLC. Peptide C4F, which contains a fluorophore on the cysteine, was used for transport assays. The peptide K5F, which contains a fluorophore on the lysine, was used for EPR experiments. Peptide K5F was used for the trans-inhibition experiments and was synthesized in the Tampé lab. At first, the lysine was labelled with fluorescein and then the peptide was synthesized by solid-phase synthesis with the modified amino acid. In further experiments, the peptide K5F was provided by the company JPT from Berlin. The sequences are shown in Table 1.

Table 1: Sequences of peptides used as substrates for TmrAB. The abbreviation FL stands for the fluorophore fluorescein and is indicated in front of the labelled amino acid.

Peptide	Sequence
C4F	RRY ^{FL} CKSTEL
K5F	RRYC ^{FL} KSTEL

3.1.4 Chemicals

Table 2: List of chemicals and the suppliers used in this thesis.

Chemical	Company
ADP	Sigma Aldrich
Agar-agar	Roth
Agarose	Biozym
Aluminium chloride	Sigma Aldrich
AMP-PNP	Sigma Aldrich
Ampicillin	Roth
Argon	Praxair
ATP	Sigma Aldrich
Beryllium sulphate	Sigma Aldrich
Bio-Beads SM-2	Bio-Rad
Calcium chloride	Roth/Merck
d ⁸ -glycerol	Euriso-top
DDM	Roth
Disodium hydrogen phosphate	VWR
DMSO	Thermo Scientific
DNase	AppliChem
dNTP	Fermentas
DOPC	Avanti Polar Lipids

E.coli polar lipid extract	Avanti Polar Lipids
EDTA	Roth
Ethidium bromide	Roth
Fast digest buffer	Thermo Scientific
Glycerol	Roth
HEPES	Roth
Imidazole	Sigma Aldrich
IPTG	Roth
Lysozyme	Sigma Aldrich
Magnesium chloride	Roth
Manganese chloride	Roth
β-Mercaptoethanol	Roth
MOPS	Roth
MTSSL	Toronto Research Chemicals
PEI	Sigma Aldrich
Phusion GC buffer	Thermo Scientific
Phusion HF buffer	Thermo Scientific
PIPES	Sigma Aldrich
Potassium acetate	Sigma Aldrich
Potassium chloride	Roth
Potassium dihydrogen phosphate	Roth
Rubidium chloride	Roth
SDS	Roth
Sodium chloride	Roth
Sodium fluoride	Fluka
Sodium hydroxide	Roth
Sodium orthovanadate	Sigma Aldrich
TEMPOL	Sigma Aldrich
TRIS	Roth
Triton X-100	Fluka
Tryptone/peptone ex casein	Roth
Yeast extract	Roth

3.1.5 Nucleotides and trapping reagents

The nucleotides ATP, ADP and AMP-PNP were diluted in water and the pH was adjusted to 7.0 before use. As a non-hydrolysable ATP analogue AMP-PNP can be used to trap the transporter in the ATP-state without hydrolysis.

The vanadate solution was prepared according to the product information of Sigma Aldrich.¹⁰⁰ Afterwards the solution was stored at -20 °C. Before being used, the vanadate solution was heated up to 95 °C for 20 minutes. For the trapping with beryllium fluoride or aluminium fluoride, the stock solutions of sodium fluoride in water and beryllium sulphate in water or aluminium chloride in water were mixed directly with the protein solution.

3.1.6 Kits and columns

Table 3: List of kits and columns used in this thesis and their suppliers.

Kit or column	Company
Amicon Ultra-5 Centrifugal filters	Merck Millipore
Econo-Pac 10DG Columns	Bio Rad
Micro Bio-Spin 6 Chromatography Columns	Bio Rad
Ni-NTA Agarose	AppChem Qiagen
QIAprep Spin Miniprep Kit	Qiagen

3.1.7 Equipment

In Table 4 the equipment which was used during this thesis is listed, further used equipment, like the buildup of the EPR spectrometer are explained in sections 3.2.14 for cw and 3.2.15 for PELDOR.

Table 4: List of equipment and the suppliers used in this thesis.

Description	Model	Company
Autoclave	VE-150	Systec
Balance	440-49N	Kern
	EMB 500-1	Kern
Camera	C5060WZ	Olympia
Cell density meter	Ultrospec 10	Amersham Biosciences
Centrifuge	5417R	Eppendorf
	Avanti J-26 XP	Beckman Coulter
	RC 5B Plus	Sorvall
	Optima XE-90 Ultracentrifuge	Beckman Coulter
	Optima L-90K Ultracentrifuge	Beckman Coulter

	Optima TLX Ultracentrifuge Heraeus Fresco 21 Megafuge 16R	Beckman Coulter Thermo Scientific Thermo Scientific
Extruder	Extruder 400 nm filter membranes	Avestin Avestin
French press	Basic Z model	IUL Instruments GmbH
Freezer -20 °C		Biacore
Freezer -80°C	HFC series Forma 900 Series	Thermo Scientific Thermo Scientific
Fridge	Profi line	Liebherr
Heating chamber		Ehret
Ice machine	AF80	Scotsman
Incubation shaker	Innova 4330 Innova 43	New Brunswick Scientific New Brunswick Scientific
Incubator	Kelvitron	Heraeus instruments
Magnetic stirrer	IKA MAG RET	Sigma Aldrich
Microwave		Severin
NanoDrop		Thermo Scientific
Plate reader	Clario Star Plus	BMG Labtech
Platform shaker	KS250 basic	Ika Labortechnik
pH meter	FiveEasy Plus pH meter FP20 pH electrode	Mettler Toledo SI Analytics
Rotation evaporator	461 Water bath RE111 Rotavapor Rotary vane pump	BÜCHI BÜCHI vacuubrand
Rotor	JLA 8.1 GSA Ti45 TLA110	Beckman Coulter Sorvall Beckman Coulter Beckman Coulter
Shaker	AG CH- 4103 bottmingen	Infors HT
Sonifier	Branson sonifier 250	Thermo Scientific
Test tube rotator	34528 CMV-ROM	Snijders Fröbel Labortechnik GmbH
Thermo cycler	T personal T advanced	Biometra Biometra
Thermomixer	Compact Thermo Stat plus Universal	Eppendorf Eppendorf Labortechnik
Ultrasonic bath	Sonorex	Bandelin
UV light	UST-20 M-BR	biostep

UV-Vis spectrophotometer	Varian Cary 50 Bio	Agilent technologies
Voltage source	E143	Consort
	E835	Consort
Vortexer	Lab dancer	VWR
Water preparation	Milli-Q	Millipore

3.1.8 Enzymes and cells

Table 5: List of enzymes and cells used in this thesis and their suppliers.

Enzymes, Antibodies and Cells	Company
Phusion High-Fidelity DNA Polymerase	Thermo-Scientific
<i>DpnI</i>	Thermo-Scientific
XL1 (from <i>E. coli</i>)	Agilent technologies
BL21 (DE3) (from <i>E. coli</i>)	Merck

3.1.9 Buffers, media and solutions

Table 6: List of buffers, media and solution and their composition used in this thesis.

Buffer/Media/Solution	Composition
Elution buffer for nickel column	300 mM imidazole In HEPES buffer 0.05% DDM
HEPES buffer	20 mM HEPES 300 mM sodium chloride pH 7.5
LB-medium (1 L)	10 g trypton 5 g yeast extract 10 g sodium chloride
Low-salt LB-agar (1 L)	10 g trypton 5 g yeast extract 5 g sodium chloride 20 g agar-agar
PBS buffer	140 mM sodium chloride 10 mM disodium hydrogen phosphate 2.7 mM potassium chloride 1.8 mM potassium dihydrogen phosphate pH 7.3
Reconstitution buffer	20 mM HEPES 140 mM sodium chloride 5% glycerol pH 7.5

TAE buffer	40 mM TRIS-acetate pH 8 1mM EDTA
TFB1	30 mM potassium acetate 10 mM CaCl ₂ 50 mM MnCl ₂ 100 mM RbCl 15% glycerol pH 5.8
TFB2	10 mM MOPS or PIPES 75 mM CaCl ₂ 10 mM RbCl 15% glycerol pH 6.5
TSK buffer	20 mM HEPES 150 mM sodium chloride pH 7.2
Transport buffer for transport assay	20 mM HEPES 107 mM sodium chloride 5% glycerol pH 7.5
Wash buffer for nickel column	50 mM imidazole 1mM β-mercaptoethanol In HEPES buffer 0.05% DDM

3.1.10 Molecular rulers and loading dyes

Table 7: List of molecular rulers and loading dyes used in this thesis and their suppliers.

Description	Company
6x DNA loading dye	Thermo Scientific
GeneRuler 1 kb Plus DNA ladder	Thermo Scientific

3.1.11 Software

Table 8: List of software used in this thesis and their application.

Software	Application
ChemBioDraw Ultra 12.0	Chemical structures
CLC sequence viewer	Sequence alignment
Corel Draw X8/2018	Creating Figures
DD6c	PELDOR data evaluation
DeerAnalysis 2016	PELDOR data evaluation
MATLAB R2017a/R2018b	For MMM, DeerAnalysis and DD
Mendeley	Reference management
Microsoft Office Excel	Calculations
Microsoft Office Picture Manager	Image modification
Microsoft Office Word	Thesis writing
MMM 2015/2017.2	MTSSL rotamers and interspin distance simulations
Origin 2018/2019	Data plotting
PyMOL 2.2.3	Protein structure viewing

3.2 Methods

3.2.1 Cloning of TmrAB cysteine single or double mutants

PCR-based site-directed mutagenesis with Phusion High-Fidelity DNA Polymerase (Thermo-Scientific) was used for the cloning of TmrAB cysteine single or double mutants. The Phusion DNA Polymerase has a 5'→3' DNA polymerase activity and 3'→5' exonuclease activity and is generating blunt ends.¹⁰¹

For every mutation, a forward and a reverse primer with the wanted cysteine mutation were designed, with 9 bp before and 27 bp after the mutation position. All primers, which were used in this thesis, are shown in Table 9 and were provided by Eurofins Genomics¹⁰². The primers for the double mutants TmrA_T61C TmrB_R56C and TmrA_K585C TmrB_A562C are not presented here since the mutants were cloned during previous studies.⁹⁵ For all mutants, the cysteinless plasmid with the TmrA_C416A mutation was used as a template and for simplification, this mutation is not further mentioned.

Table 9: Primers used for the cloning of the cysteine double mutants of TmrAB. The mutated bases are highlighted in red. The primers for TmrA are written in capital letters and primers for TmrB in lowercase letters.

Primer	Sequence
A_V288C	CGG GGC GCC TGC TCC TTG GGG CTT CTC GTG GCC TTC GTG
A_V288C_rev	CCC CAA GGA GCA GGC GCC CCG CAC CAC CTC CCC GCC CCC
B_E272C	gtc cgg ggg tgt ctg agc gtg ggg gag ctc gtc cag ttc
B_E272C_rev	cac gct cag aca ccc ccg gac cac cat ggc gcc ccc ggc
A_D112C	CTC AGG AGC TGC CTT TTC GCC AAG CTC ATG CGC CTC CAC
A_D112C_rev	GGC GAA AAG GCA GCT CCT GAG GTC AAA GAG GAC CCG CTG
B_D97C	ctg agg cgg tgc ctc ctc cac cac ctc ctc acc ttg gac
B_D97C_rev	gtg gag gag gca ccg cct cag gtc gta ctc cac ctg gcg
A_V461C	GAC CCC AGC TGT CCC CCG GAG CGG GTG GAG GAG GTG GCC
A_V461C_rev	CTC CGG GGG ACA GCT GGG GTC AAA GAG GCG CAG GTT GTC
B_D349C	ctc aag cgg tgc ggg cgc tgg ctc ctt agg ggc ctc acc
B_D349C_rev	cca gcg ccc gca ccg ctt gag ccc cac ccc ttc aaa gcg
A_A416C	CAG AGG GGG TGC GTC TTC TTG GAC GGG GTG GAC GTG CGG
A_A416C_rev	CAA GAA GAC GCA CCC CCT CTG GGG GTC GTA GAA GCG GGC
B_L458C	gag gag atc tgc gcc ttt ccc aag ggg tac gag acg gtc
B_L458C_rev	ggg aaa ggc gca gat ctc ctc gtg gat ccc ggc gag ccg
A_E538C	CGC CTC CAG TGC GCC CTT TAC AAG GCC ATG GAA GGG AGG
A_E538C_rev	GTA AAG GGC GCA CTG GAG GCG CTT CTC CGT CTC CGA GTC
B_R549C	gac ggg ggg tgc atc gtg gag gag ggg acc cac gag agc
B_R549C_rev	ctc cac gat gca ccc ccc gtc cag gac gat gat cca gtc
A_S578C	GAG GAG GGG TGC CAC GAG GAG CTT CTG GCC AAG GGC GGC
A_S578C_rev	CTC CTC GTG GCA CCC CTC CTC CAC GAG CCT CCC CTT GCG
B_T555C	gag gag ggg tgc cac gag agc ctc ctt cag gcc gga ggc
B_T555C_rev	gct ctc gtg gca ccc ctc ctc cac gat cct ccc ccc gtc
A_E523Q	ATC CTG GAC CAG GCC ACG GCC AGC GTG GAC TCG GAG ACG
A_E523Q_rev	GGC CGT GGC CTG GTC CAG GAT GAG GAG GAT GTC GGG GCT

In Table 10 the reaction mixture for the used PCR is shown, whereby both cysteine mutations were introduced at the same time. As already mentioned, cys-less TmrAB was used as a template for the PCR. In the case of single mutants, the final volume was adjusted by adding more water to the reaction mixture. For the additional E-to-Q-mutation, which was introduced to some double mutants, the double mutant was used as a template. In every case two mixtures were prepared, one with GC buffer and one with HF buffer. Generally, HF buffer is the favourable buffer, because of the high error rate of Phusion DNA

Polymerase with the GC buffer, but since TmrAB is a GC-rich protein the GC buffer is sometimes more effective.¹⁰¹

Table 10: PCR mixture for the generation of double cysteine mutagenesis of TmrAB with Phusion HF or Phusion GC buffer. The final volume was adjusted via the amount of water in case of the generation of single cysteine mutants.

	Volume [μ L]	Final concentration
5x Phusion GC/HF	10	1x
dNTPs (10 mM)	1	0.2 mmol/L
N-terminal primer 1(100μM)	1.25	0.25 mmol/L
C-terminal primer 1(100μM)	1.25	0.25 mmol/L
N-terminal primer 2(100μM)	1.25	0.25 mmol/L
C-terminal primer 2(100μM)	1.25	0.25 mmol/L
Template (60 ng/ μL)	2.1	2.5 ng/ μ L
Phusion Polymerase (2 U/μL)	0.5	1 U/ μ L
DMSO	1.5	
ddH₂O	29.9	
Final volume	50	

To reduce unspecific amplifications all mixtures were pipetted on ice and polymerase was added directly before the reaction was started. In Table 11 the program used for the PCR is presented, which was performed in a thermo cycler (Biometra).

Table 11: Thermal cycling program used for the PCR-based site-directed mutagenesis of TmrAB.

	Temperature [$^{\circ}$ C]	Time [min]	Cycle
Initial denaturation	98	5	1
Annealing	75	1	
Elongation	72	4	
Denaturation	98	1	25
Annealing	75	1	
Elongation	72	4	
Final Elongation	72	10	1

To see if the PCR was successful an agarose gel electrophoresis (see section 3.2.2) was made after the PCR and afterwards, a *DpnI* (3.2.3) digestion was done.

3.2.2 Agarose gel electrophoresis

To check the DNA amplification after PCR, agarose gel electrophoresis was performed, where the length of the amplified DNA can be investigated referring to a marker.

In every case, an 1% agarose gel was used. The gel was prepared by mixing 1% w/v agarose with TAE-buffer and heating the gel in a microwave until the agarose was completely dissolved. Subsequently, the gel was cast. As reference marker Thermo Scientific 'GeneRuler 1 kb Plus DNA Ladder'¹⁰³ was used.

For every gel, one lane was loaded with a mixture of 2 μ L 6x DNA loading dye and 5 μ L DNA ladder. For the PCR samples, a mixture of 2 μ L 6x DNA loading dye and 8 μ L sample was loaded on the gel. The gels were running in TAE buffer at 120 V for approximately 35 minutes. Thereafter gels were incubated in a 0.5% ethidium bromide bath for 15 minutes. After staining, the gel was imaged with a documentation system, containing a camera connected to a computer, an UV light source and a coverage.

3.2.3 DpnI fast digest

After the PCR, not only the amplified DNA is present, but also the template DNA. With *DpnI* fast digest the methylated template DNA can be specifically removed.

On ice 10 μ L of 10x fast digest buffer, 4 μ L ddH₂O and 1 μ L *DpnI* were added to the PCR reaction tubes. Then the mixture was incubated at 37 °C for 10 minutes and afterwards at 90 °C for five minutes for inactivation of the enzyme and stopping of the digestion. The mixtures were then stored at -20 °C.

3.2.4 Generation of competent *E. coli* cells

For the generation of competent *E. coli* cells, XL1 and BL21 (DE3) cells were used and prepared with rubidium chloride, which is supposed to make the cells more competent. Here, the protocol will be described for completeness, but the preparation was done by members of the Tampé lab.

At first, an overnight culture with 2.4 mL LB medium was inoculated with a single colony from an LB plate and incubated overnight at 37 °C and 180 rpm. On the next day, the overnight culture was used to inoculate 250 mL LB medium containing 20 mM MgSO₄ in a 1 L baffled flask until an OD₆₀₀ between 0.4 and 0.6 was reached. Then the cells were

pelleted by centrifugation (4500 g, 5 min, 4 °C). Afterwards, the cell pellet was resuspended in 100 mL ice-cold TFB1 buffer and kept on ice all the time. The resuspended cells were incubated on ice for five minutes and then again pelleted by centrifugation (4500 g, 5 min, 4 °C). Thereafter the cells were resuspended in 10 mL ice-cold TFB2 buffer and incubated on ice for 15-60 minutes. Finally, the cells were aliquoted into precooled tubes and quickly frozen in liquid nitrogen and stored at -80 °C.

3.2.5 Transformation and retransformation

After the *DpnI* digestion, the plasmids were transformed into *E. coli* XL1 competent cells for vector amplification. With higher concentrated plasmids, which were gained by vector amplification, retransformations into *E. coli* XL1 competent cells were made for further amplification or retransformation into *E. coli* BL21(DE3) competent cells were made for protein expression. For this purpose, the cells were plated onto LB-agar plates containing ampicillin. Because of the ampicillin resistance gene, the plates are selective for positive clones.

For a transformation 5 µL of the PCR product after *DpnI* digestion were added to 50 µL of *E. coli* XL1 competent cells. For a retransformation 1 µL of higher concentrated plasmid solution was added to either *E. coli* XL1 competent cells or *E. coli* BL21(DE3) competent cells. The mixture was mixed with the pipette tip and incubated for 5 minutes on ice. Afterwards, the mixture was plated onto an LB-agar-plate (preheated 37 °C, 15 min), containing ampicillin (100 µg/mL). The plates were then incubated at 37 °C overnight.

3.2.6 Sequencing

For the sequencing of the plasmids, an overnight culture of *E. coli* XL1 cells was prepared with 5 mL LB-medium containing 100 µg/mL ampicillin inoculated with a clone from a transformation plate. After incubation in a shaker at 37 °C and 180 rpm overnight, the plasmid was purified with the QIAprep Spin Miniprep Kit from Qiagen. The plasmid concentrations after purification were determined with a NanoDrop.

For sequencing 13 µL of the plasmid solution (~100 ng/ µL) was mixed with 2 µL primer solution (1.2 pM) and sent as a premixed sample to Eurofins Genomics.¹⁰² All used primers are shown in Table 12. Sequence alignment was made with the CLC sequence viewer software.¹⁰⁴

Table 12: Primers used for the sequencing of TmrAB cysteine mutations.

Primer	Sequence
Seq 1	GGC CTG GTT CCA GGA CCT GA
Seq 2	CTC GCC TTT CCC AAG GGG TA
Seq 3	TCC GAC GTG GAC GCC ATC AA
Seq 4	TCA TCG CCC GCT TCT ACG AC
T7_promoter	TAA TAC GAC TCA CTA TAG GG
T7_terminator	CCC AAG GGG TTA TGC TAG

3.2.7 Expression

An overnight culture with 150 mL LB-medium containing 100 µg/mL ampicillin and a clone from a transformation plate with *E. coli* BL21(DE3) competent cells was prepared in a baffled flask and incubated in a shaker at 37 °C at 180 rpm.

For the expression, 2 L LB-medium containing 100 µg/mL ampicillin was inoculated with 20 mL of the overnight culture in a 5 L baffled flask. The culture was incubated in a shaker at 37 °C and 160 rpm until an OD₆₀₀ between 0.6 and 0.8 was reached. Afterwards, the culture was induced with 1 mL of 1M IPTG (Isopropyl-β-D-thiogalactopyranoside), typically after approximately two hours. The culture was then incubated for another 3.5-4 hours at 37 °C and 160 rpm, while the protein expression took place. Finally, the cells were harvested using centrifugation (4500 rpm, 15 min, 4 °C) and the obtained cell pellet was weighted (typically ~45 g for 12 L culture) and stored at -80 °C.

3.2.8 Purification

Initially, the purification is starting with the membrane preparation, whereby the cells are lysed to isolate the membranes, which contain the protein. Therefore, the cell pellet was suspended in HEPES buffer containing 100 µg/mL lysozyme. For cell lysis with a French press, a small amount of DNase was added to remove the remaining DNA. The cells were then lysed with the French press and a pressure of 1 kbar. If the French press was not used, then the cells were disrupted using a sonifier (duty cycle 60, output control 6, 2-3 min). In both cases the cell fragments were pelleted by centrifugation (8000 rpm, 15 min, 4 °C) and afterwards the supernatant containing the membranes was centrifuged (42000xg, 1 h, 4 °C) to pellet the membranes, which were then stored at -80 °C (normally ~10 g from ~45 g cells).

To obtain the protein the membrane pellet was resuspended in HEPES buffer until a homogenous mixture was reached. Afterwards, 1% *n*-dodecyl- β -D-maltopyranoside (DDM) was added for solubilisation and the mixture was stirred for one hour at 4 °C. The membrane suspension was centrifuged (42000xg, 30 min, 4 °C) to pellet the membranes, whereby the protein remained in solution.

Since the protein includes a 10x His-tag, which can bind to Ni-NTA, the protein can get purified via IMAC (immobilized metal ion chromatography). Further description about how the 10x His-tag can bind to the Ni-NTA can be found in the user manual from Qiagen.¹⁰⁵ Fresh Ni-beads from Qiagen were washed with water and transferred to HEPES buffer via resuspending in water or buffer, centrifugation (2000xg, 5 min, 4 °C) and removing the supernatant (this procedure was repeated two times). Afterwards, the Ni-beads were resuspended in HEPES buffer (200 mM HEPES, 300 mM NaCl) in a 1:1 v/v ratio. Already used Ni-beads were restored by washing with 0.5 M sodium hydroxide solution for 30 minutes and the same washing procedure with water or buffer, whereby the washing with water was repeated four times.

In order to bind the 10x His-tag on the Ni-beads the supernatant from ultracentrifugation was stirred for one hour at 4 °C with 30 mM imidazole, 1 mM β -mercaptoethanol and 5 mL of Ni-beads (1:1 v/v ratio in HEPES buffer, for ~10 g membrane pellet). Then the mixture was loaded on a column and the flow-through was discarded. Afterwards, the Ni-beads with protein-bound via the 10x His-tag were washed with 10x column volume washing buffer (HEPES buffer with 50 mM imidazole, 1 mM β -mercaptoethanol and 0.05% DDM). Finally, 10 fractions, 0.5 mL each, were eluted with elution buffer (HEPES buffer containing 300 mM imidazole and 0.05% DDM). The protein concentration was determined for all fractions via NanoDrop and the six fractions with the highest concentration were pooled. Then a buffer exchange to TSK buffer containing 0.05% DDM was performed by using Econo-Pac 10DG columns (desalting columns), leading to a final protein solution of 4 mL volume, typically with a concentration of 0.7-1 mg/mL.

During previous studies⁹⁵, it was found that the purity of the protein at this stage is sufficient for EPR spectroscopy, therefore no further purification steps were done. The protein solution was directly spin labelled or if cys-less protein was used, it was also proceeded like further described in the spin labelling section (3.2.9).

3.2.9 MTSSL labelling of TmrAB or K5F

Via site-directed spin labelling, MTSSL can be attached to the cysteine of the protein of interest. During previous studies⁹⁵ different conditions for labelling time, temperature or concentration of MTSSL were tested and the method with the best efficiency and least effort was further used.

For the spin labelling, a stock solution of MTSSL in DMSO (100 mM) was used, which was added in 40 fold molar excess to the 4 mL protein solution in TSK buffer with 0.05% DDM. To prevent the formation of biradicals in the aqueous solution, where the probability for biradical formation is higher than in DMSO, the pipette tip was moved in the solution carefully while adding the stock solution slowly. Then the mixture was incubated on an overhead rotor for 30 minutes at room temperature.

Since the free spin label needs to be removed and a higher concentration of protein would be optimal for EPR spectroscopy, the protein was concentrated with Amicon Ultra-5 Centrifugal filters to a volume of approximately 50 μ L. Afterwards, the solution was added to Micro Bio-Spin 6 Chromatography Columns, which were previously equilibrated with TSK buffer containing 0.05% DDM, for the separation of free spin label. The final protein concentration was determined via NanoDrop.

Labelling efficiency was tested with cw spectroscopy (section 3.2.14). Samples for PELDOR measurements (3.2.15) were either directly prepared in detergent solution or the protein was reconstituted into liposomes (3.2.11), either for transport assays (3.2.12) or for PELDOR measurements in liposomes. Sample preparation is further described in chapter 3.3.

For some experiments, spin labelled K5F peptide was required, which contains one free cysteine in the sequence. For spin labelling of K5F, 200 μ M peptide in water was mixed with 200 μ M MTSSL label and incubated for two hours at room temperature. The spin-labelled peptide was stored at -20 °C.

3.2.10 Preparation of liposomes

Before the protein could be reconstituted into liposomes, the liposomes itself had to be prepared. Therefore, 1.4 mL of *E. coli* polar lipid extract (25 mg/mL in chloroform, from Avanti Polar Lipids) and 0.6 mL DOPC (dioleoyl-*sn*-glycero-3-phosphocholine, 25 mg/mL in chloroform, from Avanti Polar Lipids) were mixed and the chloroform was removed with a rotary evaporator (20 min at 300 mbar and 20 min at 100 mbar). Since the dried liposomes have a high risk for oxidation, they needed to be protected by an inert gas atmosphere (argon), which was introduced through the rotary evaporator. Afterwards, the liposomes were resuspended in 2.5 mL reconstitution buffer (to 20 mg/mL) with the help of an ultrasonic bath until the solution was clear. Aliquots of the solution were frozen in liquid nitrogen and warmed to room temperature for five times (freeze and thaw). Finally, the aliquots were stored at -80 °C.

3.2.11 Reconstitution of protein into liposomes

Protein was reconstituted into liposomes for two different purposes, either for transport assays or for EPR measurements in liposomes, which is more similar to the natural membrane environment compared to detergent micelles.

In both cases, the liposomes were brought to room temperature and extruded 11 times through a 400 nm polycarbonate filter membrane. After destabilizing the liposomes (20 mg/mL) with Triton X-100 for 30 minutes at 4 °C, spin-labelled TmrAB or wild type TmrAB was added at a molar protein-to-lipid ratio of 1:15,000 for transport assays or 1:2,000 for EPR measurements. For transport assays, the sample volume was adjusted to a final lipid concentration of 2.5 mg/mL and for EPR samples to 10 mg/mL, respectively. After another 30 minutes incubation at 4 °C Bio-Beads were added for removing the detergent and to facilitate the insertion of the proteins into liposomes. For this purpose, Bio-Beads were added in steps and always incubated at 4 °C on an overhead rotor. In a first step, approximately 40 mg Bio-Beads were added and after one hour another 40 mg Bio-Beads were added. After one night incubation, approximately 80 mg Bio-Beads were added and after two hours 80 mg Bio-Beads were added again. Following another two hours of incubation, the Bio-Beads were removed and the solution was transferred into an ultracentrifugation tube. Proteoliposomes were harvested by ultracentrifugation (80000 rpm, 30 min, 4 °C) and the supernatant was discarded. For transport assays, the proteoliposomes were resuspended in reconstitution buffer to a final concentration of 5 mg/mL, whereas for EPR spectroscopy the proteoliposomes were resuspended with

reconstitution buffer to a final volume of approximately 20-30 μL . Reconstitution efficiency was determined with cw EPR spectroscopy.

3.2.12 Transport assay

If the transporter is reconstituted into liposomes, two orientations of the transporter are possible in proteoliposomes since the transporter can adopt a right-side-in or right-side-out orientation. The right-side-out orientation can be used for transport assays to observe the transport of substrate, in which conventional methods are using isotopically labelled substrates. In addition, also other methods for determining the transport activity can be used, for example with a fluorescent substrate.

Typically for a transport assay, 6 samples were prepared with the composition shown in Table 13.

Table 13: Transport assay mixture for determination of substrate transport of TmrAB.

Compound	Volume [μL]
Magnesium chloride (100 mM)	1.5
Reconstituted protein sample (5 mg/mL)	10
Peptide C4F (300 μM)	0.5
Transport buffer	33

5 μL ATP (30 mM) was added to three out of the six samples, where the ATP hydrolysis and therefore substrate transport can take place. 5 μL transport buffer was added to the remaining three samples, which served as a negative control and background measurements since here no ATP for substrate transport is present. Directly after adding either ATP or the buffer, the samples were heated up to 68 $^{\circ}\text{C}$, if not stated different, for 5 minutes. Afterwards, the transport was stopped by adding 200 μL PBS buffer with 10 mM EDTA. EDTA is a chelate ligand, which can coordinate free magnesium in solution and thereby prevent ATP hydrolysis. Furthermore, a filter plate (0.65 μm , Durapore) was incubated for 20 minutes with 0.3% polyethyleneimine (PEI) and afterwards, the PEI was removed by a vacuum pump. Then the 250 μL samples were transferred to the filter plate and the solution was removed by a vacuum pump, hereby only the proteoliposomes remain on the filter. Afterwards, the samples were washed two times with 250 μL PBS buffer containing 10 mM EDTA. For the final measurement, the samples were incubated for 10 minutes with 250 μL PBS buffer containing 0.1% SDS. Then, 150 μL of the samples were transferred into a black

96^{er} ELISA plate. For quantification, a standard curve was recorded with PBS buffer containing 0.1% SDS as a blank sample. In addition, standard samples of the C4F peptide in the same buffer were measured with different concentrations. Concentrations of 2 nM, 4 nM, 10 nM, 50 nM and 100 nM were used. Fluorescence was measured with a CLARIO star plate reader from BMG labtech.

3.2.13 MMM software

The software MMM⁸³ (Multiscale Modeling of Macromolecular systems) which can be implemented into MatLab, was used to choose the labelling positions in a protein. This is important because positions with spatial restrictions can lead to insufficient labelling. In addition, structure and/or function of the protein can be influenced by a spin label on restricted sites. On the other side, labelling of a completely unrestricted position with high flexibility can lead to a broad distance distribution, which results in no clear information about the investigated system.

These problems can be overcome with careful analysis of labelling sites and therefore the rotamer library approach⁸⁴ of the MMM program is a good and helpful tool. Moreover, distance distributions can be simulated with MMM based on a crystal structure or homology model. With this software, the relative energies of the spin rotamers attached to a specific position are calculated as a sum of pairwise Lennard-Jones potential energies between atoms of the spin label and atoms of the protein. These spin rotamers were calculated from the MD trajectories of the dihedral angles of free MTSSL. As a result, for every position, a number of rotamers with a partition function Z can be given. Hereby the partition function Z is a measure of the tightness of the labelling site, whereby small values correspond to a high net interaction energy between the label and the environment surrounding the protein molecule, leading to possible labelling failure. For the MTSSL rotamer library at 175 K, Z values <0.05 are regarded as tight sites, which means labelling could fail or could lead to significant influences on the protein structure.⁸⁴

3.2.14 Continuous wave measurements

For all continuous wave (cw) EPR measurements 20 μ L sample was transferred into Blaubrand-intramark micropipettes (Brand) with a micropipette controller (Brand) and sealed with heamtocrit sealing kit (Brand). All cw EPR measurements were performed at X-band frequency (9.4 GHz) using a Bruker E500 spectrometer with a SHQE cavity, with

the following experimental parameters: 100 kHz modulation frequency, 1.5 G modulation amplitude, 0.6 mW microwave power, 20.48 ms time constant, 81.92 ms conversion time, 1024 points and 200 G sweep width. The EPR signal was recorded as the first derivative of the absorption signal. For spin counting the signal was double integrated and the intensity compared to a TEMPOL reference sample.

3.2.15 PELDOR measurements

For PELDOR measurements 10-15 μL of a sample containing 20 % deuterated glycerol was transferred into a 1.6 mm outer diameter and 1.1 mm inner diameter quartz EPR tube (Suprasil, Wilmad LabGlass) and was immediately frozen in liquid nitrogen. All PELDOR data were measured on an ELEXSYS E580 EPR spectrometer (Bruker) equipped with a PELDOR unit (E580-400U, Bruker), a continuous-flow helium cryostat (CF935, Oxford Instruments), an arbitrary waveform generator (SpinJet-AWG) and a temperature control system (ITC 502, Oxford Instruments). The experiments were performed at Q-band frequencies (33.7 GHz) using an ELEXSYS SuperQ-FT accessory unit and a Bruker AmpQ 10 or 150W TWT (Applied Systems Engineering Inc.) amplifier with a Bruker EN5107D2 cavity at 50 K. For 4-pulse PELDOR (DEER), a dead-time free 4-pulse sequence with phase-cycled $\pi/2$ -pulses was used. Thereby typical pulse lengths for the observer pulses were 16 and 32 ns (for $\pi/2$ and π pulses) and 12 ns (π pulse with 150 W) or 20 ns (π pulse with 10 W) for the pump pulse. The frequency of the pump pulse was set to the maximum of the echo-detected field swept spectrum, and the observer pulses were adjusted 80 MHz lower, hence on the high-field side of the EPR spectrum. Deuterium modulations were averaged out by increasing the first interpulse delay by 16 ns for eight steps. The 7-pulse Carr-Purcell measurements were done with the help of Dr Philipp E. Spindler, who also removed the artefact occurring in these measurements. For 7-pulse Carr-Purcell PELDOR, typical pulse lengths were 32 ns ($\pi/2$ and π) for the observer pulses and 400 ns (π) for the sech/tanh pump pulses. Hereby the interpulse delays τ_1 , τ_2 , and τ_3 were chosen to be as close to each other as possible while avoiding overlap with any of the unwanted echoes created by the four observer pulses. While the second pump pulse was kept fixed, the first and the third pump pulses were moved in equal but opposite time increments of 24 ns and the third pump pulse was reversed in time to avoid signal distortion from ringing. The form factor was obtained after background correction and artefact removal with a home-written MATLAB script by Dr Philipp E. Spindler.

For determination of distance distributions the software DeerAnalysis¹⁰⁶ version 2016 was used, in which the normalized primary PELDOR data $V(t)/V(0)$ were processed to remove the background function from intermolecular interactions and the resulting form factors $F(t)/F(0)$ were fitted with a model-free Tikhonov regularization or Gaussian function(s) to obtain the distance distributions.

For distance distributions with more than two distances the software DD¹⁰⁷ version 6c was used, which fits the dipolar evolution trace as a sum of up to eight Gaussian distance distributions.

3.3 Sample preparation

3.3.1 Samples for the investigation of the alternating access mechanism of TmrAB

For the investigation of the alternating access mechanism, various samples with different nucleotides have been prepared to introduce conformational changes. The protein concentration was always in the range of 30-60 μM for the samples in detergent micelles (β -DDM). For the apo-state, no nucleotides were added and the sample was either prepared in detergent micelles or reconstituted into proteoliposomes, as described in section 3.2.11. For the pre-hydrolysis-state, 10 mM ATP and 0.5 mM EDTA (ATP-EDTA) or 10 mM AMP-PNP, which is a non-hydrolysable ATP analog, and 10 mM Mg^{2+} (AMP-PNP- Mg^{2+}) were added. In addition, the system can be trapped in the pre-hydrolysis-state by adding 10 mM ATP, 16 mM sodium fluoride, 4 mM beryllium sulfate and 10 mM Mg^{2+} (ATP- BeF_3^- - Mg^{2+}). The transition-state was induced by adding 10 mM ATP, 10 mM ortho-vanadate and 10 mM Mg^{2+} (ADP- V_i - Mg^{2+}) in detergent micelles and also reconstituted into proteoliposomes. For the samples in proteoliposomes, the trapped protein was added to the proteoliposomes as described in section 3.2.11, whereby in every step the concentration of ATP, ortho-vanadate and Mg^{2+} was kept constant. Another possibility to obtain the transition-state is by adding 10 mM ATP, 16 mM sodium fluoride, 4 mM aluminium chloride and 10 mM Mg^{2+} (ADP- AlF_4^- - Mg^{2+}). For the post-hydrolysis-state, 10 mM ADP and 10 mM Mg^{2+} (ADP- Mg^{2+}) were added and for hydrolysing conditions 10 mM ATP and 10 mM Mg^{2+} (ATP- Mg^{2+}) were added. All samples with nucleotides in detergent micelles were incubated for five minutes at 68 °C. For PELDOR samples 15-20% (v/v) deuterated glycerol was added, and after transfer into the PELDOR tube the sample was directly frozen in liquid nitrogen and stored at -80 °C.

3.3.2 Samples for the investigation of the conformational equilibrium by ATP binding

For the investigation of the conformational equilibrium by ATP binding, the protein concentration was always fixed to 50 μM ; only in one case 40 μM was used, due to a low concentration of the protein solution. As the protein concentration is taken into account in the calculations of the K_{eq} , this difference is not further discussed. All samples were prepared in detergent micelles (β -DDM). For the investigation of the equilibrium of the ATP-EDTA state with different ATP concentrations 0.5 mM EDTA was used and the ATP concentration was varied as indicated. All samples were incubated for five minutes at 68 $^{\circ}\text{C}$. For the thermodynamical investigations of the ATP-EDTA equilibrium 50 mM ATP and 0.5 mM EDTA were used and the samples were incubated for five minutes at the indicated temperature. For PELDOR samples 15-20% (v/v) deuterated glycerol was added, and after transfer into the PELDOR tube the sample was directly frozen in liquid nitrogen and stored at -80 $^{\circ}\text{C}$.

3.3.3 Samples for the investigation of the trans-inhibition by K5F peptide

To investigate the mechanism of trans-inhibition of TmrAB, the protein concentration was always fixed to 50 μM . All the samples were prepared in detergent micelles (β -DDM). For the investigations in the ATP-EDTA state 10 mM ATP and 0.5 mM EDTA were used and for ATP- Mg^{2+} 10 mM ATP and 10 mM Mg^{2+} were used. To achieve an excess of substrate typically 500 μM K5F was added, if not stated differently. All samples were incubated for five minutes at 68 $^{\circ}\text{C}$. For PELDOR samples 15-20% (v/v) deuterated glycerol was added and after transfer into the PELDOR tube, the sample was directly frozen in liquid nitrogen and stored at -80 $^{\circ}\text{C}$.

4 Results

In Figure 22 the proposed transport cycle for the heterodimeric ABC exporter TmrAB is shown, which served as a working model for this thesis.

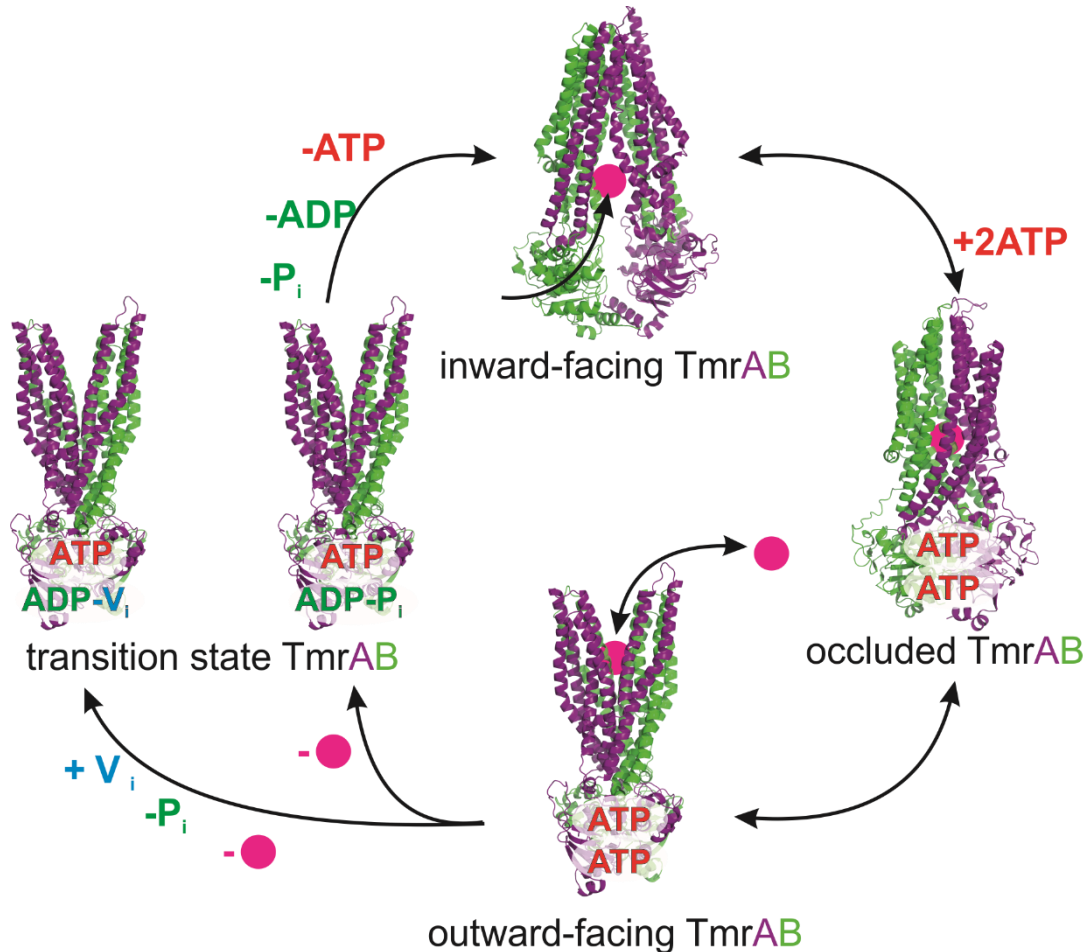


Figure 22: Proposed transport cycle for the heterodimeric ABC exporter TmrAB. The cycle starts on top with the inward-facing structure of TmrAB (pdb code 5MKK), where the substrate, indicated as a pink dot, is supposed to access the transporter from the cytosolic side. Continuing clockwise, by ATP binding the transporter should close the NBDs and first change to an occluded conformation, where the substrate is surrounded by the TMDs, which are closed on the cytosolic side and on the periplasmic side. The occluded conformation is illustrated by a homology model of TmrAB, based on the occluded structure of McjD (pdb code 4PL0). Afterwards, the TMDs are supposed to open on the periplasmic side, whereby the substrate can be released. The outward-facing structure is shown with a homology model of TmrAB based on the outward-facing structure of Sav1866 with bound AMP-PNP (pdb code 2ONJ). Via a transition state, after hydrolysis of one ATP, the transporter can move back to the inward-facing conformation, by the release of ATP, ADP and P_i . If vanadate is present, it can insert into the phosphate bond after ATP hydrolysis and thereby trap the transporter in the transition state.

With X-ray crystallography, it was so far only possible to crystallize the inward-facing structure of TmrAB (apo-state) without any nucleotide. For other heterodimeric ABC exporters, no occluded or outward-facing structure is available as well. It is assumed that the transport cycle can be different compared to homodimeric export systems and, so far, studies on the homodimeric transporter MsbA¹⁰⁸, the heterodimeric exporter BmrCD¹⁰⁹ and the heterodimeric exporter TM287/288¹¹⁰ could show that EPR spectroscopy is a useful tool to investigate this highly important transporter class, which still is not well understood. As shown in Figure 22 a mechanism can be proposed, which is starting in the inward-facing state, where the substrate (indicated as a pink dot) presumably binds in the binding pocket in the TMDs, coming from the cytosolic side. By ATP binding, the transporter should then close the NBDs and change to an occluded conformation, in which both sides of the TMDs are closed and capture the substrate. By the opening of the TMDs on the periplasmic side, the substrate can be released. To restore the transporter for the next transport cycle, ATP hydrolysis is taking place on the consensus ATP binding site, and ATP, ADP and P_i get released before the transporter moves back to the inward-facing conformation. This so-called transition state can be trapped by vanadate, which inserts into the phosphate bond of ADP after hydrolysis and thereby locks the transporter in the outward-facing conformation. In the following sections, several aspects of this cycle are further investigated. These are the conformational changes of the alternating access mechanism (section 4.1) and the equilibrium between the inward-facing and outward-facing structure and how this can be influenced by changing the ATP concentration or the temperature (section 4.2). Moreover, the role of the substrate is further investigated in relation to how trans-inhibition is influencing the transporter (section 4.3).

4.1 Alternating access mechanism of TmrAB

4.1.1 Mutant planning and simulations of labelling positions

For the investigation of the transport cycle presented in Figure 22, double mutants were needed to monitor conformational changes. For this purpose, the inward-facing structures of the ABC exporters MsbA¹¹¹, TM287/288³¹ and Sav1866⁹⁷ were compared to the structure with bound nucleotides in the outward-facing conformation. The transmembrane domains act as gates, which is clearly visible in the different conformations, whereby the TMDs are closed to the periplasm and open to the cytoplasm in the inward-facing state and the other way around in the outward-facing state. Therefore, the part of the protein located in the periplasm is called the periplasmic gate and the part in the cytoplasm is called cytosolic

gate. These two gates are key positions in substrate uptake and release, where distance changes should be clearly visible.

Moreover, the nucleotide binding domains are very important for the whole transport cycle since they should close by nucleotide binding and open after hydrolysis and nucleotide release. Therefore, central positions were chosen in the NBDs to observe the global movement in the NBDs. In an asymmetric ABC exporter, one ATP binding site is the consensus site, which is supposed to bind and hydrolyse ATP, and the other site is degenerated, which means that this site is supposed to bind ATP without hydrolysis. Therefore, these two sites are also key positions to observe their different behaviour.

Due to the available crystal structures of ABC exporters and related EPR studies on MsbA¹⁰⁸ and BmrCD¹⁰⁹ analogous position were found in TmrAB. These positions were further analysed with the MATLAB-based simulation package MMM⁸³ to investigate the quality of the labelling positions concerning the accessibility for spin labelling and the expected interspin distances. Thereby the distances from the inward-facing crystal structure of TmrAB² were compared to a homology model based on the outward-facing structure of Sav1866⁹⁷ with bound AMP-PNP. In Table 14 all analysed positions are shown, whereby R1 stands for the side chain formed after MTSSL labelling of the cysteines. As already mentioned, the basis for all mutants was the cys-less version with the TmrA_C416A mutation. For the TmrA_A416C TmrB_L458C mutant, the cysteine was restored. For sake of clarity, this is handled as a mutation.

Table 14: Cysteine double mutants of TmrAB analysed with MMM. R1 is the side chain formed after spin labelling of the cysteines. The spin-labelled double mutants are indicated further in the text by the given abbreviations. If the position in the transporter is described, TM stands for the transmembrane helix which has been labelled.

Position	Position in the transporter	Abbreviation
TmrA_T61R1 B_R56R1	periplasmic gate (TM1-TM2)	TmrA61B56
TmrA_V288R1 B_E272R1	periplasmic gate (TM5-TM6)	TmrA288B272
TmrA_D112R1 B_D97R1	cytosolic gate (TM2)	TmrA112B97
TmrA_V461R1 B_D349R1	consensus site/NBDs	TmrA461B349
TmrA_C416R1 B_L458R1	degenerate site/NBDs	TmrA416B458
TmrA_E538R1 B_R549R1	consensus site/NBDs	TmrA538B549
TmrA_S578R1 B_T555R1	global/NBDs	TmrA578B555
TmrA_K585R1 B_A562R1	C-terminal helix/NBDs	TmrA585B562

At the time when these mutants were planned, already two ABC exporters had been investigated by EPR spectroscopy, namely the heterodimeric exporter BmrCD¹⁰⁹ and the homodimeric exporter MsbA¹⁰⁸. For BmrCD no crystal structure was available, therefore the mutants were chosen on a homology model based on the crystal structure of TM287/288³¹. In this work, the published EPR studies and the crystal structure of Sav1866 were used to choose appropriate labelling positions. After the mutant planning was done for this project, an EPR study on TM287/288¹¹⁰ was published. The labelling positions used in the TM287/288 study are not directly comparable to the ones which were used in this thesis. In the following, the analogous or corresponding positions are described for BmrCD and MsbA, if they were used for the published EPR studies, and further for Sav1866 since its outward-facing structure could propose if a significant difference can be observed due to a conformational change.

In the periplasmic gate, the position TmrA61B56 is equivalent to BmrC55D416, MsbA-61-61 and Sav1866-51-51. For the other periplasmic gate position TmrA288B272, no analogous position was investigated for BmrCD or MsbA. The corresponding position in Sav1866 is Sav1866-275-274. In the cytosolic gate, TmrA112B97 is equivalent to BmrC188D96, MsbA-103-103 and Sav1866-102-102. In the NBDs on the consensus site, TmrA461B349 is analogous to BmrC440D441 and Sav1866-442-351 and TmrA538B549 is analogous to BmrC515D641 and Sav1866-518-549. On the degenerate NBSs, TmrA416B458 is equivalent to BmrC392B552 and Sav1866-397-461. The NBD mutant for the global motion TmrA578B555 is analogous to BmrC555D647 and Sav1866-558-558. On the C-terminal helix in the NBDs, TmrA585B562 is equivalent to Sav1866-566-566 and comparable to BmrCD 533R1/625R1 and MsbA 539R1/539R1.

In Figure 23 all the labelling positions of TmrAB are illustrated. All positions were simulated with the simulation software MMM, by using the inward-facing crystal structure of TmrAB. The resulting rotamers are also shown in Figure 23. Important information, which is given by the software, is the number of populated rotamers and the partition function, which were further explained in section 3.2.13.

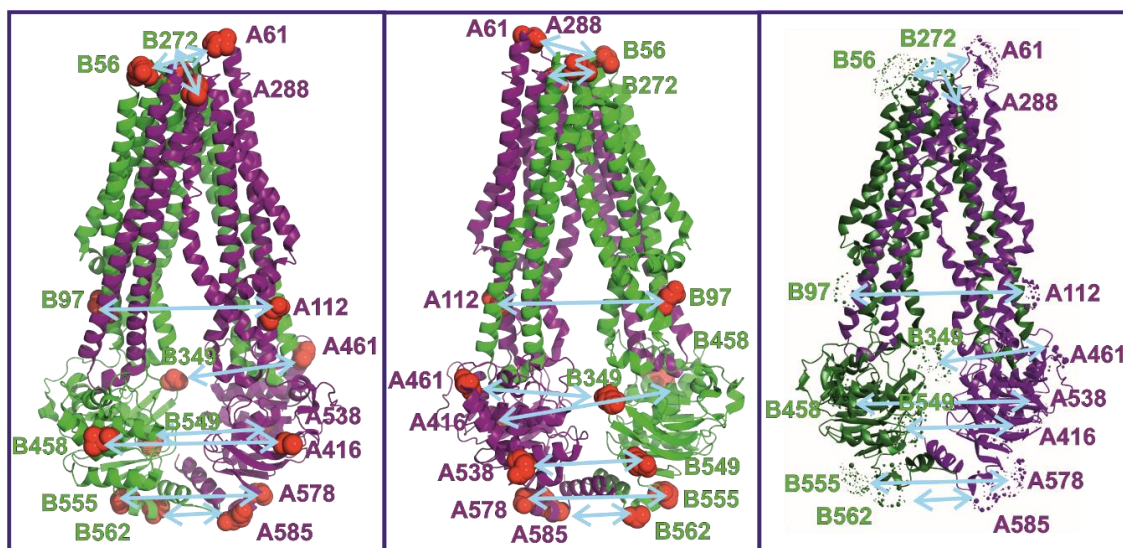


Figure 23: Labelling position in TmrAB, with TmrA in violet and TmrB in green. On the left, the labelled amino acids are shown as red spheres and the light blue arrows indicate a spin label pair. The mutants on the degenerate site are in the front. In the middle, the transporter is shown from the other side for a better view on the consensus site mutants. On the right, the MMM-simulated rotamers are indicated for all positions (same colour code). Rotamers are shown in violet for TmrA mutations and in green for TmrB mutations. The ball represents the N-O midpoint and the size is corresponding to the probability of each rotamer.

In Table 15 the number of rotamers and the partition function are shown for the chosen labelling positions. The values for TmrA51B56 and TmrA585B562 are not listed since they were already prepared previously.⁹⁵

Table 15: Number of rotamers and partition functions for the spin labelled positions, calculated with MMM.

Residue	Rotamers	Partition function
TmrA288R1B	18	1.14583
TmrAB272R1	47	1.27614
TmrA112R1B	46	1.21887
TmrAB97R1	28	3.06907
TmrA461R1B	21	0.69443
TmrAB349R1	93	1.28568
TmrA416R1B	43	3.21450
TmrAB458R1	65	0.80850
TmrA538R1B	84	1.06306
TmrAB549R1	94	1.28568
TmrA578R1B	67	0.58379
TmrAB555R1	102	0.67417

For all of these positions, the number of rotamers and the partition function are in an acceptable range, although the partition function for TmrAB97R1 and TmrA416R1B is rather high. For TmrAB97R1 the simulation was made with an older version of MMM, whereby the resulting value was in the acceptable range. For TmrA416R1B the natural cysteine of TmrAB was restored and therefore the higher value was not further considered.

In Figure 24 the simulated distances for TmrAB in the inward-facing state are shown, which are further compared to simulations of the homology models based on Sav1866 with bound AMP-PNP in the outward-facing state and McjD in the occluded conformation. These are the three states which are significant for the proposed cycle and are presented in Figure 22.

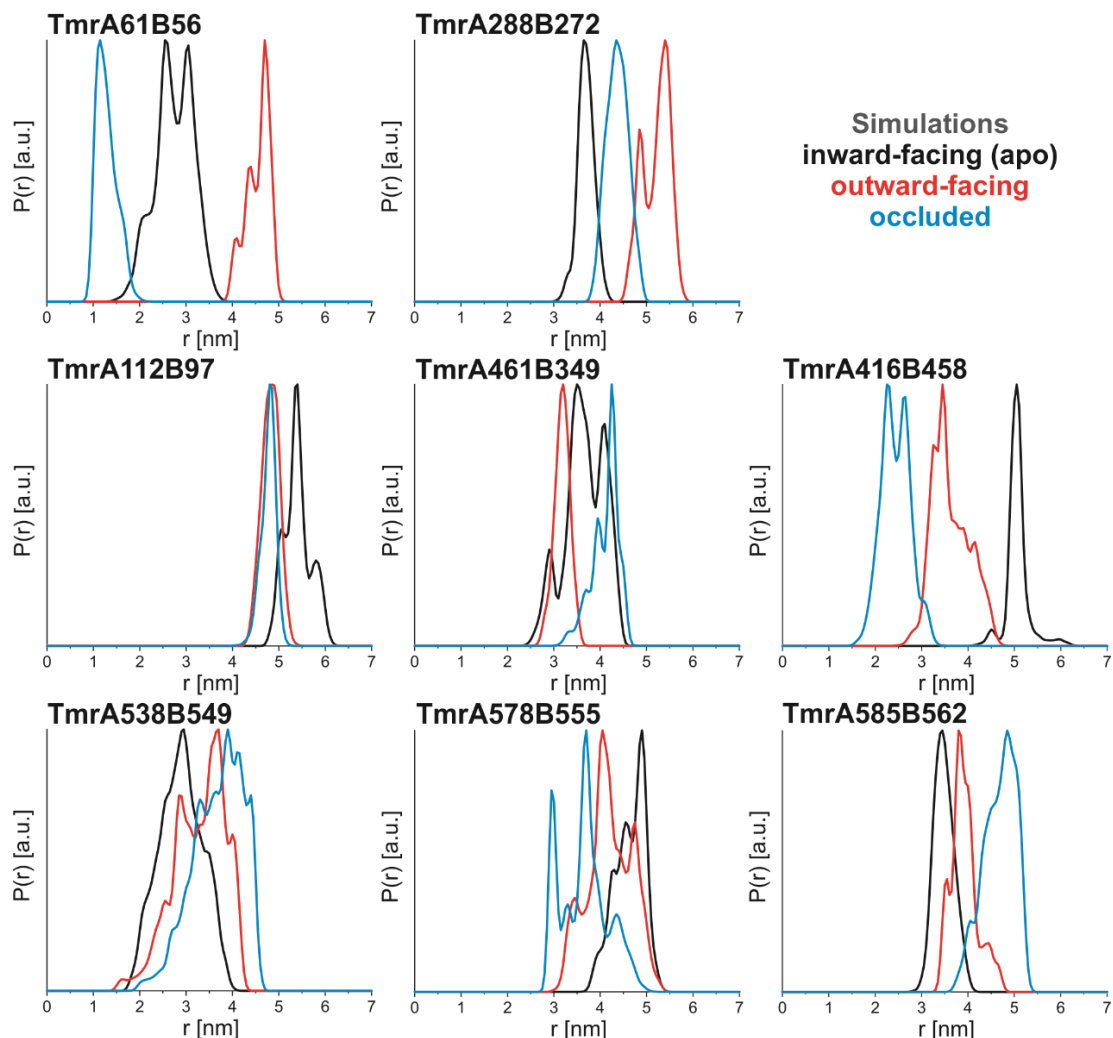


Figure 24: MMM-simulated interspin distances for all the double mutants (the positions are indicated). The inward-facing state (apo-state) is shown in black and is based on the crystal structure of TmrAB (pdb 5MKK). For the outward-facing state, simulations on the homology model based on Sav1866 with bound AMP-PNP (pdb code 2ONJ) were done. The occluded conformation was simulated with the homology model based on McjD (pdb code 4PL0).

For the positions shown in Figure 24, the proposed distances for the three states are listed in Table 16. In all cases a clear difference between the inward-facing state and the outward-facing state is visible. All mutants together are supposed to give a good overview over the whole transporter. The experimentally measured distances are shown in the next section.

Table 16: Simulated distances with the MMM software. Simulated distances and widths for the inward-facing state (apo-state) are based on the crystal structure of TmrAB (pdb 5MKK), for the outward-facing state on the homology model based on Sav1866 with bound AMP-PNP (pdb code 2ONJ) and for the occluded conformation with the homology model based on McjD (pdb code 4PLO).

Position	Inward-facing state (apo)	Outward-facing state	Occluded state
TmrA61B56	2.7 ± 0.4 nm	4.6 ± 0.3 nm	1.3 ± 0.3 nm
TmrA288B272	3.7 ± 0.2 nm	5.2 ± 0.3 nm	4.4 ± 0.3 nm
TmrA112B97	5.6 ± 0.3 nm	4.8 ± 0.2 nm	4.8 ± 0.2 nm
TmrA461B349	3.8 ± 0.4 nm	3.2 ± 0.2 nm	4.1 ± 0.3 nm
TmrA416B458	5.1 ± 0.3 nm	3.6 ± 0.4 nm	2.4 ± 0.3 nm
TmrA538B549	2.8 ± 0.5 nm	3.3 ± 0.6 nm	3.7 ± 0.6 nm
TmrA578B555	4.8 ± 0.3 nm	4.2 ± 0.5 nm	3.7 ± 0.5 nm
TmrA585B562	3.2 ± 0.4 nm	3.9 ± 0.3 nm	4.7 ± 0.4 nm

For the degenerated NBS mutant TmrA416B458 a clearer differentiation between the different states is expected, compared to the simulations for the mutants TmrA461B349 and TmrA538B549 on the consensus site. The comparable mutant TmrA480B391 on the consensus site was cloned, but unfortunately, several attempts to express and purify the protein failed, therefore the other mutants were used.

For all important mutants it was shown that they are active in substrate transport (Figure 25) and the activity is compared to the wild type protein. For the mutants TmrA61B56 and TmrA585B562, this was already shown in previous studies.⁹⁵ In case of the mutant TmrA538B549, which was only used as a control for the consensus site, and TmrA578B555, which did not lead to significant information about the transporter, no transport activity was tested. Figure 25 also shows one example of an E-to-Q-mutant, in which the catalytic glutamic acid of the consensus site is substituted by glutamine and thereby gets inactive.

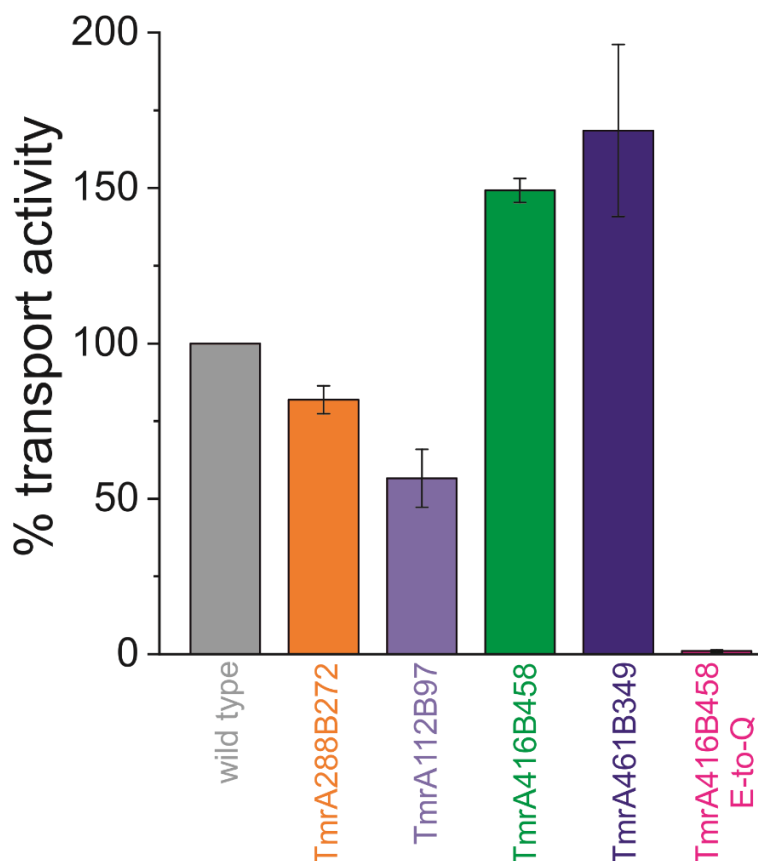


Figure 25: Transport activity of TmrAB mutants. The transport activity of spin labelled TmrAB is presented as the percentage of wild type, which was 1.89 ± 0.09 or 3.0 ± 0.4 $\text{nmol min}^{-1} \text{mg}^{-1}$ protein in two different measurements. All mutants are transporting active, except for the E-to-Q-mutant of TmrA416B458, whereby the catalytic glutamic acid is substituted to glutamine on the consensus site.

4.1.2 Experimental distance measurements on TmrAB

The transporter was measured in various intermediate states of the transport cycle, as shown in Figure 22. At first, TmrAB was measured in the apo-state without any nucleotides and furthermore in the different states with nucleotides or nucleotide analogues. The pre-hydrolysis state is presented by the samples ATP-EDTA, AMP-PNP- Mg^{2+} and ATP- BeF_3^- - Mg^{2+} , which means nucleotides are bound in the transporter, but no hydrolysis should take place. Mg^{2+} is very important as a catalyst for ATP hydrolysis, which can be coordinated by the chelate ligand EDTA with high affinity. The transporter can be trapped in the transition state with ortho-vanadate (ADP-V_i - Mg^{2+}) or with aluminium fluoride (ADP-AlF_4^- - Mg^{2+}), which describes the state after ATP hydrolysis, whereby ADP gets trapped in the binding pocket by insertion of vanadate or aluminium fluoride into the hydrolysed phosphate bond. The post-hydrolysis state describes the state which is populated with ADP-Mg^{2+} . It is the state after hydrolysis and before nucleotide release. With ATP- Mg^{2+} the transporter can be observed under hydrolysing conditions.

For all samples, the labelling efficiency was tested with cw EPR spectroscopy and was in the range of 80-100% and the reconstitution efficiency, which was also tested by cw EPR spectroscopy was in the range of 30-50% in proteoliposomes.

4.1.2.1 Periplasmic gate

In the periplasmic gate, the two mutants TmrA61B56 and TmrA288B272 were investigated. For the mutant TmrA61B56, which was already used in previous studies⁹⁵, it was shown that trapping with ortho-vanadate opens the periplasmic gate. The ATP-EDTA sample, which was also measured during these studies, was incubated at room temperature and not heated to 68 °C, therefore the preparation was repeated. In Figure 26 the resulting distances for TmrA61B56 are shown. For completeness, also the previously measured apo-state and ADP-V_i-Mg²⁺ are shown. In addition, the distances under hydrolysing conditions with ATP-Mg²⁺ are presented. Previously also ADP-Mg²⁺ and AMP-PNP-Mg²⁺ was measured, but could not show a difference compared to the apo conformation. Also shown are the apo-state and ADP-V_i-Mg²⁺ measured in proteoliposomes (PLS), whereby the distance in the vanadate-trapped state is approximately 1 nm larger compared to the measurement in detergent micelles.

For the apo-state, which corresponds to the inward-facing conformation, an interspin distance of approximately $r = 2.2 \pm 0.4$ nm was determined, which is slightly smaller than what was simulated based on the crystal structure (2.7 ± 0.4 nm). This shows that the periplasmic gate is closer in the apo-state than predicted from the crystal structure. With ADP-V_i-Mg²⁺ corresponding to the outward-facing conformation, an interspin distance of $r = 4.0 \pm 0.4$ nm can be determined in detergent micelles and of $r = 5.2 \pm 0.2$ nm in PLS. In the simulation, a value of $r = 4.6 \pm 0.3$ nm was predicted, which lies between the two determined distances. This is the only position where a small difference between detergent micelles and proteoliposomes was visible. As this was not particularly significant, measurements were performed in general in detergent micelles. With ATP-EDTA and ATP-Mg²⁺, an equilibrium between the two distances corresponding to the inward-facing and the outward-facing conformation is populated.

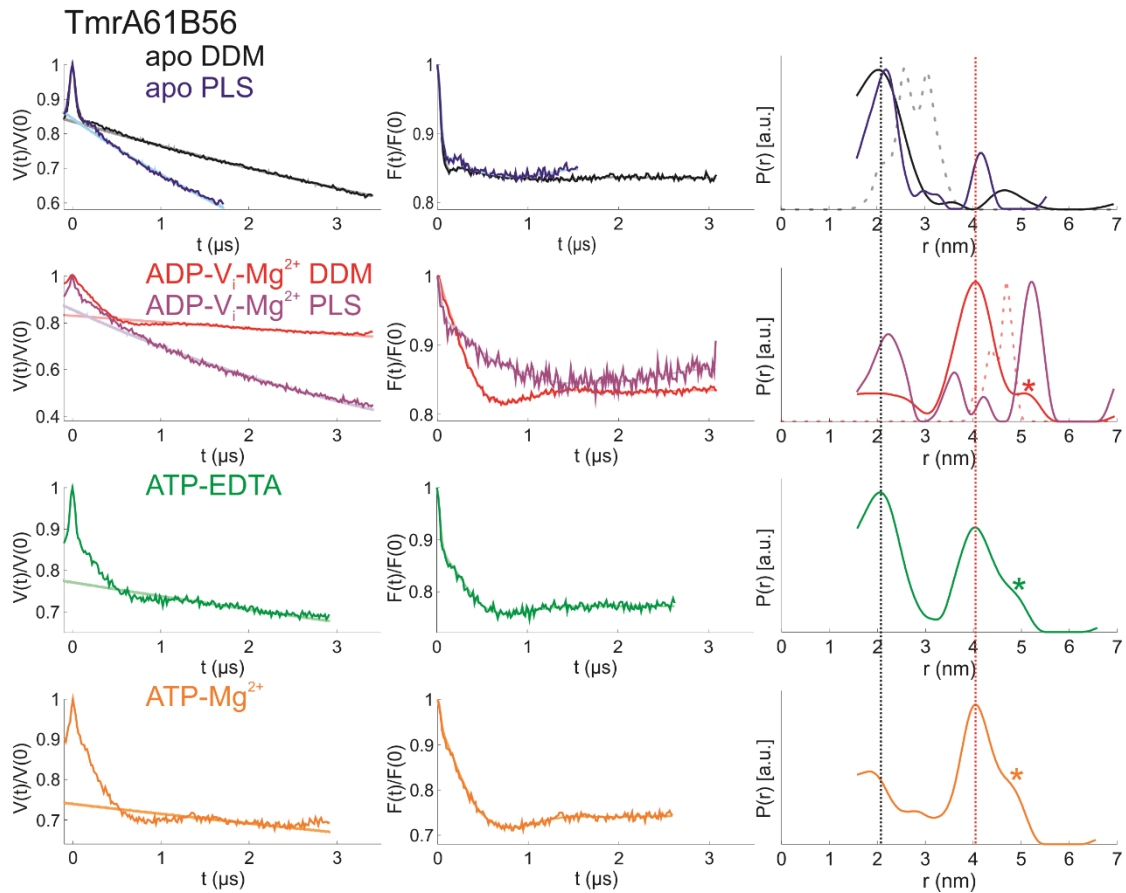


Figure 26: Conformational changes at the periplasmic gate TmrA61B56. Distances were obtained with Tikhonov regularization. Original data $V(t)/V(0)$ are displayed on the left, background corrected data $F(t)/F(0)$ are displayed in the middle and the distance distributions $P(r)$ are shown on the right. By trapping with ortho-vanadate the periplasmic gate opens by 2 nm compared to the apo conformation in detergent micelles and by approximately 3 nm in proteoliposomes (PLS). Corresponding simulations are indicated with dotted lines. With ATP-EDTA or with hydrolysing conditions with ATP- Mg^{2+} an equilibrium between the two states is populated. The asterisks indicate distance peaks with a significant uncertainty in their shape and width due to the length of the dipolar evolution trace. The vertical lines indicate the most probable distance in the closed (black) and open (red) states. (Data analysis performed with DeerAnalysis 2016)

If the catalytic glutamic acid on the consensus site is substituted by glutamine (E523Q) the transporter is transport-inactive, as shown in Figure 25. In Figure 27 the distance distributions are shown for the periplasmic gate mutant TmrA61B56-E-to-Q, whereby the most important states like apo-state, ADP- V_i - Mg^{2+} and ATP-EDTA are shown. While in the apo-state and with ADP- V_i - Mg^{2+} no difference compared to the transport-active mutant can be observed, the fraction of the open outward-facing conformation is significantly increased with ATP-EDTA.

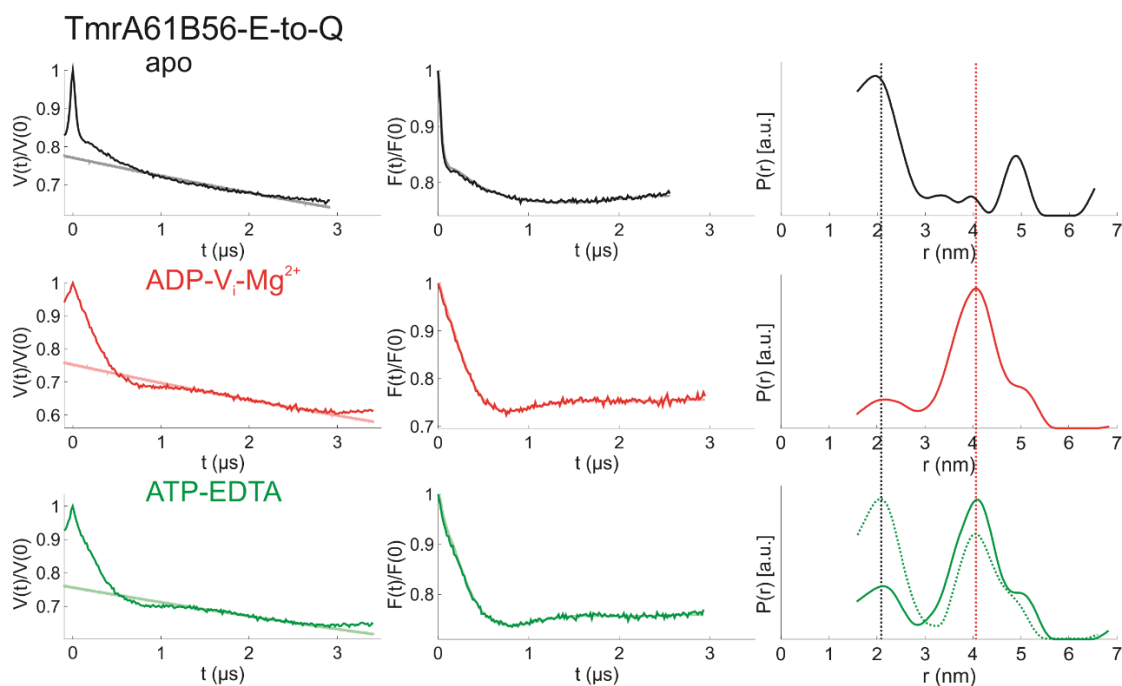


Figure 27: Conformational changes at the periplasmic gate *TmrA61B56-E-to-Q*. Distances were obtained with Tikhonov regularization. Original data $V(t)/V(0)$ are displayed on the left, background corrected data $F(t)/F(0)$ are displayed in the middle and the distance distributions $P(r)$ are shown on the right. No difference to the *TmrA61B56* data can be observed for the apo-state or $\text{ADP-V}_i\text{-Mg}^{2+}$, whereas for ATP-EDTA a shift to the open outward-facing conformation can be observed. The equilibrium of *TmrA61B56* ATP-EDTA is shown in dotted lines for comparison. The vertical lines indicate the most probable distance in the closed (black) and open (red) states. (Data analysis performed with DeerAnalysis 2016)

For the other periplasmic gate mutant, *TmrA288B272*, the most important states are presented in Figure 28. The apo-state or inward-facing conformation shows an interspin distance of $r = 3.4 \pm 0.3$ nm, which is comparable to the simulated interspin distance of $r = 3.7 \pm 0.2$ nm. With the 7-pulse CP-PELDOR measurement, an interspin distance of $r = 5.2 \pm 0.3$ nm for $\text{ADP-V}_i\text{-Mg}^{2+}$ could be determined, which was performed with the help of Dr Philipp E. Spindler. This distance fits perfectly to the simulated distance for the outward-facing state, which was also $r = 5.2 \pm 0.3$ nm. In addition, the 4-pulse measurement can be fitted with a Two-Gaussian fit, by using these two defined distances and fitting by Tikhonov regularization leads to a comparable result. For the ATP-EDTA and ATP-Mg^{2+} states, the data were fitted with Two-Gaussian models since the time windows were too short for reliable distance analysis with Tikhonov regularization. Both states form an equilibrium of the inward-facing and the outward-facing conformation, whose ratios are similar in both cases. With ATP binding 67% of the transporter changes to the open conformation and under hydrolysing conditions 69%. The distance of the open conformation is approximately

2 nm larger compared to the closed conformation, which is comparable to the other periplasmic gate mutant.

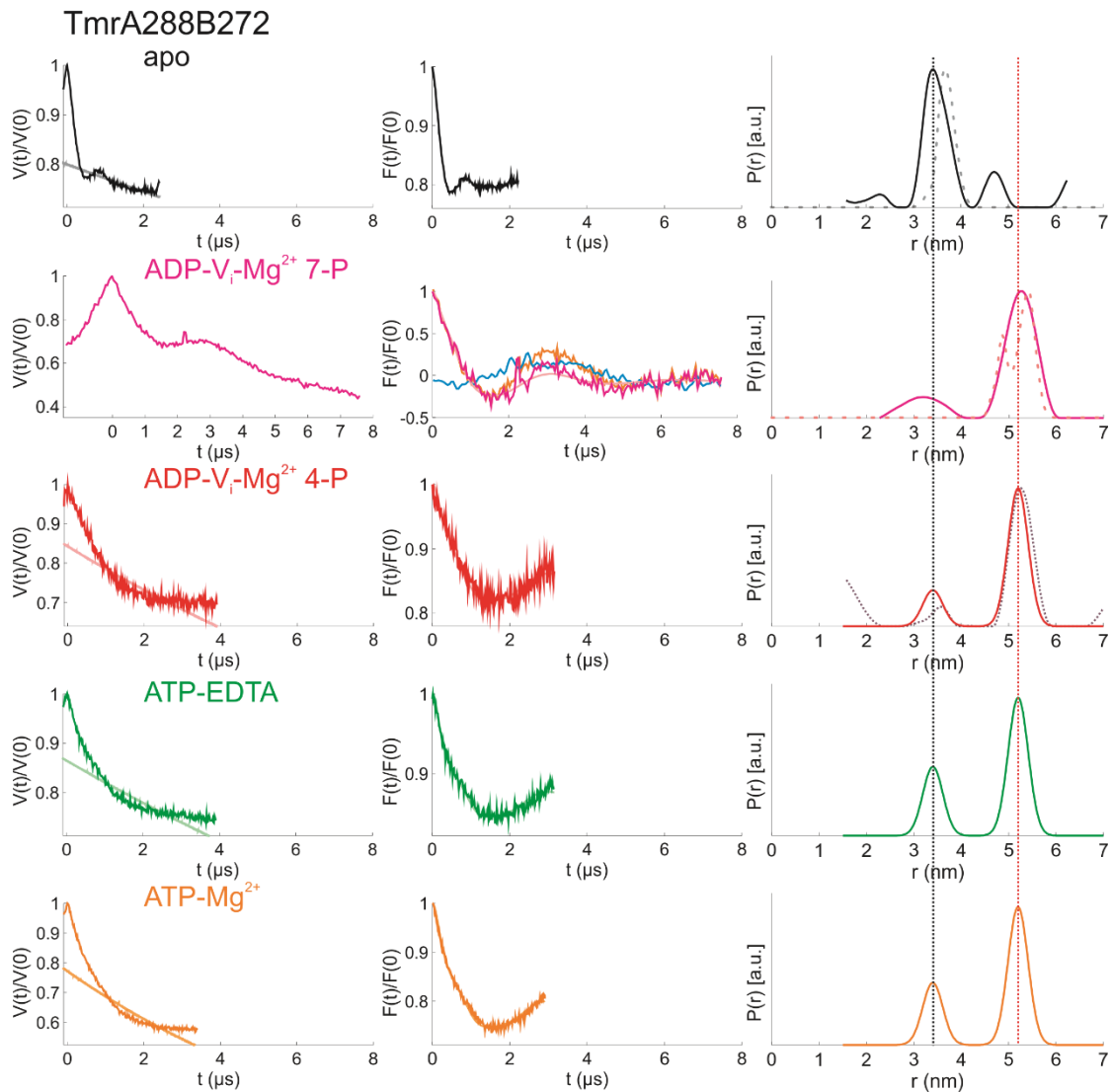


Figure 28: Conformational changes at the periplasmic gate TmrA288B272. Distances were obtained with Tikhonov regularization for the apo-state and the ADP- V_i - Mg^{2+} 7-pulse data. In all other cases, the distances were determined with Two-Gaussian fits, with the mean distances being $r = 3.4 \pm 0.3$ nm for the apo-state inward-facing conformation and $r = 5.2 \pm 0.3$ nm for the outward-facing conformation. Original data $V(t)/V(0)$ are displayed on the left, background corrected data $F(t)/F(0)$ are displayed in the middle and the distance distributions $P(r)$ are shown on the right. For the 7-pulse data, the background corrected data with the artefact is shown in orange and the artefact itself is shown in blue. By trapping with ortho-vanadate the periplasmic gate opens by 2 nm compared to the apo conformation in detergent micelles. Corresponding simulations are indicated in dotted lines. For the ADP- V_i - Mg^{2+} 4-pulse data, the Tikhonov fit is indicated with dotted lines. With ATP-EDTA or hydrolysing conditions with ATP- Mg^{2+} , an equilibrium between the two states gets populated. The vertical lines indicate the most probable distance in the closed (black) and open (red) states. (Data analysis performed with DeerAnalysis 2016)

With ADP-Mg²⁺ or AMP-PNP-Mg²⁺, no significant differences compared to the apo-state can be observed. In all cases, the closed- or inward-facing conformation is the dominant fraction. However, it is also visible that in the apo-state already a small fraction is opening (Fig.29, red line), which is also seen with ADP-Mg²⁺ or AMP-PNP-Mg²⁺. All relevant states are shown in Figure 29, where also the apo-state in proteoliposomes is presented, which shows no difference compared to the measurement in detergent micelles. For the apo-state, the fit was done with a Tikhonov regularization and all other measurements were fitted with a Two-Gaussian model based on the predefined distances for the closed and open conformation. If one of the two fractions has a very low probability close to zero a perfect fitting is not possible.

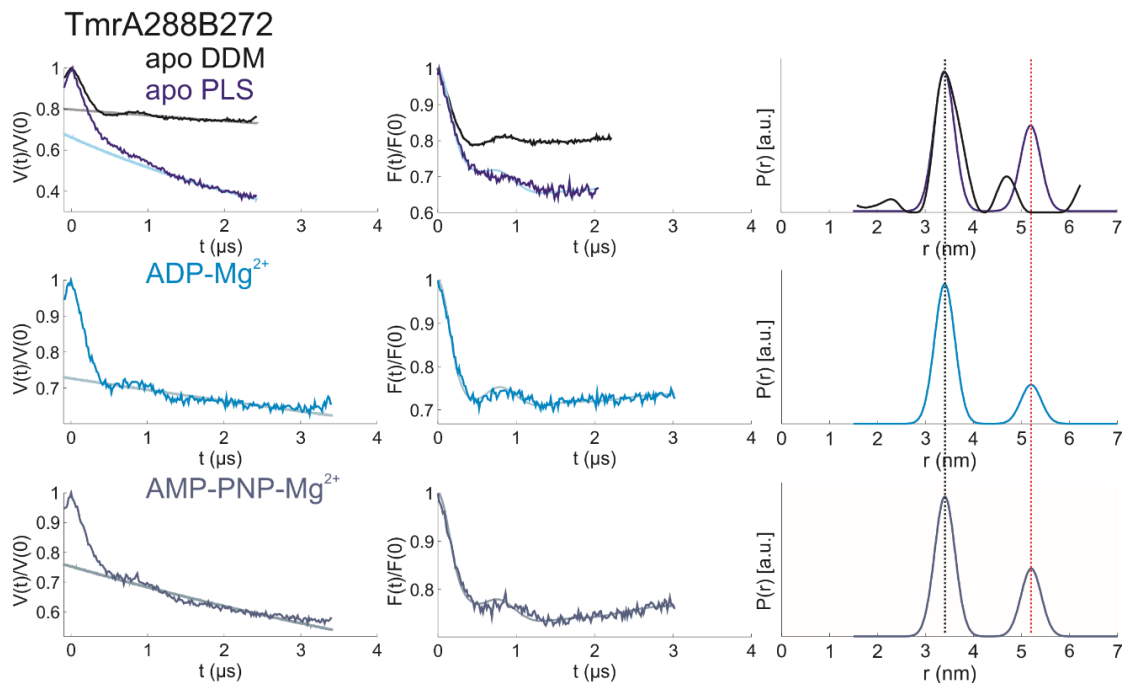


Figure 29: Apo-like states at the periplasmic gate TmrA288B272. Distances were obtained with Tikhonov regularization for the apo-state in detergent micelles. In all other cases, the distances were determined with Two-Gaussian fits, with mean distances of $r = 3.4 \pm 0.3$ nm for the apo-state inward-facing conformation and $r = 5.2 \pm 0.3$ nm for the outward-facing conformation. Original data $V(t)/V(0)$ are displayed on the left, background corrected data $F(t)/F(0)$ are displayed in the middle and the distance distributions $P(r)$ are shown on the right. For the apo-state in proteoliposomes, no difference compared to the measurement in detergent micelles can be observed. For ADP-Mg²⁺ and AMP-PNP-Mg²⁺ no significant change can be observed compared to the apo-state. In all cases, a small open fraction is visible, also without any nucleotide. The vertical lines indicate the most probable distances in the closed (black) and open (red) states. (Data analysis performed with DeerAnalysis 2016)

With $\text{ATP-BeF}_3^- \text{-Mg}^{2+}$ the pre-hydrolysis state should be trapped, in which only ATP is binding. With $\text{ADP-AlF}_4^- \text{-Mg}^{2+}$ the post-hydrolysis state should be populated, like with $\text{ADP-V}_i \text{-Mg}^{2+}$, where the outward-facing conformation gets populated. Both states show mostly the outward-facing conformation, similar to a state trapped with ortho-vanadate. The results are shown in Figure 30. Also presented are the samples prepared with $\text{ADP-V}_i \text{-Mg}^{2+}$ in detergent micelles and proteoliposomes, whereby no differences are visible in case of the distances that can be observed. However, the probability of the inward-facing conformation increases, showing that the trapped state is not as stable in proteoliposomes as in detergent micelles.

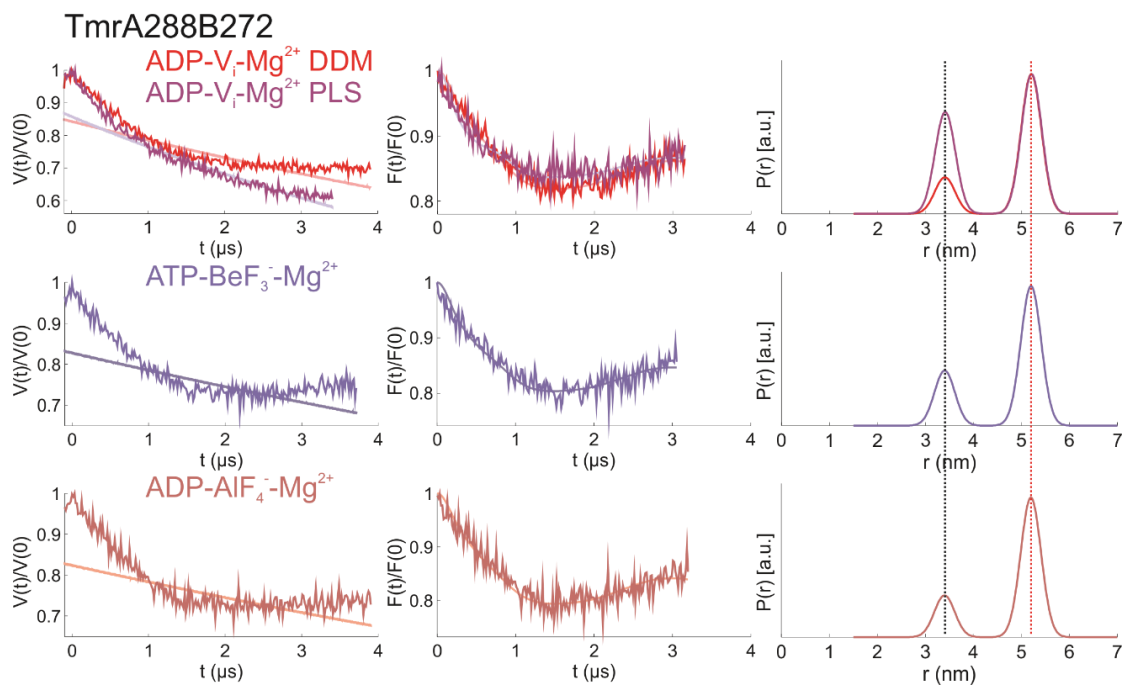


Figure 30: $\text{ADP-V}_i \text{-Mg}^{2+}$ -like states at the periplasmic gate TmrA288B272. Distances were obtained with Two-Gaussian fits, with the mean distances being $r = 3.4 \pm 0.3$ nm for the apo-state inward-facing conformation and $r = 5.2 \pm 0.3$ nm for the outward-facing conformation. Original data $V(t)/V(0)$ are displayed on the left, background corrected data $F(t)/F(0)$ are displayed in the middle and distance distributions $P(r)$ are shown on the right. No difference can be seen between the populated distances for $\text{ADP-V}_i \text{-Mg}^{2+}$ in proteoliposomes and in detergent micelles. For $\text{ATP-BeF}_3^- \text{-Mg}^{2+}$ and $\text{ADP-AlF}_4^- \text{-Mg}^{2+}$ no significant changes can be observed compared to the $\text{ADP-V}_i \text{-Mg}^{2+}$ -state. In all cases, the outward-facing open conformation is the main fraction. The vertical lines indicate the most probable distance in the closed (black) and open (red) states. (Data analysis performed with DeerAnalysis 2016)

The two presented double mutants, TmrA61B56 and TmrA288B272, represent the structural rearrangement in the periplasmic gate, which means the part of the

transmembrane domains which is located on the site to the periplasm. To see the response on the other side of the transmembrane domains, the cytosolic gate was investigated.

4.1.2.2 Cytosolic gate

The cytosolic gate is located between the transmembrane domains and the nucleotide binding domains, where the substrate is supposed to enter the transporter in the inward-facing conformation. To investigate the structural rearrangements of this gate the mutant TmrA112B97 was used, for which the most important states are shown in Figure 31.

As shown in Figure 31 the determined interspin mean distance for the apo conformation is $r = 5.7 \pm 0.4$ nm, which is comparable to the mean distance of $r = 5.6 \pm 0.3$ nm determined by the simulation with the crystal structure. Since the time trace is long enough to define the mean distance, but not the width of the distance distribution, a validation with different background lengths was performed with DeerAnalysis and the error range is indicated in Figure 31. For ADP- V_i - Mg^{2+} an interspin distance of $r = 4.6 \pm 0.2$ nm could be determined, which is comparable to the simulated distance of $r = 4.8 \pm 0.2$ nm in the outward-facing conformation. With ATP-EDTA an equilibrium between both states, the inward-facing and the outward-facing state, gets populated. For the ATP- Mg^{2+} state, the measurement was too short for a reliable distance fitting, therefore the original measurement was superimposed with the ATP-EDTA measurement, whereby no significant difference was visible.

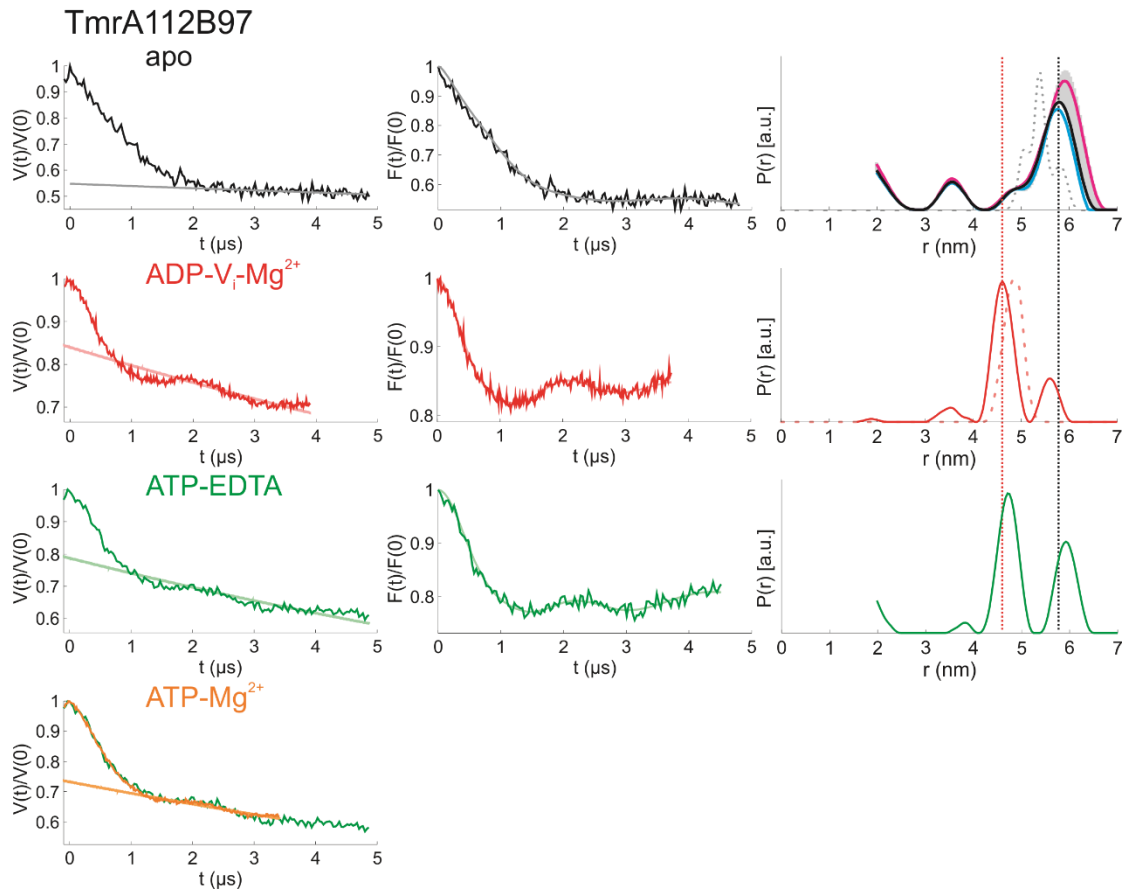


Figure 31: Conformational changes at the cytosolic gate TmrA112B97. Original data $V(t)/V(0)$ are displayed on the left, background corrected data $F(t)/F(0)$ are displayed in the middle and the distance distributions $P(r)$ are shown on the right. Distances were obtained with Tikhonov regularization for the apo-state, ADP- V_i - Mg^{2+} and ATP-EDTA. For the apo-state inward-facing conformation a mean distance of $r = 5.7 \pm 0.4$ nm was determined for the most probable distance distribution (black). Validation was done for the apo-state, whereby the background starting point was varied between 1000-3000 μ s in 100 steps. The endpoint was always 4800 μ s. Minimal and maximal distance distributions are shown in cyan and magenta and the area between these two distributions is shown in grey. For ADP- V_i - Mg^{2+} or the outward-facing conformation a mean distance of $r = 4.6 \pm 0.2$ nm was determined. The corresponding simulations are indicated in dotted lines. With ATP-EDTA an equilibrium between the two states gets populated. For the hydrolysing conditions with ATP- Mg^{2+} , the time trace was superimposed with the ATP-EDTA time trace, whereby no significant differences can be observed. The vertical lines indicate the most probable distance in the closed (black) and open (red) states. (Data analysis performed with DeerAnalysis 2016)

In Figure 32 the ADP- Mg^{2+} and AMP-PNP- Mg^{2+} states are shown, for which no difference compared to the apo-state was visible in the periplasmic gate. Also in the cytosolic gate, no significant difference is visible if the time traces are superimposed with the apo-state. This procedure is necessary since the time traces are too short for a reliable distance analysis with Tikhonov regularization. Data for ATP- BeF_3^- - Mg^{2+} (pre-hydrolysis state) and ADP- AlF_4^- - Mg^{2+} (post-hydrolysis state) in the periplasmic gate showed the same outward-facing

conformation as the data for ADP- V_i - Mg^{2+} . As an example, ADP- AlF_4^- - Mg^{2+} is shown with the time trace superimposed with the ADP- V_i - Mg^{2+} trace, which shows no significant difference (Fig. 32 right side).

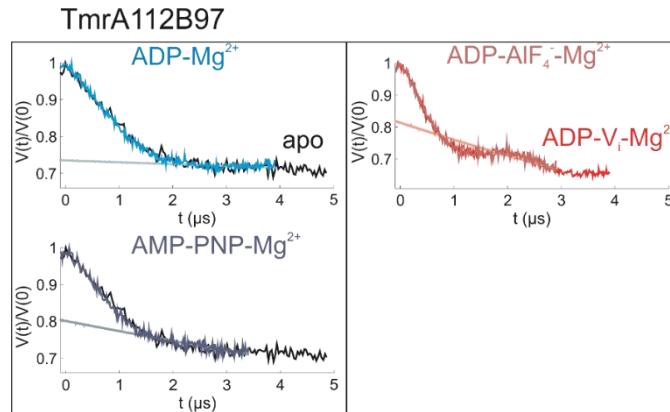


Figure 32: Apo-like and ADP- V_i - Mg^{2+} -like states at the cytosolic gate TmrA112B97. On the left original data $V(t)/V(0)$ are compared to the apo-state for ADP- Mg^{2+} and AMP-PNP- Mg^{2+} . On the right, the original data $V(t)/V(0)$ is compared to the ADP- V_i - Mg^{2+} for ADP- AlF_4^- - Mg^{2+} . For all shown traces no significant differences in the original data are visible. Further distance analysis with Tikhonov regularization is not possible for these traces since the time window is too short. (Data analysis performed with DeerAnalysis 2016)

The measurements on the cytosolic gate and the periplasmic gate reveal comparable results. As expected, the cytosolic gate closes in the outward-facing conformation, while the periplasmic gate opens. This can be seen from the distance change from the apo-state to the ADP- V_i - Mg^{2+} post-hydrolysis-state, where the distance gets approximately 1 nm smaller. As before, with ATP-EDTA and hydrolysing conditions and with ATP- Mg^{2+} an equilibrium between inward- and outward-facing conformations gets populated.

4.1.2.3 Nucleotide binding domains

For the substrate transport, the transmembrane domains are significant since they build the translocation pathway. The substrate can enter the transporter through the open cytosolic gate in the inward-facing conformation and exit the transporter through the periplasmic gate, which is opening in the outward-facing conformation while the cytosolic gate is closing. The necessary energy is supposed to come from ATP hydrolysis, which is taking place in the nucleotide binding domains (NBDs). In case of TmrAB, it is not only important how the NBDs change their conformation during nucleotide binding, due to the asymmetry of one consensus and one degenerate ATP binding site, the specific response to nucleotides

of both sites may be different. For the global motion of the NBDs, the mutants TmrA585B562 and TmrA578B555 were investigated. For the specific motions of the consensus site, TmrA461B349 was investigated and TmrA538B549 served as a control for further experiments presented in section 4.2.1. To investigate the specific motions of the degenerate site, TmrA416B458 was investigated.

For TmrA585B562 and TmrA578B555, the apo-state and ADP-V_i-Mg²⁺ are shown in Figure 33. In the case of TmrA585B562, the detergent data is shown, which was measured and discussed in previous studies.⁹⁵ This data shows a slightly larger interspin distance with ADP-V_i-Mg²⁺ $r = 4.8 \pm 0.3$ nm compared to the apo-state, where the main peak has an interspin distance of $r = 4.3 \pm 0.2$ nm. This change is resulting from a rotational motion of the spin-labelled C-terminal helix via closing of the NBDs. In proteoliposomes, no significant differences in the distance distribution can be observed compared to detergent micelles. For TmrA578B555 a main distance peak in the apo-state is found at $r = 5.1 \pm 0.5$ nm, which is comparable to the simulated distance of $r = 4.8 \pm 0.3$ nm. In the case of ADP-V_i-Mg²⁺, the determined interspin distance is $r = 4.8 \pm 0.5$ nm, which is slightly larger than the simulated distance of $r = 4.2 \pm 0.5$ nm. It is clear for both mutants that the distance distributions are broader compared to the simulations from the crystal structure. These data reveal that this part of the transporter is more flexible than predicted, apparently, these mutants are therefore not useful for investigating the global motion of the NBDs.

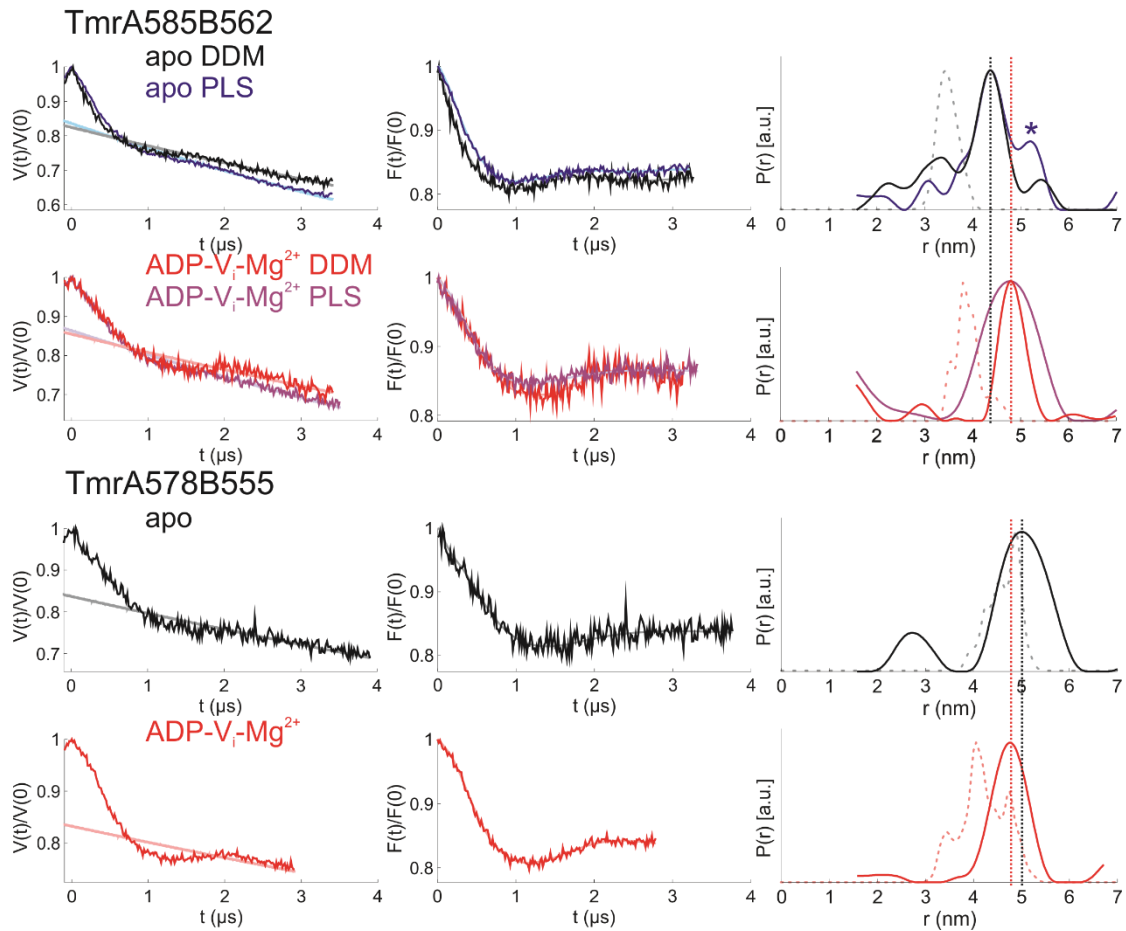


Figure 33: Conformational changes at the NBDs TmrA585B562 and TmrA578B555. Original data $V(t)/V(0)$ are displayed on the left, background corrected data $F(t)/F(0)$ are displayed in the middle and the distance distributions $P(r)$ are shown on the right. Distances were obtained with Tikhonov regularization for the apo-state, $ADP-V_i-Mg^{2+}$. For TmrA585B562 the distance distribution is very broad in the apo-state, with a distance of the main peak of $r = 4.3 \pm 0.3$ nm and with $ADP-V_i-Mg^{2+}$ the mean distance is $r = 4.8 \pm 0.3$ nm, which is slightly larger due to a rotational motion of the C-terminal helix during NBD closing. No significant differences can be observed for the measurement in proteoliposomes compared to measurement in detergent micelles. For TmrA578B555 a distance of $r = 5.1 \pm 0.3$ nm can be determined for the main peak in the apo-state. For the $ADP-V_i-Mg^{2+}$ -sample, the distance is slightly smaller with $r = 4.8 \pm 0.5$ nm. The asterisk indicates distance peaks with uncertainty in shape and width corresponding to the length of the dipolar evolution time detected. Corresponding simulations are indicated with dotted lines and the vertical lines indicate the most probable distance in the closed (black) and open (red) states. (Data analysis performed with DeerAnalysis 2016)

Furthermore, the specific motions of the consensus nucleotide binding site (NBS), which is supposed to bind and hydrolyse ATP, and of the degenerate NBS, which is supposed to bind ATP without hydrolysis, were investigated. Such a study is supposed to reveal differences in the response of the two NBSs. For the degenerate site, the mutant to observe

conformational changes is TmrA416B458, for which the most important states are presented in Figure 34.

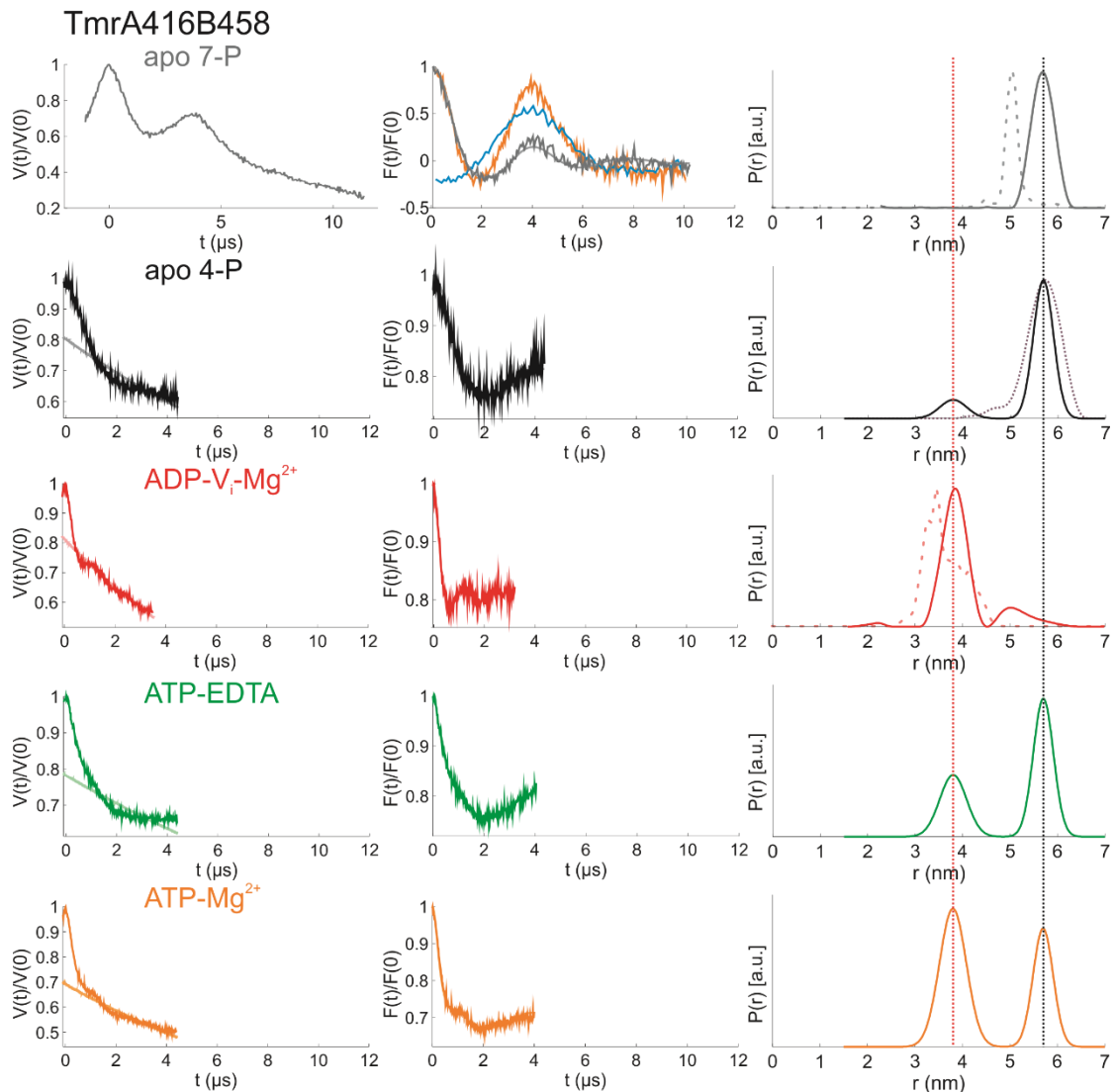


Figure 34: Conformational changes at the degenerate NBS TmrA416B458. Distances were obtained with Tikhonov regularization for the apo-state and the ADP- V_i - Mg^{2+} 7-pulse data. In all other cases, the distances were determined with Two-Gaussian fits, with the mean distances being $r = 5.7 \pm 0.3$ nm for the open-state and $r = 3.8 \pm 0.4$ nm for the closed-state. Original data $V(t)/V(0)$ are displayed on the left, background corrected data $F(t)/F(0)$ are displayed in the middle and distance distributions $P(r)$ are shown on the right. For the 7-pulse data, the background corrected data with the artefact is shown in orange and the artefact itself is shown in blue. By trapping with ortho-vanadate the degenerate NBS closes by 2 nm compared to the apo conformation in detergent micelles. Corresponding X-ray simulations are indicated in dotted lines. For the ADP- V_i - Mg^{2+} 4-pulse data, the Tikhonov fit is indicated with dotted lines. With ATP-EDTA or under hydrolysing conditions with ATP- Mg^{2+} an equilibrium between the two states gets populated. The vertical lines indicate the most probable distance in the closed (black) and open (red) states. (Data analysis performed with DeerAnalysis 2016)

The 7-pulse data were measured by Dr Philipp E. Spindler, who also did the artefact subtraction. For the apo-state or inward-facing conformation, an interspin distance of $r = 5.7 \pm 0.3$ nm was determined, which is slightly larger than the simulated distance of $r = 5.1 \pm 0.3$ nm. For ADP- V_i - Mg^{2+} an interspin distance of $r = 3.8 \pm 0.4$ nm was determined, which is comparable to the simulated distance of $r = 3.6 \pm 0.4$ nm. The distances get smaller in the post-hydrolysis state, due to the closing of the NBDs for ATP binding. With ATP-EDTA and hydrolysing conditions with ATP- Mg^{2+} , an equilibrium between the open and closed conformation of the NBS can be observed.

For ADP- Mg^{2+} and AMP-PNP- Mg^{2+} the distance distributions, like in the TMDs, do not show any difference compared to the apo-state with open NBDs, as shown in Figure 35.

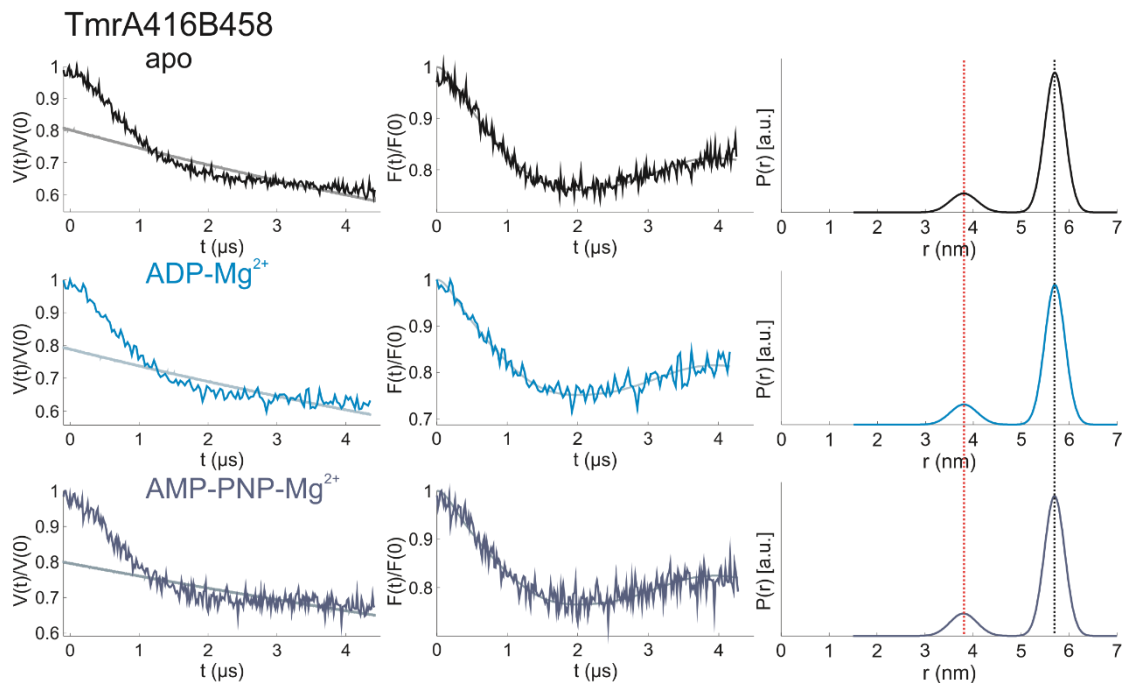


Figure 35: Apo-like states at the degenerate NBS TmrA416B458. Distances were obtained with Two-Gaussian fits, with the main distances $r = 5.7 \pm 0.3$ nm for the open-state and $r = 3.8 \pm 0.4$ nm for the closed-state. Original data $V(t)/V(0)$ are displayed on the left, background corrected data $F(t)/F(0)$ are displayed in the middle and the distance distributions $P(r)$ are shown on the right. For ADP- Mg^{2+} and AMP-PNP- Mg^{2+} no significant changes can be observed compared to the apo-state. In all cases the degenerate NBS stays in an open conformation, only a minimal fraction of the closed conformation can be observed. The vertical lines indicate the most probable distance in the closed (black) and open (red) states. (Data analysis performed with DeerAnalysis 2016)

As presented for the TMDs, ADP- AlF_4^- - Mg^{2+} shows the same effect as ADP- V_i - Mg^{2+} , the degenerate site is predominantly closed. This is displayed in Figure 36, where the two states are compared to each other.

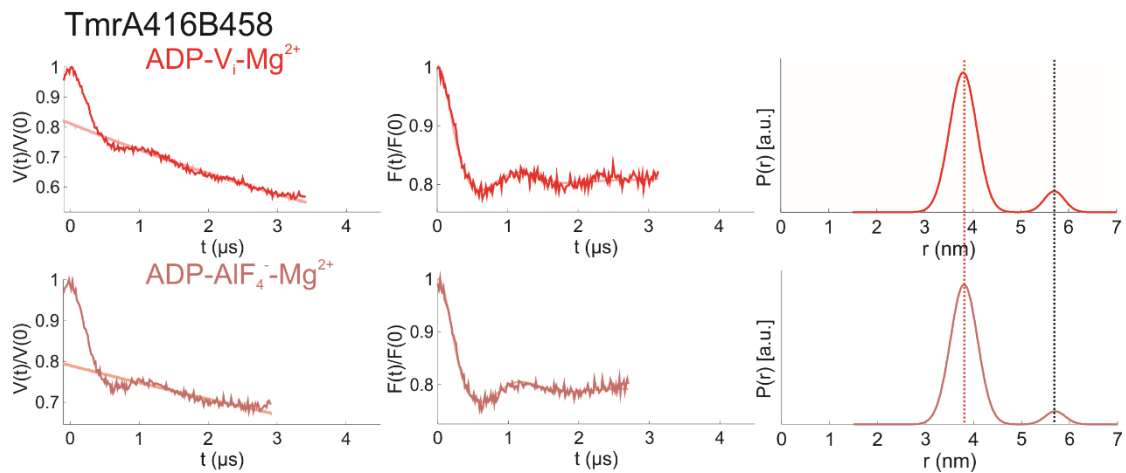


Figure 36: $ADP-V_i-Mg^{2+}$ -like state at the degenerate NBS TmrA416B458. Distances were obtained with Two-Gaussian fits, with the distances $r = 5.7 \pm 0.3$ nm for the open-state and $r = 3.8 \pm 0.4$ nm for the closed-state. Original data $V(t)/V(0)$ are displayed on the left, background corrected data $F(t)/F(0)$ are displayed in the middle and the distance distributions $P(r)$ are shown on the right. For $ADP-AIF_4-Mg^{2+}$ no significant change can be observed compared to the $ADP-V_i-Mg^{2+}$ -state. In both cases, the closed conformation is the main fraction. The vertical lines indicate the most probable distance in the closed (black) and open (red) states. (Data analysis performed with DeerAnalysis 2016)

Figure 37 shows the PELDOR data for the inactive mutant TmrA416B458-E-to-Q in the apo-state, with $ADP-V_i-Mg^{2+}$ and with ATP-EDTA. As observed in the periplasmic gate, in the apo-state and with $ADP-V_i-Mg^{2+}$ no difference compared to the transport-active mutant can be observed. With ATP-EDTA, however, the fraction of the closed conformation is significantly increased compared to the active mutant. A Two-Gaussian model was not able to fit the PELDOR data of the apo-state in a perfect manner. This is because of the low probability of one fraction.

The measured data for the degenerate NBS is consistent with the previously presented data for the TMDs. While the periplasmic gate is opening in the outward-facing conformation, at the same time the cytoplasmic gate is closing, which is stabilized by trapping with orthovanadate. Following ATP binding, which is necessary for subsequent ATP hydrolysis, the transporter needs to close the NBDs, as shown for the degenerate NBS (Fig. 34). For the consensus NBS, the mutants TmrA461B349 and TmrA538B549 were introduced. As already mentioned, the mutant directly comparable to the one introduced to monitor the degenerate site, which was supposed to have the same clear differentiation between the two states, was cloned but could not be purified.

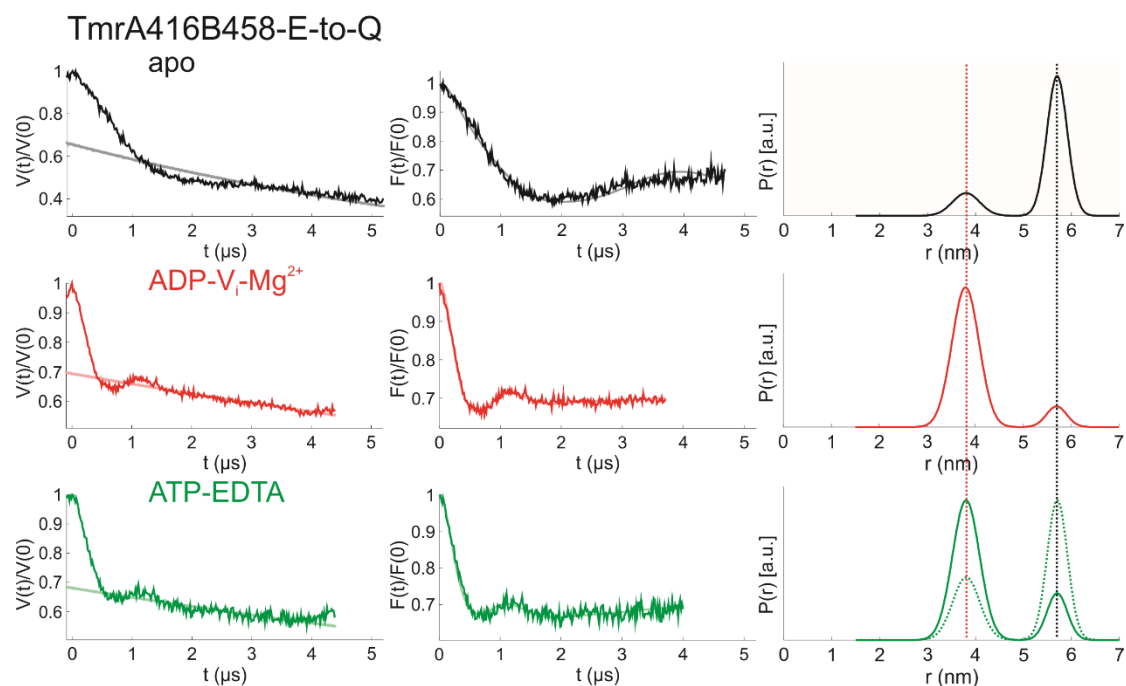


Figure 37: Conformational changes at the degenerate NBS TmrA416B458-E-to-Q. Distances were obtained with Two-Gaussian fits, with the distances $r = 5.7 \pm 0.3$ nm for the open-state and $r = 3.8 \pm 0.4$ nm for the closed-state. Original data $V(t)/V(0)$ displayed on the left, background corrected data $F(t)/F(0)$ displayed in the middle and the distance distributions $P(r)$ are shown on the right. No difference to the TmrA416B458 data can be observed for the apo-state or ADP-V_i-Mg²⁺, whereas for ATP-EDTA a shift to the closed conformation can be observed. The equilibrium of TmrA416B458 ATP-EDTA is shown in dotted lines for comparison. The vertical lines indicate the most probable distance in the closed (black) and open (red) states. (Data analysis performed with DeerAnalysis 2016)

The most important states for TmrA461B349 are presented in Figure 38, where the apo-state gives an interspin distance of $r = 3.9 \pm 0.5$ nm, which is very close to the simulated distance of the crystal structure with $r = 3.8 \pm 0.4$ nm. For ADP-V_i-Mg²⁺ an interspin distance of $r = 3.1 \pm 0.4$ nm was determined, which is also close to the simulated distance of the closed NBDs with $r = 3.2 \pm 0.2$ nm. In all cases, a small fraction with a larger distance is appearing (marked with an asterisk). This fraction is so small that it is not taken further into account. Since this fraction is already appearing without any nucleotides, it might be a minor second population occurring in the inward-facing conformation. From apo-state to ADP-V_i-Mg²⁺ the consensus NBS is closing at this position by approximately 1 nm and is populating an equilibrium between both states with ATP-EDTA or under hydrolysing conditions with ATP-Mg²⁺. In summary, these results are consistent with the previous observation at the TMDs and on the degenerate NBS.

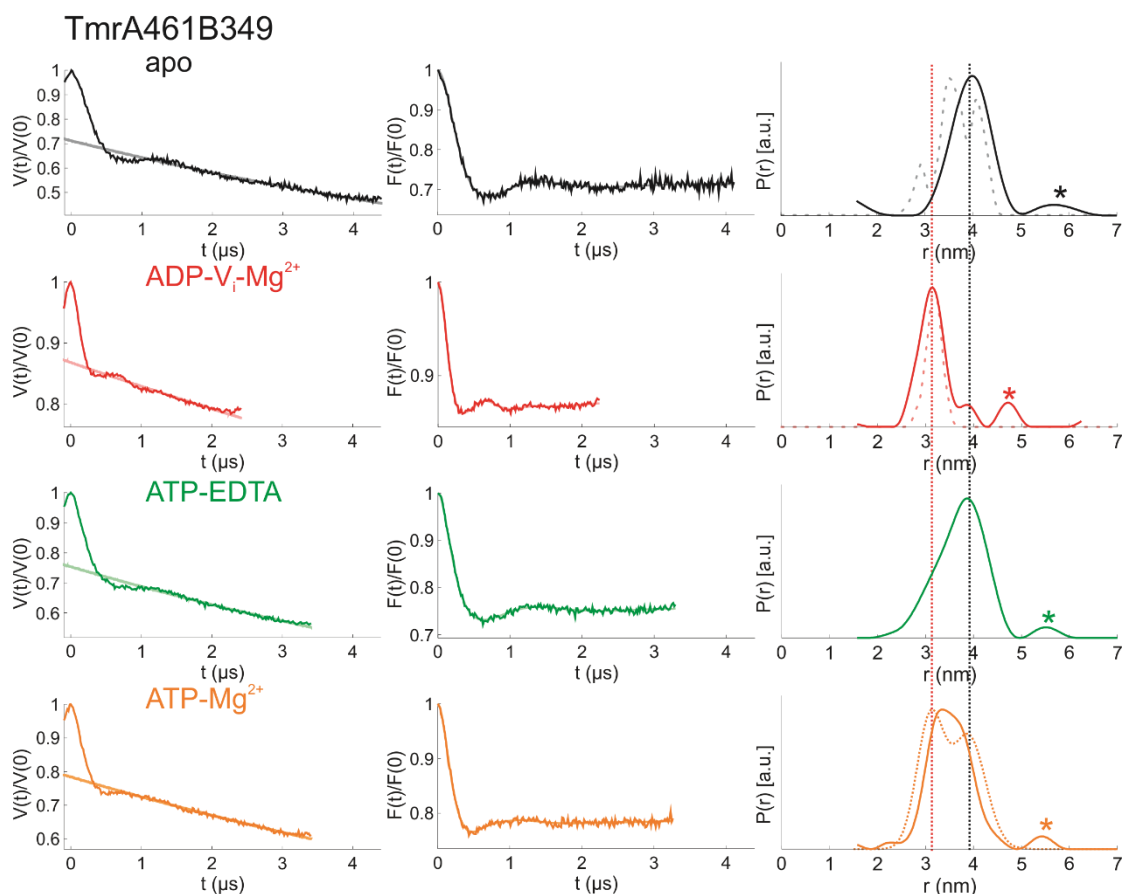


Figure 38: Conformational changes at the consensus NBS TmrA461B349. Distances were obtained with Tikhonov regularization and the distances of $r = 3.9 \pm 0.5$ nm for the open-state and $r = 3.1 \pm 0.4$ nm for the closed-state were obtained. Original data $V(t)/V(0)$ are displayed on the left, background corrected data $F(t)/F(0)$ are displayed in the middle and the distance distributions $P(r)$ are shown on the right. By trapping with ortho-vanadate the consensus NBS closes by 1 nm compared to the apo conformation in detergent micelles. Corresponding X-ray simulations are indicated in dotted lines. For the ATP- Mg^{2+} data, a Two-Gaussian fit is indicated with dotted lines. The asterisks mark a small population, which is already occurring without any nucleotides, which is very small and therefore not further taken into account. The vertical lines indicate the most probable distance in the closed (black) and open (red) states. (Data analysis performed with DeerAnalysis 2016)

As shown in Figure 39, for the apo-state no significant difference can be observed between the measurement in proteoliposomes and in detergent micelles. As already shown for the other presented mutants, ADP- Mg^{2+} and AMP-PNP- Mg^{2+} cannot induce conformational changes with respect to the apo-state.

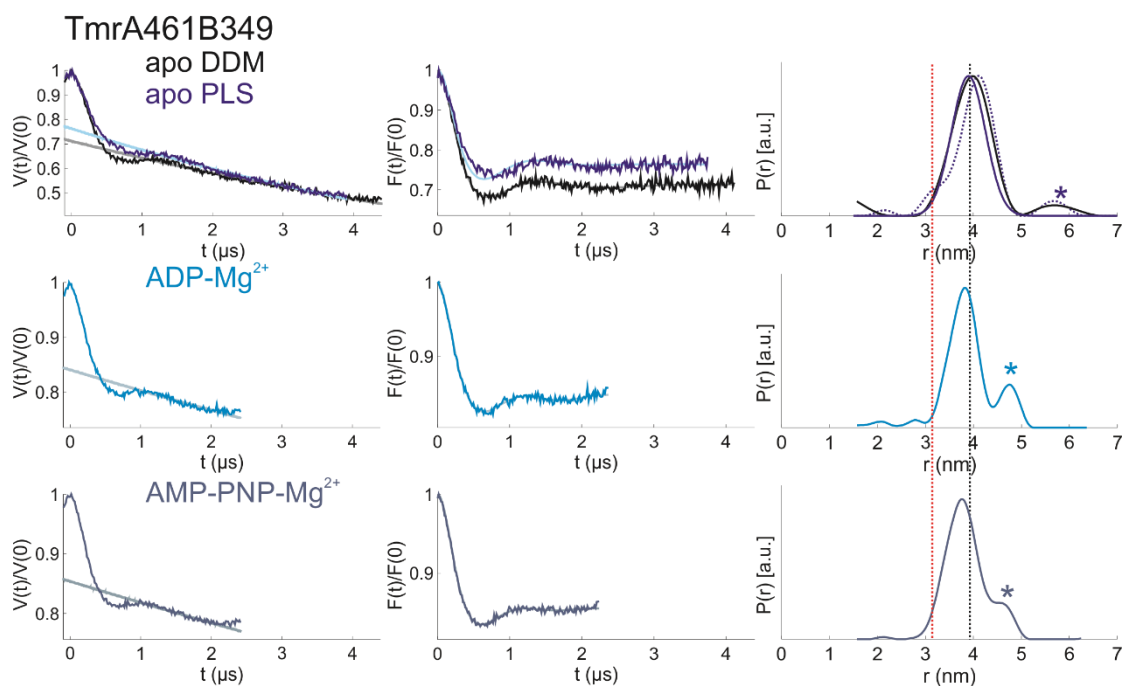


Figure 39: Apo-like states at the consensus NBS TmrA461B349. Distances were obtained with Two-Gaussian fits for the apo-state in proteoliposomes with distances of $r = 3.9 \pm 0.5$ nm for the open-state and $r = 3.1 \pm 0.4$ nm for the closed-state. In dotted lines, the corresponding Tikhonov regularization is shown. All other traces were fitted with Tikhonov regularization. Original data $V(t)/V(0)$ are displayed on the left, background corrected data $F(t)/F(0)$ are displayed in the middle and the distance distributions $P(r)$ are shown on the right. No difference can be observed between the apo-state data in detergent micelles and proteoliposomes. For ADP- Mg^{2+} and AMP-PNP- Mg^{2+} no conformational changes compared to the apo-state can be observed. The asterisks mark a small population, which is already occurring without any nucleotides. This fraction is very small and therefore not further taken into account. The vertical lines indicate the most probable distance in the closed (black) and open (red) states. (Data analysis performed with DeerAnalysis 2016)

As shown in Figure 40, for ADP- V_i - Mg^{2+} no significant difference can be observed between the measurement in proteoliposomes and in detergent micelles. For ADP- AlF_4^- - Mg^{2+} and ATP- BeF_3^- - Mg^{2+} the consensus NBS is closing, as with ADP- V_i - Mg^{2+} . This is consistent with the observations for the other mutants.

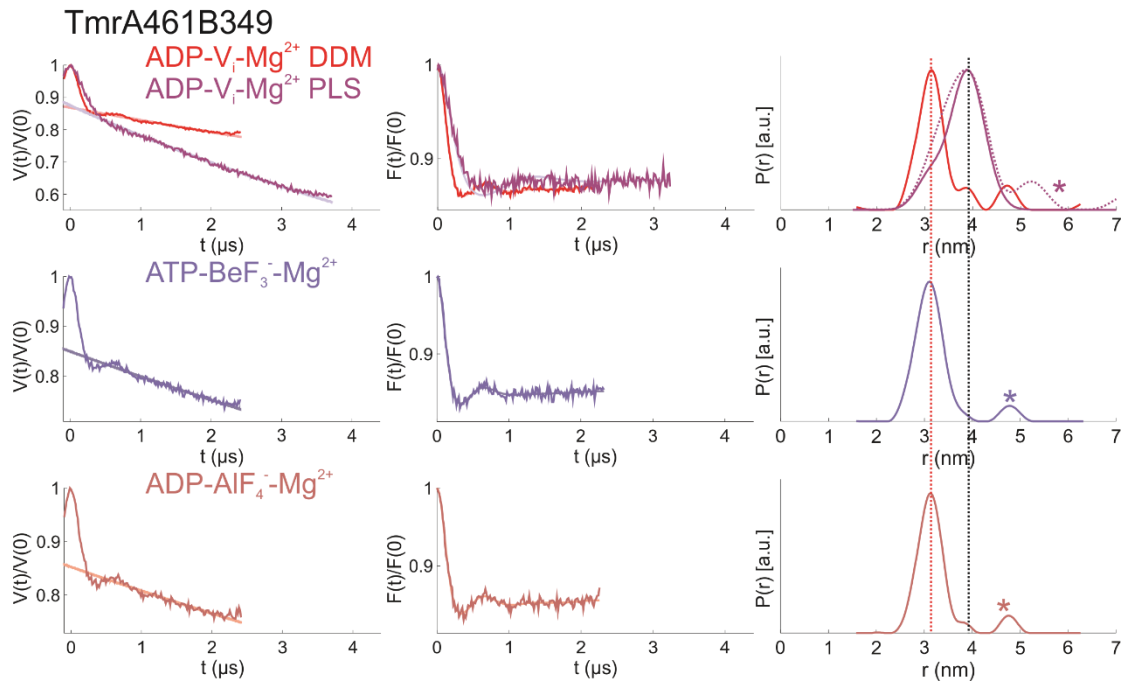


Figure 40: ADP- V_i - Mg^{2+} -like states at the consensus NBS TmrA461B349. Distances were obtained with Two-Gaussian fits for ADP- V_i - Mg^{2+} in proteoliposomes with a distance of $r = 3.9 \pm 0.5$ nm for the open-state and $r = 3.1 \pm 0.4$ nm for the closed-state. In dotted lines, the corresponding Tikhonov regularization is shown and all other traces were fitted with Tikhonov regularization. Original data $V(t)/V(0)$ are displayed on the left, background corrected data $F(t)/F(0)$ are displayed in the middle and the distance distributions $P(r)$ are shown on the right. No difference can be observed between the ADP- V_i - Mg^{2+} data in detergent micelles and proteoliposomes. For ATP- BeF_3^- - Mg^{2+} and ADP- AlF_4^- - Mg^{2+} the consensus NBS is closing as observed for ADP- V_i - Mg^{2+} . The asterisks mark a small population, which is already occurring without any nucleotides, which is very small and therefore is not further taken into account at this point. The vertical lines indicate the most probable distance in the closed (black) and open (red) states. (Data analysis performed with DeerAnalysis 2016)

For the corresponding inactive mutant, TmrA461B349-E-to-Q, the apo-state, ADP- V_i - Mg^{2+} and ATP-EDTA are shown in Figure 41. As observed in the periplasmic gate and for the degenerate NBS (Fig. 27 and Fig. 37), in the apo-state and with ADP- V_i - Mg^{2+} no difference can be observed compared to the transport-active mutant. With ATP-EDTA the fraction of the closed conformation is clearly increased compared to the active mutant, but not as much as for the degenerate NBS (Fig. 37). At this point, both sides, consensus and degenerate NBS, behave slightly different because on the degenerate site almost a complete shift to the closed conformation for the inactive mutant can be observed, while on the consensus site only a partial shift is visible.

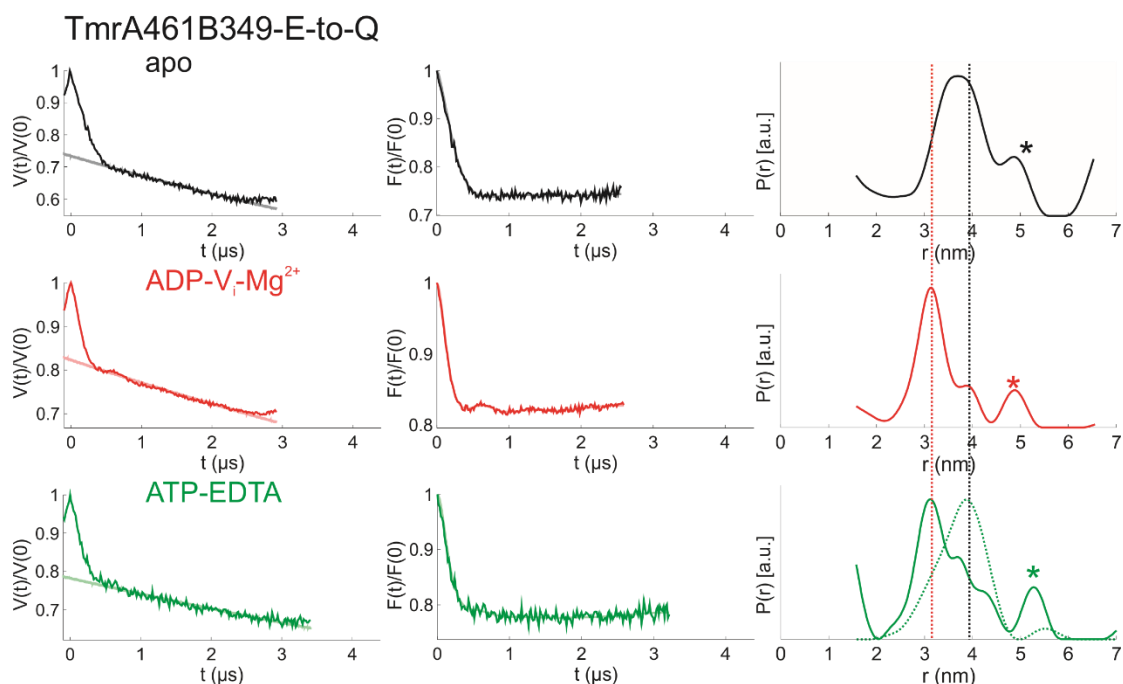


Figure 41: Conformational changes at the consensus NBS TmrA461B349-E-to-Q. Distances were obtained with Tikhonov regularization. Original data $V(t)/V(0)$ are displayed on the left, background corrected data $F(t)/F(0)$ are displayed in the middle and the distance distributions $P(r)$ are shown on the right. No difference to the TmrA461B349 data can be observed for the apo-state or ADP- V_i - Mg^{2+} , whereas for ATP-EDTA a shift to the closed conformation can be observed, but not as large as on the degenerate NBS. The equilibrium of TmrA461B349 ATP-EDTA is shown in dotted lines for comparison. The asterisks mark a small population, which is already occurring without any nucleotides. This fraction is small and not changing so much in the different states and therefore it is not further taken into account. The vertical lines indicate the most probable distance in the closed (black) and open (red) states. (Data analysis performed with DeerAnalysis 2016)

In total, the conformational changes on the consensus NBS fit qualitatively to the changes on the degenerate NBS. Except for the inactive E-to-Q-mutant, no differences between the two NBSs can be observed. To determine if the observed effects are from the specific NBS or might be introduced by the spin labels, another mutant for the consensus NBS, TmrA538B549, was investigated (relevant for experiments described in section 4.2.1). The apo-state, ATP- V_i - Mg^{2+} and ATP-EDTA are shown in Figure 42. For the apo-state, an interspin distance of $r = 3.8 \pm 0.7$ nm, which is far from the simulated distance of the crystal structure with $r = 2.8 \pm 0.5$ nm, was obtained. For ADP- V_i - Mg^{2+} an interspin distance of $r = 3.2 \pm 0.5$ nm was determined, which is close to the simulated distance of the closed NBDs with $r = 3.3 \pm 0.6$ nm. From a comparison of the simulation of the crystal structure, and the simulation of the outward-facing state homology model a distance increase was proposed. This cannot be seen for the TmrA538B549 mutant since the distance was approximately 1 nm larger than predicted from the crystal structure. This results in an

experimental determined final change of 0.6 nm between the two states. This makes it hard to distinguish the two states, but since this mutant is only used as control these results are sufficient. With ATP-EDTA the time trace can be fitted as a combination of the open and closed state.

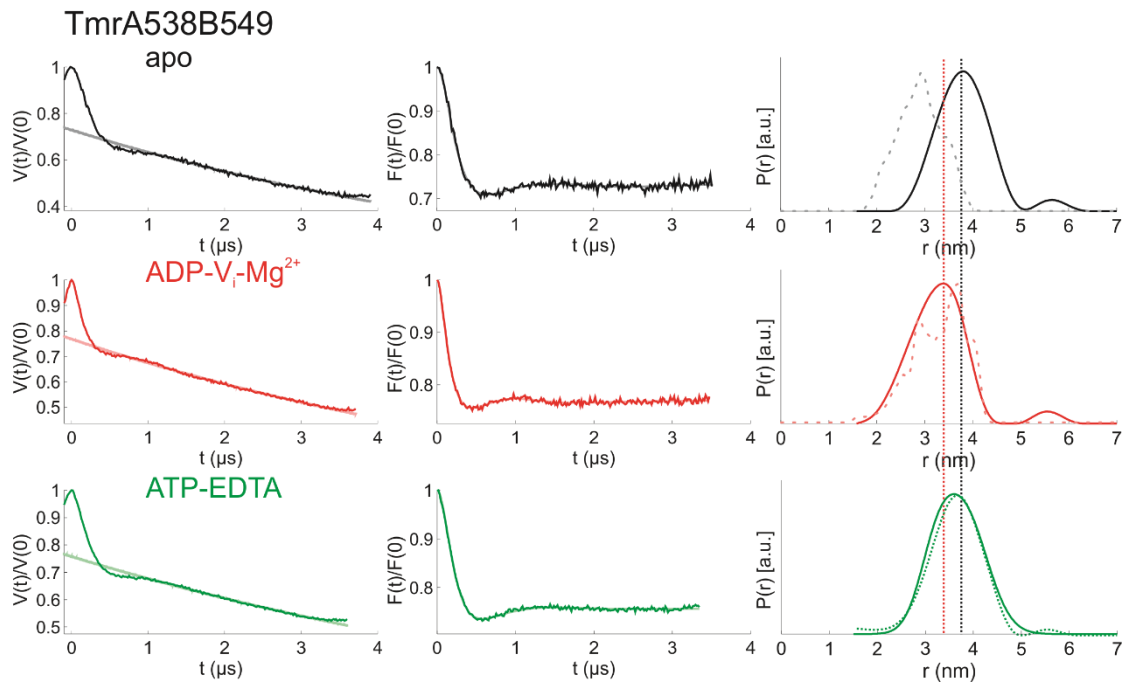


Figure 42: Conformational changes at the consensus NBS TmrA538B549. Distances were obtained with Tikhonov regularization for the apo-state and ATP- V_i - Mg^{2+} . For ATP-EDTA a Two-Gaussian model with distances of $r = 3.8 \pm 0.7$ nm for the open-state and $r = 3.2 \pm 0.5$ nm for the closed-state was used. The Tikhonov regularization is superimposed in dotted lines for ATP-EDTA. Original data $V(t)/V(0)$ are displayed on the left, background corrected data $F(t)/F(0)$ are displayed in the middle and the distance distributions $P(r)$ are shown on the right. By trapping with ortho-vanadate the consensus NBS closes by 0.6 nm compared to the apo conformation. Corresponding simulations are indicated in dotted lines. For the apo-state, the distance distribution is 1 nm larger than expected from the simulation. With ATP-EDTA an equilibrium between the two states gets populated. The vertical lines indicate the most probable distance in the closed (black) and open (red) states. (Data analysis performed with DeerAnalysis 2016)

4.1.3 Discussion of the alternating access mechanism of TmrAB

In Figure 22 the proposed alternating access mechanism of TmrAB was previously presented. With the first experiments, whereby nucleotides, catalytic magnesium ions and trapping reagents were added, mainly two states could be observed. In the apo-state without any nucleotides, an inward-facing conformation with a closed periplasmic gate and open NBDs and the cytosolic gate could be observed for all mutants. With ADP-V_i-Mg²⁺ an outward-facing conformation could be populated with the periplasmic gate open and the cytosolic gate, as well as the NBDs, closed. The nucleotides ADP-Mg²⁺ or AMP-PNP-Mg²⁺, a non-hydrolysable ATP analogon, were not able to introduce this conformational changes to populate the outward-facing conformation. For the transition to the outward-facing conformation, also ADP-AlF₄⁻-Mg²⁺ or ATP-BeF₃⁻-Mg²⁺ can be used, which should populate the post-hydrolysis or the pre-hydrolysis state, respectively. It has been shown in all these cases, that ATP-EDTA and hydrolysing conditions with ATP-Mg²⁺ induce an equilibrium between inward- and outward-facing conformations, whereas the amount of the outward-facing conformation is slightly larger under hydrolysing conditions. All these investigations so far have been carried out without substrate, only nucleotides introduced these conformational changes. In Figure 43 the conformational states which could be observed in the alternating access mechanism are highlighted.

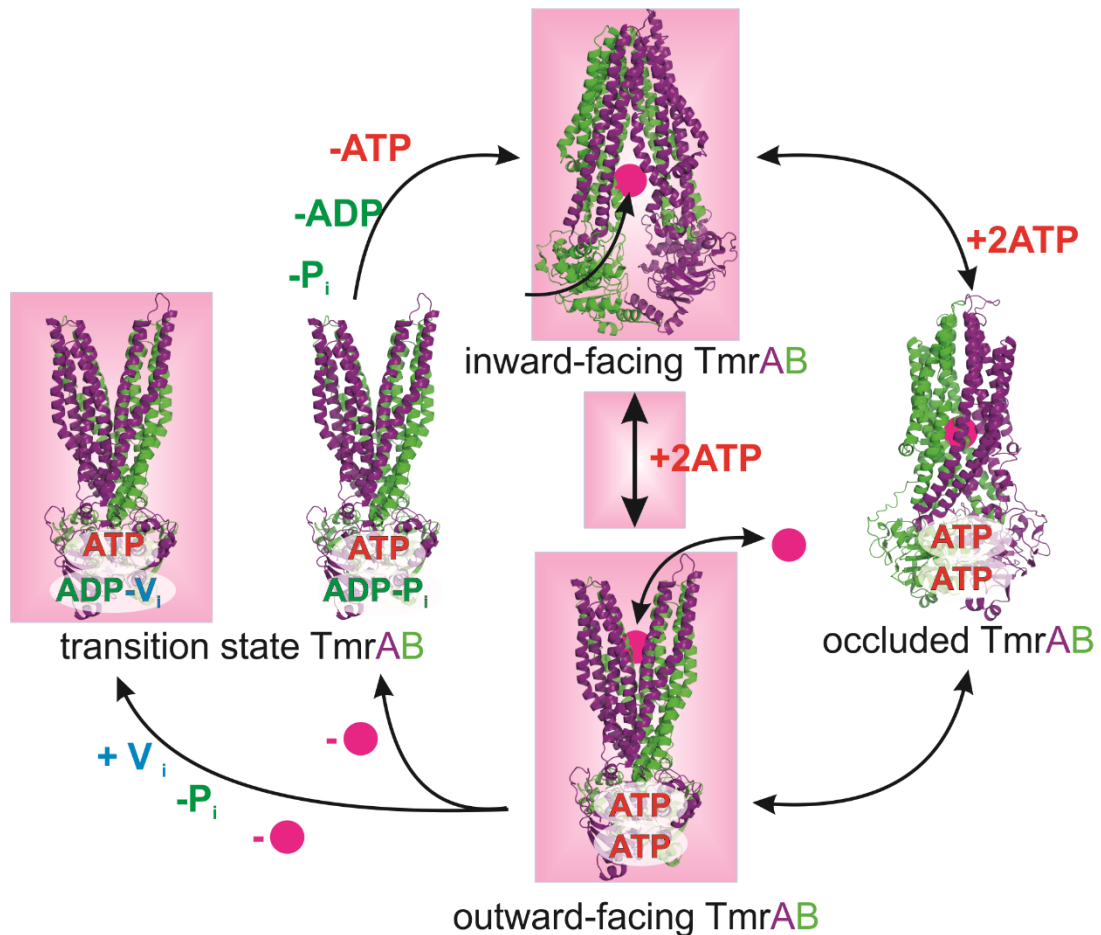


Figure 43: Alternating access mechanism of TmrAB where the states which could be observed experimentally with nucleotides are marked with pink boxes. Without any nucleotide, the transporter was observed in the inward-facing state (top) and by trapping with e.g. ortho-vanadate the transporter could be observed in the transition-state, like shown on the left. For ATP binding only or under hydrolysing conditions the transporter was populating an equilibrium between the inward-facing conformation (top) and the outward-facing conformation (bottom). The equilibrium with bound ATP is indicated by an arrow and all observed states are highlighted with a pink box. During the experiments so far no substrate was present, which is indicated in the proposed cycle with pink dots.

As already mentioned, EPR data are available for the homodimeric ABC exporter MsbA¹⁰⁸, the heterodimeric ABC exporters TM287/288¹¹⁰ and BmrCD¹⁰⁹. These data can be compared with the observed results of the heterodimeric ABC exporter TmrAB. Asymmetric NBDs are a typical feature of heterodimeric ABC exporters, which is also found in several human ABC exporters like CFTR, MRP1 and SUR1.

The structures of TmrAB⁶⁷ and TM287/288¹¹⁰ showed partially engaged NBDs; this conformation is further validated by the PELDOR results of TmrA578B555 and TmrA585B562. In the apo-state, TmrA578B555 shows an interspin distance of $r = 5.1 \pm 0.5$ nm, which is close to the crystal structure simulation, which showed a distance of $r =$

4.8 ± 0.3 nm. For ATP-V_i-Mg²⁺ an interspin distance of $r = 4.8 \pm 0.3$ nm was determined, which is slightly larger than the distance of $r = 4.2 \pm 0.5$ nm, which was simulated with the homology model based on the outward-facing structure of Sav1866 with bound AMP-PNP. For TmrA585B562 an interspin distance of $r = 4.3 \pm 0.2$ nm was determined in the apo-state, this is larger than the simulated distance from the crystal structure, $r = 3.2 \pm 0.4$ nm, but significantly smaller than in MsbA, where $r = 6.0 \pm 0.5$ nm at the comparable position MsbA-539-539. A comparison to BmrC555B647 and BmrC533B625 is difficult since for BmrCD a large and broad opening is visible and a well-defined inward-facing state can be only seen with AMP-PNP-Mg²⁺ or ADP-Mg²⁺. For BmrC533D625 no difference can be seen between the inward-facing and the outward-facing state but for BmrC555D647, which is comparable to TmrA578B555, a closing can be observed. For BmrC555D647 the distance in the well-defined inward-facing state is around 5.5 nm, which is just slightly larger than in TmrAB and the closure is around 1 nm.

For BmrCD in general, a wide-open conformation is seen for the NBDs in the apo-state, which are further engaged with AMP-PNP-Mg²⁺, ADP-Mg²⁺ or ATPγS-Mg²⁺ (slowly-hydrolysable ATP analogue). The human single-polypeptide exporters CFTR⁴³, MRP1¹¹² and SUR1⁴⁵ all contain asymmetric NBSs, which are disengaged with the smallest separation in SUR1. Different to BmrCD, in TmrAB the NBDs can be fully closed by addition of ATP, but ADP or AMP-PNP has no influence on the conformation. With the EPR studies on BmrCD¹⁰⁹ and TM287/288¹¹⁰, it was shown that ATP binding is sufficient for the switching to the outward-facing conformation for TM287/288, whereas for BmrCD ATP hydrolysis is necessary. For TmrAB, ATP binding is sufficient for the transition to the outward-facing conformation, like in TM287/288.

At the periplasmic gate TmrA61B56 and TmrA288B272 were investigated and at the cytosolic gate, TmrA112B97 was investigated. For TmrA61B56 an interspin distance in the inward-facing conformation of $r = 2.2 \pm 0.4$ nm was observed, which is slightly smaller than proposed from the crystal structure with a simulated distance of $r = 2.7 \pm 0.4$ nm and also smaller than the comparable distance for MsbA with $r = 3.0 \pm 0.4$ nm. For the comparable position BmrC55D146, the periplasmic gate is further opened at this position with approximately 4.5 nm. In TmrAB the periplasmic gate is opening by about 2 nm with ATP-V_i-Mg²⁺, resulting in an interspin distance of $r = 4.0 \pm 0.4$ nm in detergent micelles. In proteoliposomes, the gate opening is resulting in an interspin distance of $r = 5.2 \pm 0.2$ nm. The simulated distance for the homology model in the outward-facing state proposed a distance of $r = 4.6 \pm 0.3$ nm, which is between the distance in detergent micelles and

proteoliposomes. For BmrC55D146 the periplasmic gate opening is in a comparable range, however, the distance distribution is much broader. For MsbA-61-61 a distance of $r = 4.0 \pm 0.3$ nm was observed, which is the same as for TmrAB in detergent micelles. This corresponds to an opening of only 1 nm compared to the inward-facing state. For TmrA288B272 the interspin distance in the apo-state is $r = 3.4 \pm 0.3$ nm, which is comparable to the simulation of the crystal structure, where a distance of $r = 3.7 \pm 0.2$ nm was extracted. No comparable position was measured for BmrCD or MsbA, but with the transition to the outward-facing state, this gate is also opening by about 2 nm, resulting in an interspin distance of $r = 5.2 \pm 0.3$ nm. This is exactly the distance that was simulated from the homology model for the outward-facing state.

In the cytosolic gate, TmrA112B97 showed an interspin distance of $r = 5.7 \pm 0.4$ nm in the apo-state, which is very close to the simulated distance in the crystal structure of $r = 5.6 \pm 0.3$ nm. This open state is comparable to the distance in BmrC188D96 of approximately 6 nm. In MsbA-103-103 the opening is larger with $r = 7.2 \pm 0.5$ nm. The cytosolic gate is closing in the outward-facing state by 1 nm, resulting in a distance of $r = 4.6 \pm 0.2$ nm, which is comparable to $r = 4.8 \pm 0.2$ nm, which was simulated for the outward-facing state. In BmrC188D96 the closing step of the cytosolic gate is comparable, leading to an outward-facing distance of approximately 4.5 nm. In MsbA-103-103 a distance of $r = 4.7 \pm 0.1$ nm is showing a similar closing step.

For all these positions in the TMDs of TmrAB, a small population of the outward-facing state can be observed, even in the absence of ATP. As observed with P-gp¹¹³ or TM287/288¹¹⁰, this might happen through an independent motion of the TMDs, whereas both NBSs do not close without ATP. Furthermore, ATP acts as a ligand which shifts the equilibrium of inward- to outward-facing conformation and stabilizes the outward-facing conformation. These observations are in agreement with electrophysiology data for CFTR^{114,115}, which show that ATP-independent channel opening has a low probability and that ATP-dependent channel activation is in the nM range. In addition, this is analogous to the allosteric regulation in ligand-gated ion channels, where ligand binding shifts the equilibrium to the open state. For CFTR it is rather clear that ATP binding gates the channel activity in an allosteric way.¹¹⁶ It seems like the conformational switching in TmrAB and CFTR by ATP behave qualitatively like the gating mechanism of ligand-gated ion-channels. To further investigate this equilibrium, labels on the consensus and the degenerate NBSs are important. TmrA416B458 is located on the degenerate site and yields in the apo-state an interspin distance of $r = 5.7 \pm 0.3$ nm, which is slightly larger than the distance simulated

from the crystal structure with $r = 5.1 \pm 0.3$ nm. The comparable inward-facing state with AMP-PNP for BmrC392D552 shows a distance of around 4 nm, which is smaller than in TmrAB. By closing the degenerate site by 2 nm an interspin distance of $r = 3.8 \pm 0.4$ nm is resulting, which is comparable to the simulated outward-facing distance of $r = 3.6 \pm 0.4$ nm. For BmrC392D552 the degenerate site closed by 1.5 nm resulting in a distance around 2.5 nm, which is smaller than in TmrAB. For the consensus site TmrA461B349 an interspin distance of $r = 3.9 \pm 0.5$ nm was obtained, which is comparable to the simulated distance of $r = 3.8 \pm 0.4$ nm and smaller than the inward-facing state of BmrC440D441. For BmrC440D441 with AMP-PNP, a distance of $r = 4-6$ nm was obtained.

In the closed NBS state, an interspin distance of $r = 3.1 \pm 0.4$ nm can be measured, which is comparable to the simulated closed distance of $r = 3.2 \pm 0.2$ nm and to BmC440D441, where a distance of $r = 3-5$ nm was measured for the closing gate. In addition, TmrA538B549 is located on the consensus site, which shows an interspin distance of $r = 3.8 \pm 0.7$ nm in the apo-state, which is significantly larger than $r = 2.8 \pm 0.5$ nm simulated from the crystal structure, but comparable to BmrC515D641 with AMP-PNP, which shows a distance of around 4 nm. In the closed state, only a small closing step to a distance of $r = 3.2 \pm 0.5$ nm can be observed, which is comparable to the outward-facing simulation with $r = 3.3 \pm 0.6$ nm and BmrC515D641 with a distance of approximately 3.5 nm in the closed state.

In summary, these positions offer insights into the role of the asymmetry, which was already observed in the transport-inactive E-to-Q mutant. On the periplasmic gate and in the NBDs the outward-facing conformation is stabilized with ATP-EDTA for the transport-inactive mutant, where the equilibrium gets shifted. This has also been seen for TM287/288¹¹⁰, where clear shifts could be observed with these inactive mutants. Comparing the degenerate and consensus site of TmrAB with the E-to-Q mutation, an almost complete shift could be obtained for the degenerate site with ATP-EDTA, whereas on the consensus site only an increase of the fraction was visible. Compared to the other investigated transporters, for TmrAB typically well-defined states can be observed, which makes it possible to distinguish the different conformations.

4.2 The conformational equilibrium induced by ATP binding

With ATP-EDTA or under hydrolysing conditions (ATP-Mg²⁺) an equilibrium between the inward- and outward-facing conformation is populated. Under hydrolysing conditions, two states are possible, which could be observed. These are either the ATP-bound state or the transition state, with one ATP on the degenerate site and one ADP on the consensus site. The actual conformation under hydrolysing conditions is unclear, while for ATP-EDTA it is clear which equilibrium is observed. In this case, ATP can be bound on both NBSs, but cannot be hydrolysed since no catalytic free magnesium ions are available. Therefore, in this section, the equilibrium between inward-facing (apo) and outward-facing ATP-bound TmrAB is investigated, which is shown in Figure 44.

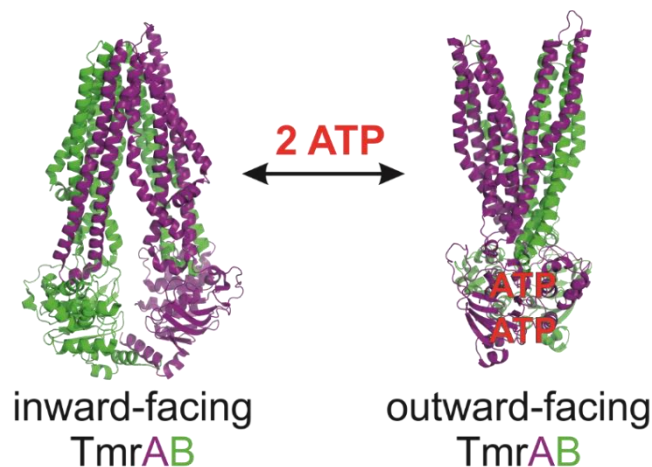


Figure 44: Conformational equilibrium induced by ATP binding in TmrAB. The inward-facing structure of TmrAB (pdb code 5MKK) is in equilibrium with the outward-facing structure shown with a homology model of TmrAB based on the outward-facing structure of Sav1866 with bound AMP-PNP (pdb code 2ONJ).

Based on this equilibrium different important questions of the transport mechanism were tackled. First of all, the response of the consensus and degenerate site to ATP binding and how the conformational changes on the NBSs are coupled to the TMDs, were investigated. TmrAB has a turnover of 9 ATP molecules per second, with a $K_{m,ATP}$ value close to 0.9 mM⁶⁶, whereby ATP binds predominantly due to interactions with the A-loop, Walker A and Walker B motifs^{31,117}. This could possibly lead to an allosteric interaction between the consensus and the degenerate NBS and to a cooperative movement along with the conformational space during the closing motion.⁴⁸ Therefore, the transporter was titrated with different ATP concentrations from 0.5 mM to 50 mM in the ATP-EDTA state and the populations of both the inward- and outward-facing conformation were observed for the periplasmic gate and both NBS (section 4.2.1).

In addition, the thermodynamics of this conformational change were investigated by varying the incubation temperature from 0 °C to 80 °C. The response at these different temperatures was observed in the periplasmic gate and on both NBSs (section 4.2.2). For the temperature titrations 50 mM ATP was used, to saturate the protein with ATP and to only observe the effect of temperature.

4.2.1 Influence of different ATP concentrations to the conformational equilibrium

To investigate the response of the consensus and degenerate NBS and the coupling to the TMDs, TmrAB was titrated with different ATP concentrations. More in detail, the mutants TmrA416B458 on the degenerate NBS, TmrA461B349 on the consensus NBS and TmrA288B272 on the periplasmic gate were investigated under identical conditions. Furthermore, TmrA538B549 was investigated as a control for the consensus site to show that the observations describe the response of the NBS and are not an effect induced by the spin labels. All the measurements were done with 50 μ M TmrAB and 0.5 mM EDTA.

In Figure 45 the measured data for the degenerate NBS 416-458 are shown, which were fitted with a Two-Gaussian model, based on the measured distances in the apo- or open-state of $r = 5.7 \pm 0.3$ nm and a distance of $r = 3.8 \pm 0.4$ nm in the closed-state. It is evident from the data that the population of the closed state is monotonically increasing, with increasing ATP concentrations from 0.5 to 50 mM ATP. The probability of the open and closed conformation (P_{closed} and P_{open}) and the corresponding fractional closure θ (defined as $P_{\text{closed}}/(P_{\text{closed}}+P_{\text{open}})$) are presented in Table 17.

Table 17: Probability of the open and closed conformation at the degenerate NBS TmrA416B458, modulated by ATP. The corresponding fractional closure θ is defined as $P_{\text{closed}}/(P_{\text{closed}}+P_{\text{open}})$.

ATP concentration	P_{closed}	P_{open}	Fractional closure θ
0.5 mM	0.11	0.89	0.11
1 mM	0.14	0.86	0.14
10 mM	0.37	0.63	0.37
25 mM	0.59	0.41	0.59
50 mM	0.69	0.31	0.69

The probability of the closed state was determined by Two-Gaussian fitting with DeerAnalysis.

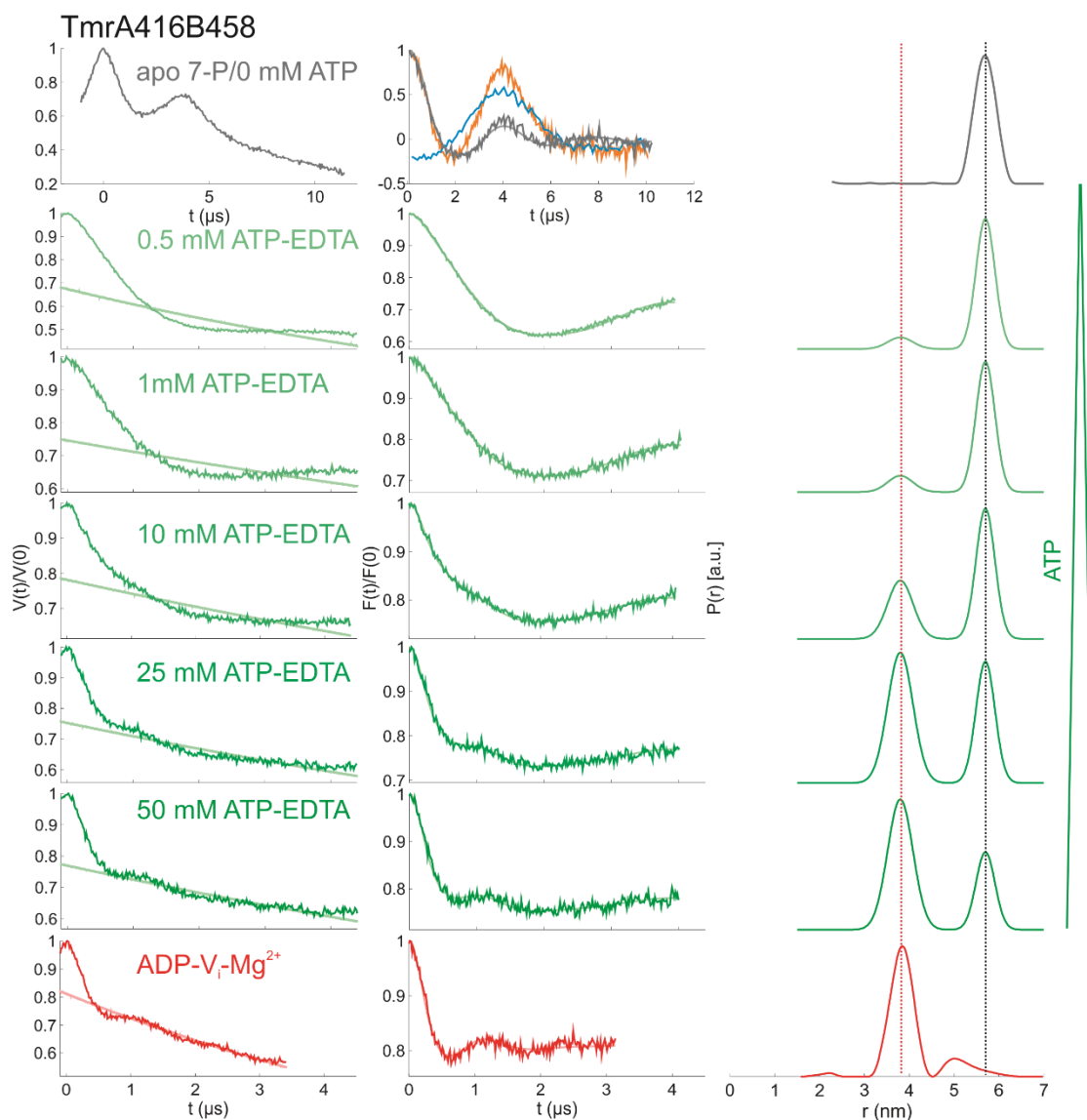


Figure 45: ATP modulates the conformational equilibrium at the degenerate NBS TmrA416B458. Apo-state and ADP- V_i - Mg^{2+} were fitted with a Tikhonov regularization. The open state (0 mM) was determined with 7-pulse CP-PELDOR. A distance in the apo- or open-state of $r = 5.7 \pm 0.3$ nm and a distance in the closed-state of $r = 3.8 \pm 0.4$ nm, were used for Two-Gaussian fitting of the titration data. Original data $V(t)/V(0)$ are displayed on the left, background corrected data $F(t)/F(0)$ are displayed in the middle and the distance distributions $P(r)$ are shown on the right. The degenerate site closes in a monotonic response to increasing ATP (0.5 to 50 mM) concentration. ATP- V_i - Mg^{2+} is representing the completely closed state. The vertical lines indicate the most probable distance in the closed (black) and open (red) states. (Data analysis performed with DeerAnalysis 2016)

For the consensus NBS, the mutant TmrA461B349 was investigated, which is shown in Figure 46. A Two-Gaussian model was applied, using a distance in the apo- or open-state of $r = 3.9 \pm 0.5$ nm and a distance in the closed-state of $r = 3.1 \pm 0.4$ nm. A small fraction of a larger distance can be observed, which is neglected since it is too small to disturb the fit with two distances. For completeness, the fits obtained by Tikhonov regularization are

overlaid in dotted lines. Different to the degenerate site, the consensus site is showing a saturation response at 25 mM ATP.

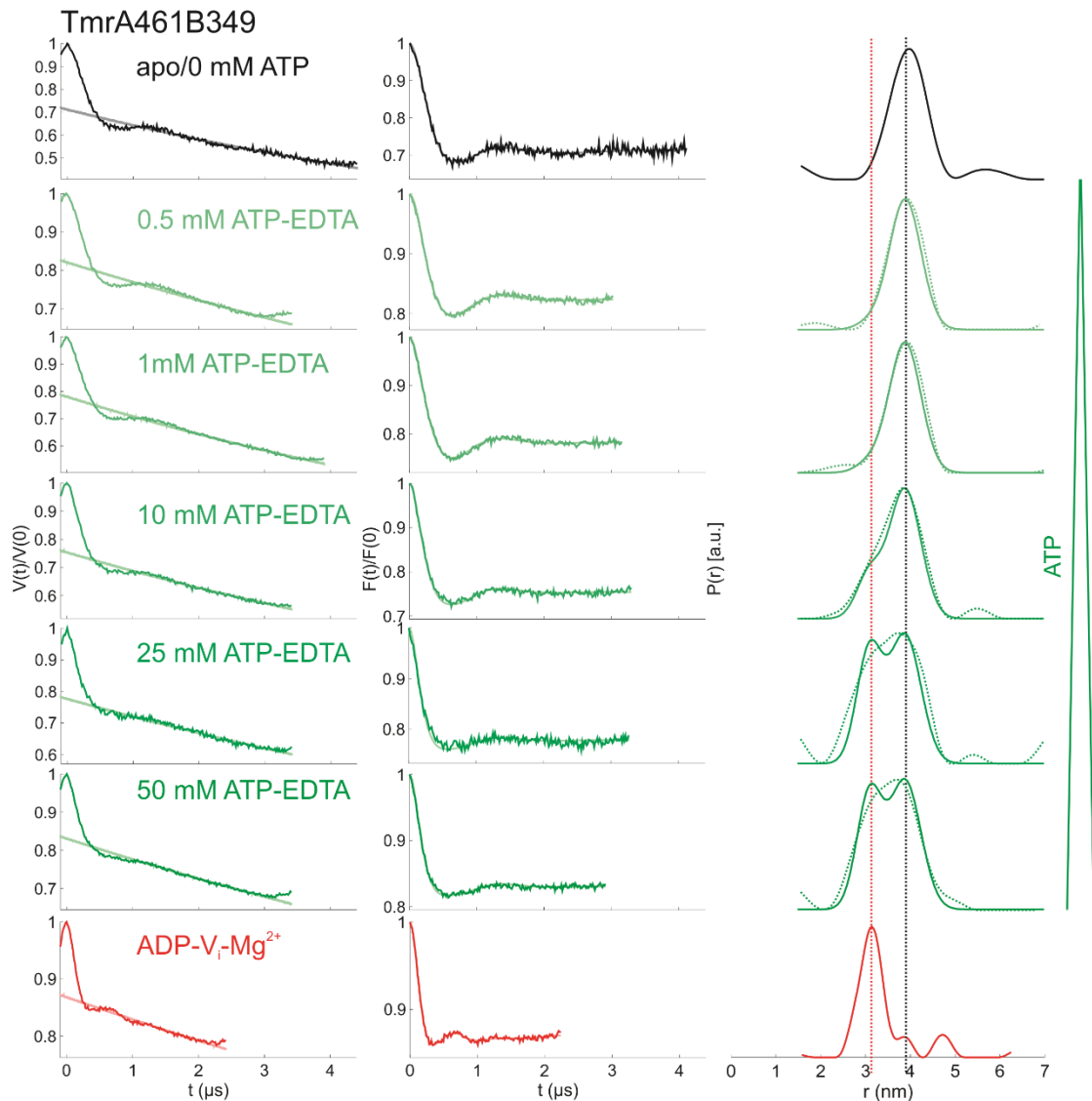


Figure 46: ATP modulates the conformational equilibrium at the consensus NBS TmrA461B349. Apo-state and ADP- V_i - Mg^{2+} were fitted with a Tikhonov regularization. A distance in the apo- or open-state of $r = 3.9 \pm 0.5$ nm and a distance in the closed-state of $r = 3.1 \pm 0.4$ nm were used for Two-Gaussian fitting of the titration data and fits obtained by Tikhonov regularization are overlaid in dotted lines. Original data $V(t)/V(0)$ are displayed on the left, background corrected data $F(t)/F(0)$ are displayed in the middle and the distance distributions $P(r)$ are shown on the right. The consensus site closes with increasing ATP concentration but shows a saturation response at 25 mM ATP. ATP- V_i - Mg^{2+} is representing the completely closed state. The vertical lines indicate the most probable distance in the closed (black) and open (red) states. (Data analysis performed with DeerAnalysis 2016)

The probability of the open and closed conformations determined by DeerAnalysis and the corresponding fractional closure θ (defined as $P_{\text{closed}}/(P_{\text{closed}}+P_{\text{open}})$) are presented in Table 18.

Table 18: Probability of the open and closed conformation at the consensus NBS TmrA461B349, modulated by ATP. The corresponding fractional closure θ is defined as $P_{\text{closed}}/(P_{\text{closed}}+P_{\text{open}})$.

ATP concentration	P_{closed}	P_{open}	Fractional closure θ
0.5 mM	0.04	0.96	0.04
1 mM	0.06	0.94	0.06
10 mM	0.21	0.79	0.21
25 mM	0.41	0.59	0.41
50 mM	0.42	0.58	0.42

As a control for the consensus NBS also TmrA538B549 was investigated (Figure 47). For TmrA538B549 a Two-Gaussian model was applied, using a distance in the apo- or open-state of $r = 3.8 \pm 0.7$ nm and a distance in the closed-state of $r = 3.2 \pm 0.5$ nm. As it was observed for TmrA461B349 on the consensus site, also TmrA538B549 is showing a saturation response at 25 mM ATP. This shows that this particular behaviour originates from the consensus NBS and is not induced by the spin label. The probability of the open and closed conformations (determined by DeerAnalysis) and the corresponding fractional closure θ (defined as $P_{\text{closed}}/(P_{\text{closed}}+P_{\text{open}})$) are presented in Table 19. For 1 mM ATP the closed fraction was too small and rounded to zero (the PELDOR trace for 1 mM ATP was shorter than for 0.5 mM ATP, which made it difficult to fit this small fraction).

Table 19: Probability of the open and closed conformation at the consensus NBS TmrA538B549, modulated by ATP. The corresponding fractional closure θ is defined as $P_{\text{closed}}/(P_{\text{closed}}+P_{\text{open}})$.

ATP concentration	P_{closed}	P_{open}	Fractional closure θ
0.5 mM	0.02	0.98	0.02
1 mM	0.00	1	0.00
10 mM	0.24	0.76	0.24
25 mM	0.38	0.62	0.38
50 mM	0.42	0.58	0.42

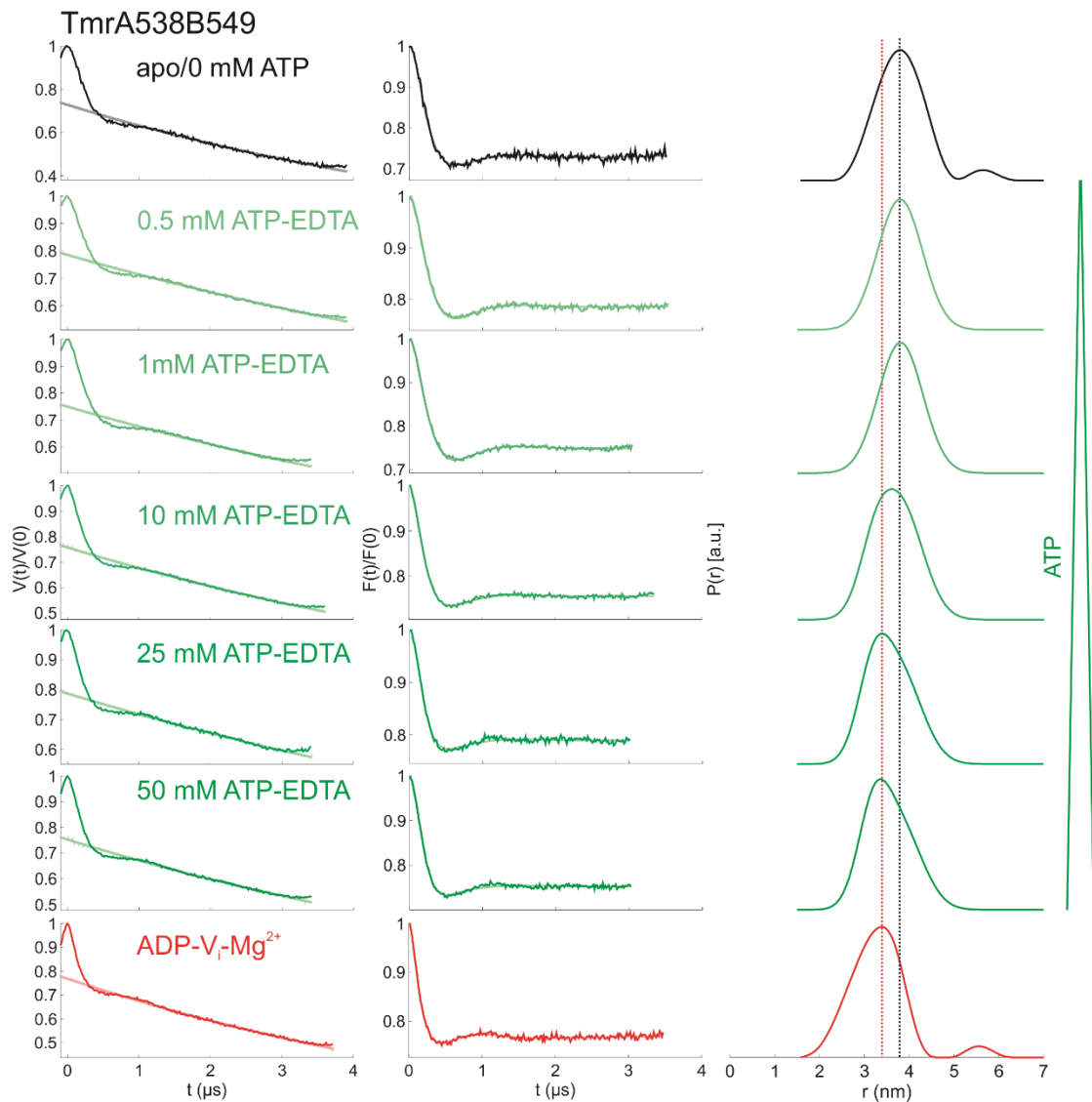


Figure 47: ATP modulates the conformational equilibrium at the consensus NBS TmrA538B549. Apo-state and ADP- V_i - Mg^{2+} were fitted with Tikhonov regularization. A distance in the apo- or open-state of $r = 3.8 \pm 0.7$ nm and a distance in the closed-state of $r = 3.2 \pm 0.5$ nm were used for Two-Gaussian fitting of the ATP titration data. Original data $V(t)/V(0)$ are displayed on the left, background corrected data $F(t)/F(0)$ are displayed in the middle and the distance distributions $P(r)$ are shown on the right. The consensus site closes with increasing ATP concentration but shows a saturation response at 25 mM ATP, as for TmrA461B349 on the consensus site. ATP- V_i - Mg^{2+} is representing the completely closed state. The vertical lines indicate the most probable distance in the closed (black) and open (red) states. (Data analysis performed with DeerAnalysis 2016)

In Figure 48 the measured data for the periplasmic gate TmrA288B272 are shown, which were fitted with a Two-Gaussian model, based on a measured distance in the apo- or closed-state of $r = 3.4 \pm 0.3$ nm and a distance in the open-state of $r = 5.2 \pm 0.3$ nm. Already in the apo-state, a small fraction of the open-state can be observed, as previously discussed. With increasing ATP concentration the open-state fraction is increasing.

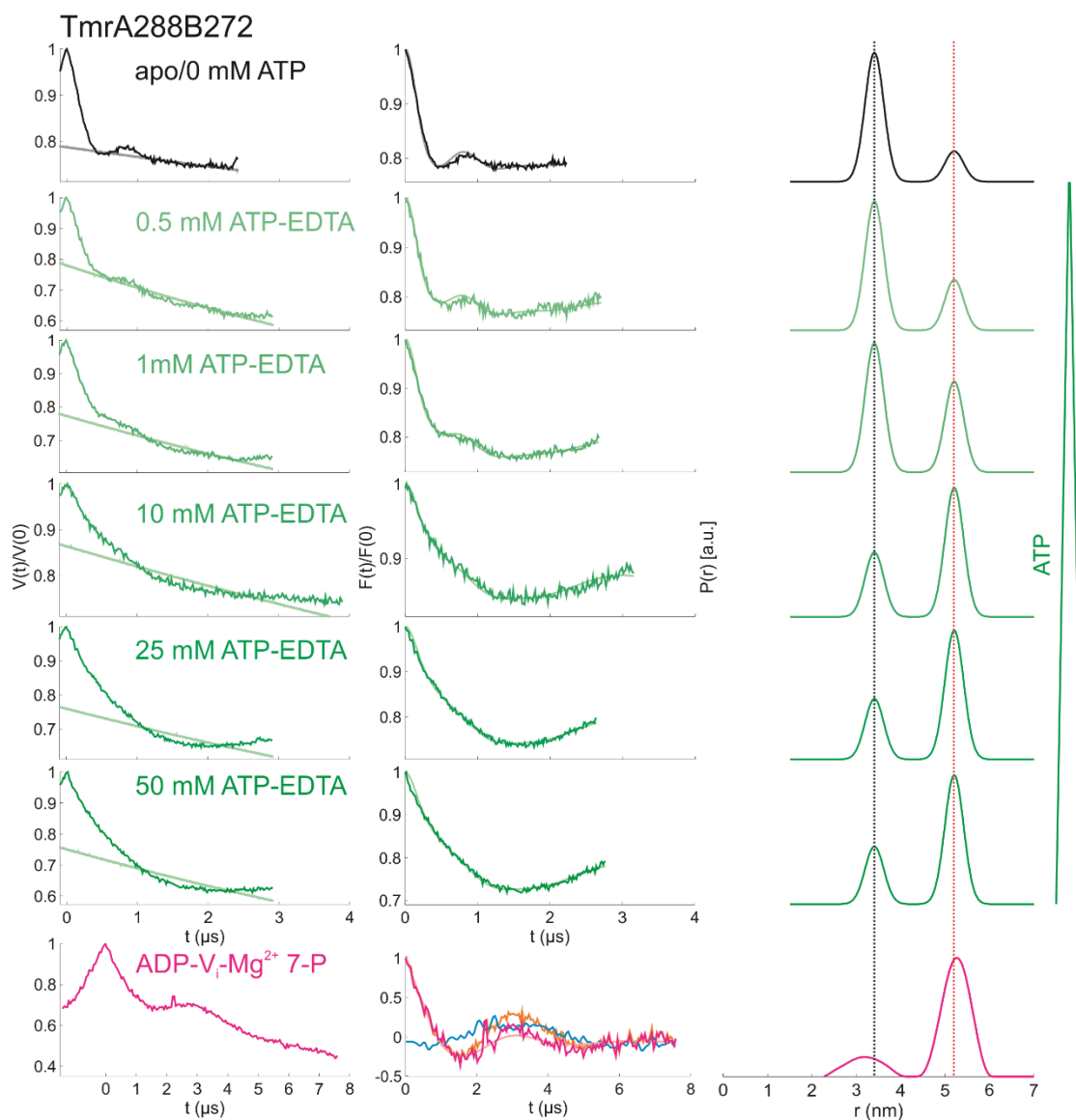


Figure 48: ATP modulates the conformational equilibrium at the periplasmic gate TmrA288B272. The ADP- V_i - Mg^{2+} state was measured with 7P-CP-PELDOR and was fitted with a Tikhonov regularization. A distance in the apo- or open-state of $r = 5.2 \pm 0.3$ nm and a distance in the closed-state of $r = 3.4 \pm 0.3$ nm were used for Two-Gaussian fitting of the ATP titration data and the apo-state. Original data $V(t)/V(0)$ are displayed on the left, background corrected data $F(t)/F(0)$ are displayed in the middle and the distance distributions $P(r)$ are shown on the right. As discussed previously, already a small open fraction is observed in the apo-state and with increasing ATP concentration the open-state at the periplasmic gate is increasing. ATP- V_i - Mg^{2+} is representing the completely closed state. The vertical lines indicate the most probable distance in the closed (black) and open (red) states. (Data analysis performed with DeerAnalysis 2016)

The probability of the open and closed conformation and the corresponding opening probability P_0 (defined as $P_{\text{open}}/(P_{\text{open}}+P_{\text{closed}})$) are presented in Table 20.

Table 20: Probability of the open and closed conformation at the periplasmic gate TmrA288B272, modulated by ATP. The corresponding opening probability P_0 is defined as $P_{open}/(P_{open}+P_{closed})$.

ATP concentration	P_{closed}	P_{open}	Opening Probability P_0
0 mM/apo-state	0.81	0.19	0.19
0.5 mM	0.72	0.28	0.28
1 mM	0.59	0.41	0.41
10 mM	0.33	0.67	0.67
25 mM	0.32	0.68	0.68
50 mM	0.31	0.69	0.69

The dose-response curves for both NBS and the periplasmic gate are shown in Figure 49; the data were analysed by fitting the Hill equation with the Origin software (function ‘Hill1’). Both mutants at the consensus NBS, TmrA461B349 and TmrA538B549, show similar curves.

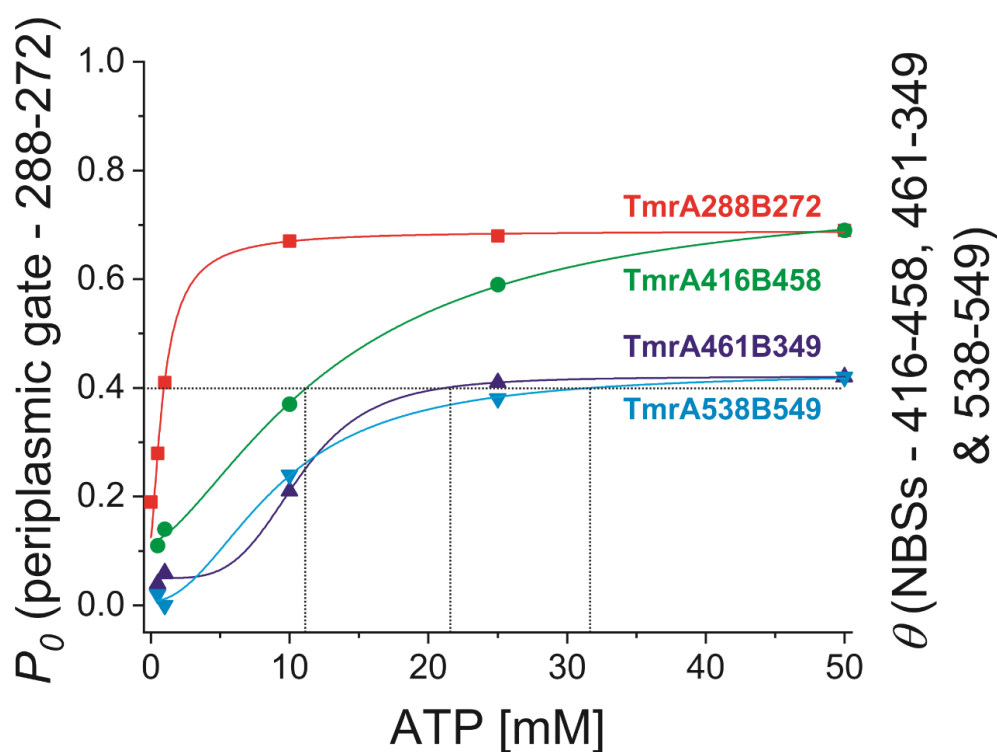


Figure 49: Dose-response curves for both NBS and the periplasmic gate. The consensus NBS are shown in dark blue for TmrA461B349 and in cyan for TmrA538B549. The degenerate NBS TmrA416B458 is shown in green and the periplasmic gate TmrA288B272 is shown in red. For the NBS, the fractional closure θ (defined as $P_{closed}/(P_{closed}+P_{open})$) and for the periplasmic gate the open probability P_0 (defined as $P_{open}/(P_{open}+P_{closed})$) is plotted against the ATP concentration. The horizontal line indicates 40% closure and the vertical lines show the corresponding ATP concentration for the NBSs. Overall θ and P_0 varied by 5% between independent measurements.

As shown in Figure 49 ATP gradually enhanced the closure (θ) of both NBS, resulting in characteristic dose-response curves fingerprinting the two NBSs. The consensus NBS reached a saturation response at 25 mM, where more than 40% closure was reached, while it was almost completely closed with ATP- V_i - Mg^{2+} . This implies that the ATP affinity is not the major limiting factor for the closure since the equilibrium is close to a 1:1 ratio, showing that the open and closed state have similar energy. In contrast to that, the degenerate NBS was more linearly closing upon increasing ATP concentration, resulting in a significantly enhanced closure compared to the consensus NBS. Overall the closed conformation is more stable at the degenerate NBS, where it reached the 40% closure at a 2-fold lower ATP concentration as compared to the consensus NBS.

The D-loop could play an important role for this additional stability.¹¹⁸ Mutation of the catalytic glutamate at the consensus NBS (E523Q) in TmrA increased the closure of both NBS, as shown in Figure 37 for the degenerate site and Figure 39 for the consensus site. This enhancement is significantly larger in case of the degenerate site.

In accordance with the observations on both NBS, increasing of the ATP concentration also enhanced the opening of the periplasmic gate at the TMDs. Plotting of the opening probability (P_o) yields the dose-response curve shown in Figure 49, which shows a saturation behaviour close to 10 mM ATP. As previously discussed, this gate already showed a small population of the open conformation in the absence of ATP. Compared to the closure of both NBS, for the periplasmic gate, an earlier transition to the open state can be observed. At 10 mM ATP a similar response can be observed for TmrA61B56 (Fig. 26) and TmrA112B97 (Fig. 31). In all labelling positions in the TMDs, the opening in the periplasmic gate or closing in the cytosolic gate is approximately the sum of the fractional closure values of both NBSs. This leads to the assumption that the closure of one NBS appears to be sufficient to open the periplasmic gate. At 25 and 50 mM ATP, the gate opening is no longer increasing significantly; this correlates well with the saturation of the consensus NBS, whereas the degenerate NBS is still closing. Between the apo-state and 50 mM ATP P_o is increasing from 0.19 to 0.69, showing that the closure of the NBSs upon ATP binding shifts the equilibrium at the periplasmic gate towards the open conformation. This behaviour of TmrAB is qualitatively more similar to an allosteric regulation in a ligand-gated ion channel, rather than to the strictly coupled alternating-access mechanism for ABC transporters. It has been shown for CFTR, that ATP enhanced the channel activation in a concentration-dependent manner in the range of 0 to 30 mM¹¹⁴ and the gating by ATP presents features of allosteric regulation¹¹⁵. Since the closed conformation is more

favoured at the degenerate NBS it might have a higher influence on the periplasmic gate opening. Since the closed- and open-state are energetically similar on the consensus NBS, this could probably explain why for CFTR only the degenerate site could be photo labelled with 8-azido ATP¹¹⁹.

Finally, these results reveal that the consensus NBS might control the lifetime of the outward-facing state and that ATP hydrolysis at this site leads to the opening of both NBSs, which results in the restoring of the transporter to the inward-facing conformation.

4.2.2 Influence of different temperatures to the conformational equilibrium

Even though a number of structural studies were done over recent years, a mechanism determining the energy-landscape of a transport cycle remains unknown. In 2016 Zhang et al.²⁷ reviewed the current state of knowledge, with a special focus on the coupling of ATP hydrolysis to conformational changes during a transport cycle, based on the available structural and biochemical data. Especially in exporters, e.g. for P-gp, it was observed that by trapping of the transition state with ADP-V_i-Mg²⁺ the substrate affinity is 30-fold lower compared to the affinity in the inward- and outward-facing state, which show the same affinity without trapping.¹²⁰ These observations lead to the assumption that ATP hydrolysis is the driving force for substrate release. MD simulations could use e.g. structural data to investigate thermodynamics, but although a lot of structures are available, still not enough input data is available to observe a transport cycle.²³ In addition, computational limitations restrict the possibilities of MD. Since structures are a snapshot of specific states, for which the conditions were optimized for the crystallization progress and not for the lowest-energy conformation, differences to the natural behaviour can occur. An approach to look into thermodynamics is the temperature dependence of an equilibrium, which can be described by the van't Hoff equation. This approach has been previously used for the maltose-binding protein from *Thermotoga maritima* (TmMBP), where the substrate binding to the protein has been investigated with UV spectroscopy at different temperatures.¹²¹ With a linear van't Hoff model they observed that the substrate-binding is entropy-driven.

In this thesis, the conformational equilibrium induced by ATP binding in TmrAB is investigated at different temperatures at an ATP concentration of 50 mM to fully saturate the protein. By determining the temperature dependence of this equilibrium, the thermodynamics underlying the energy coupling during ATP-induced conformational changes in TmrAB can be studied. For this purpose, both NBSs and the periplasmic gate were investigated to observe the overall motion in the transporter. Temperatures between 0

and 80 °C were chosen, which are the conditions that were previously used to investigate the ATPase activity of TmrAB⁶⁶. The ATPase activity has its maximum at approximately 70 °C, which is close to the incubation temperature of 68 °C typically used for PELDOR experiments. In Supp. Figure 1 transport assays are shown at different temperatures for wildtype and the spin-labelled TmrA416B458, which both show the same maximum at 70°C. In Figure 50 the temperature-dependent PELDOR data for the consensus NBS are shown. Since for this experiment, the data is analysed quantitatively, for each position two sample sets from different protein purification batches were measured. From these measurements, the average value was used for analysis and the error resulting from differences in the activity of the protein was taken into account for the final error. For the consensus NBS TmrA461B349, the software DD was used for analysis and a Three Gaussian fitting was done since in these measurements the intensity of the additional distance at $r = 6.0 \pm 0.5$ nm was much larger than in the previous measurements. Since this component already occurred in the inward-facing state without any nucleotides, this fraction was added to the open probability (P_{open}). In Table 21 the probabilities for the closed conformation (P_{closed}) and the open conformation (P_{closed}) are shown for both sample sets.

Table 21: Probability of the open and closed conformation at the consensus NBS TmrA461B349, modulated by temperature.

Temperature	P_{closed} (first sample set / second sample set)	P_{open} (first sample set / second sample set)
0 °C	0.03 / 0.07	0.97 / 0.93
25 °C	0.34 / 0.27	0.66 / 0.73
40 °C	0.51 / 0.43	0.49 / 0.57
50 °C	0.52 / 0.44	0.48 / 0.56
60 °C	0.44 / 0.35	0.56 / 0.65
70 °C	0.37 / 0.39	0.63 / 0.61
80 °C	0.37 / 0.28	0.63 / 0.72

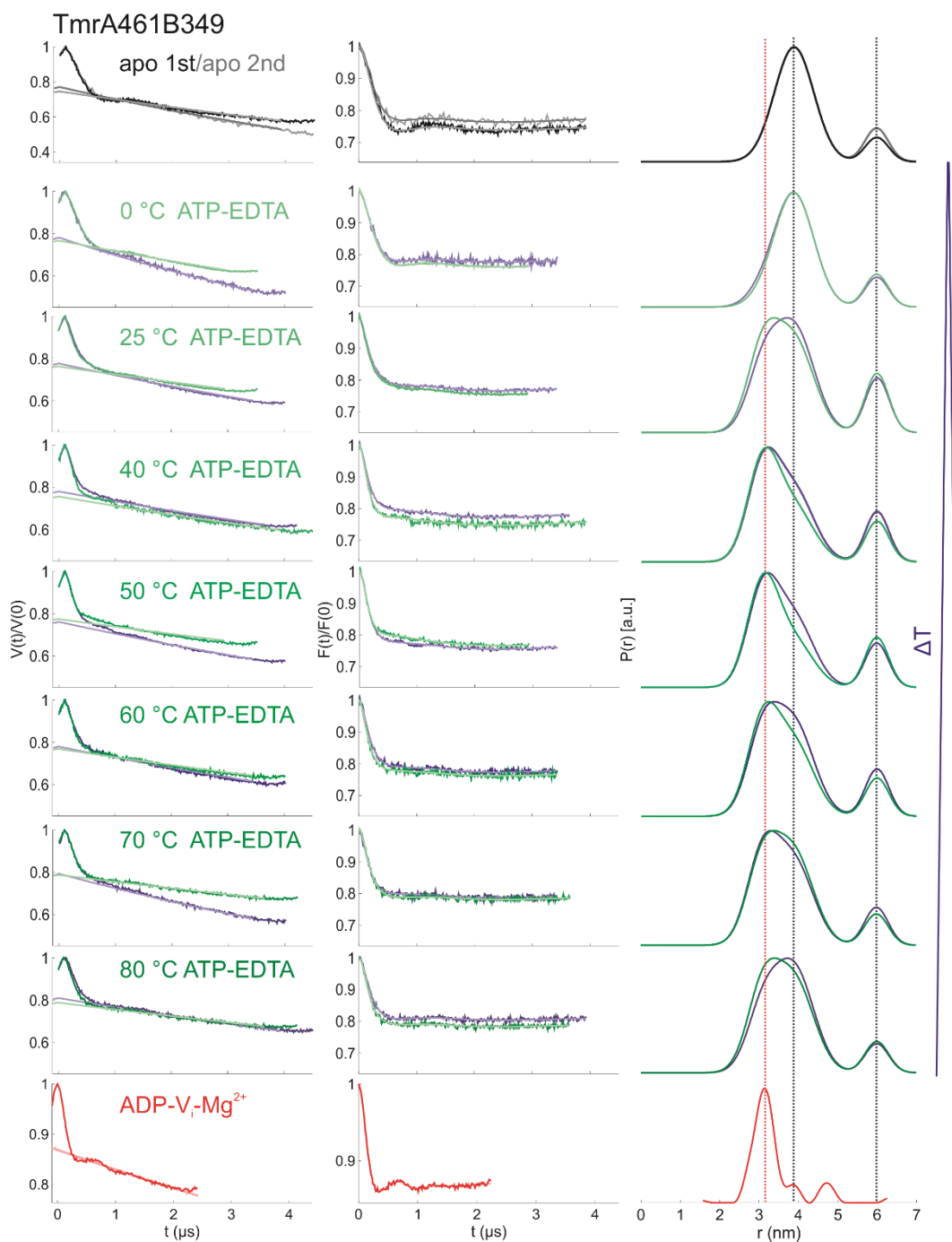


Figure 50: Temperature dependence of the conformational equilibrium induced by ATP binding at the consensus NBS TmrA461B349. ADP- V_i - Mg^{2+} was analysed with Tikhonov regularization. Distances in the apo- or open-state of $r = 3.9 \pm 0.5$ nm and $r = 6.0 \pm 0.5$ nm and a distance in the closed-state of $r = 3.1 \pm 0.4$ nm were used for Three-Gaussian fitting of the temperature-dependent data and the apo-state. Original data $V(t)/V(0)$ are displayed on the left, background corrected data $F(t)/F(0)$ are displayed in the middle and the distance distributions $P(r)$ are shown on the right. The degenerate site closes linearly with increasing temperature up to 50 °C, whereas at higher temperatures the open conformation is increasing. The first sample set is shown in green, the second sample set is underlaid in blue. ATP- V_i - Mg^{2+} is representing the completely closed state. The vertical lines indicate the most probable distance in the closed (black) and open (red) states. (Data analysis performed with DeerAnalysis 2016 for the apo-state and ADP- V_i - Mg^{2+} and with DD6c for ATP-EDTA)

With the populations of the states and the knowledge of the concentrations, the equilibrium constant (K_{eq}) can be calculated. If both NBS are closing due to ATP binding either one or two ATP could be bound. Since this cannot be clarified with the done experiments, both models were used for further calculations. In Equation (31) the calculation of K_{eq} for one bound ATP is described and in Equation (32) the equivalent equation is shown for the case that two ATP are bound to the transporter in the outward-facing state.

$$K_{eq,1ATP} = \frac{[TmrAB - ATP]}{[TmrAB] \cdot [ATP]} \quad (31)$$

$$K_{eq,2ATP} = \frac{[TmrAB - 2ATP]}{[TmrAB] \cdot [ATP]^2} \quad (32)$$

Concentrations are indicated by square brackets. In the numerator is the ATP bound outward-facing complex and in the denominator the ATP-free inward-facing protein.

Based on Equations (31) and (32) K_{eq} was calculated for both cases at all temperatures. The corresponding concentrations and K_{eq} values for both sample sets are shown in Supp. Table 1 in the supporting information section. The error was calculated with Equation (33) and (34), according to Gaussian error propagation, with an assumed error in the protein concentration of 20%.

$$\Delta K_{eq,1ATP} = \sqrt{\left(\frac{1}{[TmrAB] \cdot [ATP]}\right)^2 \cdot (0.2 \cdot [TmrAB - ATP])^2 + \left(-\frac{[TmrAB - ATP]}{[TmrAB]^2 \cdot [ATP]}\right)^2 \cdot (0.2 \cdot [TmrAB])^2} \quad (33)$$

$$\Delta K_{eq,2ATP} = \sqrt{\left(\frac{1}{[TmrAB] \cdot [ATP]^2}\right)^2 \cdot (0.2 \cdot [TmrAB - ATP])^2 + \left(-\frac{[TmrAB - ATP]}{[TmrAB]^2 \cdot [ATP]^2}\right)^2 \cdot (0.2 \cdot [TmrAB])^2} \quad (34)$$

For the calculation of the $K_{eq,av}$ the average of the two sample sets ($K_{eq,1st}$ and $K_{eq,2nd}$) was used (Equation (35)) and the corresponding error was calculated with Equation (36) using Gaussian error propagation.

$$K_{eq,av} = \frac{K_{eq,1st} + K_{eq,2nd}}{2} \quad (35)$$

$$\Delta K_{eq,av} = \sqrt{\left(\frac{1}{2}\right)^2 \cdot (\Delta K_{eq,1st})^2 + \left(\frac{1}{2}\right)^2 \cdot (\Delta K_{eq,2nd})^2} \quad (36)$$

For the graphical plotting, the natural logarithm was taken from $K_{eq,av}$, and the final error was calculated with Gaussian error propagation (Equation (37)).

$$\Delta \ln K_{eq,av} = \sqrt{\left(\frac{1}{K_{eq,av}}\right)^2 \cdot (\Delta K_{eq,av})^2} \quad (37)$$

The resulting values for $K_{eq,av}$, the corresponding errors and the natural logarithm are shown in Table 22.

Table 22: The average equilibrium constants for the consensus NBS TmrA461B349, modulated by temperature.

Temp.	$K_{eq,av}$ [1/M] (1 ATP)	$\Delta K_{eq,av}$ [1/M] (1 ATP)	$\ln K_{eq,av}$ (1 ATP)	$\Delta \ln K_{eq,av}$ (1 ATP)	$K_{eq,av}$ [1/M ²] (2 ATP)	$\Delta K_{eq,av}$ [1/M ²] (2 ATP)	$\ln K_{eq,av}$ (2ATP)	$\Delta \ln K_{eq,av}$ (2 ATP)
0 °C	1.0	0.3	0.03	0.2	21	5	3.0	0.2
25 °C	8.7	1.8	2.2	0.2	170	40	5.2	0.2
40 °C	18	4	2.9	0.2	350	70	5.9	0.2
50 °C	19	4	2.9	0.2	370	80	5.9	0.2
60 °C	13	3	2.6	0.2	260	60	5.6	0.2
70 °C	12	3	2.5	0.2	240	50	5.5	0.2
80 °C	10	2	2.3	0.2	190	40	5.3	0.2

For the degenerate NBS TmrA461B349, the data analysis was done similarly, the data is shown in Figure 51. In Table 23 the probabilities for the closed conformation (P_{closed}) and the open conformation (P_{open}) are shown for both sample sets.

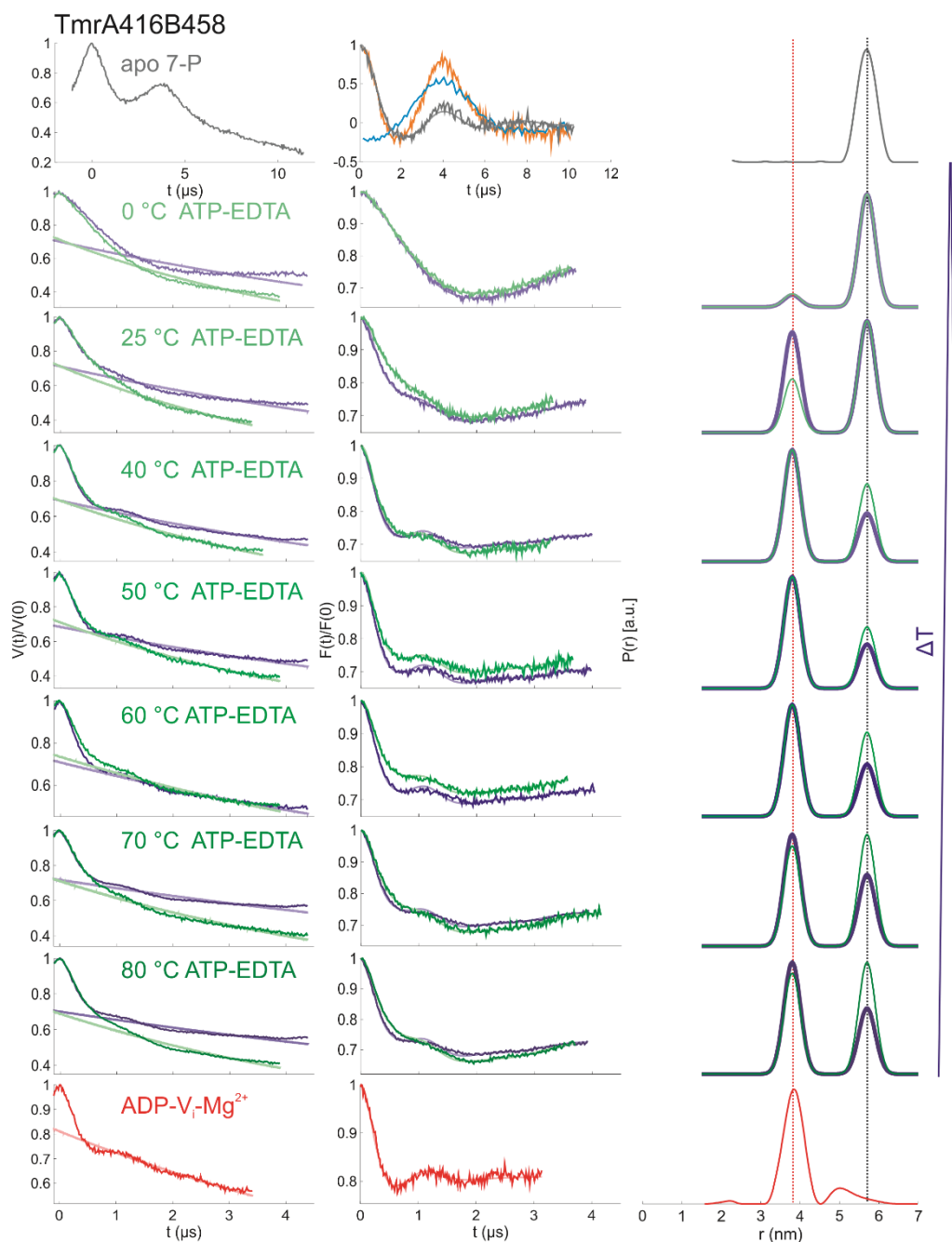


Figure 51: Temperature dependence of the conformational equilibrium induced by ATP binding at the degenerate NBS TmrA416B458. Apo-state and ADP- V_i - Mg^{2+} were analysed with Tikhonov regularization. The open-state (0 mM) was measured with 7-pulse CP-PELDOR. A distance in the apo- or open-state of $r = 5.7 \pm 0.3$ nm and a distance in the closed-state of $r = 3.8 \pm 0.4$ nm were used for Two-Gaussian fitting of the temperature-dependent data. Original data $V(t)/V(0)$ are displayed on the left, background corrected data $F(t)/F(0)$ are displayed in the middle and the distance distributions $P(r)$ are shown on the right. The degenerate site closes linearly with increasing temperature up to 50 °C. At higher temperatures, the open conformation is increasing. A first sample set is shown in green, a second sample set is underlaid in blue. ATP- V_i - Mg^{2+} represents the completely closed state. The vertical lines indicate the most probable distance in the closed (black) and open (red) states. (Data analysis performed with DeerAnalysis 2016)

Table 23: Probability of the open and closed conformation at the degenerate NBS TmrA416B458, modulated by temperature.

Temperature	P _{closed} (first sample set / second sample set)	P _{open} (first sample set / second sample set)
0 °C	0.10 / 0.10	0.90 / 0.90
25 °C	0.33 / 0.47	0.67 / 0.53
40 °C	0.59 / 0.70	0.41 / 0.30
50 °C	0.65 / 0.72	0.35 / 0.28
60 °C	0.57 / 0.68	0.43 / 0.32
70 °C	0.47 / 0.61	0.53 / 0.39
80 °C	0.47 / 0.63	0.53 / 0.37

$K_{eq,av}$ was calculated as described for the consensus NBS TmrA461B349. In Figure 51 it can be seen, that the differences between the two sample sets are larger compared to the other positions. Therefore, the error estimation with Gaussian error propagation would underestimate the error. In this case the error $\Delta K_{eq,av}$ was calculated with Equation (38), in which the standard deviation multiplied with the student factor is calculated. The student factor is a correction factor for small ensembles and in this case, the factor for 95% probability was used. In Supp. Table 2 the concentrations for the calculations are shown and in Table 24 the final average equilibrium constants with the corresponding error are shown.

$$\Delta K_{eq,av} = \sqrt{\frac{(K_{eq,1st} - K_{eq,av})^2 + (K_{eq,2nd} - K_{eq,av})^2}{1}} \cdot 2.92 \quad (38)$$

Table 24: The average equilibrium constants for the degenerate NBS TmrA416B458, modulated by temperature.

Temp.	$K_{eq,av}$ [1/M] (1 ATP)	$\Delta K_{eq,av}$ [1/M] (1 ATP)	$\ln K_{eq,av}$ (1 ATP)	$\Delta \ln K_{eq,av}$ (1 ATP)	$K_{eq,av}$ [1/M ²] (2 ATP)	$\Delta K_{eq,av}$ [1/M ²] (2 ATP)	$\ln K_{eq,av}$ (2ATP)	$\Delta \ln K_{eq,av}$ (2 ATP)
0 °C	2.2	0.5	0.8	0.2	44	9	3.8	0.2
25 °C	14	18	2.6	1.3	280	60	5.6	1.3
40 °C	40	40	3.6	1.0	750	160	6.6	1.0
50 °C	40	30	3.8	0.7	870	180	6.8	0.7
60 °C	40	30	3.5	1.0	700	150	6.5	1.0
70 °C	30	30	3.2	1.1	490	110	6.2	1.1
80 °C	30	40	3.3	1.3	520	110	6.3	1.3

To observe the overall structural rearrangement, also the periplasmic gate TmrA288B272 was investigated following the same approach as for both NBS. The data are shown in Figure 52. In contrast to both NBS, in the periplasmic gate, an increase in the open state is observed up to 70 °C. The corresponding probabilities for the closed conformation (P_{closed}) and the open conformation (P_{open}) are shown in Table 25.

Table 25: Probability of the open and closed conformation at the periplasmic gate TmrA288B272, modulated by temperature.

Temperature	P_{closed} (first sample set / second sample set)	P_{open} (first sample set / second sample set)
0 °C	0.82 / 0.77	0.18 / 0.23
25 °C	0.67 / 0.67	0.33 / 0.33
40 °C	0.53 / 0.53	0.47 / 0.47
50 °C	0.41 / 0.41	0.59 / 0.59
60 °C	0.36 / 0.39	0.64 / 0.61
70 °C	0.33 / 0.35	0.67 / 0.65
80 °C	0.35 / 0.39	0.65 / 0.61

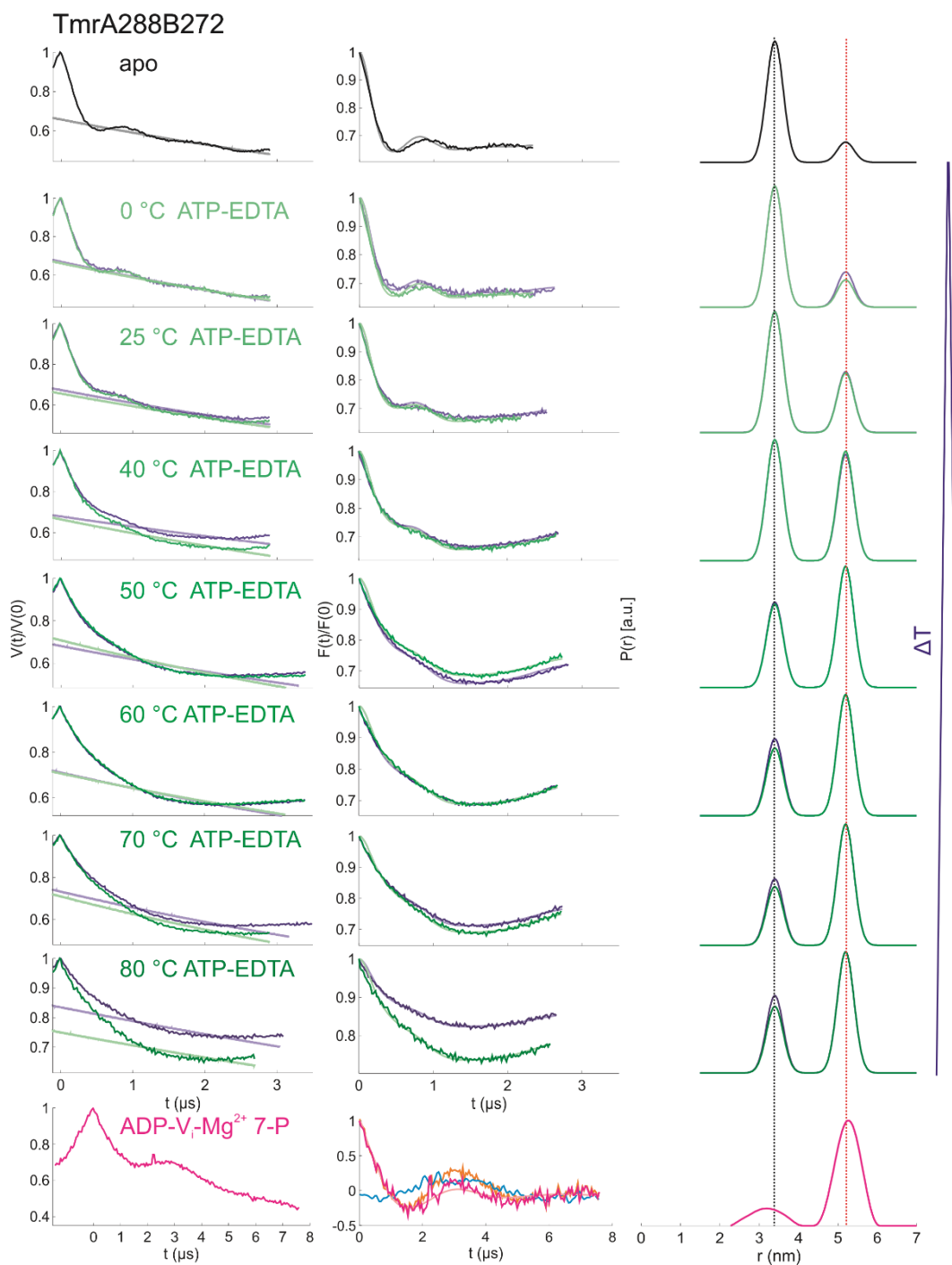


Figure 52: Temperature dependence of the conformational equilibrium induced by ATP binding at the periplasmic gate TmrA288B272. The 7-pulse CP-PELDOR measurement of ADP- V_i - Mg^{2+} was fitted with a Tikhonov regularization. A distance in the apo- or closed-state of $r = 3.4 \pm 0.3$ nm and a distance in the open-state of $r = 5.2 \pm 0.3$ nm, were used for Two-Gaussian fitting of the temperature-dependent data and the apo-state. Original data $V(t)/V(0)$ are displayed on the left, background corrected data $F(t)/F(0)$ are displayed in the middle and the distance distributions $P(r)$ are shown on the right. The periplasmic gate opens linearly with increasing temperature up to 70 °C. The first sample set is shown in green, the second sample set is underlaid in blue. ATP- V_i - Mg^{2+} is representing the completely closed state. The vertical lines indicate the most probable distance in the closed (black) and open (red) states. (Data analysis performed with DeerAnalysis 2016)

Calculations of $K_{eq,av}$ and the corresponding errors for the periplasmic gate TmrA288B272 were identical to the procedure as performed for the consensus NBS. In Supp. Table 3 the concentrations for the calculations are shown and the calculated average equilibrium constants with the corresponding error are presented in Table 26.

Table 26: The average equilibrium constants for the periplasmic gate TmrA288B272, modulated by temperature.

Temp.	$K_{eq,av}$ [1/M] (1 ATP)	$\Delta K_{eq,av}$ [1/M] (1 ATP)	$\ln K_{eq,av}$ (1 ATP)	$\Delta \ln K_{eq,av}$ (1 ATP)	$K_{eq,av}$ [1/M ²] (2 ATP)	$\Delta K_{eq,av}$ [1/M ²] (2 ATP)	$\ln K_{eq,av}$ (2ATP)	$\Delta \ln K_{eq,av}$ (2 ATP)
0 °C	5.2	1.1	1.6	0.2	100	20	4.6	0.2
25 °C	10	2	2.3	0.2	200	40	5.3	0.2
40 °C	18	4	2.9	0.2	360	70	5.9	0.2
50 °C	29	6	3.4	0.2	380	120	6.4	0.2
60 °C	34	7	3.5	0.2	670	140	6.5	0.2
70 °C	39	8	3.7	0.2	780	160	6.7	0.2
80 °C	34	7	3.5	0.2	680	140	6.5	0.2

When the peptide K5F was added to TmrAB288B272 no difference in the data could be observed for temperatures of 25 and 50 °C (Supp. Figure 2). This shows that ATP binding is the most important step in the transition from inward- to outward-facing conformation and that the substrate is not changing the energetic state.

In Figure 53 the reciprocal temperature for both NBSs and the periplasmic gate is plotted against the natural logarithm of the average equilibrium constant ($K_{eq,av}$). At higher temperatures above 50 °C the behaviour of both NBSs is not linear anymore. One possible reason for the decreasing $\ln K_{eq}$ at higher temperature could be that the reaction rates at higher temperatures are faster than the rates of the freezing process. This would mean that the equilibrium would go back to the lower-energy state, in this case, the apo-state, in a temperature-dependent manner.

A linear fit was done between the values at 0 °C and 50 °C since this was the range in which both NBSs are linearly closing. With these fits the enthalpy change and entropy change can be estimated through the van't Hoff-equation, which is shown in Equation (39), whereby R is the universal gas constant ($R= 8.31448 \text{ JK}^{-1}\text{mol}^{-1}$).

$$\ln K_{eq} = -\frac{\Delta H}{RT} + \frac{\Delta S}{R} \quad (39)$$

From the slope and the intercept of the linear fits in Figure 53, the entropy change and enthalpy change can be calculated according to Equation (40) for the entropy change (ΔS_{VH}^0) and Equation (41) for the enthalpy change (ΔH_{VH}^0).

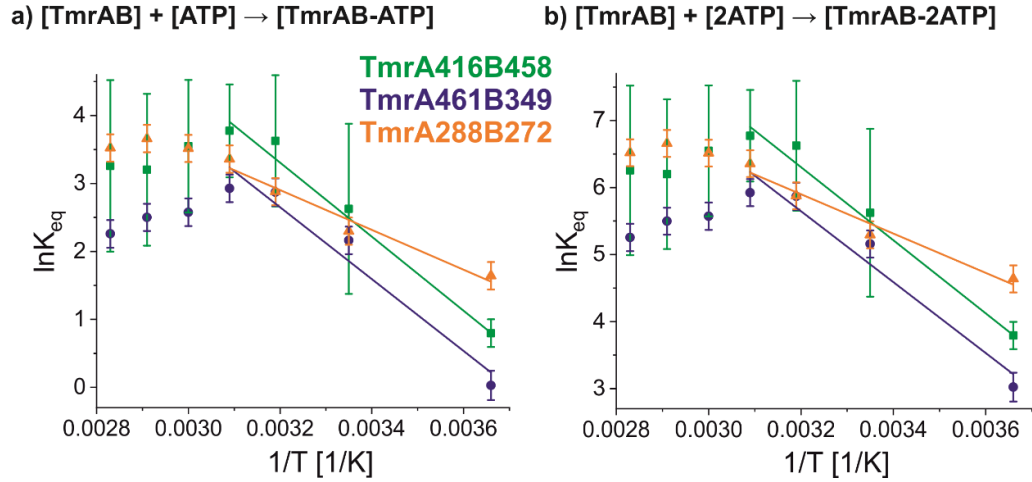


Figure 53: Linear van't Hoff fit of both NBSs and the periplasmic gate. Shown are the degenerate NBS TmrA416B458 in green, the consensus NBS TmrA461B349 in blue and the periplasmic gate TmrA288B272 in orange. The values between 0 °C and 50 °C were fitted with a linear function and the slope and intercept were used to calculate the van't Hoff enthalpy change and entropy change. In a) the values are shown for the assumption of one ATP bound to the transporter and in b) for two bound ATP, respectively.

$$\Delta S_{VH}^0 = \text{intercept} \cdot R \quad (40)$$

$$\Delta H_{VH}^0 = -\text{slope} [T] \cdot R \quad (41)$$

If $\Delta S_{VH}^0 > 0$ the reaction is entropy-driven and if $\Delta H_{VH}^0 < 0$ the reaction is enthalpy-driven. With the determined enthalpy change and entropy change of the van't Hoff plot the Gibbs free energy change (ΔG_{VH}^0) can be calculated (Equation (42)).

$$\Delta G_{VH}^0 = \Delta H_{VH}^0 - \Delta S_{VH}^0 \cdot T \quad (42)$$

In general a $\Delta G_{VH}^0 < 0$, corresponds to an exergonic reaction, which would take place spontaneously. Whereas with $\Delta G_{VH}^0 > 0$ the energy barrier first would need to be overcome.

The errors of the enthalpy change, entropy change and Gibbs free energy change can be calculated with Equations (43)-(45) with the help of Gaussian error propagation.

$$\Delta\Delta S_{VH}^0 = \sqrt{R^2 \cdot \Delta intercept^2} \quad (43)$$

$$\Delta\Delta H_{VH}^0 = \sqrt{(-R)^2 \cdot \Delta slope^2} \quad (44)$$

$$\Delta\Delta G_{VH}^0 = \sqrt{1^2 \cdot \Delta\Delta H_{VH}^0^2 + (-T)^2 \cdot \Delta\Delta S_{VH}^0^2} \quad (45)$$

In Table 27 the slopes and intercepts with corresponding errors for the linear fits are presented. Both models are shown, where either one or two bound ATP.

Table 27: Slopes and intercepts determined with the linear van't Hoff plot. Shown are the values for both NBSs and the periplasmic gate with corresponding errors and for both models, with either one or two bound ATP.

	<i>Slope [T]</i>	<i>Δslope [T]</i>	<i>Intercept</i>	<i>Δintercept</i>
TmrA416B458 (1 ATP)	-5500	300	20.7	1.0
TmrA416B458 (2 ATP)	-5500	300	23.7	1.0
TmrA461B349 (1 ATP)	-5300	900	20	3
TmrA461B349 (2 ATP)	-5300	900	23	3
TmrA288B272 (1 ATP)	-2900	400	12.3	1.3
TmrA288B272 (2 ATP)	-2900	400	15.3	1.3

From these values the entropy change (ΔS_{VH}^0) and the enthalpy change (ΔH_{VH}^0) can be calculated, which are presented in Table 28.

Table 28: The enthalpy change (ΔH_{VH}^0) and the entropy change (ΔS_{VH}^0), from the linear van't Hoff plot. Shown are the values for both NBSs and the periplasmic gate with corresponding errors and for both models, with either one or two bound ATP.

	ΔH_{VH}^0	ΔS_{VH}^0
TmrA416B458 (1 ATP)	$45 \pm 3 \frac{\text{kJ}}{\text{mol}}$	$172 \pm 8 \frac{\text{J}}{\text{Kmol}}$
TmrA416B458 (2 ATP)	$45 \pm 3 \frac{\text{kJ}}{\text{mol}}$	$198 \pm 8 \frac{\text{J}}{\text{Kmol}}$
TmrA461B349 (1 ATP)	$44 \pm 7 \frac{\text{kJ}}{\text{mol}}$	$160 \pm 30 \frac{\text{J}}{\text{Kmol}}$
TmrA461B349 (2 ATP)	$44 \pm 7 \frac{\text{kJ}}{\text{mol}}$	$190 \pm 30 \frac{\text{J}}{\text{Kmol}}$
TmrA288B272 (1 ATP)	$24 \pm 4 \frac{\text{kJ}}{\text{mol}}$	$100 \pm 11 \frac{\text{J}}{\text{Kmol}}$
TmrA288B272 (2 ATP)	$24 \pm 4 \frac{\text{kJ}}{\text{mol}}$	$128 \pm 11 \frac{\text{J}}{\text{Kmol}}$

For both models, it can be clearly seen that for all three positions the conformational transition from inward- to outward-facing state by ATP binding results on a gain in entropy. Yet the enthalpy change is positive, which means that the transition is endothermic and an energetic barrier has to be overcome. Table 29 shows the temperature-dependent Gibbs free energy change, which was calculated with Equation (41). For the calculation, the same temperature values were used that were used for the determination of the enthalpy change and entropy change.

Table 29: The Gibbs free energy change (ΔG_{VH}^0) calculated from the enthalpy and entropy determined by the linear van't Hoff plot. Shown are the values for both NBSs and the periplasmic gate with corresponding errors and for both models, with either one or two bound ATP.

	ΔG_{VH}^0 0 °C	25 °C	40 °C	50 °C
TmrA416B458 (1 ATP)	$-2 \pm 3 \frac{\text{kJ}}{\text{mol}}$	$-6 \pm 4 \frac{\text{kJ}}{\text{mol}}$	$-9 \pm 4 \frac{\text{kJ}}{\text{mol}}$	$-10 \pm 4 \frac{\text{kJ}}{\text{mol}}$
TmrA416B458 (2 ATP)	$-9 \pm 3 \frac{\text{kJ}}{\text{mol}}$	$-14 \pm 4 \frac{\text{kJ}}{\text{mol}}$	$-17 \pm 4 \frac{\text{kJ}}{\text{mol}}$	$-19 \pm 4 \frac{\text{kJ}}{\text{mol}}$
TmrA461B349 (1 ATP)	$-0.3 \pm 10 \frac{\text{kJ}}{\text{mol}}$	$-4 \pm 10 \frac{\text{kJ}}{\text{mol}}$	$-7 \pm 10 \frac{\text{kJ}}{\text{mol}}$	$-9 \pm 11 \frac{\text{kJ}}{\text{mol}}$
TmrA461B349 (2 ATP)	$-7 \pm 10 \frac{\text{kJ}}{\text{mol}}$	$-12 \pm 10 \frac{\text{kJ}}{\text{mol}}$	$-15 \pm 10 \frac{\text{kJ}}{\text{mol}}$	$-17 \pm 11 \frac{\text{kJ}}{\text{mol}}$
TmrA288B272 (1 ATP)	$-4 \pm 5 \frac{\text{kJ}}{\text{mol}}$	$-6 \pm 5 \frac{\text{kJ}}{\text{mol}}$	$-8 \pm 5 \frac{\text{kJ}}{\text{mol}}$	$-9 \pm 5 \frac{\text{kJ}}{\text{mol}}$
TmrA288B272 (2 ATP)	$-10 \pm 5 \frac{\text{kJ}}{\text{mol}}$	$-14 \pm 5 \frac{\text{kJ}}{\text{mol}}$	$-15 \pm 5 \frac{\text{kJ}}{\text{mol}}$	$-17 \pm 5 \frac{\text{kJ}}{\text{mol}}$

Since the errors of the enthalpy change and entropy change are both taken into account for the calculations of the error of the Gibbs free energy change, the errors are in some cases rather large, especially for TmrA461B349. Yet, the Gibbs free energy change is consistently negative for all three positions and both models. Especially by using the model with two bound ATP the gain in energy is approximately 17-19 kJ per mol. This suggests that the

model with two bound ATP has a higher probability than the model with one bound ATP. This shows that the transition from the inward- to the outward-facing state induced by ATP binding is taking place spontaneously and is entropy-driven. Since no substrate was present and no ATP hydrolysis could take place in this state, these results reveal that ATP binding alone drives the global conformational switching from the inward- to outward-facing conformation.

For the linear fitting, which is shown in Figure 53, the values from 60-80 °C are not taken into account since both NBS stopped further closing. Another possibility for this behaviour is a temperature dependence of the enthalpy change and entropy change, thus leading to a smaller $\ln K_{eq}$ at higher temperatures. In this case, a non-linear van't Hoff fit can be applied which is shown in Figure 54. The corresponding fitting parameters, determined for a polynomial fit of second order are shown in Supp. Table 4. A non-linear polynomial fit of second-order was subsequently used, for which the formula is shown in Equation (46).

$$\ln k_{eq} = a + b \cdot \frac{1}{T} + c \cdot \left(\frac{1}{T}\right)^2 \quad (46)$$

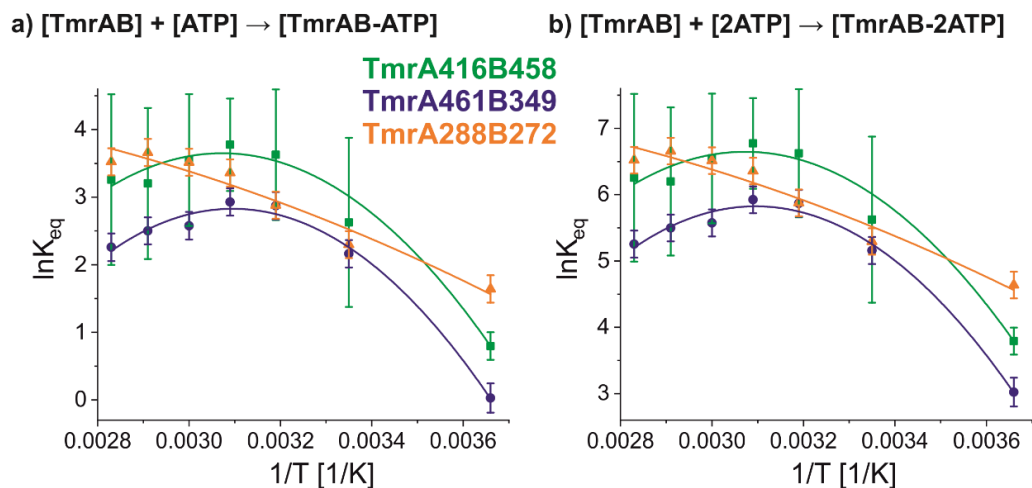


Figure 54: Non-linear van't Hoff fit of both NBSs and the periplasmic gate. Shown are the degenerate NBS TmrA416B458 in green, the consensus NBS TmrA461B349 in blue and the periplasmic gate TmrA288B272 in orange. The values between 0 °C and 80 °C were fitted with a polynomial function of second order. In a) the values are shown for the assumption of one ATP bound to the transporter and in b) for two bound ATP.

From this non-linear fitting, the periplasmic gate TmrA288B272 shows a mostly linear behaviour, whereas both NBS behave non-linearly. In principle, a non-linear behaviour

could mean that the enthalpy change is temperature-dependent. In 2017, Vieira et al. investigated the non-linear van't Hoff behaviour in pulmonary surfactant model membranes.¹²² In this publication the authors report how the heat capacity change, enthalpy change, entropy change and Gibbs free energy change can be calculated from the fitting parameters. Similar calculations were done for the non-linear van't Hoff fit of TmrAB. The calculation of the heat capacity change (ΔC_{VH}^0) is shown in Equation (47) and the corresponding error can be calculated through Gaussian error propagation (Equation (48)).

$$\Delta C_{VH}^0 = 2 \cdot R \cdot \left(\frac{c}{T^2}\right) \quad (47)$$

$$\Delta\Delta C_{VH}^0 = \sqrt{\left(\frac{2R}{T^2}\right)^2 \cdot \Delta c^2} \quad (48)$$

In this, a, b and c are the constants of the polynomial. The calculation for the enthalpy change and the corresponding error are shown in Equations (49) and (50).

$$\Delta H_{VH}^0 = -R \cdot \left(b + \frac{2 \cdot c}{T}\right) \quad (49)$$

$$\Delta\Delta H_{VH}^0 = \sqrt{(-R)^2 \cdot \Delta b^2 + \left(-\frac{2 \cdot R}{T}\right)^2 \cdot \Delta c^2} \quad (50)$$

Calculations for the entropy change are presented in Equations (51) and (52), respectively.

$$\Delta S_{VH}^0 = R \cdot \left(a - \frac{c}{T^2}\right) \quad (51)$$

$$\Delta\Delta S_{VH}^0 = \sqrt{R^2 \cdot \Delta a^2 + \left(-\frac{R}{T^2}\right)^2 \cdot \Delta c^2} \quad (52)$$

Finally, the calculation of the Gibbs free energy change and the corresponding error is described in Equation (53) and Equation (54).

$$\Delta G_{VH}^0 = -R \cdot \left(a \cdot T + b + \frac{c}{T} \right) \quad (53)$$

$$\Delta \Delta G_{VH}^0 = \sqrt{(-R \cdot T)^2 \cdot \Delta a^2 + (-R)^2 \cdot \Delta b^2 + \left(-\frac{R}{T}\right)^2 \cdot \Delta c^2} \quad (54)$$

In Figure 55, the resulting curves for the enthalpy change, entropy change, Gibbs free energy change and the heat capacity are shown for the case that one ATP binds to the transporter.

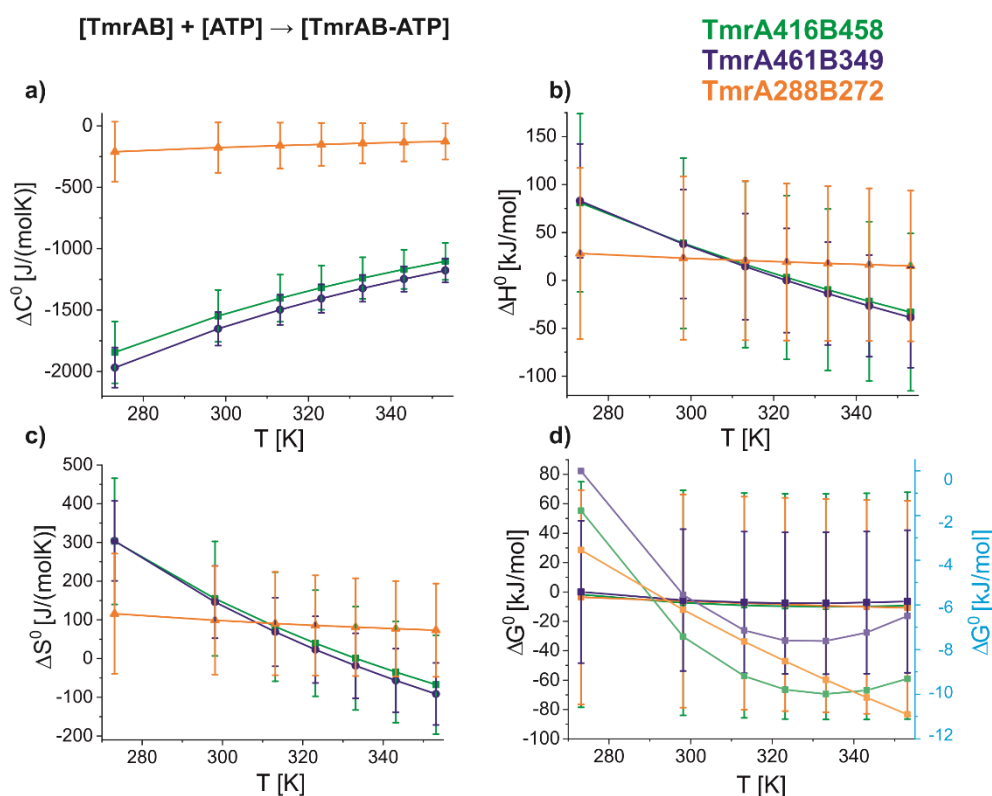


Figure 55: Heat capacity change, enthalpy change, entropy change and Gibbs free energy change for the non-linear van't Hoff plot in case of one ATP binding to the transporter. Shown are the degenerate NBS TmrA416B458 in green, the consensus NBS TmrA461B349 in blue and the periplasmic gate TmrA288B272 in orange. On the left a) shows the heat capacity change at different temperatures. On the right b) shows the enthalpy change at different temperatures, in the lower line c) shows the entropy change at different temperatures and d) shows the Gibbs free energy change; for a better readability the behaviour of the curves without errors is shown in lighter colour and the corresponding y-axis is on the right side of the plot (cyan).

In Figure 56, the resulting curves are shown for the case that two ATP bind to the transporter. Since no perfect non-linear fit was possible as visible in Figure 54, the errors

of the different fitting parameters are rather large. In the case of the enthalpy change, entropy change and heat capacity change the resulting curves with the corresponding error still look reasonable. For the Gibbs free energy change, where all errors sum up, the errors are very large and therefore the results have to be considered critically.

In both models, the behaviour of the curves are the same, only the intensity is changing, therefore both models are described together. What can be deduced from the analysis is that the Gibbs free energy change is decreasing with increasing temperature as seen for the linear van't Hoff fit up to 50 °C. At temperatures above 50 °C, the periplasmic gate TmrA288B272 is continuing to show a linear behaviour. For both NBS, however, at higher temperatures, the Gibbs free energy change starts to increase, which fits to the observations in Figure 54, where K_{eq} is getting smaller at higher temperatures.

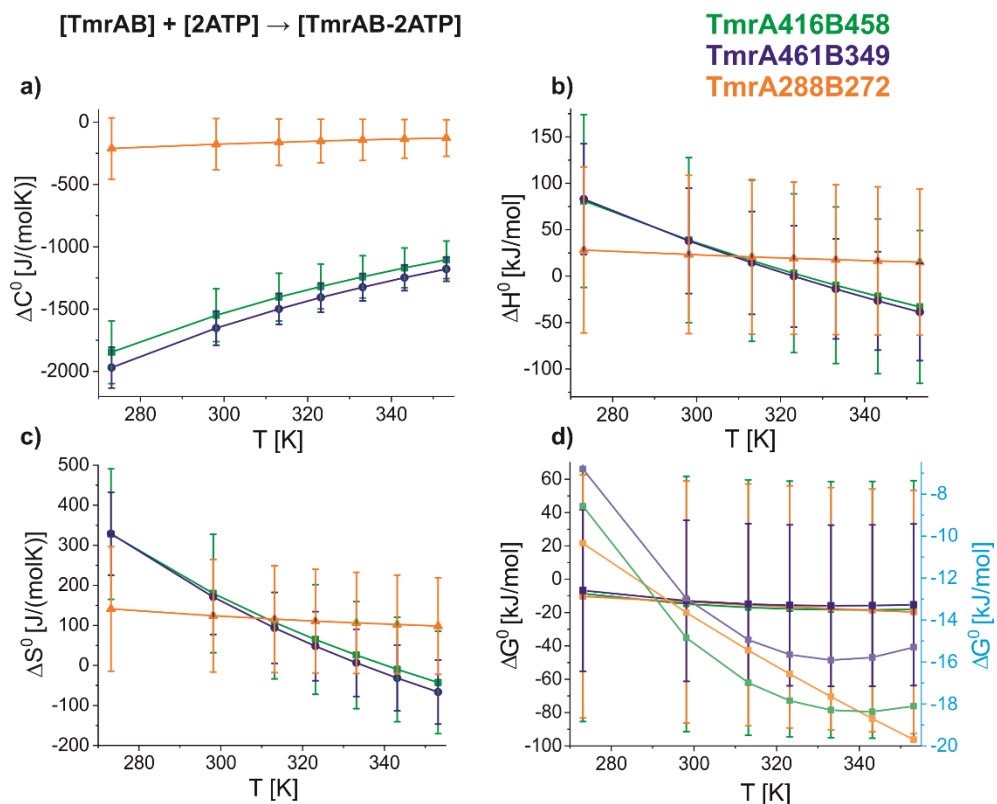


Figure 56: Heat capacity change, enthalpy change, entropy change and Gibbs free energy change for the non-linear van't Hoff plot in case of two ATP binding to the transporter. Shown are the degenerate NBS TmrA416B458 in green, the consensus NBS TmrA461B349 in blue and the periplasmic gate TmrA288B272 in orange. On the left a) shows the heat capacity change at different temperatures. On the right b) shows the enthalpy change at different temperatures, in the lower line c) shows the entropy change at different temperatures and d) shows the Gibbs free energy change; for a better readability the behaviour of the curves without errors is shown in lighter colour and the corresponding y-axis is on the right side of the plot (cyan).

In Table 30 the resulting values are presented for the heat capacity change at the temperatures between 0 and 80 °C.

Table 30: The heat capacity change (ΔC_{VH}^0) at different temperatures from the non-linear van't Hoff plot. Shown are the values for both NBSs and the periplasmic gate with corresponding errors and for both models, with either one or two bound ATP.

	ΔC_{VH}^0	0 °C	25 °C	40 °C	50 °C	60 °C	70 °C	80 °C
TmrA416 B458 (1 ATP)	-1800 ± 300 $\frac{J}{molK}$	-1500 ± 200 $\frac{J}{molK}$	-1400 ± 200 $\frac{J}{molK}$	-1300 ± 200 $\frac{J}{molK}$	-1200 ± 200 $\frac{J}{molK}$	-1200 ± 200 $\frac{J}{molK}$	-1100 ± 200 $\frac{J}{molK}$	
TmrA416 B458 (2 ATP)	-1800 ± 300 $\frac{J}{molK}$	-1500 ± 200 $\frac{J}{molK}$	-1400 ± 200 $\frac{J}{molK}$	-1300 ± 200 $\frac{J}{molK}$	-1200 ± 200 $\frac{J}{molK}$	-1200 ± 200 $\frac{J}{molK}$	-1100 ± 200 $\frac{J}{molK}$	
TmrA461 B349 (1 ATP)	-2000 ± 200 $\frac{J}{molK}$	-1700 ± 200 $\frac{J}{molK}$	-1500 ± 200 $\frac{J}{molK}$	-1400 ± 100 $\frac{J}{molK}$	-1300 ± 100 $\frac{J}{molK}$	-1200 ± 100 $\frac{J}{molK}$	-1200 ± 100 $\frac{J}{molK}$	
TmrA461 B349 (2 ATP)	-2000 ± 200 $\frac{J}{molK}$	-1700 ± 200 $\frac{J}{molK}$	-1500 ± 200 $\frac{J}{molK}$	-1400 ± 100 $\frac{J}{molK}$	-1300 ± 100 $\frac{J}{molK}$	-1200 ± 100 $\frac{J}{molK}$	-1200 ± 100 $\frac{J}{molK}$	
TmrA288 B272 (1 ATP)	-200 ± 300 $\frac{J}{molK}$	-180 ± 200 $\frac{J}{molK}$	-160 ± 200 $\frac{J}{molK}$	-150 ± 200 $\frac{J}{molK}$	-140 ± 200 $\frac{J}{molK}$	-130 ± 200 $\frac{J}{molK}$	-130 ± 200 $\frac{J}{molK}$	
TmrA288 B272 (2 ATP)	-200 ± 300 $\frac{J}{molK}$	-180 ± 200 $\frac{J}{molK}$	-160 ± 200 $\frac{J}{molK}$	-150 ± 200 $\frac{J}{molK}$	-140 ± 200 $\frac{J}{molK}$	-130 ± 200 $\frac{J}{molK}$	-130 ± 200 $\frac{J}{molK}$	

In Table 31 the resulting values are presented for the enthalpy change at the temperatures between 0 and 80 °C.

Table 31: The enthalpy change (ΔH_{VH}^0) at different temperatures from the non-linear van't Hoff plot. Shown are the values for both NBSs and the periplasmic gate with corresponding errors and for both models, with either one or two bound ATP.

	ΔH_{VH}^0	0 °C	25 °C	40 °C	50 °C	60 °C	70 °C	80 °C
TmrA416 B458 (1 ATP)	80 $\pm 100 \frac{\text{kJ}}{\text{mol}}$	40 $\pm 20 \frac{\text{kJ}}{\text{mol}}$	20 $\pm 90 \frac{\text{kJ}}{\text{mol}}$	3 $\pm 90 \frac{\text{kJ}}{\text{mol}}$	-10 $\pm 90 \frac{\text{kJ}}{\text{mol}}$	-20 $\pm 90 \frac{\text{kJ}}{\text{mol}}$	-30 $\pm 90 \frac{\text{kJ}}{\text{mol}}$	
TmrA416 B458 (2 ATP)	80 $\pm 100 \frac{\text{kJ}}{\text{mol}}$	40 $\pm 20 \frac{\text{kJ}}{\text{mol}}$	20 $\pm 90 \frac{\text{kJ}}{\text{mol}}$	3 $\pm 90 \frac{\text{kJ}}{\text{mol}}$	-10 $\pm 90 \frac{\text{kJ}}{\text{mol}}$	-20 $\pm 90 \frac{\text{kJ}}{\text{mol}}$	-30 $\pm 90 \frac{\text{kJ}}{\text{mol}}$	
TmrA461 B349 (1 ATP)	80 $\pm 60 \frac{\text{kJ}}{\text{mol}}$	40 $\pm 60 \frac{\text{kJ}}{\text{mol}}$	10 $\pm 60 \frac{\text{kJ}}{\text{mol}}$	-0.15 $\pm 60 \frac{\text{kJ}}{\text{mol}}$	-14 $\pm 60 \frac{\text{kJ}}{\text{mol}}$	-30 $\pm 60 \frac{\text{kJ}}{\text{mol}}$	-40 $\pm 60 \frac{\text{kJ}}{\text{mol}}$	
TmrA461 B349 (2 ATP)	80 $\pm 60 \frac{\text{kJ}}{\text{mol}}$	40 $\pm 60 \frac{\text{kJ}}{\text{mol}}$	10 $\pm 60 \frac{\text{kJ}}{\text{mol}}$	-0.15 $\pm 60 \frac{\text{kJ}}{\text{mol}}$	-14 $\pm 60 \frac{\text{kJ}}{\text{mol}}$	-30 $\pm 60 \frac{\text{kJ}}{\text{mol}}$	-40 $\pm 60 \frac{\text{kJ}}{\text{mol}}$	
TmrA288 B272 (1 ATP)	30 $\pm 90 \frac{\text{kJ}}{\text{mol}}$	20 $\pm 90 \frac{\text{kJ}}{\text{mol}}$	20 $\pm 90 \frac{\text{kJ}}{\text{mol}}$	19 $\pm 80 \frac{\text{kJ}}{\text{mol}}$	18 $\pm 80 \frac{\text{kJ}}{\text{mol}}$	16 $\pm 80 \frac{\text{kJ}}{\text{mol}}$	15 $\pm 80 \frac{\text{kJ}}{\text{mol}}$	
TmrA288 B272 (2 ATP)	30 $\pm 90 \frac{\text{kJ}}{\text{mol}}$	20 $\pm 90 \frac{\text{kJ}}{\text{mol}}$	20 $\pm 90 \frac{\text{kJ}}{\text{mol}}$	19 $\pm 80 \frac{\text{kJ}}{\text{mol}}$	18 $\pm 80 \frac{\text{kJ}}{\text{mol}}$	16 $\pm 80 \frac{\text{kJ}}{\text{mol}}$	15 $\pm 80 \frac{\text{kJ}}{\text{mol}}$	

In Table 32 the resulting values are presented for the entropy change at the temperatures between 0 and 80 °C.

Table 32: The entropy change (ΔS_{VH}^0) at different temperatures from the non-linear van't Hoff plot. Shown are the values for both NBSs and the periplasmic gate with corresponding errors and for both models, with either one or two bound ATP.

	ΔS_{VH}^0	0 °C	25 °C	40 °C	50 °C	60 °C	70 °C	80 °C
TmrA416 B458 (1 ATP)	300 $\pm 200 \frac{\text{J}}{\text{molK}}$	150 $\pm 200 \frac{\text{J}}{\text{molK}}$	80 $\pm 200 \frac{\text{J}}{\text{molK}}$	40 $\pm 200 \frac{\text{J}}{\text{molK}}$	1 $\pm 200 \frac{\text{J}}{\text{molK}}$	-30 $\pm 200 \frac{\text{J}}{\text{molK}}$	-70 $\pm 200 \frac{\text{J}}{\text{molK}}$	
TmrA416 B458 (2 ATP)	300 $\pm 200 \frac{\text{J}}{\text{molK}}$	180 $\pm 200 \frac{\text{J}}{\text{molK}}$	110 $\pm 200 \frac{\text{J}}{\text{molK}}$	60 $\pm 200 \frac{\text{J}}{\text{molK}}$	30 $\pm 200 \frac{\text{J}}{\text{molK}}$	-10 $\pm 200 \frac{\text{J}}{\text{molK}}$	-40 $\pm 200 \frac{\text{J}}{\text{molK}}$	
TmrA461 B349 (1 ATP)	300 $\pm 100 \frac{\text{J}}{\text{molK}}$	150 $\pm 100 \frac{\text{J}}{\text{molK}}$	70 $\pm 90 \frac{\text{J}}{\text{molK}}$	20 $\pm 90 \frac{\text{J}}{\text{molK}}$	-19 $\pm 90 \frac{\text{J}}{\text{molK}}$	-60 $\pm 80 \frac{\text{J}}{\text{molK}}$	-90 $\pm 80 \frac{\text{J}}{\text{molK}}$	
TmrA461 B349 (2 ATP)	330 $\pm 100 \frac{\text{J}}{\text{molK}}$	170 $\pm 100 \frac{\text{J}}{\text{molK}}$	100 $\pm 90 \frac{\text{J}}{\text{molK}}$	50 $\pm 90 \frac{\text{J}}{\text{molK}}$	10 $\pm 90 \frac{\text{J}}{\text{molK}}$	-30 $\pm 80 \frac{\text{J}}{\text{molK}}$	-70 $\pm 80 \frac{\text{J}}{\text{molK}}$	
TmrA288 B272 (1 ATP)	120 $\pm 160 \frac{\text{J}}{\text{molK}}$	100 $\pm 140 \frac{\text{J}}{\text{molK}}$	90 $\pm 140 \frac{\text{J}}{\text{molK}}$	90 $\pm 130 \frac{\text{J}}{\text{molK}}$	80 $\pm 130 \frac{\text{J}}{\text{molK}}$	80 $\pm 130 \frac{\text{J}}{\text{molK}}$	70 $\pm 120 \frac{\text{J}}{\text{molK}}$	
TmrA288 B272 (2 ATP)	140 $\pm 160 \frac{\text{J}}{\text{molK}}$	120 $\pm 140 \frac{\text{J}}{\text{molK}}$	120 $\pm 140 \frac{\text{J}}{\text{molK}}$	110 $\pm 130 \frac{\text{J}}{\text{molK}}$	110 $\pm 130 \frac{\text{J}}{\text{molK}}$	100 $\pm 130 \frac{\text{J}}{\text{molK}}$	100 $\pm 120 \frac{\text{J}}{\text{molK}}$	

In Table 33 the different values are presented for the Gibbs free energy change at the temperatures between 0 and 80 °C

Table 33: The Gibbs free energy change (ΔG_{VH}^0) at different temperatures from the non-linear van't Hoff plot. Shown are the values for both NBSs and the periplasmic gate with corresponding errors and for both models, with either one or two bound ATP.

	ΔG_{VH}^0	0 °C	25 °C	40 °C	50 °C	60 °C	70 °C	80 °C
TmrA416 B458 (1 ATP)	-2 $\pm 80 \frac{\text{kJ}}{\text{mol}}$	-7 $\pm 80 \frac{\text{kJ}}{\text{mol}}$	-9 $\pm 80 \frac{\text{kJ}}{\text{mol}}$	-10 $\pm 80 \frac{\text{kJ}}{\text{mol}}$	-10 $\pm 80 \frac{\text{kJ}}{\text{mol}}$	-10 $\pm 80 \frac{\text{kJ}}{\text{mol}}$	-9 $\pm 80 \frac{\text{kJ}}{\text{mol}}$	-9 $\pm 80 \frac{\text{kJ}}{\text{mol}}$
TmrA416 B458 (2 ATP)	-9 $\pm 80 \frac{\text{kJ}}{\text{mol}}$	-15 $\pm 80 \frac{\text{kJ}}{\text{mol}}$	-17 $\pm 80 \frac{\text{kJ}}{\text{mol}}$	-18 $\pm 80 \frac{\text{kJ}}{\text{mol}}$				
TmrA461 B349 (1 ATP)	-0.010 $\pm 50 \frac{\text{kJ}}{\text{mol}}$	-6 $\pm 50 \frac{\text{kJ}}{\text{mol}}$	-7 $\pm 50 \frac{\text{kJ}}{\text{mol}}$	-8 $\pm 50 \frac{\text{kJ}}{\text{mol}}$	-8 $\pm 50 \frac{\text{kJ}}{\text{mol}}$	-7 $\pm 50 \frac{\text{kJ}}{\text{mol}}$	-6 $\pm 50 \frac{\text{kJ}}{\text{mol}}$	-6 $\pm 50 \frac{\text{kJ}}{\text{mol}}$
TmrA461 B349 (2 ATP)	-7 $\pm 50 \frac{\text{kJ}}{\text{mol}}$	-13 $\pm 50 \frac{\text{kJ}}{\text{mol}}$	-15 $\pm 50 \frac{\text{kJ}}{\text{mol}}$	-16 $\pm 50 \frac{\text{kJ}}{\text{mol}}$	-16 $\pm 50 \frac{\text{kJ}}{\text{mol}}$	-16 $\pm 50 \frac{\text{kJ}}{\text{mol}}$	-15 $\pm 50 \frac{\text{kJ}}{\text{mol}}$	-15 $\pm 50 \frac{\text{kJ}}{\text{mol}}$
TmrA288 B272 (1 ATP)	-4 $\pm 80 \frac{\text{kJ}}{\text{mol}}$	-6 $\pm 80 \frac{\text{kJ}}{\text{mol}}$	-8 $\pm 80 \frac{\text{kJ}}{\text{mol}}$	-9 $\pm 80 \frac{\text{kJ}}{\text{mol}}$	-9 $\pm 80 \frac{\text{kJ}}{\text{mol}}$	-10 $\pm 80 \frac{\text{kJ}}{\text{mol}}$	-11 $\pm 80 \frac{\text{kJ}}{\text{mol}}$	-11 $\pm 80 \frac{\text{kJ}}{\text{mol}}$
TmrA288 B272 (2 ATP)	-10 $\pm 80 \frac{\text{kJ}}{\text{mol}}$	-14 $\pm 80 \frac{\text{kJ}}{\text{mol}}$	-15 $\pm 80 \frac{\text{kJ}}{\text{mol}}$	-17 $\pm 80 \frac{\text{kJ}}{\text{mol}}$	-18 $\pm 80 \frac{\text{kJ}}{\text{mol}}$	-19 $\pm 80 \frac{\text{kJ}}{\text{mol}}$	-20 $\pm 80 \frac{\text{kJ}}{\text{mol}}$	-20 $\pm 80 \frac{\text{kJ}}{\text{mol}}$

With this non-linear fitting, the temperature-dependence of the enthalpy change and entropy change can be taken into account. In the case of the periplasmic gate, TmrA288B272 the enthalpy change, entropy change and heat capacity change consistently show a linear behaviour, which means the values are not temperature-dependent for this position. In the case of both NBSs, the enthalpy change and entropy change are decreasing with higher temperatures and also changes in the heat capacity change can be observed.

The most important difference between the periplasmic gate and the two NBSs is that in the NBSs ATP binds, while the periplasmic gate is far away from the nucleotide binding pockets. The heat capacity change of ATP is $-3 \text{ kJ/K}^{-1}\text{mol}^{-1}$, which was published previously by Kodama in 1981.¹²³ With the heat capacity change, the enthalpy can be calculated (Equation (55)).

$$\Delta H^0 = \Delta C_p \cdot T \quad (55)$$

In Figure 57 the temperature-dependent enthalpy change plots for the periplasmic gate and both NBSs of TmrAB are shown and compared with the temperature-dependent enthalpy change of ATP. As it can be seen in Figure 57, the changes in the enthalpy change of both NBS are in between the linear enthalpy change of the periplasmic gate TmrA288B272 and the temperature-dependent enthalpy change of ATP.

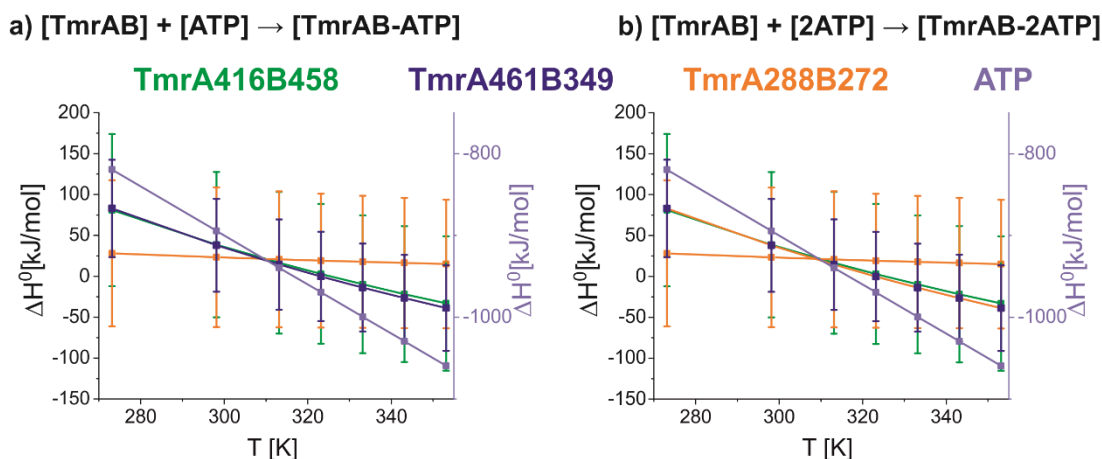


Figure 57: Temperature-dependent enthalpy of the periplasmic gate and both NBS of TmrAB compared to ATP. Shown are the degenerate NBS TmrA416B458 in green, the consensus NBS TmrA461B349 in blue and the periplasmic gate TmrA288B272 in orange. The graph for ATP is shown in light blue with the corresponding y-axis on the right. On the left a) the model with one bound ATP is shown and on the right b) shows the enthalpy with two bound ATP.

This shows, that it is possible that the non-linear behaviour of both NBSs is mainly coming from the influence of ATP, which is located in the NBSs and might be too far away from the periplasmic gate to influence its behaviour. For the periplasmic gate also the non-linear fit reveals constant values for the enthalpy change and entropy change, which are comparable to the values determined with the linear van't Hoff fit. Since the non-linear behaviour is mainly found at temperatures higher than 50 °C, the linear fit up to this temperature might be more dependent on the NBS and is not influenced by ATP as much as at higher temperatures.

Further experiments are necessary to reveal if the behaviour at higher temperatures is coming from different reaction rates or non-linear behaviour. In first future experiments, the K_{eq} could be observed in a time-dependent manner. So far, the samples were incubated for 5 minutes at different temperatures. By observing K_{eq} at different incubation times, it could be observed if the times at which the equilibrium is reached deviates at higher temperatures. Furthermore, the samples were incubated in Eppendorf tubes and afterwards transferred into the PELDOR sample tubes. By incubation directly in the sample tube at higher temperatures, it could be observed if the results differ with a shorter time before freezing. The latter was tested at 25 and 50 °C, but in these cases, no differences could be observed.

4.2.3 Discussion of the conformational equilibrium induced by ATP binding

The focus of this chapter is the equilibrium between the apo, inward-facing and the ATP-bound, outward-facing states as illustrated in Figure 58. The equilibrium of interest is highlighted with a yellow box. For this equilibrium, the concentration of ATP was changed to observe the response of both NBS and the coupling to the TMDs. Furthermore, the conformational thermodynamics have been investigated, whereby information about the Gibbs free energy change, enthalpy change and entropy change were investigated.

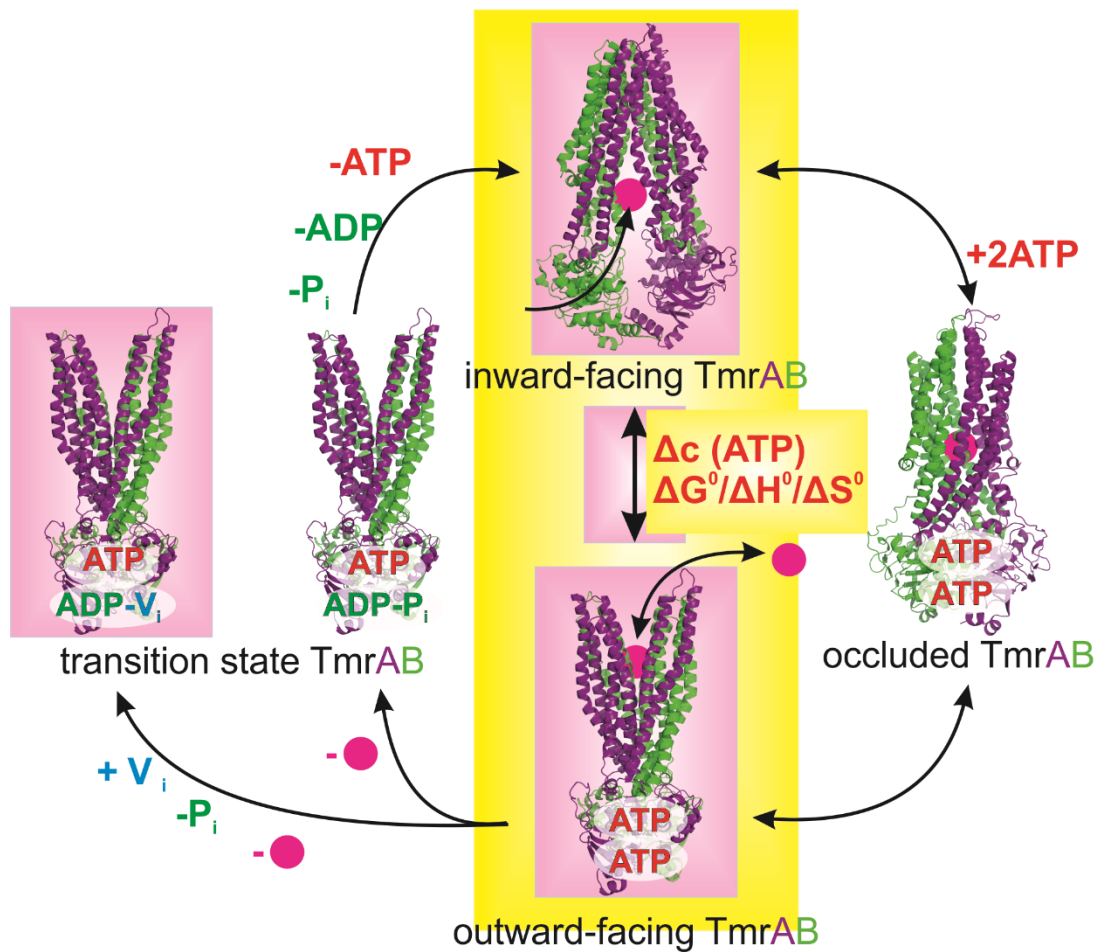


Figure 58: Alternating access mechanism of TmrAB, with the conformational equilibrium induced by ATP binding highlighted by a yellow box. Upon ATP binding, the transporter is populating an equilibrium between the inward-facing conformation (top) and the outward-facing conformation (bottom). The equilibrium with bound ATP is indicated by an arrow and the two states are highlighted with a yellow box. To investigate the equilibrium, the concentration of ATP ($\Delta c(ATP)$) was varied and the response of both NBS and the coupling to the TMDs was monitored. Furthermore, the conformational thermodynamics have been investigated (ΔG^0 , ΔH^0 and ΔS^0). During these experiments, no substrate which is indicated in the proposed cycle with pink dots was present.

The titration experiments with different ATP concentrations reveal that the closed conformation is more favoured at the degenerate NBS, which was not observed for BmrCD¹⁰⁹ or TM287/288¹¹⁰. Overall, ABC exporters with asymmetric NBS show significant differences in the apo-state and in the response of their NBSs in the presence of different nucleotides, which might be important due to their different function and regulation. Modulation of the ATP binding equilibrium in an allosteric manner, as shown here for TmrAB, presents a novel feature of an ABC transporter.

Each NBD monomer consists of a RecA-like subdomain, which is connected to an α -helical subdomain by a flexible bilobal hinge.¹¹⁷ The A-loop, Q-loop, H-loop, Walker A and Walker B motifs from the RecA-like domain of one NBD interact with the ABC signature motif and the D-loop of the α -helical subdomain of the other NBD, whereupon two ATP binding sites are formed. Due to ATP binding, a rotation of the α -helical subdomain towards the RecA like subdomain gets induced. Previous studies^{124–126} already proposed that the two NBSs may open or close independently, but how this is coupled to the conformation of the TMDs remained unknown. This question was tackled in this chapter by observing both NBSs and the periplasmic gate in the presence of ATP. While the closed state is more favoured at the degenerate NBS, the consensus NBS shows that the open and closed state has a comparable energetic state.

With the E-to-Q-mutation, the asymmetric response was further increased by a change of the fractional closure from $\theta = 0.37$ to $\theta = 0.81$ at the degenerate NBS and only from $\theta = 0.21$ to $\theta = 0.45$ at the consensus NBS (Gaussian fitting for these two measurements are shown in Supp. Figure 3). The increase in fractional closure for the E-to-Q-mutation happens most likely due to an increase in ATP affinity and has also been observed for TM287/288¹¹⁰.

Furthermore, the closure either one of the NBSs seems to be sufficient to open the periplasmic gate, leading to a more efficient change to the outward-facing conformation. Already at low ATP concentrations, where a low fractional closure of both NBSs was observed, the combined effect of these latter opened the periplasmic gate in a much larger fraction. Since already in the apo-state a small opening can be observed at the periplasmic gate, this intrinsic opening might also support further opening.

By observing the equilibrium at a constant ATP concentration at different temperatures, the conformational thermodynamics could be investigated. Based on previous studies on P-gp, where the transporter has a lower substrate affinity in the vanadate-trapped transition state, it is assumed that ATP hydrolysis is the driving force of substrate release.¹²⁰ It is

furthermore assumed that the energy from ATP hydrolysis is stored and used for substrate translocation and conformational changes occurring thereby.²⁷ These observations are also in agreement with observations for the transporter associated with antigen processing (TAP), which becomes bidirectional and less transport efficient upon mutations in the NBD dimer.¹¹⁸ In the ABC exporter LptB₂FG, which is the energy source for LPS transport, the substrate is binding in the outward-facing conformation, at the post-transition state of ATP-hydrolysis.^{127,128} A similar mechanism is suggested for PglK for the transport of lipid-linked oligosaccharide from the inner to the outer leaflet.⁵⁴

The results for TmrAB show that ATP binding alone drives the conformational change from the inward- to outward-facing conformation. No ATP hydrolysis took place and also no substrate was influencing the transporter. Furthermore, the linear van't Hoff fits between 0 and 50 °C show that the conformational switching is entropy-driven. Because of the decreasing $\ln K_{eq}$ at higher temperatures, a non-linear van't Hoff data analysis was also performed. A possible reason for this behaviour at higher temperatures could be the temperature dependence of the enthalpy change of ATP which might be influencing both NBSs. This is supported by the fact that the thermodynamic properties of the periplasmic gate are not changing with higher temperatures. Another possible reason for the non-linear behaviour at higher temperatures could be that the reaction rates are faster than freezing at higher temperatures, which would lead to a shift to the lower-energy state (apo-state) at a higher temperature. What is actually happening at higher temperatures needs further investigation. Within the linear range, for both NBSs an entropy gain of approximately $170 \text{ JK}^{-1}\text{mol}^{-1}$, if one bound ATP is assumed, or $190 \text{ JK}^{-1}\text{mol}^{-1}$, with two bound ATP, can be determined. For both models, the energetic barrier or the enthalpy change is approximately $44/45 \text{ kJmol}^{-1}$. Out of these two values, a negative Gibbs free energy change can be calculated, which is larger for the model with two bound ATP, suggesting a higher probability of two bound ATP. For the periplasmic gate an entropy gain of approximately $100 \text{ JK}^{-1}\text{mol}^{-1}$, if one bound ATP is assumed, or $130 \text{ JK}^{-1}\text{mol}^{-1}$, with two bound ATP, can be determined. These values are both lower compared to the entropy gain of both NBSs, also the enthalpy change or the energy barrier is lower with approximately 24 kJmol^{-1} . For the periplasmic gate also a negative Gibbs free energy change was calculated, which is larger for the model with two bound ATP, suggesting a higher probability of two bound ATP.

In summary, these observations are in agreement with previous findings, where lower concentrations of ATP are sufficient for periplasmic gate opening, while for both NBS the

equivalent closing needs higher ATP concentrations. Since the energy barrier is lower in the periplasmic gate, this might lead to an earlier switching to the outward-facing state and might also be a reason for the small open fraction in the apo-state.

PELDOR spectroscopy is able to look into the conformational thermodynamics of larger membrane protein complex and could be used for similar proteins. Already published data clearly shows, that not every exporter is behaving in the same way. It is, therefore, necessary to investigate every transporter on its own to gain a better understanding of the mechanistic differences.

4.3 The role of substrate in the transport mechanism of TmrAB

Since the purpose of an ABC transporter is to transport substrates through membranes, it is also important to see how the substrate is influencing the transporter during conformational changes. For this purpose, the transporter was inhibited with a high amount of substrate and the changes in the conformations were observed with PELDOR spectroscopy.

4.3.1 Trans-inhibition of TmrAB

Transport of substrate is the major function of an ABC transporter, but there is a limit of substrate concentration which can be transported. If the concentration of the substrate is too high, the transporter becomes inhibited and cannot transport substrate anymore. This trans-inhibition has been shown biochemically for the hydrolysis and/or transport of TAP¹¹⁸ and TAPL¹²⁹. For TmrAB, trans-inhibition has been shown with an ATPase assay by Susanne Hank.³

In this thesis, the major goal was to understand the structural rearrangements during trans-inhibition, which is illustrated in Figure 59. Normally, the transporter undergoes a transport cycle and gets restored for a new transport cycle by ATP hydrolysis and following ADP and P_i release. In the case of trans-inhibition, the transporter is inhibited by an excess of the substrate to be transported; this has been shown biochemically. Too much substrate is filling the transport pathway from both sites and therefore blocks the substrate entrance or exit, hence no transport can take place. It is still unclear what the exact mechanism of trans-inhibition is. With PELDOR distance measurements under high substrate concentrations in the ATP bound ATP-EDTA state or under hydrolysing conditions, this question can be tackled.

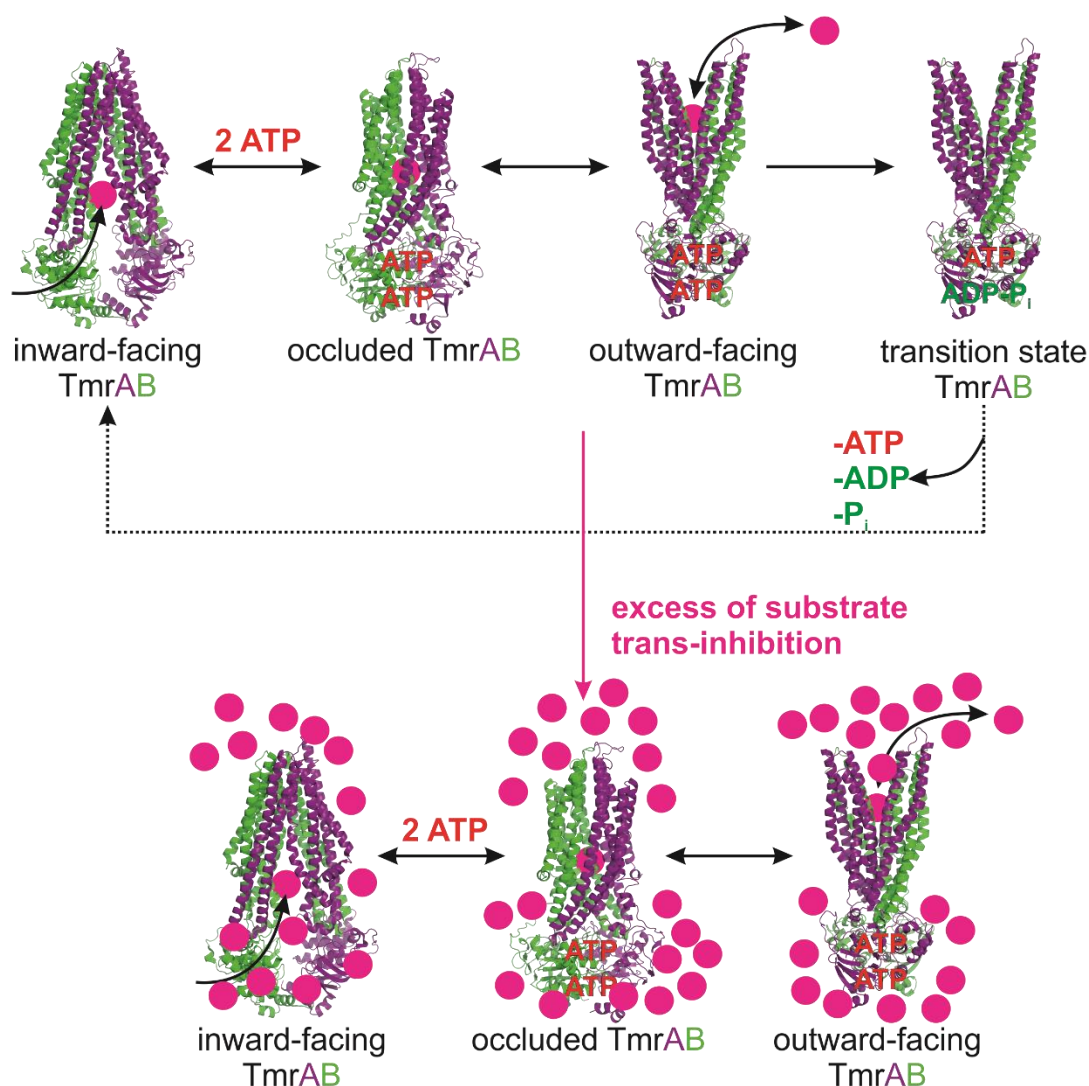


Figure 59: Illustration of the process of trans-inhibition. On top, the classical transport mechanism is shown, which has been already explained. The inward-facing structure of TmrAB (pdb code 5MKK), the substrate is indicated as a pink dot, the occluded conformation is illustrated by a homology model of TmrAB, based on the occluded structure of McjD (pdb code 4PL0) and the outward-facing structure is shown with a homology model of TmrAB based on the outward-facing structure of Sav1866 with bound AMP-PNP (pdb code 2ONJ). The lower part of the Figure illustrates the process of trans-inhibition, where the transport pathway is filled with substrate. It has been shown biochemically that no transport cycle is taking place, but it is unclear what the major conformation induced by trans-inhibition is.

To evaluate the overall response of TmrAB to trans-inhibition, the periplasmic gate, the cytosolic gate and both NBSs were investigated in the ATP-EDTA state and under hydrolysing conditions. In the apo-state or with ADP-V_i-Mg²⁺, no differences after addition of an excess of the peptide K5F can be observed, which is shown for the periplasmic gate in Supp. Figure 4. In Figure 60 (light pink) it is also shown that no difference is visible if 50 μM K5F is added to 50 μM TmrA288B272 in the ATP-EDTA state (1:1 ratio).

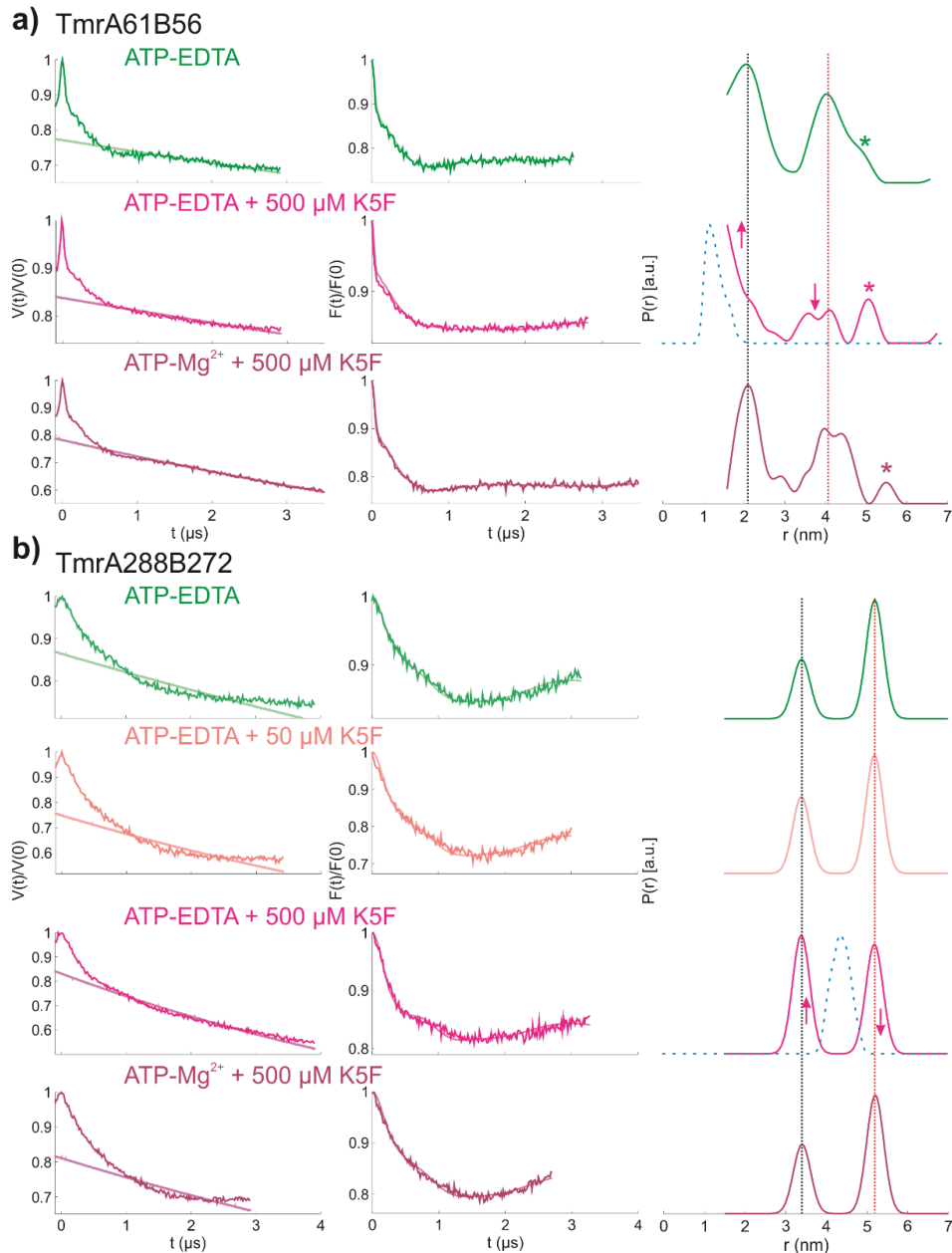


Figure 60: Trans-inhibition by K5F at the periplasmic gate TmrA61B56 and TmrA288B272. In green, ATP-EDTA is shown without substrate, in light pink peptide is added in a 1:1 ratio, in pink trans-inhibition conditions with 500 μM peptide is shown and in dark pink hydrolysing conditions with 500 μM peptide is shown. Simulations for the occluded conformation are indicated in blue dotted lines. Original data $V(t)/V(0)$ are displayed on the left, background corrected data $F(t)/F(0)$ are displayed in the middle and the distance distributions $P(r)$ are shown on the right. TmrA61B56 a) is fitted by Tikhonov regularization and shows a higher fraction of the closed conformation due to trans-inhibition. Under hydrolysing conditions, these changes are smaller. The asterisks indicate peaks with uncertainty in the shape and width, which occurs due to a small length of the detected dipolar evolution time. For TmrA288B272 b) the data were fitted with a Two-Gaussian fitting model using distances of $r = 3.4 \pm 0.3$ nm and $r = 5.3 \pm 0.3$ nm. Also for TmrA288B272, the inward-facing state is increasing under trans-inhibition conditions, while peptide in a 1:1 ratio cannot introduce significant changes. Under hydrolysing conditions, the effects are smaller than the ones observed with ATP-EDTA. (Data analysis performed with DeerAnalysis 2016)

If an excess of the substrate is added (500 μM K5F) which inhibits the transporter, a clear closing motion can be observed for both, the periplasmic gate mutants TmrA61B56 and TmrA288B272. Under hydrolysing conditions, the high amount of peptide cannot induce the same effect, only minor changes are observed. In Figure 60, the ATP-EDTA data with 500 μM K5F was also compared with the simulation of the occluded state from the homology model based on McjD. For TmrA61B56, the distance in the occluded state is supposed to be smaller than for McjD. Although the proposed distance is shorter than the lower limit of PELDOR, the data suggest that the measured distance is smaller than the distance observed for the apo-state. For TmrA288B272, the proposed distance for the occluded conformation is between the two distances which can be observed in the open- and closed state. In summary, for the periplasmic gate, a closing motion towards the inward-facing conformation can be observed upon trans-inhibition.

To see the overall structural rearrangement of the TMDs during trans-inhibition, also the cytosolic gate TmrA112B97 was investigated. As presented in Figure 61, the ATP-EDTA state with an excess of the substrate leads to a significant decrease of the outward-facing closed conformation and to a small increase of the inward-facing conformation. In addition, a new fraction characterized by a shorter interspin distance of $r = 3.4 \pm 0.4$ nm was observed. This new state is remarkably more closed than the outward-facing state (for a better comparison the presented ATP-EDTA PELDOR trace was shortened to the same length as the measurement with K5F and fitted accordingly). These results suggest the presence of an occluded conformation since both the periplasmic gate on top of the TMDs and the cytosolic gate at the bottom of the TMDs and at the border to the NBDs are mainly closed. Under hydrolysing conditions, the same new fraction can be observed, but with lower probability. A simulation-based on the McjD homology model suggests a larger distance for the occluded conformation.

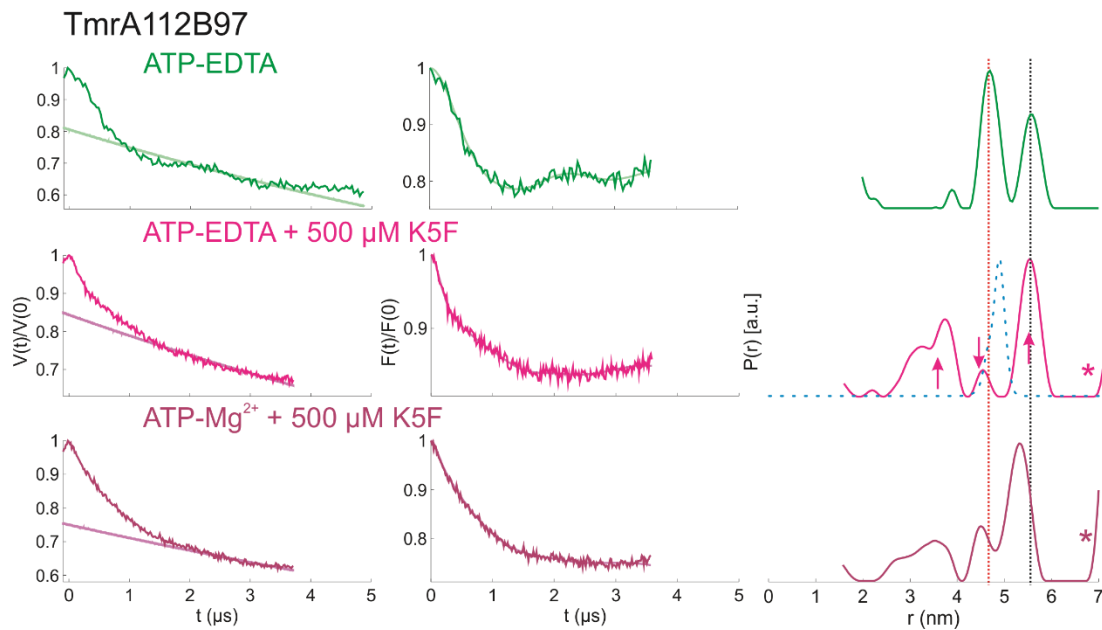


Figure 61: Trans-inhibition by K5F at the cytosolic gate TmrA112B97. In green ATP-EDTA is shown without substrate, in pink trans-inhibition conditions with 500 μM peptide are shown and in dark pink hydrolysing conditions with 500 μM peptide are shown. Simulations for the occluded conformation are indicated in blue dotted lines. Data are fitted by Tikhonov regularization and the length of the original data of ATP-EDTA was shortened to the length of the measurements with K5F for a better comparison. Original data $V(t)/V(0)$ are displayed on the left, background corrected data $F(t)/F(0)$ are displayed in the middle and the distance distributions $P(r)$ are shown on the right. Due to trans-inhibition, a new fraction with shorter distance is occurring at $r = 3.4 \pm 0.4$ nm. Since both periplasmic gate and cytosolic gate are closed, these observations suggest an occluded conformation. Under hydrolysing conditions, this fraction also appears, but smaller as observed with ATP-EDTA. The asterisks indicate peaks with uncertainty in the shape and width, which occurs due to a too-small length of the detected dipolar evolution time. (Data analysis performed with DeerAnalysis 2016)

To further reveal if trans-inhibition is resulting in an occluded conformation, both NBSs which are supposed to be closed, have been investigated. In Figure 62, it is clear that in both NBSs the inward-facing or open-state is increasing in the ATP-EDTA state with an excess of K5F. By comparison of the changes between the TMDs and NBSs, the differences in the NBSs are much smaller. Especially for the degenerate site, the closing probability θ changes only from 0.37 in the ATP-EDTA state to 0.22 in the ATP-EDTA state with substrate excess. Under hydrolysing conditions with substrate excess, the closed fraction also appears to be larger than in the ATP-EDTA state in both cases. Taking all of these results together, they show that, due to trans-inhibition, the transporter mainly adopts the occluded conformation, where the NBSs and the TMDs are closed (on both sides). Nevertheless, a small fraction also changes to the inward-facing conformation.

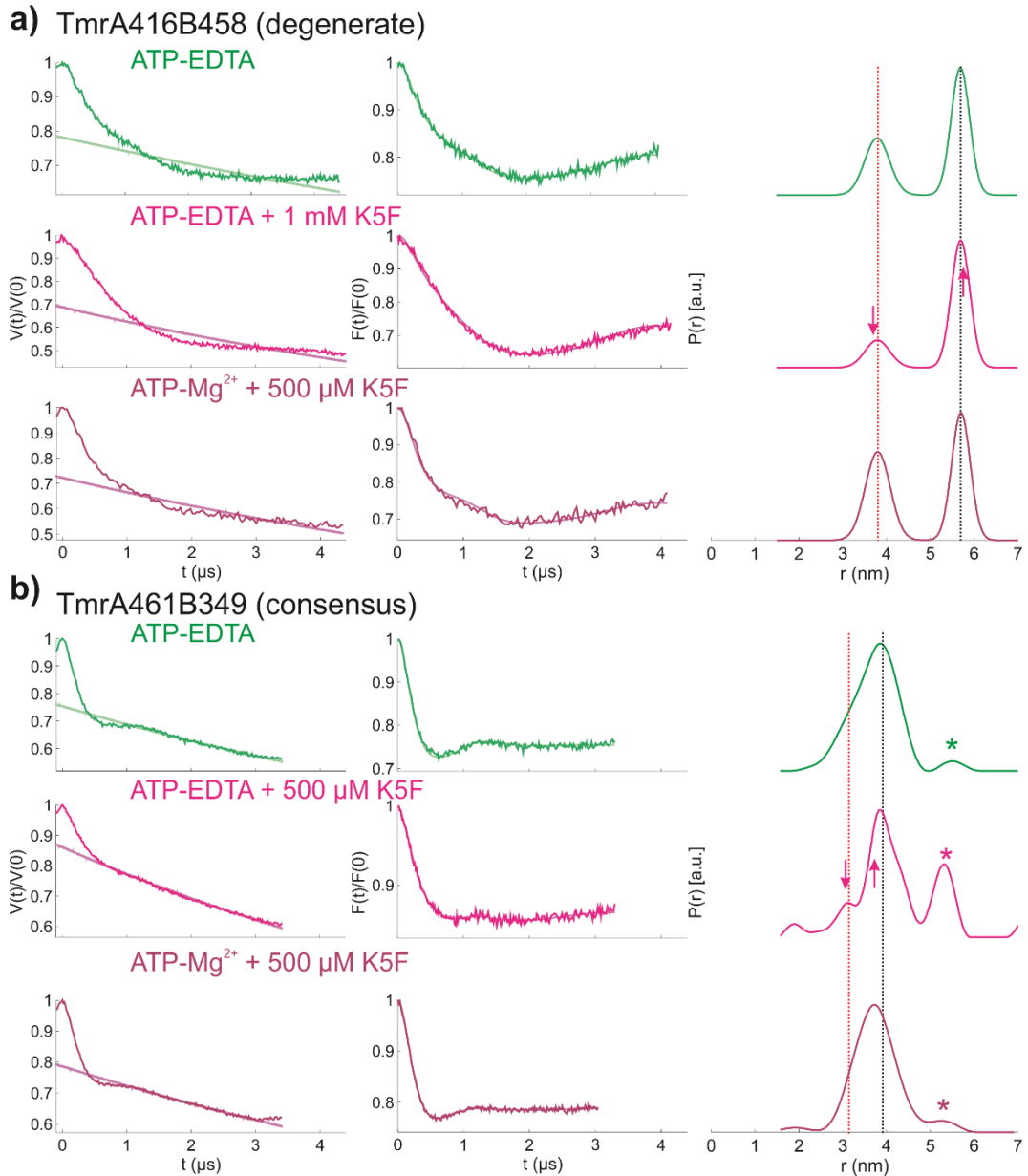


Figure 62: Trans-inhibition by K5F at both NBSs TmrA416B458 and TmrA461B349. In green ATP-EDTA is shown without substrate, in pink trans-inhibition conditions with 500 μM or 1 mM peptide are shown and in dark pink hydrolysing conditions with 500 μM peptide are shown. Original data $V(t)/V(0)$ are displayed on the left, background corrected data $F(t)/F(0)$ are displayed in the middle and the distance distributions $P(r)$ are shown on the right. For the degenerate NBS TmrA416B458, a) data were fitted with a Two-Gaussian model based on distances of $r = 3.8 \pm 0.4$ nm and $r = 5.7 \pm 0.3$ nm. The closed state is decreasing from $\theta = 0.37$ in the ATP-EDTA state to 0.22 in the presence of an excess of substrate. Under hydrolysing conditions, the closed state is increasing slightly in the presence of an excess of substrate. The consensus NBS TmrA461B349 b) is fitted with Tikhonov regularization and shows a higher fraction of the open conformation, due to trans-inhibition. Under hydrolysing conditions, these changes are smaller. The asterisks indicate peaks with uncertainty in the shape and width, which occurs due to a too-small length of the detected dipolar evolution time. In summary, for both NBSs transitions to the open conformation can be observed, but the magnitude of the differences is smaller as in the TMDs, suggesting that the main fraction of the NBS stays closed as in an occluded conformation. (Data analysis performed with DeerAnalysis 2016)

4.3.2 Discussion of the trans-inhibition of TmrAB

TAP is an active transporter, whose transport function is blocked by a high luminal peptide concentration.¹¹⁸ This process is called trans-inhibition and might protect the ER from the stress response and the unfolded protein response at high peptide concentrations inside the lumen. The work presented in this chapter revealed that mechanistically, the excess of peptide reversed the transporter into the occluded conformation. In Figure 63, the alternating access mechanism of TmrAB is shown including the new knowledge of the trans-inhibition mechanism.

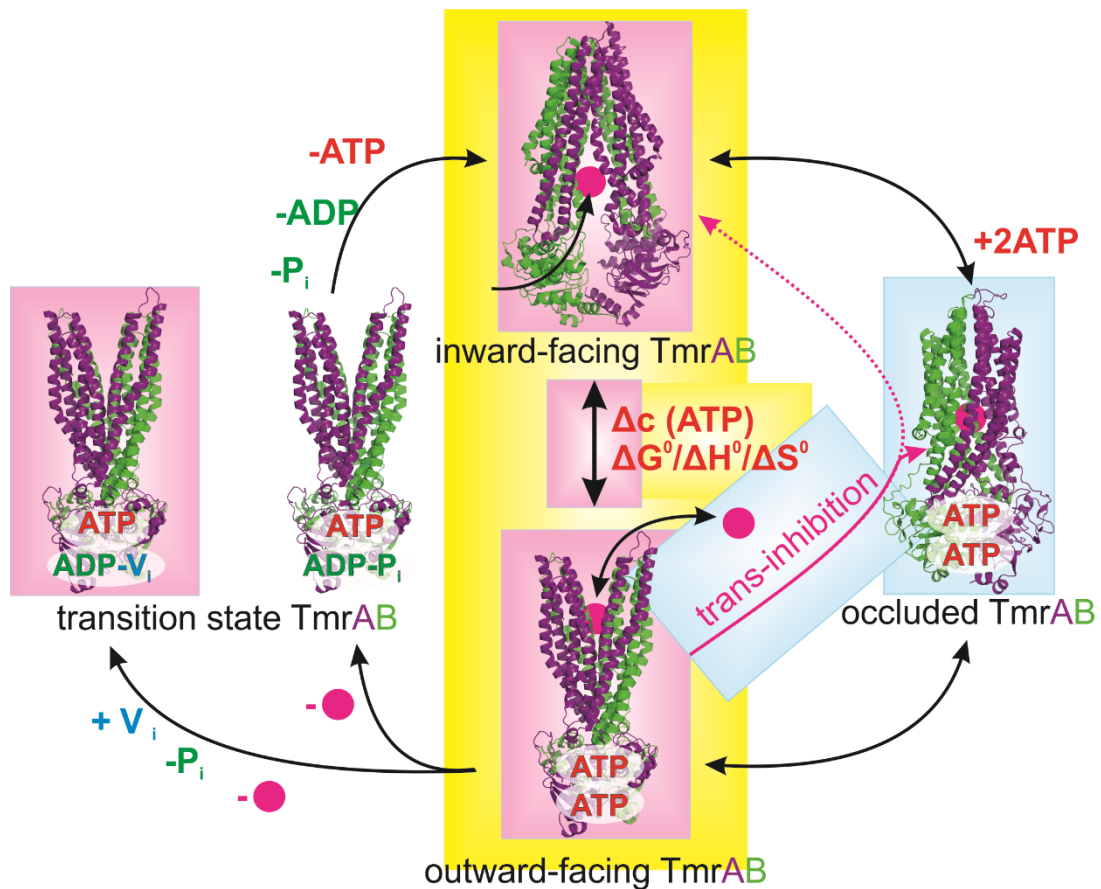


Figure 63: Alternating access mechanism of TmrAB, with highlighted trans-inhibition. Due to trans-inhibition by an excess of the substrate K5F, the transporter gets inhibited and moves in the cycle from the ATP-bound outward-facing state mainly back to the occluded conformation and partially to the inward-facing conformation. This pathway is indicated by pink arrows. The positions in the cycle relevant for the trans-inhibition pathway are highlighted with light blue boxes.

Trans-inhibition includes the interaction of the peptide with a second low-affinity binding site in the outward-facing conformation. If the determined interspin distances in the occluded conformation are compared to the simulated distances based on the homology model, a smaller cavity in TmrAB is suggested compared to the exporter McjD⁹⁸. This

difference could be due to the fact that the crystal structure of McjD in the occluded conformation is without substrate. Another reason could be that the peptide for the studies with TmrAB is smaller than the peptide used for McjD (9 vs 21 amino acids).^{2,98} Since only a small fraction of the transporter is further reversed to the inward-facing conformation, the energy barrier for the occluded to inward-facing transitions is expected to be high. Although the occluded conformation was observed for McjD and PCAT, the mechanistic role in the conformational cycle remained unknown. To the best of the author's knowledge, the presented results on TmrAB are the first experimental evidence for this occluded conformation in the transport cycle of a heterodimeric ABC exporter. Furthermore, it shows the central role of this conformation in the mechanism of trans-inhibition.

4.4 Summary

The presented data of section 4.1, 4.2 and 4.3 can be summarized into a mechanistic model for transport and trans-inhibition, which is presented in Figure 64. The substrate must bind to the transporter in the apo-state, where the transport cavity is open at the cytosolic gate. It has been shown that already the closure of one of the NBSs leads to the outward-facing conformation. By ATP binding to one or both NBSs, the transporter can spontaneously switch to the occluded conformation, which is transient under transporting conditions and switches immediately to the outward-facing conformation. This has to be the case since with the addition of nucleotides or nucleotide analogues the occluded-state could not be observed. The occluded state could only be populated during trans-inhibition. Under transporting conditions, the substrate can exit from the translocation pathway in the outward-facing state. If the substrate is present in an excess, which means trans-inhibition occurs, the conformational cycle is reversed, mainly to the occluded conformation. Since this state is reversible, the data suggest that ATP hydrolysis may follow substrate translocation, which would be an irreversible step. This is further confirmed by the ATPase inhibition during trans-inhibition³ which was done by Susanne Hank. After hydrolysis at the consensus site, nucleotides might dissociate from both NBSs and the transporter is restored to the inward-facing nucleotide-free state, which was suggested for CFTR¹³⁰.

which are important for human health and diseases. By understanding the mechanism of trans-inhibition the development of new drugs to modulate this trans-inhibition effect could be developed, which is of medical interest. Also, the PELDOR techniques which was used to determine the conformational thermodynamics, might be useful to investigate other similar proteins. Furthermore, it has been shown that there are differences in similar transport systems, which suggest that although there are several similarities in the mechanism, every transporter has some specific details that have to be individually investigated.

In summary, in this thesis, the molecular mechanism for the conformational coupling between NBSs and TMDs, the conformational thermodynamics and the structural basis for trans-inhibition in TmrAB, an ortholog of the human antigen transporter complex TAP, were unravelled. It was shown that the closure of either one of the NBSs is sufficient to trigger the opening of the periplasmic gate located on the TMDs. Furthermore, this transition from inward- to outward-facing state is entropy-driven and has a negative Gibbs free energy change, showing that ATP binding alone drives the conformational change and no ATP hydrolysis or substrate binding is necessary. During trans-inhibition, the peptide interacts with the transporter in the outward-facing state and reverses the transporter to the occluded conformation. A reversible conformational equilibrium upon ATP binding plays a central role in the function and regulation of TmrAB. In addition, it could be shown that pulsed EPR spectroscopy is a powerful method to resolve and investigate conformational equilibria at specific labelling positions in a large molecular complex and to get insights into the overall structural rearrangements by combining results on various labelling positions.

4.5 Outlook

In this thesis, important results were obtained to understand the conformational cycle of TmrAB. Some experiments led to new important questions. During the investigation of the E-to-Q mutants, which are inactive in substrate transport, it was observed that the outward-facing state with ATP-EDTA is stabilized. Furthermore, as shown in Figure 65, it is also possible to open the periplasmic gate and close both NBSs by ADP binding with this inactive mutant.

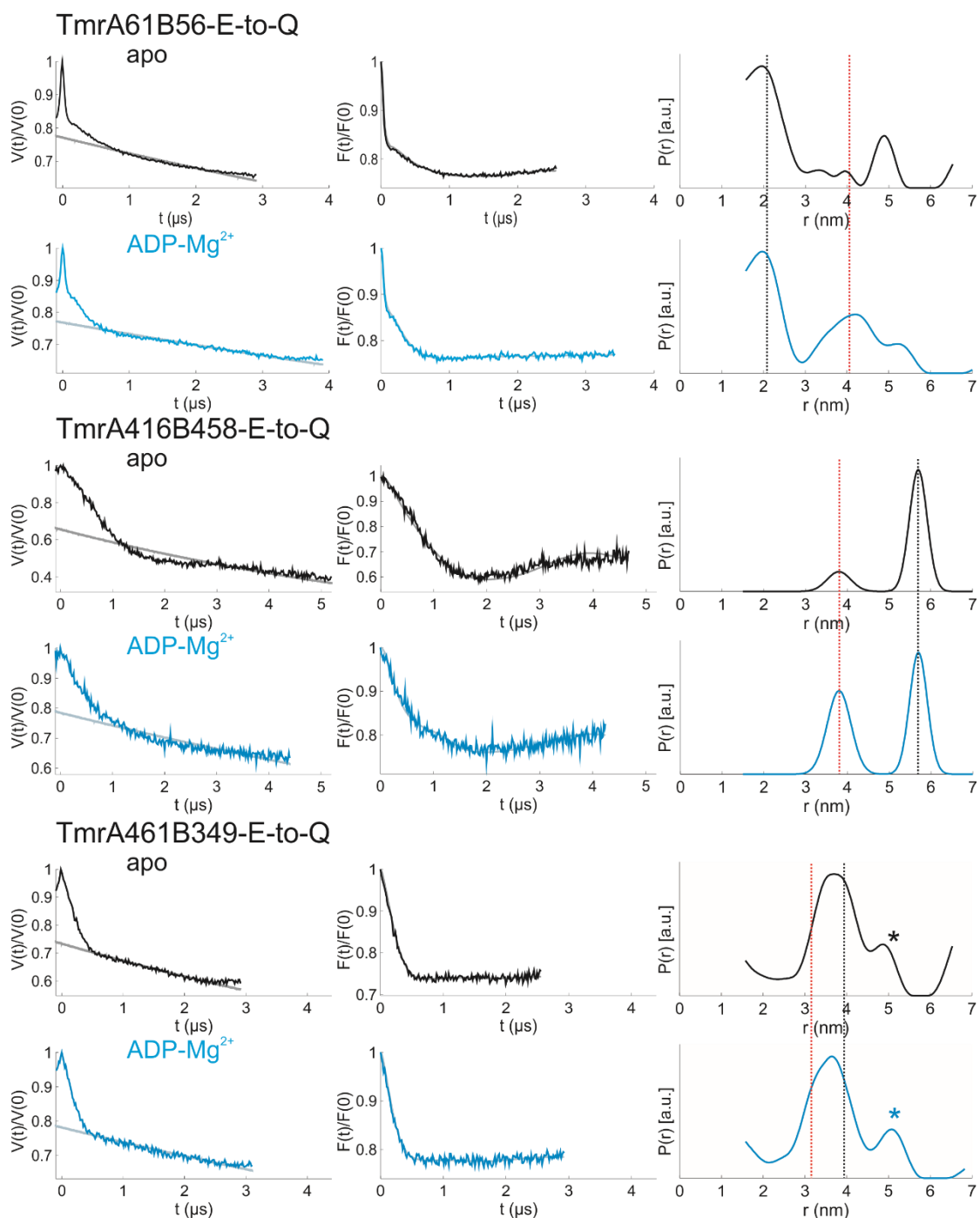


Figure 65: Conformational changes induced by ADP binding with the inactive E-to-Q mutants. Data for the periplasmic gate TmrA61B56-E-to-Q and the consensus NBS TmrA461B349-E-to-Q were fitted with Tikhonov regularization. For the degenerate NBS TmrA416B458, a distance in the apo- or open-state of $r = 5.7 \pm 0.3$ nm and a distance in the closed-state of $r = 3.8 \pm 0.4$ nm were used for Two-Gaussian fitting. Original data $V(t)/V(0)$ are displayed on the left, background corrected data $F(t)/F(0)$ are displayed in the middle and the distance distributions $P(r)$ are shown on the right. With ADP-Mg²⁺ the population of the outward-facing state is significantly increasing, showing that ADP binding is sufficient to open the periplasmic gate and to close both NBS. The asterisks indicate peaks with uncertainty in the shape and width, which occurs due to a too-small length of the detected dipolar evolution time. The vertical lines indicate the most probable distance in the closed (black) and open (red) states. (Data analysis performed with DeerAnalysis 2016)

By this mutation in TmrA at the Walker B motif in the consensus NBS (TmrAE523QB), the transporter becomes inactive in substrate transport but is still able to bind nucleotides. While the addition of ADP-Mg²⁺ was not sufficient to introduce conformational changes for the active transporter, for this inactive mutant it is sufficient. This shows that the Walker B motif has an important role in the transition between inward- and outward-facing state. Therefore, this inactive mutant should be further investigated to unravel its specific role. For example, investigations of the conformational thermodynamics of this mutant, as done for the active variant, could show how the energetic behaviour is changing. In addition, different ADP or ATP concentrations could show if the equilibrium between inward- and outward-facing state can still be modulated.

In the presented studies about the conformational thermodynamics, the question if the model with one or two bound ATP is correct could not be tackled. For this purpose, hyperfine spectroscopy could help. This was shown previously for the heterodimeric ABC exporter BmrCD¹³², where the magnesium ions were substituted by manganese ions. By observing the coupling to the present nucleotides, it could be quantitatively shown that there is an asymmetric behaviour during ATP hydrolysis. For this purpose, pulsed electron-nuclear double resonance (ENDOR) and electron-electron double resonance (ELDOR)-detected nuclear magnetic resonance (EDNMR) can be used to observe the coupling between Mn²⁺ and the different nucleotides. The transport assay for TmrAB with magnesium and manganese ions (Figure 66) shows that the transporter is still active in transport with manganese, which makes it usable for ENDOR and EDNMR experiments.

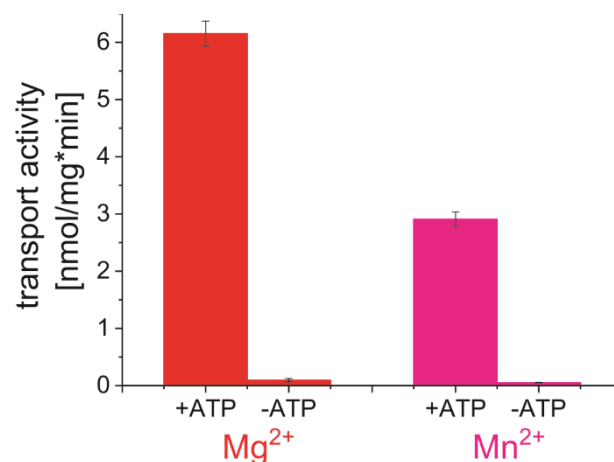


Figure 66: Transport assay of TmrAB with magnesium or manganese ions. In red the transport activity is shown for wildtype TmrAB performed with magnesium ions and in pink with manganese ions. Although the transport efficiency is lower with manganese ions, there is still a significant activity.

The results from the conformational thermodynamics experiments could be used to further improve the input for MD simulations on TmrAB. Typically, certain structural data is used as a starting point for MD simulation. These structures are obtained from a crystal, which was crystallized under optimized conditions for crystallization, and this might not present the lowest energy state of the transporter under physiological conditions. For TM287/288, MD simulations showed the transitions from the inward-facing state over an occluded conformation to the outward-facing state. These MD data could be compared to the EPR data on this system, whereby the occluded conformation could not be validated by measurements.^{110,133} With TmrAB, however, a validation for the occluded conformation would be possible.

So far, the main focus was on the transporter and not on the substrate binding and transport. Studies were done to observe the binding of the peptide K5F with a spin-labelled peptide (Supp. Figure 5). In these studies, the binding was observed in the apo-state and by parallel addition of the peptide and ATP-V_i-Mg²⁺. Since already a significant amount of peptide binding could be observed at a 1:1 ratio of peptide and protein, this ratio was used for distance measurements between single labelled TmrAB and the MTSSL-labelled peptide. For TmrA61B in the periplasmic gate and TmrA112B in the cytosolic gate, the results are shown in Figure 67. Further measurements with TmrAB56 and TmrAB97 are presented in Supp. Figure 6. According to the transport cycle, substrate binding in the apo-state and substrate release in the ATP-V_i-Mg²⁺ state are expected. This yields to a very low modulation depth in the ATP-V_i-Mg²⁺ state; furthermore, no clear distances could be obtained. Yet distance measurements are possible in both the apo and the ATP-V_i-Mg²⁺ states, whereby the modulation depth is only slightly decreasing, showing probably that there is more than one possible substrate binding position.

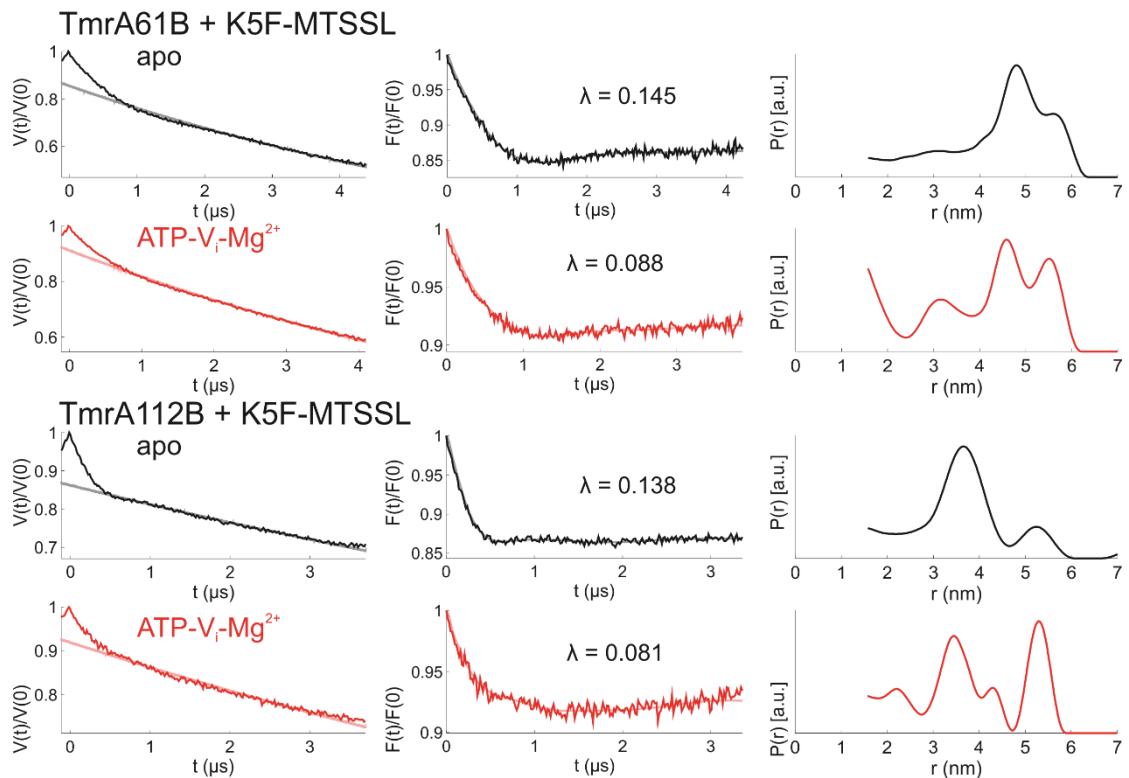


Figure 67: Distance measurements between single-labelled TmrAB and the MTSSL-labelled K5F peptide. Original data $V(t)/V(0)$ are displayed on the left, background corrected data $F(t)/F(0)$ are displayed in the middle and the distance distributions $P(r)$ are shown on the right. Shown are the apo-states in black and the $ATP-V_i-Mg^{2+}$ -states in red for TmrA61B at the periplasmic gate and TmrA112B at the cytosolic gate. The modulation depth (λ) is slightly decreasing with $ATP-V_i-Mg^{2+}$, and no clear distance distributions could be obtained in any of the examined cases. (Data analysis performed with DeerAnalysis 2016)

Since all of these measurements were obtained in detergent micelles, a different environment could probably help to improve the results. Proteoliposomes would give a more natural environment but would make it difficult to introduce the nucleotides and substrate to the transporter. Therefore, nanodiscs could help, which were already successfully used during the investigation of TAP¹³⁴. Nanodiscs surround the protein like they would be also situated in a membrane environment. However, the translocation pathway and the NBDs would still be accessible from the outside. A natural environment is probably necessary to observe specific substrate binding.

Deutsche Zusammenfassung

Die Klasse von Membranproteinen spielt eine große Rolle in der Zellkommunikation, dem Transport durch die Membran, den Gebrauch von Energie und Anstoßen von Signalübertragungswegen.⁴ Da Membranproteine wichtig sind in der Entwicklung von medizinischen Wirkstoffen, ist es besonders essentiell ihre Strukturen und darauf aufbauend ihre Mechanismen zu verstehen.^{4,5} Es existieren primär-aktive Transporter wie ATP-bindende Kasette (ABC-) Transporter, welche die Energie der ATP Hydrolyse nutzen und sekundär-aktive Transporter, die Energie durch Ionen-Translokation nutzen.⁵ Durch beispielsweise Kristallstrukturanalyse⁸ oder Kryo-Elektronenmikroskopie¹¹ können Strukturen aufgeklärt werden. Diese Strukturen ergeben aber nur ein statisches Bild, aus welchem viele Informationen über das System gezogen werden können. Die Funktion, Dynamik und der Mechanismus von Membranproteinen sind daraus jedoch nicht ableitbar. Hierfür können spektroskopische Methoden wie z.B. magnetische Kernresonanz-Spektroskopie (NMR)¹², Elektronen-Spin-Resonanz-Spektroskopie (ESR/EPR)^{17,18} oder Förster Resonanz Energie Transfer (FRET)¹⁶ genutzt werden. In dieser Arbeit wurde EPR-Spektroskopie verwendet um einen heterodimerischen ABC Exporter zu untersuchen.

Die Klasse von ABC Transportern nutzt die Bindung von ATP und die anschließende Hydrolyse um Substrat durch Membranen zu transportieren.^{1,24,25} Die Umwandlung von ATP zu ADP und Orthophosphat gibt etwa $-30.5 \text{ kJ mol}^{-1}$ Energie frei. Anhand der Richtung des Transports können ABC Transporter unterteilt werden in Importer, Exporter und Extruder. Viele verschiedene Substrate können hierbei transportiert werden, wie Antibiotika, Gifte, Vitamine, Steroide, Lipide, Ionen, Polysaccharide, Peptide und Proteine.¹ Während ABC-Exporter in Bakterien, Säugetieren und Pflanzen auftreten, sind ABC-Importer nur in Bakterien, Chloroplasten und Mitochondrien von Pflanzen zu finden.³¹ Im allgemeinen bestehen ABC Transporter aus zwei konservierten nukleotid-bindenden Domänen (NBDs) die ATP binden und hydrolysieren, sowie aus zwei Transmembran-Domänen (TMDs), welche in ihrer Struktur variieren und den Transportweg für das Substrat bilden. Die TMDs befinden sich größtenteils in der Membran und sind im Zytoplasma über Kopplungshelizes mit den NBDs verbunden. In ABC Exportern, welche hier behandelt werden, kann das Substrat durch das sogenannte zytoplasmatische Gate zwischen die TMDs wandern und auf der anderen Seite der Membran durch das periplasmatische Gate den Transporter verlassen. Hierfür sind strukturelle Änderungen im Transporter durch einen Transportzyklus notwendig. Zunächst befindet sich der Transporter in einer nach Innen gerichteten Konformation, bei der die NBDs separiert sind

und das zytoplasmatische Gate geöffnet ist. Währenddessen sind die TMDs am periplasmatischen Gate geschlossen. Wenn ATP in den NBDs gebunden wird, werden diese und das zytoplasmatische Gate geschlossen. Es wird somit eine geschlossene Konformation erreicht, da die TMDs an beiden Seiten zu sind und das Substrat in dem TMDs eingeschlossen ist. Direkt danach öffnet das periplasmatische Gate, wodurch Substrat den Transporter verlassen kann. Der Transporter liegt dann in einer nach Außen gerichteten Konformation vor, bei der das periplasmatische Gate geöffnet ist und die NBDs, sowie das zytoplasmatische Gate geschlossen sind. Durch das Hydrolysieren von ATP und anschließendem Entweichen von ADP aus den Bindungstaschen kann der Exporter in der nach Innen gerichteten Konformation wiederhergestellt werden.

Es ist zwischen homodimerischen und heterodimerischen ABC Transportern zu unterscheiden. In homodimerischen Transportern können zwei ATP gebunden und hydrolysiert werden, während in heterodimerischen zwar zwei ATP gebunden werden können, aber nur eines davon hydrolysiert werden kann. Das liegt daran, dass die NBDs viele wichtige konservierte Motive enthalten, die die verschiedenen Schritte der ATP Bindung und Hydrolyse unterstützen. Wenn aber wie in heterodimerischen Transportern einzelne Aminosäuren ausgetauscht werden, kann dieses Motiv seine Rolle nicht mehr erfüllen und es ist keine Hydrolyse mehr möglich. Daher spricht man in diesem Fall von asymmetrischen NBDs, wobei eine consensus Seite mit allen üblichen Motiven und eine degenerierte Seite ohne Hydrolysefunktion vorliegen.

Um das Protein zu untersuchen wurde EPR Spektroskopie verwendet, womit Systeme mit ungepaarten Elektronenspins untersucht werden können. Hierbei können nicht nur natürliche paramagnetische Systeme untersucht werden, es können auch paramagnetische Spinsonden oder Übergangsmetalle in das diamagnetische System eingeführt werden.⁶ Durch ortsspezifisches Spin Labeling (SDSL), eine Methode die erstmals für Bacteriorhodopsin^{74,75} verwendet wurde, kann ein Protein selektiv gelabelt werden. Hierfür ist zunächst ein Protein ohne Cystein notwendig, in welches anschließend an den gewünschten Stellen Cystein eingeführt wird. Anschließend wird mit MTSSL gelabelt, welches mit dem freien Schwefelatom am Cystein eine Schwefelbrücke bildet. Mittels Continuous-Wave (cw) wird die Labeling-Effizienz bestimmt und mittels Pulsed Electron-Electron Double Resonance (PELDOR), können Abstände zwischen zwei Elektronenspins gemessen werden. Da mit cw EPR nur Abstände bis zu 2 nm gemessen werden können, sind für größere Abstände gepulste EPR Methoden notwendig. PELDOR (auch double electron-electron resonance (DEER) genannt) detektiert schwache dipolare Kopplungen zwischen ungepaarten Elektronen, die einen

Abstand von 2-8 nm besitzen, in sehr guten Fällen bis zu 10 nm.¹⁸ Hauptsächlich in dieser Arbeit verwendet wurde die Totzeit-freie 4-Puls-Sequenz⁸⁶ und in wenigen Fällen die 7-Puls-Carr-Purcel (CP)-Sequenz²¹, mit der das Zeitfenster der Messung verlängert werden kann. Bei 4-Puls-PELDOR existieren zwei Typen von Elektronenspins, die Beobachterspins und die Pumpspins. In der Beobachterfrequenz wird ein Echo durch eine refokussierte Echo-Sequenz generiert. Dieses Echo wird durch Anregung des Pumpspins zu verschiedenen Zeitpunkten modelliert, wobei sich das lokale magnetische Feld der Beobachterspins ändert. Die experimentellen Daten bestehen zum einen aus der Hintergrundfunktion, welche intermolekulare Wechselwirkungen enthält und den gewollten Interaktionen der zwei Spins innerhalb des Proteins, auch intramolekulare Wechselwirkungen genannt. Daher muss zunächst eine Hintergrundkorrektur vorgenommen werden. Anschließend könne die Daten entweder mittels Tikhonov Regularisierung ausgewertet werden oder mittels Gaussfits. Auswertungen erfolgten größtenteils mit der DeerAnalysis Software¹⁰⁶ oder für drei-Gaussfits mit der DD Software¹⁰⁷.

In dieser Arbeit stand der heterodimerische ABC Exporter TmrAB von *Thermus Thermophilus* im Fokus, welcher ein funktionelles Homolog des menschlichen Antigen-Translokations-Komplex TAP ist. Eine Kristallstruktur von TmrAB ist bereits bekannt² und mit dieser Struktur sowie auf Basis der Positionen die für den heterodimerischen ABC Exporter BmrCD¹⁰⁹ gemessen wurden, wurden Labelingpositionen für TmrAB geplant. Es wurden Spinsonden im periplasmatischen Gate, im zytoplasmatischen Gate und jeweils an der consensus und der degenerierten Nukleotid-bindenden Seite (NBS) eingeführt. Darüber hinaus wurden auch Messungen an globaleren Positionen in den NBDs durchgeführt um die gesamte Bewegung der NBDs widerzuspiegeln. Diese Positionen erwiesen sich jedoch als nicht so aussagekräftig. Im apo bzw. dem nukleotidfreien Zustand wurde eine nach Innen gerichtete Konformation beobachtet, wobei in den TMDs bereits eine kleine Fraktion von der nach Außen gerichteten Konformation zu beobachten war. Dies spricht für eine unabhängige Bewegung der TMDs, da in den NBDs ohne Nukleotide keine Schließung erfolgt. Mittels Abstandsmessungen wurde nach der Zugabe von ATP, Vanadat und Magnesiumionen eine fast komplette Änderung von der nach Innen gerichteten Konformation zu der nach Außen gerichteten Konformation beobachtet. Hierbei wird das ATP an beiden NBSs gebunden, aber voraussichtlich nur an der consensus Seite hydrolysiert, anschließend insertiert das Vanadat in die gebrochene Phosphatbindung und hält den Transporter in dem gebundenen Zustand fest. Durch die Zugabe von ATP und den Chelatliganden EDTA konnte der Zustand der reinen ATP Bindung untersucht werden, da falls katalytische Magnesiumionen vorliegen diese durch das EDTA

abgefangen werden. In diesem Zustand konnte für alle Positionen ein Gleichgewicht zwischen der nach Innen gerichteten und der nach Außen gerichteten Konformation beobachtet werden. Ein ähnliches Gleichgewicht, nur mit Abweichungen in den Wahrscheinlichkeiten, wurde auch unter hydrolysierenden Bedingungen beobachtet (nach der Zugabe von ATP und Magnesiumionen). Während für BmrCD¹⁰⁹ beobachtet wurde, dass AMP-PNP Einfluss auf den Transporter hat und ATP Hydrolyse notwendig ist um die nach-außen-gerichtete Konformation zu erlangen, konnte mit TmrAB keine Änderung mit AMP-PNP, dem nicht hydrolysierbaren ATP Analogon, erreicht werden. Zu dem heterodimerischen ABC Exporter TM287/288¹¹⁰ können mehr Übereinstimmungen im Zyklus beobachten werden, da dieser wie TmrAB rein durch ATP Bindung die nach Außen gerichtete Konformation einnehmen kann und auch keine Änderung durch AMP-PNP zeigt. Durch die Zugabe von ADP und Magnesiumionen konnte keine Änderung bei aktivem TmrAB herbeigeführt werden.

Das Gleichgewicht, welches durch die Zugabe von ATP und EDTA entsteht, wurde anschließend weiter untersucht, wobei der Transporter zum einen mit Spinsonden am periplasmatischen Gate und zum anderen mit Spinsonden an beiden NBSs untersucht wurde. Zunächst wurde die Konzentration von ATP zwischen 0.5 bis 50 mM bei konstanter Proteinkonzentration variiert. Hierbei war am periplasmatischen Gate eine konstant steigende Öffnungswahrscheinlichkeit bei steigender ATP Konzentration zu beobachten, während an beiden NBS die Schließungswahrscheinlichkeit weniger stark anstieg. Bei genauerer Betrachtung ist zu sehen, dass bei der Zugabe von 25 mM ATP an der consensus NBS eine Sättigung erreicht wird, wobei die Schließungswahrscheinlichkeit nicht über 0.4 steigt. An der degenerierten NBS kann darüber hinaus bis zu einer Schließungswahrscheinlichkeit von etwa 0.7 bei 50 mM ATP ein linearer Anstieg beobachtet werden. Für das periplasmatische Gate ist eine stark steigende Öffnungswahrscheinlichkeit bereits bei geringen ATP Konzentration zu beobachten, die zeigt, dass wahrscheinlich bereits die Schließung einer NBS bereits ausreicht um das periplasmatische Gate zu öffnen. Das asymmetrische Verhalten der beiden NBSs kann auch beobachtet werden, wenn der Transporter durch Einführen einer E-zu-Q-Mutation (E523Q) in TmrA inaktiv gemacht wird. Auch hier kann mit ATP-EDTA eine Schließung der NBSs erfolgen. Während an der consensus Seite die Wahrscheinlichkeit des geschlossenen Zustand etwas steigt, wird an der degenerierten Seite eine fast komplette Schließung durch diese Mutation beobachtet. Insgesamt zeigt dies, dass der geschlossene Zustand an der degenerierten NBS energetisch bevorzugt wird, während an der consensus NBS der energetische Zustand der beiden Konformationen wohl sehr ähnlich ist.

Weiterhin wurde die Temperatur während der Inkubation mit ATP und EDTA von 0 bis 80 °C variiert. Die ATP Konzentration betrug 50 mM um im gesättigten Bereich zu sein. Auf diesem Weg konnte die Thermodynamik für die Konformationsänderung durch ATP Bindung untersucht werden. Hierbei war zu beobachten, dass bei einer Temperatur über 50 °C für beide NBSs ein Abfall in der Schließungswahrscheinlichkeit zu beobachten ist, während die Öffnungswahrscheinlichkeit am periplasmatischen Gate weiter steigt. Durch eine nicht-lineare van-'t-Hoff-Auftragung und einen Vergleich mit der Enthalpieänderung von ATP konnte gezeigt werden, dass das nicht-lineare Verhalten bei erhöhten Temperaturen möglicherweise auf den Einfluss von ATP und dessen Temperaturabhängigkeit zurückzuführen ist. Eine andere Möglichkeit wäre, dass die Reaktionsraten bei höheren Temperaturen schneller sind und dadurch der Transporter bei höheren Temperature schneller in den nach Innen gerichteten Zustand zurückfällt, als er eingefroren werden könnte. Mit linearen van-'t-Hoff-Fits konnte für alle Positionen bestimmt werden, dass die Konformationsänderung Entropiegetrieben ist. In allen Fällen wurde eine negative Änderung der Gibbs Energie festgestellt. Hierbei wurden zwei Modelle benutzt, zum einen, dass ein ATP in den NBSs gebunden wird und zum anderen, dass zwei ATP gebunden werden. Das Modell mit zwei ATP Molekülen ist aufgrund des höheren Energiegewinns der freien Gibbs Energie wahrscheinlicher. Weiterhin ist die Enthalpieänderung stark positiv in allen Fällen, wobei die Energiebarriere für beide NBSs etwa doppelt so groß ist im Vergleich zum periplasmatischen Gate. Die kleinere energetische Barriere im periplasmatischen Gate ist in Übereinstimmung mit den Beobachtungen bei verschiedenen ATP Konzentration, wo schnellere Änderungen erzielt werden konnten. Die hier präsentierten Ergebnisse zeigen, dass die ATP Bindung alleine die Konformationsänderung antreibt.

Darüber hinaus wurde das Phänomen der Trans-Inhibierung untersucht, was bedeutet, dass durch einen starken Substratüberschuss kein Substrattransport mehr möglich ist. Diese Inhibierung ist vermutlich ein Schutzmechanismus in der Zelle. In dieser Arbeit wurde hauptsächlich der ATP gebundener Zustand mit einem Überschuss an Peptid untersucht. Hierbei zeigte sich am periplasmatischen Gate, dass der nach Innen gerichtete Zustand in der Wahrscheinlichkeit stark ansteigt. Am zytoplasmatischen Gate sinkt der Anteil der nach Außen gerichteten Konformation und es gibt einen kleinen Anstieg der nach Innen gerichteten Konformation. Hauptsächlich ist jedoch eine neue Population zu erkennen, die einen kleineren Abstand im Vergleich zur nach Außen gerichteten Konformation aufweist. Beide NBSs zeigen einen leichten Anstieg in der geöffneten Population, aber bleiben größtenteils geschlossen. Zusammenfassend bedeutet dies, dass die NBSs hauptsächlich geschlossen sind, während die

TMDs auch an beiden Seiten geschlossen sind, was eine Occluded-Konformation bedeutet. Dies zeigt, dass durch Trans-Inhibierung der Transportweg vom ATP-gebundenen nach Außen gerichteten Zustand umgekehrt wird zu einem kleinen Teil in die nach Innen gerichteten Konformation und zum größten Teil in die occluded-Konformation. Vermutlich ist die Energiebarriere für eine Umkehrung der occluded-Konformation zu der nach innen-gerichteten Konformation größer. Für einen heterodimerischen ABC Exporter ist dies, soweit bekannt, das erste Mal, dass der occluded-Zustand experimentell nachgewiesen werden konnte.

In dieser Arbeit wird gezeigt, dass das umkehrbare Konformationsgleichgewicht eine große Rolle in der Funktion und Regulation eines ABC Exporters spielt. Weiterhin wurde zum ersten Mal gezeigt, dass es möglich ist die Thermodynamiken der Konformationsänderungen zu untersuchen. Da es in der Gruppe der heterodimerischen ABC Exporter teilweise viele Überschneidungen gibt, jeder Exporter aber viele individuellen Eigenschaften im Transportmechanismus besitzt, muss jeder Transporter auch individuell untersucht werden. Die hier genutzten Methoden der gepulsten EPR Spektroskopie können hilfreich sein, um andere Transporter mit asymmetrischen NBS oder auch allgemein ähnliche Proteine zu untersuchen.

List of amino acids

Amino acid	Three letter code	One letter code
Alanine	Ala	A
Arginine	Arg	R
Asparagine	Asn	N
Aspartic acid	Asp	D
Cysteine	Cys	C
Glutamine	Gln	Q
Glutamic acid	Glu	E
Glycine	Gly	G
Histidine	His	H
Isoleucine	Ile	I
Leucine	Leu	L
Lysine	Lys	K
Methionine	Met	M
Phenylalanine	Phe	F
Proline	Pro	P
Serine	Ser	S
Threonine	Thr	T
Tryptophan	Trp	W
Tyrosine	Tyr	Y
Valine	Val	V

List of figures

Number	Title	Page
Figure 1	<i>Schematical architecture of an ABC transporter.</i>	20
Figure 2	<i>Conserved motifs of the NBDs shown by the heterodimeric ABC exporter TmrAB (pdb code 5MKK).</i>	21
Figure 3	<i>Schematic representation of NBDs and coupling helices.</i>	23
Figure 4	<i>Representative bacterial ABC importers involved in substrate uptake.</i>	24
Figure 5	<i>Mechanisms of type I and II ABC importers.</i>	25
Figure 6	<i>Representative bacterial ABC exporters.</i>	28
Figure 7	<i>Mechanisms of ABC exporters.</i>	31
Figure 8	<i>Representative Extractor (type VI) and Efflux pump (type VII).</i>	32
Figure 9	<i>The heterodimeric ABC exporter TmrAB.</i>	34
Figure 10	<i>Zeeman splitting of energy levels in a system with spin $S = \frac{1}{2}$.</i>	36
Figure 11	<i>Site-directed spin labelling</i>	40
Figure 12	<i>Structure of the unnatural side chain R1.</i>	40
Figure 13	<i>Gadolinium(III)-based labelling of cysteines.</i>	41
Figure 14	<i>Nitroxide cw spectrum ($S=1/2$, $I=1$).</i>	43
Figure 15	<i>Comparison of free MTSSL- and bound MTSSL-cw EPR spectrum.</i>	44
Figure 16	<i>Dead-time free 4-pulse PELDOR.</i>	45
Figure 17	<i>PELDOR Data Analysis example (TmrAB labelled at TmrA288 and TmrB272 with MTSSL).</i>	46
Figure 18	<i>Pulse Sequence for 7P-CP-PELDOR.</i>	48
Figure 19	<i>Tikhonov regularization L curve (DeerAnalysis 2016).</i>	52
Figure 20	<i>Data analysis with the DD software (TmrAB labelled at TmrA288 and TmrB272 with MTSSL).</i>	53
Figure 21	<i>Schematic description of the pET22 vector, which carries the TmrAB gene.</i>	57
Figure 22	<i>Proposed transport cycle for the heterodimeric ABC exporter TmrAB.</i>	79
Figure 23	<i>Labelling position in TmrAB, with TmrA in violet and TmrB in green.</i>	83
Figure 24	<i>MMM simulated interspin distances for all double mutants.</i>	84
Figure 25	<i>Transport activity of TmrAB mutants.</i>	86
Figure 26	<i>Conformational changes at the periplasmic gate TmrA61B56.</i>	88
Figure 27	<i>Conformational changes at the periplasmic gate TmrA61B56-E-to-Q.</i>	89
Figure 28	<i>Conformational changes at the periplasmic gate TmrA288B272.</i>	90
Figure 29	<i>Apo-like states at the periplasmic gate TmrA288B272.</i>	91
Figure 30	<i>ADP-V_i-Mg^{2+}-like states at the periplasmic gate TmrA288B272.</i>	92
Figure 31	<i>Conformational changes at the cytosolic gate TmrA112B97.</i>	94
Figure 32	<i>Apo-like and ADP-V_i-Mg^{2+}-like states at the cytosolic gate TmrA112B97.</i>	95

Figure 33	<i>Conformational changes at the NBDs TmrA585B562 and TmrA578B555.</i>	97
Figure 34	<i>Conformational changes at the degenerate NBS TmrA416B458.</i>	98
Figure 35	<i>Apo-like states at the degenerate NBS TmrA416B458.</i>	99
Figure 36	<i>ADP-V_i-Mg²⁺-like state at the degenerate NBS TmrA416B458.</i>	100
Figure 37	<i>Conformational changes at the degenerate NBS TmrA416B458-E-to-Q.</i>	101
Figure 38	<i>Conformational changes at the consensus NBS TmrA461B349.</i>	102
Figure 39	<i>Apo-like states at the consensus NBS TmrA461B349.</i>	103
Figure 40	<i>ADP-V_i-Mg²⁺-like states at the consensus NBS TmrA461B349.</i>	104
Figure 41	<i>Conformational changes at the consensus NBS TmrA461B349-E-to-Q.</i>	105
Figure 42	<i>Conformational changes at the consensus NBS TmrA538B549.</i>	106
Figure 43	<i>Alternating access mechanism of TmrAB where the states which could be observed experimentally with nucleotides are marked with pink boxes.</i>	108
Figure 44	<i>Conformational equilibrium induced by ATP binding in TmrAB.</i>	112
Figure 45	<i>ATP modulates the conformational equilibrium at the degenerate NBS TmrA416B458.</i>	114
Figure 46	<i>ATP modulates the conformational equilibrium at the consensus NBS TmrA461B349.</i>	115
Figure 47	<i>ATP modulates the conformational equilibrium at the consensus NBS TmrA538B549.</i>	117
Figure 48	<i>ATP modulates the conformational equilibrium at the periplasmic gate TmrA288B272.</i>	118
Figure 49	<i>Dose-response curves for both NBS and the periplasmic gate.</i>	119
Figure 50	<i>Temperature dependence of the conformational equilibrium induced by ATP binding at the consensus NBS TmrA461B349.</i>	123
Figure 51	<i>Temperature dependence of the conformational equilibrium induced by ATP binding at the degenerate NBS TmrA416B458.</i>	126
Figure 52	<i>Temperature dependence of the conformational equilibrium induced by ATP binding at the periplasmic gate TmrA288B272.</i>	129
Figure 53	<i>Linear van't Hoff fit of both NBSs and the periplasmic gate.</i>	131
Figure 54	<i>Non-linear van't Hoff fit of both NBSs and the periplasmic gate.</i>	134
Figure 55	<i>Heat capacity change, enthalpy change, entropy change and Gibbs free energy change for the non-linear van't Hoff plot in case of one ATP binding to the transporter.</i>	136
Figure 56	<i>Heat capacity change, enthalpy change, entropy change and Gibbs free energy change for the non-linear van't Hoff plot in case of two ATP binding to the transporter.</i>	137
Figure 57	<i>Temperature-dependent enthalpy of the periplasmic gate and both NBS of TmrAB compared to ATP.</i>	141

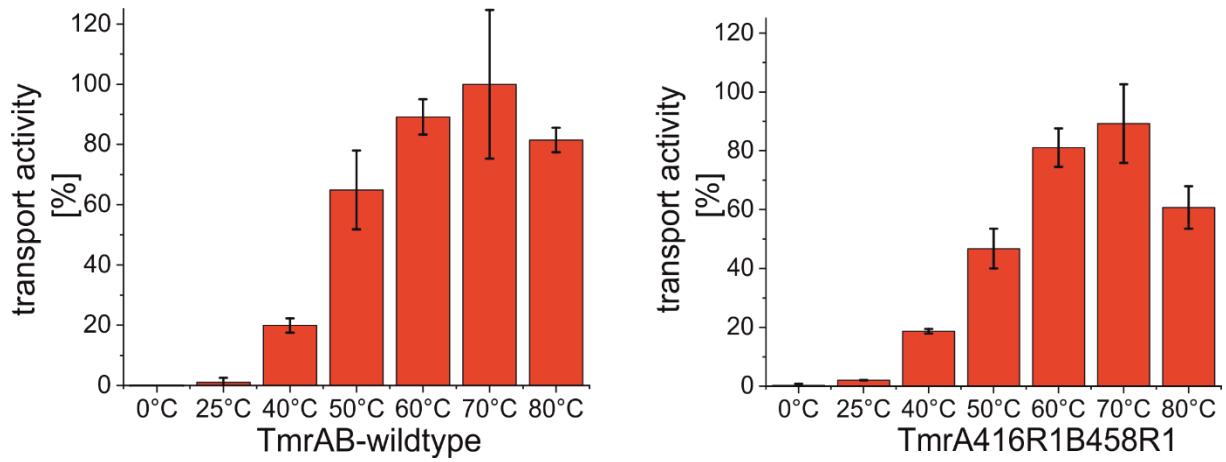
Figure 58	<i>Alternating access mechanism of TmrAB, with the conformational equilibrium induced by ATP binding highlighted by a yellow box.</i>	142
Figure 59	<i>Illustration of the process of trans-inhibition.</i>	146
Figure 60	<i>Trans-inhibition by K5F at the periplasmic gate TmrA61B56 and TmrA288B272.</i>	147
Figure 61	<i>Trans-inhibition by K5F at the cytosolic gate TmrA112B97.</i>	149
Figure 62	<i>Trans-inhibition by K5F at both NBSs TmrA416B458 and TmrA461B349.</i>	150
Figure 63	<i>Alternating access mechanism of TmrAB, with highlighted trans-inhibition.</i>	151
Figure 64	<i>Transport and trans-inhibition mechanism of TmrAB.</i>	153
Figure 65	<i>Conformational changes induced by ADP binding with the inactive E-to-Q mutants.</i>	155
Figure 66	<i>Transport assay of TmrAB with magnesium or manganese ions.</i>	156
Figure 67	<i>Distance measurements between single-labelled TmrAB and the MTSSL-labelled K5F peptide.</i>	158
Supp. Figure 1	<i>Transport assays for TmrAB wildtype and spin-labelled TmrA416B458 at different temperatures.</i>	173
Supp. Figure 2	<i>Peptide is not changing the temperature dependence of the conformational equilibrium induced by ATP binding at the periplasmic gate TmrA288B272.</i>	177
Supp. Figure 3	<i>Gaussian fitting for the ATP-EDTA states of the degenerate NBS TmrA416B456-E-to-Q and consensus NBS TmrA461B349-E-to-Q.</i>	178
Supp. Figure 4	<i>Excess of substrate is not changing the apo or ADP-V_i-Mg²⁺ state at the periplasmic gate.</i>	178
Supp. Figure 5	<i>Peptide binding observed with cw spectroscopy.</i>	179
Supp. Figure 6	<i>Distance measurements between single-labelled TmrAB and the MTSSL-labelled K5F peptide.</i>	180

List of tables

Number	Title	Page
Table 1	<i>Sequences of peptides used as substrates for TmrAB.</i>	58
Table 2	<i>List of chemicals and the provider used in this thesis.</i>	58
Table 3	<i>List of kits and columns used in this thesis and their provider.</i>	60
Table 4	<i>List of equipment and the provider used in this thesis.</i>	60
Table 5	<i>List of enzymes and cells used in this thesis and their provider.</i>	62
Table 6	<i>List of buffers, media and solution and their composition used in this thesis.</i>	62
Table 7	<i>List of molecular rulers and loading dyes used in this thesis and their provider.</i>	63
Table 8	<i>List of software used in this thesis and their application.</i>	64
Table 9	<i>Primers used for the cloning of the cysteine double mutants of TmrAB.</i>	65
Table 10	<i>PCR mixture for the generation of double cysteine mutagenesis of TmrAB with Phusion HF or Phusion GC buffer.</i>	66
Table 11	<i>Thermal cycling program used for the PCR-based site-directed mutagenesis of TmrAB.</i>	66
Table 12	<i>Primers used for the sequencing of TmrAB cysteine mutations.</i>	69
Table 13	<i>Transport assay mixture for determination of substrate transport of TmrAB.</i>	73
Table 14	<i>Cysteine double mutants of TmrAB analysed with MMM.</i>	81
Table 15	<i>Number of rotamers and partition functions for the spin labelled positions, calculated with MMM.</i>	83
Table 16	<i>Simulated distances with the MMM software.</i>	85
Table 17	<i>Probability of the open and closed conformation at the degenerate NBS TmrA416B458, modulated by ATP.</i>	113
Table 18	<i>Probability of the open and closed conformation at the consensus NBS TmrA461B349, modulated by ATP.</i>	116
Table 19	<i>Probability of the open and closed conformation at the consensus NBS TmrA538B549, modulated by ATP.</i>	116
Table 20	<i>Probability of the open and closed conformation at the periplasmic gate TmrA288B272, modulated by ATP.</i>	119
Table 21	<i>Probability of the open and closed conformation at the consensus NBS TmrA461B349, modulated by temperature.</i>	122
Table 22	<i>The average equilibrium constants for the consensus NBS TmrA461B349, modulated by temperature.</i>	125
Table 23	<i>Probability of the open and closed conformation at the degenerate NBS TmrA416B458, modulated by temperature.</i>	127
Table 24	<i>The average equilibrium constants for the degenerate NBS TmrA416B458, modulated by temperature.</i>	127

Table 25	<i>Probability of the open and closed conformation at the periplasmic gate TmrA288B272, modulated by temperature.</i>	128
Table 26	<i>The average equilibrium constants for the periplasmic gate TmrA288B272, modulated by temperature.</i>	130
Table 27	<i>Slopes and intercepts determined with the linear van't Hoff plot.</i>	132
Table 28	<i>The enthalpy change (ΔH_{VH}^0) and the entropy change (ΔS_{VH}^0), from the linear van't Hoff plot.</i>	133
Table 29	<i>The Gibbs free energy change (ΔG_{VH}^0) calculated from the enthalpy and entropy determined by the linear van't Hoff plot.</i>	133
Table 30	<i>The heat capacity change (ΔC_{VH}^0) at different temperatures from the non-linear van't Hoff plot.</i>	138
Table 31	<i>The enthalpy change (ΔH_{VH}^0) at different temperatures from the non-linear van't Hoff plot.</i>	139
Table 32	<i>The entropy change (ΔS_{VH}^0) at different temperatures from the non-linear van't Hoff plot.</i>	139
Table 33	<i>The Gibbs free energy change (ΔG_{VH}^0) at different temperatures from the non-linear van't Hoff plot.</i>	140
Supp. Table 1	<i>Calculation of the equilibrium constant for the consensus NBS TmrA461B349.</i>	174
Supp. Table 2	<i>Calculation of the equilibrium constant for the degenerate NBS TmrA416B458.</i>	175
Supp. Table 3	<i>Calculation of the equilibrium constant for the periplasmic gate TmrA288B272.</i>	176
Supp. Table 4	<i>Fitting parameters for the non-linear polynomial fit of second order.</i>	177

Supporting information



Supp. Figure 1: Transport assays for *TmrAB* wildtype and spin-labelled *TmrA416B458* at different temperatures. Transport activity is given as percentage, whereby the maximal activity of *TmrAB* wildtype was set to 100%. Both, *TmrAB* wildtype and *TmrA416R1B458R1* show a maximum transport activity at 70 °C.

Supp. Table 1: Calculation of the equilibrium constant for the consensus NBS TmrA461B349. Shown are the concentrations calculated from the ratio determined by PELDOR, based on the starting concentrations of 40 or 50 μM TmrAB and 50 mM ATP. First a) is the calculation for the first sample set with the assumption of one bound ATP and b) is the corresponding calculation with two ATP bound. Respectively c) and d) are the same calculations with the second sample set.

a)

Temp.	P_{closed}	P_{open}	[TmrAB] [M]	[ATP] [M]	[TmrAB- ATP] [M]	K_{eq} [1/M]	ΔK_{eq}
0 °C	0.03	0.97	0.0000388	0.0499988	0.0000012	0.62	0.17
25 °C	0.336	0.664	0.00002656	0.04998656	0.00001344	10	3
40 °C	0.507	0.493	0.00001972	0.04997972	0.00002028	21	6
50 °C	0.52	0.48	0.0000192	0.0499792	0.0000208	22	6
60 °C	0.439	0.561	0.00002244	0.04998244	0.00001756	16	5
70 °C	0.366	0.634	0.00002536	0.04998536	0.00001464	12	4
80 °C	0.363	0.637	0.00002548	0.04998548	0.00001452	11	4

b)

Temp.	P_{closed}	P_{open}	[TmrAB] [M]	[ATP] [M]	[TmrAB- ATP] [M]	K_{eq} [1/M ²]	ΔK_{eq}
0 °C	0.03	0.97	0.0000388	0.0499976	0.0000012	12	4
25 °C	0.336	0.664	0.00002656	0.04997312	0.00001344	200	60
40 °C	0.507	0.493	0.00001972	0.04995944	0.00002028	410	120
50 °C	0.52	0.48	0.0000192	0.0499584	0.0000208	430	130
60 °C	0.439	0.561	0.00002244	0.04996488	0.00001756	310	90
70 °C	0.366	0.634	0.00002536	0.04997072	0.00001464	230	70
80 °C	0.363	0.637	0.00002548	0.04997096	0.00001452	230	70

c)

Temp.	P_{closed}	P_{open}	[TmrAB] [M]	[ATP] [M]	[TmrAB- ATP] [M]	K_{eq} [1/M]	ΔK_{eq}
0 °C	0.067	0.933	0.00004665	0.04999665	0.00000335	1.4	0.4
25 °C	0.266	0.734	0.0000367	0.0499867	0.0000133	7	2
40 °C	0.425	0.575	0.00002875	0.04997875	0.00002125	15	4
50 °C	0.439	0.561	0.00002805	0.04997805	0.00002195	16	5
60 °C	0.347	0.653	0.00003265	0.04998265	0.00001735	11	3
70 °C	0.391	0.609	0.00003045	0.04998045	0.00001955	13	4
80 °C	0.279	0.721	0.00003605	0.04998605	0.00001395	8	2

d)

Temp.	P_{closed}	P_{open}	[TmrAB] [M]	[ATP] [M]	[TmrAB- ATP] [M]	K_{eq} [1/M ²]	ΔK_{eq}
0 °C	0.067	0.933	0.00004665	0.0499933	0.00000335	29	8
25 °C	0.266	0.734	0.0000367	0.0499734	0.0000133	150	40
40 °C	0.425	0.575	0.00002875	0.0499575	0.00002125	300	90
50 °C	0.439	0.561	0.00002805	0.0499561	0.00002195	310	90
60 °C	0.347	0.653	0.00003265	0.0499653	0.00001735	210	60
70 °C	0.391	0.609	0.00003045	0.0499609	0.00001955	260	80
80 °C	0.279	0.721	0.00003605	0.0499721	0.00001395	150	50

Supp. Table 2: Calculation of the equilibrium constant for the degenerate NBS TmrA416B458. Shown are the concentrations calculated from the ratio determined by PELDOR, based on the starting concentrations of 50 μ M TmrAB and 50 mM ATP. First a) is the calculation for the first sample set with the assumption of one bound ATP and b) is the corresponding calculation with two ATP bound. Respectively c) and d) are the same calculations with the second sample set.

a)

Temp.	P _{closed}	P _{open}	[TmrAB] [M]	[ATP] [M]	[TmrAB- ATP] [M]	K _{eq} [1/M]	Δ K _{eq}
0 °C	0.1042	0.8958	0.00004479	0.04999479	0.00000521	2.3	0.7
25 °C	0.3251	0.6749	0.000033745	0.049983745	0.000016255	10	3
40 °C	0.5901	0.4099	0.000020495	0.049970495	0.000029505	29	8
50 °C	0.6452	0.3548	0.00001774	0.04996774	0.00003226	36	11
60 °C	0.5703	0.4297	0.000021485	0.049971485	0.000028515	27	8
70 °C	0.4729	0.5271	0.000026355	0.049976355	0.000023645	18	5
80 °C	0.4744	0.5256	0.00002628	0.04997628	0.00002372	18	5

b)

Temp.	P _{closed}	P _{open}	[TmrAB] [M]	[ATP] [M]	[TmrAB- ATP] [M]	K _{eq} [1/M ²]	Δ K _{eq}
0 °C	0.1042	0.8958	0.00004479	0.04998958	0.00000521	47	13
25 °C	0.3251	0.6749	0.000033745	0.04996749	0.000016255	190	60
40 °C	0.5901	0.4099	0.000020495	0.04994099	0.000029505	580	170
50 °C	0.6452	0.3548	0.00001774	0.04993548	0.00003226	700	200
60 °C	0.5703	0.4297	0.000021485	0.04994297	0.000028515	530	150
70 °C	0.4729	0.5271	0.000026355	0.04995271	0.000023645	360	100
80 °C	0.4744	0.5256	0.00002628	0.04995256	0.00002372	360	100

c)

Temp.	P _{closed}	P _{open}	[TmrAB] [M]	[ATP] [M]	[TmrAB- ATP] [M]	K _{eq} [1/M]	Δ K _{eq}
0 °C	0.0953	0.9047	0.000045234	0.049995234	0.000004766	2.1	0.6
25 °C	0.4738	0.5262	0.00002631	0.04997631	0.00002369	18	5
40 °C	0.6987	0.3013	0.000015065	0.049965065	0.000034935	46	13
50 °C	0.7174	0.2826	0.00001413	0.04996413	0.00003587	51	15
60 °C	0.6825	0.3175	0.000015875	0.049965875	0.000034125	43	12
70 °C	0.6097	0.3903	0.000019515	0.049969515	0.000030485	31	9
80 °C	0.6294	0.3706	0.00001853	0.04996853	0.00003147	34	10

d)

Temp.	P _{closed}	P _{open}	[TmrAB] [M]	[ATP] [M]	[TmrAB- ATP] [M]	K _{eq} [1/M ²]	Δ K _{eq}
0 °C	0.0953	0.9047	0.000045234	0.049990468	0.000004766	42	12
25 °C	0.4738	0.5262	0.00002631	0.04995262	0.00002369	360	100
40 °C	0.6987	0.3013	0.000015065	0.04993013	0.000034935	900	300
50 °C	0.7174	0.2826	0.00001413	0.04992826	0.00003587	1000	300
60 °C	0.6825	0.3175	0.000015875	0.04993175	0.000034125	900	300
70 °C	0.6097	0.3903	0.000019515	0.04993903	0.000030485	630	180
80 °C	0.6294	0.3706	0.00001853	0.04993706	0.00003147	700	200

Supp. Table 3: Calculation of the equilibrium constant for the periplasmic gate TmrA288B272. Shown are the concentrations calculated from the ratio determined by PELDOR, based on the starting concentrations of 50 μ M TmrAB and 50 mM ATP. First a) is the calculation for the first sample set with the assumption of one bound ATP and b) is the corresponding calculation with two ATP bound. Respectively c) and d) are the same calculations with the second sample set.

a)

Temp.	P _{closed}	P _{open}	[TmrAB] [M]	[ATP] [M]	[TmrAB- ATP] [M]	K _{eq} [1/M]	Δ K _{eq}
0 °C	0.8163	0.1837	0.000040815	0.049990815	0.000009185	4.5	1.3
25 °C	0.6696	0.3304	0.00003348	0.04998348	0.00001652	10	3
40 °C	0.5254	0.4746	0.00002627	0.04997627	0.00002373	18	5
50 °C	0.4072	0.5928	0.00002036	0.04997036	0.00002964	29	9
60 °C	0.3588	0.6412	0.00001794	0.04996794	0.00003206	36	10
70 °C	0.3263	0.6737	0.000016315	0.049966315	0.000033685	41	12
80 °C	0.3547	0.6453	0.000017735	0.049967735	0.000032265	36	11

b)

Temp.	P _{closed}	P _{open}	[TmrAB] [M]	[ATP] [M]	[TmrAB- ATP] [M]	K _{eq} [1/M ²]	Δ K _{eq}
0 °C	0.8163	0.1837	0.000040815	0.04998163	0.000009185	90	30
25 °C	0.6696	0.3304	0.00003348	0.04996696	0.00001652	200	60
40 °C	0.5254	0.4746	0.00002627	0.04995254	0.00002373	360	100
50 °C	0.4072	0.5928	0.00002036	0.04994072	0.00002964	580	170
60 °C	0.3588	0.6412	0.00001794	0.04993588	0.00003206	700	200
70 °C	0.3263	0.6737	0.000016315	0.04993263	0.000033685	800	300
80 °C	0.3547	0.6453	0.000017735	0.04993547	0.000032265	700	200

c)

Temp.	P _{closed}	P _{open}	[TmrAB] [M]	[ATP] [M]	[TmrAB- ATP] [M]	K _{eq} [1/M]	Δ K _{eq}
0 °C	0.7747	0.2253	0.000038735	0.049988735	0.000011265	5.8	1.7
25 °C	0.6659	0.3341	0.000033295	0.049983295	0.000016705	10	3
40 °C	0.5328	0.4672	0.00002664	0.04997664	0.00002336	18	5
50 °C	0.4133	0.5867	0.000020665	0.049970665	0.000029335	28	8
60 °C	0.3885	0.6115	0.000019425	0.049969425	0.000030575	31	9
70 °C	0.3544	0.6456	0.00001772	0.04996772	0.00003228	36	11
80 °C	0.3896	0.6104	0.00001948	0.04996948	0.00003052	31	9

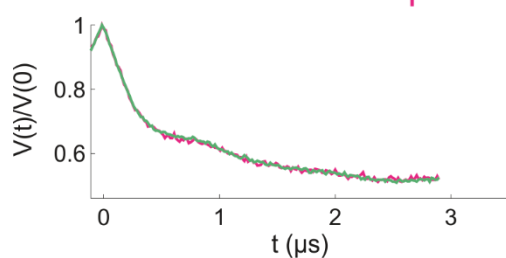
d)

Temp.	P _{closed}	P _{open}	[TmrAB] [M]	[ATP] [M]	[TmrAB- ATP] [M]	K _{eq} [1/M ²]	Δ K _{eq}
0 °C	0.7747	0.2253	0.000038735	0.04997747	0.000011265	120	40
25 °C	0.6659	0.3341	0.000033295	0.04996659	0.000016705	200	60
40 °C	0.5328	0.4672	0.00002664	0.04995328	0.00002336	350	100
50 °C	0.4133	0.5867	0.000020665	0.04994133	0.000029335	570	160
60 °C	0.3885	0.6115	0.000019425	0.04993885	0.000030575	630	180
70 °C	0.3544	0.6456	0.00001772	0.04993544	0.00003228	700	200
80 °C	0.3896	0.6104	0.00001948	0.04993896	0.00003052	630	180

TmrA288B272

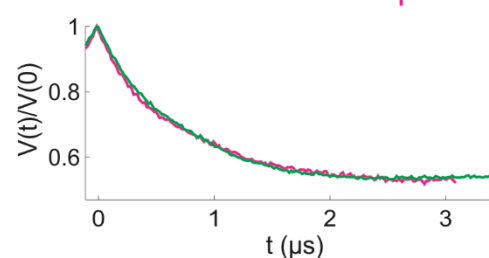
25 °C ATP-EDTA

25 °C ATP-EDTA + 50 μM K5F



50 °C ATP-EDTA

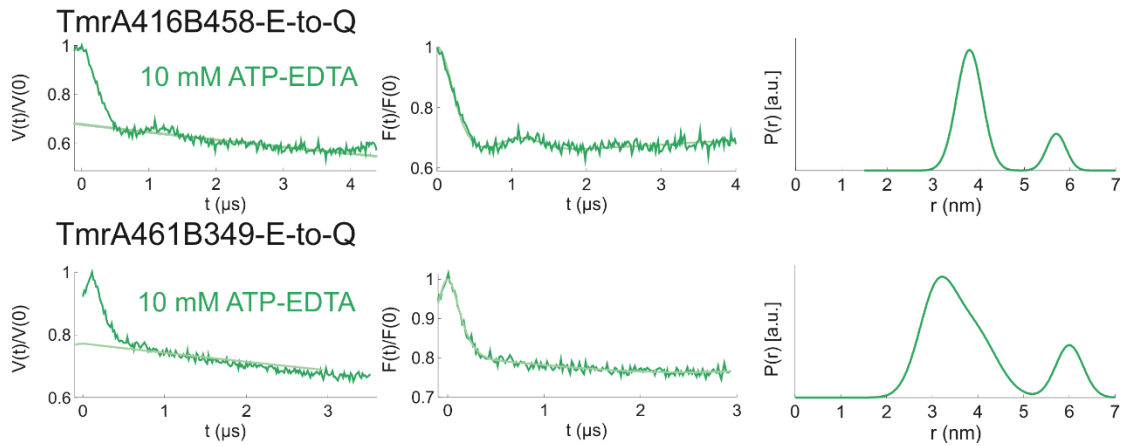
50 °C ATP-EDTA + 50 μM K5F



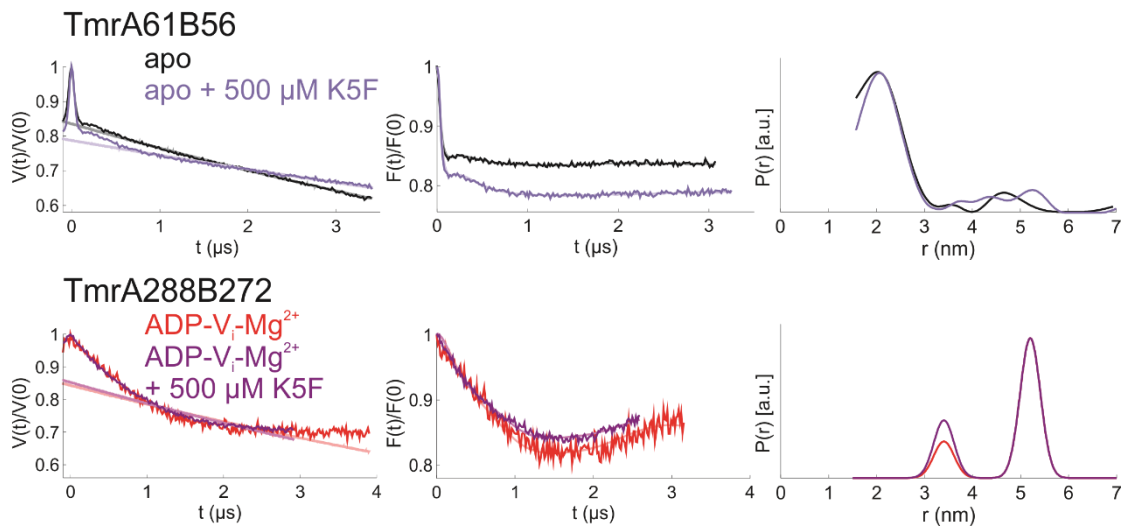
Supp. Figure 2: Peptide is not changing the temperature dependence of the conformational equilibrium induced by ATP binding at the periplasmic gate TmrA288B272. The peptide was added in a 1:1 ratio to the protein concentration and in the original data no difference between the two measurements can be observed at 25 or 50 °C. (Data analysis performed with DeerAnalysis 2016)

Supp. Table 4: Fitting parameters for the non-linear polynomial fit of second order. This is based on the equation $\ln k_{eq} = a + b \cdot \frac{1}{T} + c \cdot \left(\frac{1}{T}\right)^2$. Shown are the parameters for all positions and both models (one or two bound ATP) with errors given by origin.

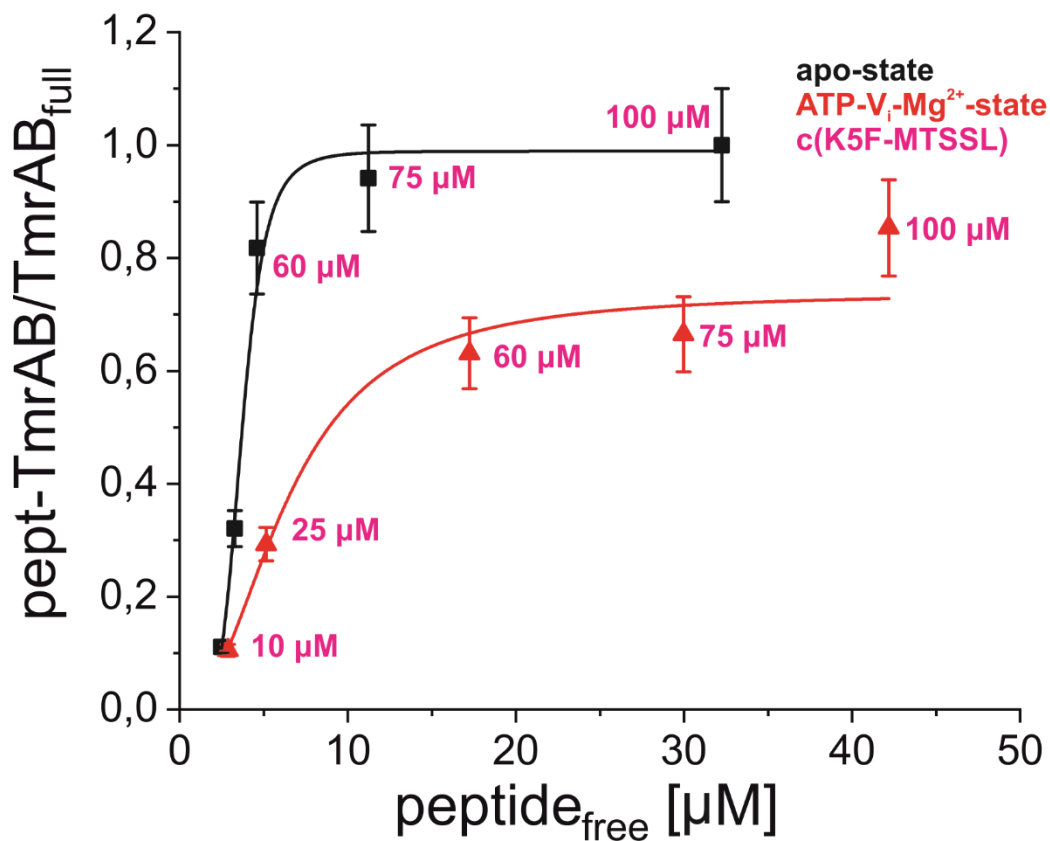
	a	b	c
TmrA416B458 (1 ATP)	-74 ± 13	51000 ± 8000	-8300000 ± 1200000
TmrA416B458 (2 ATP)	-72 ± 13	51000 ± 9000	-8300000 ± 1200000
TmrA461B349 (1 ATP)	-81 ± 8	55000 ± 5000	-9000000 ± 800000
TmrA461B349 (2 ATP)	-79 ± 8	55000 ± 5000	-9000000 ± 800000
TmrA288B272 (1 ATP)	1.2 ± 12	4000 ± 7000	-100000 ± 1100000
TmrA288B272 (2 ATP)	4.2 ± 12	4000 ± 7000	-100000 ± 1100000



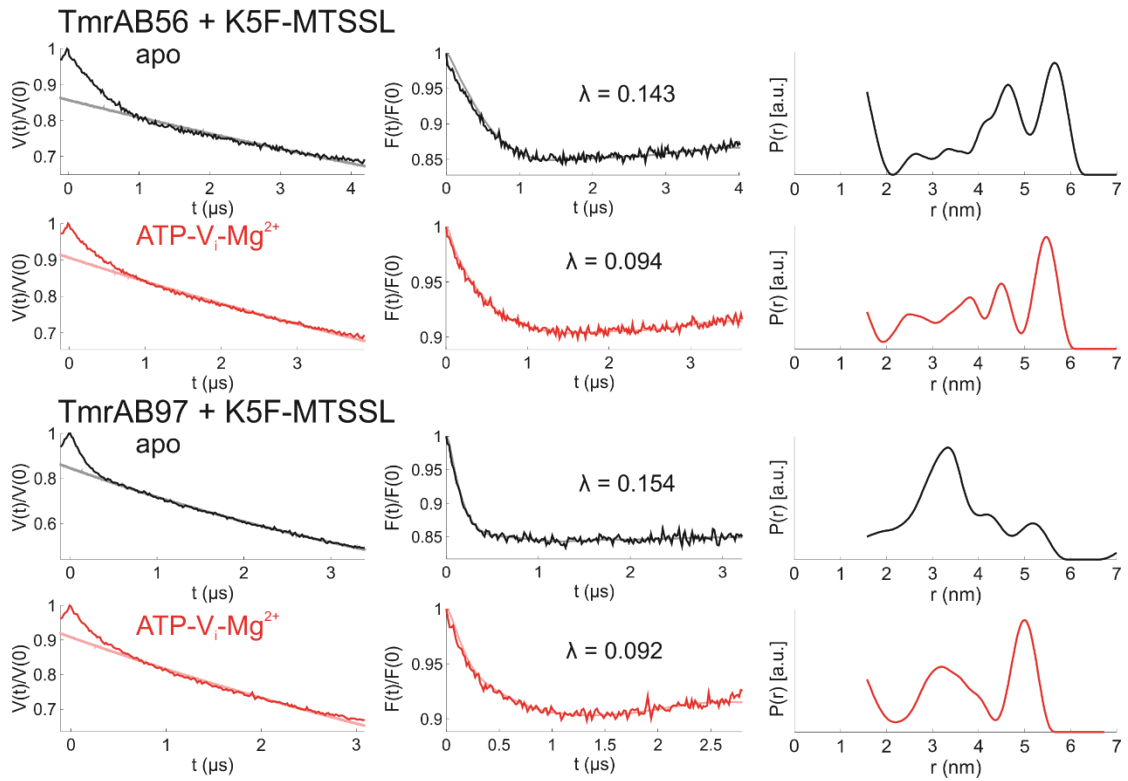
Supp. Figure 3: Gaussian fitting for the ATP-EDTA states of the degenerate NBS TmrA416B458-E-to-Q and consensus NBS TmrA461B349-E-to-Q. Two Gaussian fittings on the degenerate NBS shows a partial closure $\theta = 0.81$ and for the consensus, NBS $\theta = 0.45$. Original data $V(t)/V(0)$ are displayed on the left, background corrected data $F(t)/F(0)$ are displayed in the middle and the distance distributions $P(r)$ are shown on the right. (Data analysis performed with DeerAnalysis 2016 for TmrA416B458-E-to-Q and DD6c for TmrA461B349-E-to-Q)



Supp. Figure 4: Excess of substrate is not changing the apo or ADP- V_i - Mg^{2+} state at the periplasmic gate. On top for TmrA61B56 in the apo-state, no significant difference is visible after addition of 500 μ M K5F peptide. The data were fitted with Tikhonov regularization. Below for TmrA288B272 for ADP- V_i - Mg^{2+} with two Gaussian fittings with the distances $r = 3.4 \pm 0.3$ nm and $r = 5.2 \pm 0.3$ nm no significant difference is visible after addition of 500 μ M K5F peptide. Original data $V(t)/V(0)$ are displayed on the left, background corrected data $F(t)/F(0)$ are displayed in the middle and the distance distributions $P(r)$ are shown on the right. (Data analysis performed with DeerAnalysis 2016)



Supp. Figure 5: Peptide binding observed with cw spectroscopy. To obtain the presented curves peptide (MTSSL labelled K5F) was added in the indicated concentrations to 50 μM TmrAB (cysteinless, unlabelled) and heated to 68 $^{\circ}\text{C}$ either without any nucleotides (apo) or with 10 mM ATP, 10 mM Mg^{2+} and 10 mM ortho-vanadate (ATP-V_i-Mg²⁺). By comparison with the free spin-labelled peptide, the fraction of free and bound peptide to the transporter was calculated. The free peptide is displayed on the x-axis and the bound peptide divided by the total added peptide amount is displayed on the y-axis.



Supp. Figure 6: Distance measurements between single-labelled TmrAB and the MTSSL-labelled K5F peptide. Shown are the apo-states in black and the ATP- V_i - Mg^{2+} -states in red for TmrAB56 at the periplasmic gate and TmrAB97 at the cytosolic gate. Original data $V(t)/V(0)$ are displayed on the left, background corrected data $F(t)/F(0)$ are displayed in the middle and the distance distributions $P(r)$ are shown on the right. The modulation depth (λ) is slightly decreasing with ATP- V_i - Mg^{2+} and no clear distance distributions could be obtained in any of the analysed cases. (Data analysis performed with DeerAnalysis 2016)

Cooperation partner

All the work in this thesis has been done by myself, if not differently stated. The project was mainly supervised by Dr Benesh Joseph and Prof. Thomas F. Prisner was my PhD supervisor. Prof. Robert Tampé is the collaboration partner who gave me a lab space in his laboratories and from his group, I got the basic plasmid, with which I worked. Dr Anne Nöll (Tampé lab) introduced me to the protocols for mutant cloning, expression, purification and transport assays, which I performed by myself. The competent cells which I used were prepared by members of the Tampé lab. Susanne Hank (Tampé lab) performed an ATPase assay, which was shown in the JACS publication, which is not shown in this thesis but referred to. Dr Philipp E. Spindler (Prisner lab) performed the 7-pulse CP-PELDOR measurements and the background correction procedure for two samples; this is already mentioned in the sections where this data is shown.

References

- (1) Thomas, C.; Tampé, R. Multifaceted Structures and Mechanisms of ABC Transport Systems in Health and Disease. *Curr. Opin. Struct. Biol.* **2018**, *51*, 116–128. <https://doi.org/10.1016/j.sbi.2018.03.016>.
- (2) Nöll, A.; Thomas, C.; Herbring, V.; Zollmann, T.; Barth, K.; Mehdipour, A. R.; Tomasiak, T. M.; Brüchert, S.; Joseph, B.; Abele, R.; et al. Crystal Structure and Mechanistic Basis of a Functional Homolog of the Antigen Transporter TAP. *Proc. Natl. Acad. Sci.* **2016**, *114* (4), E438–E447. <https://doi.org/10.1073/pnas.1620009114>.
- (3) Barth, K.; Hank, S.; Spindler, P. E.; Prisner, T. F.; Tampé, R.; Joseph, B. Conformational Coupling and Trans-Inhibition in the Human Antigen Transporter Ortholog TmrAB Resolved with Dipolar EPR Spectroscopy. *J. Am. Chem. Soc.* **2018**, *140* (13), 4527–4533. <https://doi.org/10.1021/jacs.7b12409>.
- (4) McHaourab, H. S.; Steed, P. R.; Kazmier, K. Toward the Fourth Dimension of Membrane Protein Structure: Insight into Dynamics from Spin-Labeling EPR Spectroscopy. *Structure* **2011**, *19* (11), 1549–1561. <https://doi.org/10.1016/j.str.2011.10.009>.
- (5) Hellmich, U. A.; Glaubitz, C. NMR and EPR Studies of Membrane Transporters. *Biol. Chem.* **2009**, *390* (8), 815–834. <https://doi.org/10.1515/BC.2009.084>.
- (6) Claxton, D. P.; Kazmier, K.; Mishra, S.; McHaourab, H. S. Navigating Membrane Protein Structure, Dynamics, and Energy Landscapes Using Spin Labeling and EPR Spectroscopy. *Methods Enzymol.* **2015**, *564*, 1–35. <https://doi.org/10.1016/bs.mie.2015.07.026>.
- (7) Seeger, M. A. Membrane Transporter Research in Times of Countless Structures. *Biochim. Biophys. Acta - Biomembr.* **2018**, *1860* (4), 804–808. <https://doi.org/10.1016/j.bbamem.2017.08.009>.
- (8) Wlodawer, A.; Minor, W.; Dauter, Z.; Jaskolski, M. Protein Crystallography for Non-Crystallographers, or How to Get the Best (but Not More) from Published Macromolecular Structures. *FEBS J.* **2008**, *275* (1), 1–21. <https://doi.org/10.1111/j.1742-4658.2007.06178.x>.
- (9) Rambo, R. P.; Tainer, J. A. Super-Resolution in Solution X-Ray Scattering and Its

- Applications to Structural Systems Biology. *Annu. Rev. Biophys.* **2013**, *42* (1), 415–441. <https://doi.org/10.1146/annurev-biophys-083012-130301>.
- (10) Mertens, H. D. T.; Svergun, D. I. Structural Characterization of Proteins and Complexes Using Small-Angle X-Ray Solution Scattering. *J. Struct. Biol.* **2010**, *172* (1), 128–141. <https://doi.org/10.1016/j.jsb.2010.06.012>.
- (11) Murata, K.; Wolf, M. Cryo-Electron Microscopy for Structural Analysis of Dynamic Biological Macromolecules. *Biochim. Biophys. Acta - Gen. Subj.* **2018**, *1862* (2), 324–334. <https://doi.org/10.1016/j.bbagen.2017.07.020>.
- (12) Bonvin, A. M. J. J.; Boelens, R.; Kaptein, R. NMR Analysis of Protein Interactions. *Curr. Opin. Chem. Biol.* **2005**, *9* (5), 501–508. <https://doi.org/10.1016/j.cbpa.2005.08.011>.
- (13) Hong, M.; Zhang, Y.; Hu, F. Membrane Protein Structure and Dynamics from NMR Spectroscopy. *Annu. Rev. Phys. Chem.* **2014**, *63*, 1–24. <https://doi.org/10.1146/annurev-physchem-032511-143731.Membrane>.
- (14) Barnes, A. B.; De Paëpe, G.; van der Wel, P. C. A.; Hu, K.-N.; Joo, C.-G.; Bajaj, V. S.; Mak-Jurkauskas, M. L.; Sirigiri, J. R.; Herzfeld, J.; Temkin, R. J.; et al. High-Field Dynamic Nuclear Polarization for Solid and Solution Biological NMR. *Appl. Magn. Reson.* **2008**, *34* (3–4), 237–263. <https://doi.org/10.1007/s00723-008-0129-1>.
- (15) Marion, D. An Introduction to Biological NMR Spectroscopy. *Mol. Cell. Proteomics* **2013**, *12* (11), 3006–3025. <https://doi.org/10.1074/mcp.O113.030239>.
- (16) Piston, D. W.; Kremers, G. J. Fluorescent Protein FRET: The Good, the Bad and the Ugly. *Trends Biochem. Sci.* **2007**, *32* (9), 407–414. <https://doi.org/10.1016/j.tibs.2007.08.003>.
- (17) Klare, J. P. Site-Directed Spin Labeling EPR Spectroscopy in Protein Research. *Biol. Chem.* **2013**, *394* (10), 1281–1300. <https://doi.org/10.1515/hsz-2013-0155>.
- (18) Jeschke, G. DEER Distance Measurements on Proteins. *Annu. Rev. Phys. Chem.* **2012**, *63* (1), 419–446. <https://doi.org/10.1146/annurev-physchem-032511-143716>.
- (19) Loura, L. FRET in Membrane Biophysics: An Overview. *Front. Physiol.* **2011**, *2*, 82. <https://doi.org/10.3389/fphys.2011.00082>.
- (20) Pannier, M.; Veit, S.; Godt, A.; Jeschke, G.; Spiess, H. . Dead-Time Free Measurement

- of Dipole–Dipole Interactions between Electron Spins. *J. Magn. Reson.* **2000**, *142* (2), 331–340. <https://doi.org/10.1006/jmre.1999.1944>.
- (21) Spindler, P. E.; Waclawska, I.; Endeward, B.; Plackmeyer, J.; Ziegler, C.; Prisner, T. F. Carr-Purcell Pulsed Electron Double Resonance with Shaped Inversion Pulses. *J. Phys. Chem. Lett.* **2015**, *6* (21), 4331–4335. <https://doi.org/10.1021/acs.jpcclett.5b01933>.
- (22) Hospital, A.; Goñi, J. R.; Orozco, M.; Gelpí, J. Molecular Dynamics Simulations: Advances and Applications. *Adv. Appl. Bioinforma. Chem.* **2015**, *8*, 37–47. <https://doi.org/10.2147/AABC.S70333>.
- (23) Liu, H.; Li, D.; Li, Y.; Hou, T. Atomistic Molecular Dynamics Simulations of ATP-Binding Cassette Transporters. *Wiley Interdiscip. Rev. Comput. Mol. Sci.* **2016**, *6* (3), 255–265. <https://doi.org/10.1002/wcms.1247>.
- (24) Locher, K. P. Mechanistic Diversity in ATP-Binding Cassette (ABC) Transporters. *Nat. Struct. Mol. Biol.* **2016**, *23* (6), 487–493. <https://doi.org/10.1038/nsmb.3216>.
- (25) ter Beek, J.; Guskov, A.; Slotboom, D. J. Structural Diversity of ABC Transporters. *J. Gen. Physiol.* **2014**, *143* (4), 419–435. <https://doi.org/10.1085/jgp.201411164>.
- (26) Wilkens, S. Structure and Mechanism of ABC Transporters. *F1000Prime Rep.* **2015**, *7* (14), 1–9. <https://doi.org/10.12703/P7-14>.
- (27) Zhang, X. C.; Han, L.; Zhao, Y. Thermodynamics of ABC Transporters. *Protein Cell* **2016**, *7* (1), 17–27. <https://doi.org/10.1007/s13238-015-0211-z>.
- (28) Ford, R. C.; Beis, K. Learning the ABCs One at a Time: Structure and Mechanism of ABC Transporters. *Biochem. Soc. Trans.* **2019**. <https://doi.org/10.1042/BST20180147>.
- (29) Boumendjel, A.; Boutonnat, J.; Robert, J. *ABC Transporters and Multidrug Resistance*; John Wiley & Sons, Inc.: Hoboken, NJ, USA, 2009. <https://doi.org/10.1002/9780470495131>.
- (30) George, A. M. *ABC Transporters - 40 Years On*, first edit.; George, A. M., Ed.; Springer International Publishing: Cham, 2016. <https://doi.org/10.1007/978-3-319-23476-2>.
- (31) Hohl, M.; Briand, C.; Grütter, M. G.; Seeger, M. A. Crystal Structure of a Heterodimeric ABC Transporter in Its Inward-Facing Conformation. *Nat. Struct. Mol. Biol.* **2012**, *19* (4), 395–402. <https://doi.org/10.1038/nsmb.2267>.

- (32) Rees, D. C.; Johnson, E.; Lewinson, O. ABC Transporters: The Power to Change. *Nat. Rev. Mol. Cell Biol.* **2009**, *10* (3), 218–227. <https://doi.org/10.1038/nrm2646>.
- (33) Vetter, I. R.; Wittinghofer, A. Nucleoside Triphosphate-Binding Proteins: Different Scaffolds to Achieve Phosphoryl Transfer. *Q. Rev. Biophys.* **1999**, *32* (1), 1–56. <https://doi.org/10.1017/S0033583599003480>.
- (34) Oldham, M. L.; Khare, D.; Quioco, F. A.; Davidson, A. L.; Chen, J. Crystal Structure of a Catalytic Intermediate of the Maltose Transporter. *Nature* **2007**, *450* (7169), 515–521. <https://doi.org/10.1038/nature06264>.
- (35) Korkhov, V. M.; Mireku, S. A.; Locher, K. P. Structure of AMP-PNP-Bound Vitamin B 12 Transporter BtuCD-F. *Nature* **2012**, *490* (7420), 367–372. <https://doi.org/10.1038/nature11442>.
- (36) Xu, K.; Zhang, M.; Zhao, Q.; Yu, F.; Guo, H.; Wang, C.; He, F.; Ding, J.; Zhang, P. Crystal Structure of a Folate Energy-Coupling Factor Transporter from *Lactobacillus Brevis*. *Nature* **2013**, *497* (7448), 268–271. <https://doi.org/10.1038/nature12046>.
- (37) Korkhov, V. M.; Mireku, S. A.; Veprintsev, D. B.; Locher, K. P. Structure of AMP-PNP-bound BtuCD and Mechanism of ATP-Powered Vitamin B12 Transport by BtuCD-F. *Nat. Struct. Mol. Biol.* **2014**, *21* (12), 1097–1099. <https://doi.org/10.1038/nsmb.2918>.
- (38) Yu, Y.; Zhou, M.; Kirsch, F.; Xu, C.; Zhang, L.; Wang, Y.; Jiang, Z.; Wang, N.; Li, J.; Eitinger, T.; et al. Planar Substrate-Binding Site Dictates the Specificity of ECF-Type Nickel/Cobalt Transporters. *Cell Res.* **2014**, *24* (3), 267–277. <https://doi.org/10.1038/cr.2013.172>.
- (39) Schmitt, L.; Tampé, R. Structure and Mechanism of ABC Transporters. *Curr. Opin. Struct. Biol.* **2002**, *12* (6), 754–760. [https://doi.org/10.1016/S0959-440X\(02\)00399-8](https://doi.org/10.1016/S0959-440X(02)00399-8).
- (40) Dean, M.; Annilo, T. Evolution of the ATP-Binding Cassette (ABC) Transporter Superfamily in Vertebrates. *Annu. Rev. Genomics Hum. Genet.* **2005**, *6* (1), 123–142. <https://doi.org/10.1146/annurev.genom.6.080604.162122>.
- (41) Aleksandrov, A. A.; Aleksandrov, L. A.; Riordan, J. R. CFTR (ABCC7) Is a Hydrolyzable-Ligand-Gated Channel. *Pflügers Arch. - Eur. J. Physiol.* **2007**, *453* (5), 693–702. <https://doi.org/10.1007/s00424-006-0140-z>.

- (42) Zhang, Z.; Chen, J. Atomic Structure of the Cystic Fibrosis Transmembrane Conductance Regulator. *Cell* **2016**, *167* (6), 1586–1597.e9.
<https://doi.org/10.1016/J.CELL.2016.11.014>.
- (43) Liu, F.; Zhang, Z.; Csanády, L.; Gadsby, D. C.; Chen, J. Molecular Structure of the Human CFTR Ion Channel. *Cell* **2017**, *169* (1), 85–95.e8.
<https://doi.org/10.1016/J.CELL.2017.02.024>.
- (44) Bryan, J.; Muñoz, A.; Zhang, X.; Düfer, M.; Drews, G.; Krippeit-Drews, P.; Aguilar-Bryan, L. ABCC8 and ABCC9: ABC Transporters That Regulate K⁺ Channels. *Pflügers Arch. - Eur. J. Physiol.* **2007**, *453* (5), 703–718.
<https://doi.org/10.1007/s00424-006-0116-z>.
- (45) Li, N.; Wu, J.-X.; Ding, D.; Cheng, J.; Gao, N.; Chen, L. Structure of a Pancreatic ATP-Sensitive Potassium Channel. *Cell* **2017**, *168* (1–2), 101–110.e10.
<https://doi.org/10.1016/j.cell.2016.12.028>.
- (46) Martin, G. M.; Yoshioka, C.; Rex, E. A.; Fay, J. F.; Xie, Q.; Whorton, M. R.; Chen, J. Z.; Shyng, S.-L. Cryo-EM Structure of the ATP-Sensitive Potassium Channel Illuminates Mechanisms of Assembly and Gating. *Elife* **2017**, *6*.
<https://doi.org/10.7554/eLife.24149>.
- (47) Martin, G. M.; Kandasamy, B.; DiMaio, F.; Yoshioka, C.; Shyng, S.-L. Anti-Diabetic Drug Binding Site in a Mammalian KATP Channel Revealed by Cryo-EM. *Elife* **2017**, *6*. <https://doi.org/10.7554/eLife.31054>.
- (48) Dawson, R. J. P.; Locher, K. P. Structure of a Bacterial Multidrug ABC Transporter. *Nature* **2006**, *443* (7108), 180–185. <https://doi.org/10.1038/nature05155>.
- (49) Bauer, B. E.; Wolfger, H.; Kuchler, K. Inventory and Function of Yeast ABC Proteins: About Sex, Stress, Pleiotropic Drug and Heavy Metal Resistance. *Biochim. Biophys. Acta - Biomembr.* **1999**, *1461* (2), 217–236. [https://doi.org/10.1016/S0005-2736\(99\)00160-1](https://doi.org/10.1016/S0005-2736(99)00160-1).
- (50) Nürenberg, E.; Tampé, R. Tying up Loose Ends: Ribosome Recycling in Eukaryotes and Archaea. *Trends Biochem. Sci.* **2013**, *38* (2), 64–74.
<https://doi.org/10.1016/J.TIBS.2012.11.003>.
- (51) Oldham, M. L.; Grigorieff, N.; Chen, J. Structure of the Transporter Associated with Antigen Processing Trapped by Herpes Simplex Virus. *Elife* **2016**, *5*.

<https://doi.org/10.7554/eLife.21829>.

- (52) Blees, A.; Janulienė, D.; Hofmann, T.; Koller, N.; Schmidt, C.; Trowitzsch, S.; Moeller, A.; Tampé, R. Structure of the Human MHC-I Peptide-Loading Complex. *Nature* **2017**, *551* (7681), 525. <https://doi.org/10.1038/nature24627>.
- (53) Aittoniemi, J.; Fotinou, C.; Craig, T. J.; de Wet, H.; Proks, P.; Ashcroft, F. M. Review. SUR1: A Unique ATP-Binding Cassette Protein That Functions as an Ion Channel Regulator. *Philos. Trans. R. Soc. Lond. B. Biol. Sci.* **2009**, *364* (1514), 257–267. <https://doi.org/10.1098/rstb.2008.0142>.
- (54) Perez, C.; Gerber, S.; Boilevin, J.; Bucher, M.; Darbre, T.; Aebi, M.; Reymond, J.-L.; Locher, K. P. Structure and Mechanism of an Active Lipid-Linked Oligosaccharide Flippase. *Nature* **2015**, *524* (7566), 433–438. <https://doi.org/10.1038/nature14953>.
- (55) Mi, W.; Li, Y.; Yoon, S. H.; Ernst, R. K.; Walz, T.; Liao, M. Structural Basis of MsbA-Mediated Lipopolysaccharide Transport. *Nature* **2017**, *549* (7671), 233–237. <https://doi.org/10.1038/nature23649>.
- (56) Tarling, E. J.; de Aguiar Vallim, T. Q.; Edwards, P. A. Role of ABC Transporters in Lipid Transport and Human Disease. *Trends Endocrinol. Metab.* **2013**, *24* (7), 342–350. <https://doi.org/10.1016/j.tem.2013.01.006>.
- (57) Zhou, Z.; White, K. A.; Polissi, A.; Georgopoulos, C.; Raetz, C. R. Function of Escherichia Coli MsbA, an Essential ABC Family Transporter, in Lipid A and Phospholipid Biosynthesis. *J. Biol. Chem.* **1998**, *273* (20), 12466–12475. <https://doi.org/10.1074/JBC.273.20.12466>.
- (58) Bi, Y.; Mann, E.; Whitfield, C.; Zimmer, J. Architecture of a Channel-Forming O-Antigen Polysaccharide ABC Transporter. *Nature* **2018**, *553* (7688), 361–365. <https://doi.org/10.1038/nature25190>.
- (59) Morgan, J. L. W.; Acheson, J. F.; Zimmer, J. Structure of a Type-1 Secretion System ABC Transporter. *Structure* **2017**, *25* (3), 522–529. <https://doi.org/10.1016/j.str.2017.01.010>.
- (60) Luo, Q.; Yang, X.; Yu, S.; Shi, H.; Wang, K.; Xiao, L.; Zhu, G.; Sun, C.; Li, T.; Li, D.; et al. Structural Basis for Lipopolysaccharide Extraction by ABC Transporter LptB2FG. *Nat. Struct. Mol. Biol.* **2017**, *24* (5), 469–474. <https://doi.org/10.1038/nsmb.3399>.

- (61) Tran, A. X.; Dong, C.; Whitfield, C. Structure and Functional Analysis of LptC, a Conserved Membrane Protein Involved in the Lipopolysaccharide Export Pathway in *Escherichia Coli*. *J. Biol. Chem.* **2010**, *285* (43), 33529–33539. <https://doi.org/10.1074/jbc.M110.144709>.
- (62) Suits, M. D. L.; Sperandio, P.; Dehò, G.; Polissi, A.; Jia, Z. Novel Structure of the Conserved Gram-Negative Lipopolysaccharide Transport Protein A and Mutagenesis Analysis. *J. Mol. Biol.* **2008**, *380* (3), 476–488. <https://doi.org/10.1016/J.JMB.2008.04.045>.
- (63) Dong, H.; Xiang, Q.; Gu, Y.; Wang, Z.; Paterson, N. G.; Stansfeld, P. J.; He, C.; Zhang, Y.; Wang, W.; Dong, C. Structural Basis for Outer Membrane Lipopolysaccharide Insertion. *Nature* **2014**, *511* (7507), 52–56. <https://doi.org/10.1038/nature13464>.
- (64) Fitzpatrick, A. W. P.; Llabrés, S.; Neuberger, A.; Blaza, J. N.; Bai, X.-C.; Okada, U.; Murakami, S.; van Veen, H. W.; Zachariae, U.; Scheres, S. H. W.; et al. Structure of the MacAB–TolC ABC-Type Tripartite Multidrug Efflux Pump. *Nat. Microbiol.* **2017**, *2* (7), 17070. <https://doi.org/10.1038/nmicrobiol.2017.70>.
- (65) Sherman, D. J.; Xie, R.; Taylor, R. J.; George, A. H.; Okuda, S.; Foster, P. J.; Needleman, D. J.; Kahne, D. Lipopolysaccharide Is Transported to the Cell Surface by a Membrane-to-Membrane Protein Bridge. *Science* **2018**, *359* (6377), 798–801. <https://doi.org/10.1126/science.aar1886>.
- (66) Zutz, A.; Hoffmann, J.; Hellmich, U. A.; Glaubitz, C.; Ludwig, B.; Brutschy, B.; Tampé, R. Asymmetric ATP Hydrolysis Cycle of the Heterodimeric Multidrug ABC Transport Complex TmrAB from *Thermus Thermophilus*. *J. Biol. Chem.* **2011**, *286* (9), 7104–7115. <https://doi.org/10.1074/jbc.M110.201178>.
- (67) Kim, J. M.; Wu, S.; Tomasiak, T. M.; Mergel, C.; Winter, M. B.; Stiller, S. B.; Robles-Colmanares, Y.; Stroud, R. M.; Tampé, R.; Craik, C. S.; et al. Subnanometre-Resolution Electron Cryomicroscopy Structure of a Heterodimeric ABC Exporter. *Nature* **2015**, *517* (7534), 396–400. <https://doi.org/10.1038/nature13872>.
- (68) Goldfarb, D.; Stoll, S. *EPR Spectroscopy: Fundamentals and Methods*, first edit.; John Wiley & Sons Ltd: Chichester, 2018.
- (69) Weil, J. A.; Bolton, J. R. *Electron Paramagnetic Resonance*, second edi.; John Wiley

- & Sons, Inc.: Hoboken, 2006. <https://doi.org/10.1002/0470084987>.
- (70) Geschwind, S. *Electron Paramagnetic Resonance*, first edit.; Springer US: New York, 1972.
- (71) Schweiger, A.; Jeschke, G. *Principles of Pulse Electron Paramagnetic Resonance*, first edit.; Oxford University Press: New York, 2001.
- (72) Hemminga, M. A.; Berliner, L. J. *ESR Spectroscopy in Membrane Biophysics*, first edit.; Springer US: Boston, 2007. <https://doi.org/10.1007/978-0-387-49367-1>.
- (73) Drescher, M.; Jeschke, G. *EPR Spectroscopy - Applications in Chemistry and Biology*, first edit.; Drescher, M., Jeschke, G., Eds.; Springer Berlin Heidelberg: Berlin, Heidelberg, 2012. <https://doi.org/10.1007/978-3-642-28347-5>.
- (74) Altenbach, C.; Flitsch, S. L.; Khorana, H. G.; Hubbell, W. L. Structural Studies on Transmembrane Proteins. 2. Spin Labeling of Bacteriorhodopsin Mutants at Unique Cysteines. *Biochemistry* **1989**, *28* (19), 7806–7812. <https://doi.org/10.1021/bi00445a042>.
- (75) Altenbach, C.; Marti, T.; Khorana, H.; Hubbell, W. Transmembrane Protein Structure: Spin Labeling of Bacteriorhodopsin Mutants. *Science (80-.)*. **1990**, *248* (4959), 1088–1092. <https://doi.org/10.1126/science.2160734>.
- (76) Reginsson, G. W.; Schiemann, O. Pulsed Electron-Electron Double Resonance: Beyond Nanometre Distance Measurements on Biomacromolecules. *Biochem. J.* **2011**, *434* (3), 353–363. <https://doi.org/10.1042/BJ20101871>.
- (77) Jeschke, G.; Polyhach, Y. Distance Measurements on Spin-Labelled Biomacromolecules by Pulsed Electron Paramagnetic Resonance. *Phys. Chem. Chem. Phys.* **2007**, *9* (16), 1895. <https://doi.org/10.1039/b614920k>.
- (78) Fleissner, M. R.; Brustad, E. M.; Kálai, T.; Altenbach, C.; Cascio, D.; Peters, F. B.; Hideg, K.; Peuker, S.; Schultz, P. G.; Hubbell, W. L. Site-Directed Spin Labeling of a Genetically Encoded Unnatural Amino Acid. *Proc. Natl. Acad. Sci. U. S. A.* **2009**, *106* (51), 21637–21642. <https://doi.org/10.1073/pnas.0912009106>.
- (79) Raitsimring, A. M.; Gunanathan, C.; Potapov, A.; Efremenko, I.; Martin, J. M. L.; Milstein, D.; Goldfarb, D. Gd³⁺ Complexes as Potential Spin Labels for High Field Pulsed EPR Distance Measurements. *J. Am. Chem. Soc.* **2007**, *129* (46), 14138–14139.

- <https://doi.org/10.1021/JA075544G>.
- (80) Lueders, P.; Jeschke, G.; Yulikov, M. Double Electron–Electron Resonance Measured Between Gd³⁺ Ions and Nitroxide Radicals. *J. Phys. Chem. Lett.* **2011**, *2* (6), 604–609. <https://doi.org/10.1021/jz200073h>.
- (81) Yulikov, M.; Lueders, P.; Farooq Warsi, M.; Chechik, V.; Jeschke, G. Distance Measurements in Au Nanoparticles Functionalized with Nitroxide Radicals and Gd³⁺–DTPA Chelate Complexes. *Phys. Chem. Chem. Phys.* **2012**, *14* (30), 10732. <https://doi.org/10.1039/c2cp40282c>.
- (82) Lueders, P.; Jäger, H.; Hemminga, M. A.; Jeschke, G.; Yulikov, M. Distance Measurements on Orthogonally Spin-Labeled Membrane Spanning WALP23 Polypeptides. *J. Phys. Chem. B* **2013**, *117* (7), 2061–2068. <https://doi.org/10.1021/jp311287t>.
- (83) MMM software <http://www.epr.ethz.ch/software.html> (accessed Feb 12, 2019).
- (84) Polyhach, Y.; Bordignon, E.; Jeschke, G. Rotamer Libraries of Spin Labelled Cysteines for Protein Studies W. *Phys. Chem. Chem. Phys.* **2011**, *13*, 2356–2366. <https://doi.org/10.1039/c0cp01865a>.
- (85) Bordignon, E.; Steinhoff, H.-J. Membrane Protein Structure and Dynamics Studied by Site-Directed Spin-Labeling ESR. In *ESR Spectroscopy in Membrane Biophysics*; Springer US: Boston, MA, 2007; pp 129–164. https://doi.org/10.1007/978-0-387-49367-1_5.
- (86) Milov, A. D.; Salikhov, K. M.; Shchirov, M. D. Application of the Double Resonance Method to Electron Spin Echo in a Study of the Spatial Distribution of Paramagnetic Centers in Solids. *Fiz. Tverd. Tela* **1981**, *23*, 975–982.
- (87) Xu, Q.; Ellena, J. F.; Kim, M.; Cafiso, D. S. Substrate-Dependent Unfolding of the Energy Coupling Motif of a Membrane Transport Protein Determined by Double Electron-Electron Resonance. *Biochemistry* **2006**, *45* (36), 10847–10854. <https://doi.org/10.1021/bi061051x>.
- (88) Ward, R.; Bowman, A.; Sozudogru, E.; El-Mkami, H.; Owen-Hughes, T.; Norman, D. G. EPR Distance Measurements in Deuterated Proteins. *J. Magn. Reson.* **2010**, *207* (1), 164–167. <https://doi.org/10.1016/j.jmr.2010.08.002>.

- (89) Carr, H. Y.; Purcell, E. M. Effects of Diffusion on Free Precession in Nuclear Magnetic Resonance Experiments. *Phys. Rev.* **1954**, *94* (3), 630–638.
<https://doi.org/10.1103/PhysRev.94.630>.
- (90) Borbat, P. P.; Georgieva, E. R.; Freed, J. H. Improved Sensitivity for Long-Distance Measurements in Biomolecules: Five-Pulse Double Electron–Electron Resonance. *J. Phys. Chem. Lett.* **2013**, *4* (1), 170–175. <https://doi.org/10.1021/jz301788n>.
- (91) Rosenfeld, D.; Zur, Y. Is the Sech/Tanh Adiabatic Pulse Really Adiabatic? *J. Magn. Reson.* **1998**, *132* (1), 102–108. <https://doi.org/10.1006/JMRE.1998.1394>.
- (92) Jeschke, G.; Chechik, V.; Ionita, P.; Godt, A.; Zimmermann, H.; Banham, J.; Timmel, C. R.; Hilger, D.; Jung, H. DeerAnalysis2006 - a Comprehensive Software Package for Analyzing Pulsed ELDOR Data. **2006**, *30*, 473–498.
- (93) Brandon, S.; Beth, A. H.; Hustedt, E. J. The Global Analysis of DEER Data. *J. Magn. Reson.* **2012**, *218*, 93–104. <https://doi.org/10.1016/j.jmr.2012.03.006>.
- (94) Stein, R. A.; Beth, A. H.; Hustedt, E. J. A Straightforward Approach to the Analysis of Double Electron–Electron Resonance Data; 2015; pp 531–567.
<https://doi.org/10.1016/bs.mie.2015.07.031>.
- (95) Barth, K. Conformational Dynamics of TmrAB by PELDOR, Goethe University Frankfurt am Main, 2015.
- (96) Homology Model - SWISS-MODEL <https://swissmodel.expasy.org/> (accessed Mar 12, 2019).
- (97) Dawson, R. J. P.; Locher, K. P. Structure of the Multidrug ABC Transporter Sav1866 from *Staphylococcus Aureus* in Complex with AMP-PNP. *FEBS Lett.* **2007**, *581* (5), 935–938. <https://doi.org/10.1016/j.febslet.2007.01.073>.
- (98) Choudhury, H. G.; Tong, Z.; Mathavan, I.; Li, Y.; Iwata, S.; Zirah, S.; Rebuffat, S.; van Veen, H. W.; Beis, K. Structure of an Antibacterial Peptide ATP-Binding Cassette Transporter in a Novel Outward Occluded State. *Proc. Natl. Acad. Sci.* **2014**, *111* (25), 9145–9150. <https://doi.org/10.1073/pnas.1320506111>.
- (99) Bordignon, E.; Grutter, M. G.; Seeger, M. A.; Hohl, M.; Schoppe, J.; Hurlimann, L. M.; Bohm, S. Structural Basis for Allosteric Cross-Talk between the Asymmetric Nucleotide Binding Sites of a Heterodimeric ABC Exporter. *Proc. Natl. Acad. Sci.*

- 2014**, *111* (30), 11025–11030. <https://doi.org/10.1073/pnas.1400485111>.
- (100) vanadate preparation https://www.sigmaaldrich.com/content/dam/sigma-aldrich/docs/Sigma/Product_Information_Sheet/1/s6508pis.pdf (accessed Mar 7, 2019).
- (101) Thermo Scientific, Phusion High-Fidelity DNA Polymerase <https://www.thermofisher.com/order/catalog/product/F530L> (accessed Mar 7, 2019).
- (102) Eurofins Genomic <https://www.eurofinsgenomics.eu/de/home.aspx?gclid=CJeA1baylsUCFWrpgodgkKAKQ> (accessed Mar 7, 2019).
- (103) Thermo Scientific, GeneRuler 1 kb Plus DNA ladder <https://static.fishersci.com/images/F100447~wl.jpg> (accessed Mar 7, 2019).
- (104) CLC sequence viewer http://resources.qiagenbioinformatics.com/manuals/clcsequenceviewer/current/User_Manual.pdf (accessed Mar 7, 2019).
- (105) Qiagen Ni-NTA agarose manual <https://www.qiagen.com/de/resources/resourcedetail?id=79ca2f7d-42fe-4d62-8676-4cfa948c9435&lang=en> (accessed Mar 7, 2019).
- (106) DeerAnalysis software <http://www.epr.ethz.ch/software.html> (accessed Mar 12, 2019).
- (107) DD software <https://lab.vanderbilt.edu/hustedt-lab/dd/> (accessed Mar 12, 2019).
- (108) Borbat, P. P.; Surendhran, K.; Bortolus, M.; Zou, P.; Freed, J. H.; Mchaourab, H. S. Conformational Motion of the ABC Transporter MsbA Induced by ATP Hydrolysis. *PLoS Biol.* **2007**, *5* (10), e271. <https://doi.org/10.1371/journal.pbio.0050271>.
- (109) Mishra, S.; Verhalen, B.; Stein, R. A.; Wen, P. C.; Tajkhorshid, E.; Mchaourab, H. S. Conformational Dynamics of the Nucleotide Binding Domains and the Power Stroke of a Heterodimeric ABC Transporter. *Elife* **2014**, *2014* (3), 1–19. <https://doi.org/10.7554/eLife.02740>.
- (110) Timachi, M. H.; Hutter, C. A.; Hohl, M.; Assafa, T.; Böhm, S.; Mittal, A.; Seeger, M. A.; Bordignon, E. Exploring Conformational Equilibria of a Heterodimeric ABC Transporter. *Elife* **2017**, *6*, 1–28. <https://doi.org/10.7554/eLife.20236>.
- (111) Ward, A.; Reyes, C. L.; Yu, J.; Roth, C. B.; Chang, G. Flexibility in the ABC

- Transporter MsbA: Alternating Access with a Twist. *Proc. Natl. Acad. Sci.* **2007**, *104* (48), 19005–19010. <https://doi.org/10.1073/pnas.0709388104>.
- (112) Johnson, Z. L.; Chen, J. Structural Basis of Substrate Recognition by the Multidrug Resistance Protein MRP1. *Cell* **2017**, *168* (6), 1075–1085.e9. <https://doi.org/10.1016/j.cell.2017.01.041>.
- (113) Verhalen, B.; Dastvan, R.; Thangapandian, S.; Peskova, Y.; Koteiche, H. A.; Nakamoto, R. K.; Tajkhorshid, E.; McHaourab, H. S. Energy Transduction and Alternating Access of the Mammalian ABC Transporter P-Glycoprotein. *Nature* **2017**, *543* (7647), 738–741. <https://doi.org/10.1038/nature21414>.
- (114) Anderson, M. P.; Berger, H. A.; Rich, D. P.; Gregory, R. J.; Smith, A. E.; Welsh, M. J. Nucleoside Triphosphates Are Required to Open the CFTR Chloride Channel. *Cell* **1991**, *67* (4), 775–784. [https://doi.org/10.1016/0092-8674\(91\)90072-7](https://doi.org/10.1016/0092-8674(91)90072-7).
- (115) Wang, W.; Wu, J.; Bernard, K.; Li, G.; Wang, G.; Bevenssee, M. O.; Kirk, K. L. ATP-Independent CFTR Channel Gating and Allosteric Modulation by Phosphorylation. *Proc. Natl. Acad. Sci.* **2010**, *107* (8), 3888–3893. <https://doi.org/10.1073/pnas.0913001107>.
- (116) Wei, S.; Roessler, B. C.; Chauvet, S.; Guo, J.; Hartman IV, J. L.; Kirk, K. L. Conserved Allosteric Hot Spots in the Transmembrane Domains of Cystic Fibrosis Transmembrane Conductance Regulator (CFTR) Channels and Multidrug Resistance Protein (MRP) Pumps. *J. Biol. Chem.* **2014**, *289* (29), 19942–19957. <https://doi.org/10.1074/jbc.M114.562116>.
- (117) Smith, P. C.; Karpowich, N.; Millen, L.; Moody, J. E.; Rosen, J.; Thomas, P. J.; Hunt, J. F. ATP Binding to the Motor Domain from an ABC Transporter Drives Formation of a Nucleotide Sandwich Dimer. *Mol. Cell* **2002**, *10* (1), 139–149. [https://doi.org/10.1016/S1097-2765\(02\)00576-2](https://doi.org/10.1016/S1097-2765(02)00576-2).
- (118) Grossmann, N.; Vakkasoglu, A. S.; Hulpke, S.; Abele, R.; Gaudet, R.; Tampé, R. Mechanistic Determinants of the Directionality and Energetics of Active Export by a Heterodimeric ABC Transporter. *Nat. Commun.* **2014**, *5* (1), 5419. <https://doi.org/10.1038/ncomms6419>.
- (119) Aleksandrov, L.; Aleksandrov, A. A.; Chang, X. B.; Riordan, J. R. The First Nucleotide Binding Domain of Cystic Fibrosis Transmembrane Conductance Regulator

- Is a Site of Stable Nucleotide Interaction, Whereas the Second Is a Site of Rapid Turnover. *J. Biol. Chem.* **2002**, 277 (18), 15419–15425.
<https://doi.org/10.1074/jbc.M111713200>.
- (120) Sauna, Z. E.; Ambudkar, S. V. Evidence for a Requirement for ATP Hydrolysis at Two Distinct Steps during a Single Turnover of the Catalytic Cycle of Human P-Glycoprotein. *Proc. Natl. Acad. Sci.* **2002**, 97 (6), 2515–2520.
<https://doi.org/10.1073/pnas.97.6.2515>.
- (121) Wassenberg, D.; Liebl, W.; Jaenicke, R. Maltose-Binding Protein from the Hyperthermophilic Bacterium *Thermotoga Maritima*: Stability and Binding Properties. *J. Mol. Biol.* **2000**, 295 (2), 279–288. <https://doi.org/10.1006/jmbi.1999.3367>.
- (122) Vieira, E. D.; Basso, L. G. M.; Costa-Filho, A. J. Non-Linear van't Hoff Behavior in Pulmonary Surfactant Model Membranes. *Biochim. Biophys. Acta - Biomembr.* **2017**, 1859 (6), 1133–1143. <https://doi.org/10.1016/j.bbamem.2017.03.011>.
- (123) Kodama, T. Reaction Heats and Heat Capacity Changes for Intermediate Steps of the ATP Hydrolysis Catalyzed by Myosin Subfragment 1. *J. Biol. Chem.* **1981**, 256 (6), 2928–2933.
- (124) Jones, P. M.; George, A. M. Molecular-Dynamics Simulations of the ATP/Apo State of a Multidrug ATP-Binding Cassette Transporter Provide a Structural and Mechanistic Basis for the Asymmetric Occluded State. *Biophys. J.* **2011**, 100 (12), 3025–3034.
<https://doi.org/10.1016/j.bpj.2011.05.028>.
- (125) Jones, P. M.; George, A. M. Opening of the ADP-Bound Active Site in the ABC Transporter ATPase Dimer: Evidence for a Constant Contact, Alternating Sites Model for the Catalytic Cycle. *Proteins Struct. Funct. Bioinforma.* **2009**, 75 (2), 387–396.
<https://doi.org/10.1002/prot.22250>.
- (126) Senior, A. E.; Al-Shawi, M. K.; Urbatsch, I. L. The Catalytic Cycle of P-Glycoprotein. *FEBS Lett.* **1995**, 377 (3), 285–289. [https://doi.org/10.1016/0014-5793\(95\)01345-8](https://doi.org/10.1016/0014-5793(95)01345-8).
- (127) Qiao, S.; Luo, Q.; Zhao, Y.; Zhang, X. C.; Huang, Y. Structural Basis for Lipopolysaccharide Insertion in the Bacterial Outer Membrane. *Nature* **2014**, 511 (7507), 108–111. <https://doi.org/10.1038/nature13484>.
- (128) Sherman, D. J.; Lazarus, M. B.; Murphy, L.; Liu, C.; Walker, S.; Ruiz, N.; Kahne, D. Decoupling Catalytic Activity from Biological Function of the ATPase That Powers

- Lipopolysaccharide Transport. *Proc. Natl. Acad. Sci.* **2014**, *111* (13), 4982–4987. <https://doi.org/10.1073/pnas.1323516111>.
- (129) Zollmann, T.; Moiset, G.; Tumulka, F.; Tampé, R.; Poolman, B.; Abele, R. Single Liposome Analysis of Peptide Translocation by the ABC Transporter TAPL. *Proc. Natl. Acad. Sci.* **2015**, *112* (7), 2046–2051. <https://doi.org/10.1073/pnas.1418100112>.
- (130) Chaves, L. A. P.; Gadsby, D. C. Cysteine Accessibility Probes Timing and Extent of NBD Separation along the Dimer Interface in Gating CFTR Channels. *J. Gen. Physiol.* **2015**, *145* (4), 261–283. <https://doi.org/10.1085/jgp.201411347>.
- (131) Gadsby, D. C.; Vergani, P.; Csanády, L. The ABC Protein Turned Chloride Channel Whose Failure Causes Cystic Fibrosis. *Nature* **2006**, *440* (7083), 477–483. <https://doi.org/10.1038/nature04712>.
- (132) Collauto, A.; Mishra, S.; Litvinov, A.; Mchaourab, H. S.; Goldfarb, D. Direct Spectroscopic Detection of ATP Turnover Reveals Mechanistic Divergence of ABC Exporters. *Structure* **2017**, *25* (8), 1264–1274.e3. <https://doi.org/10.1016/j.str.2017.06.014>.
- (133) Göddeke, H.; Timachi, M. H.; Hutter, C. A. J.; Galazzo, L.; Seeger, M. A.; Karttunen, M.; Bordignon, E.; Schäfer, L. V. Atomistic Mechanism of Large-Scale Conformational Transition in a Heterodimeric ABC Exporter. *J. Am. Chem. Soc.* **2018**, *140* (13), 4543–4551. <https://doi.org/10.1021/jacs.7b12944>.
- (134) Eggensperger, S.; Fisette, O.; Parcej, D.; Schäfer, L. V.; Tampé, R. An Annular Lipid Belt Is Essential for Allosteric Coupling and Viral Inhibition of the Antigen Translocation Complex TAP (Transporter Associated with Antigen Processing). *J. Biol. Chem.* **2014**, *289* (48), 33098–33108. <https://doi.org/10.1074/jbc.M114.592832>.

Acknowledgement

First of all, I want to thank Prof. Thomas F. Prisner, who gave me the opportunity to make my PhD in his group. In the scientific discussions, he always gave constructive suggestions and new approaches. More than that he was in general very supporting and also shared his own experiences when it was about career planning. Especially I also want to thank Dr Benesh Joseph, who was the main supervisor of my project and introduced me at the beginning into everything that I needed to know for the EPR experiments and was always present for discussions during my whole thesis. Furthermore, I also want to thank Prof. Robert Tampé, who gave me the opportunity to work on a protein, which was established by his group, and also gave me working space in his laboratory. Moreover, we had several helpful discussion about the project with him.

I also want to thank in general all the people from the Prisner lab for the nice time, but a few members have to be mentioned in particular. First of all Dr Burkhard Endeward, who was always helping, if I had any problem with my computer or one of the spectrometers. He was always assigning measurement time as much as needed and thereby often did not take days for himself. Then I also want to thank Dr Alberto Collauto, who also was very helpful, especially with the DD software and simulations with easy spin, although he never wanted to allow me to thank him, he cannot stop me at this point ;). Dr Philipp E. Spindler, who helped to make the 7-pulse-measurements. Moreover, I want to thank Silke Schneider who was always very helpful and engaged. Sigrid Kämmerer for ordering chemicals, organisation of various things and just for being such a nice office mate. In addition, also Thilo Hetzke, who was also a great office mate and was always helping me with my computer or other issues. Dr Claudia Grytz, Dr Denise Schütz and Eva Jaumann for the nice time during lunch breaks and everything else ;). And of course, everyone who read my thesis and gave me corrections.

In addition, I also want to thank in general all people from the Tampé lab for the nice time, but also here a few members have to be mentioned in particular. Dr Anne Nöll who showed me during my master thesis, how to prepare the protein and how to make transport assays. She was always very helpful. Stefan Brüchert and Philipp Höllthaler, who always helped me if I had trouble to find something or were helping me if I had a biochemical question. Moreover, Susanne Hank who contributed the ATPase assay to the JACS publication.

I also want to thank especially for funding and support the German Research Foundation Grants SFB 807 – Membrane Transport and Communication and Cluster of Excellence EXC 115 – Dynamics of Macromolecular Complexes for funding. Moreover, the BMRZ and the institute

of physical and theoretical chemistry need to be mentioned for seminars, workshops and support.

Apart from that I also want to thank my parents who supported me during my whole life and have played a large role in where I am today. Especially I want to thank my mother and my sister, although we had a tough time in the last three years, they were always persons to rely on. And of course, I also want to thank Nemo, who came as a puppy at the beginning of my PhD and is now the best jogging partner and helps to come down after a stressing day. Now at the end of my PhD, also Finn the puppy joined our family and is also a nice distraction from a stressing day.